Understanding lignin's fast pyrolysis through examination of the thermolysis mechanisms of model oligomers

A Dissertation Presented for the

Doctor of Philosophy

Degree

The University of Tennessee, Knoxville

Ross Wesley Houston

August 2023

Copyright @ 2023 by Ross Wesley Houston
All rights reserved

Acknowledgments

I want to thank my Ph.D. advisor and mentor, Dr. Nourredine Abdoulmoumine, for allowing me this opportunity to work on this exciting project. His support has been invaluable to me, and I am incredibly grateful. I also want to thank the members of my dissertation committee: Drs. Julie Carrier, Paul Frymier, Douglas Hayes, and Philip (Xiaofei) Ye. Their advice and suggestions helped shape this dissertation into its final form.

I am extremely thankful to my loving fiancée, Rebecca. You have been with me every step of the way. Without your constant love and support, I would not have made it this far. To my family, thank you for your support and encouragement on this journey; it meant the world to have such an amazing support system around me.

I would also like to thank the Department of Biosystems Engineering and Soil Science faculty and staff at the University of Tennessee. I would especially like to thank my current and former research group members, Ekramul Ehite, Skye Li, Conner Pope, Dr. Bernard Baffour Asare Bediako, and Dr. Oluwafemi Oyedeji, for always being willing to offer help and push myself to be the best I could be.

To my dad: there were moments where I never thought I would get to say it, but its finally time, “It’s too easy!”

Abstract

The lignocellulosic biorefinery is a visionary concept that endeavors to provide an alternative to fossil-based refineries by producing biobased fungible fuels and specialty chemicals almost exclusively derived currently from petroleum refineries. This vision of the lignocellulosic biorefinery can only be realized if all fractions of lignocellulosic biomass are efficiently deconstructed and valorized to generate a diverse portfolio of products to sustain it against market vicissitudes. Of the three main structural constituents of lignocellulosic biomass (i.e., cellulose, hemicellulose, and lignin), lignin is underutilized despite being the most abundant renewable source of aromatic platform chemicals in the world.

One pathway for lignin valorization includes its efficient fractionation followed by controlled deconstruction. Through the thermochemical deconstruction route, the focus of this dissertation project, greater understanding of the thermal deconstruction or depolymerization reactions and their associated kinetics is necessary to control competing reaction pathways to improve selectivity toward desirable products and increase yields.

In this project, we seek to deepen our mechanistic understanding of the prevalent reaction pathways during the thermal deconstruction of lignin by computationally and experimentally investigating model lignin oligomers with important linkages found in lignin. Insight of the thermal deconstruction pathways of oligomeric lignin fragments with diverse linkages is a key missing piece of the puzzle

required to develop fuller and generalizable lignin thermal deconstruction mechanisms. We will employ density functional theory (DFT), a computational quantum chemistry investigative tool, to assess the reactivity of a combination of important lignin linkages in the model oligomers. We will then experimentally pyrolyze commercially available model compounds with dimers closely related to the model compounds used in the DFT investigation using a pulse heated pyrolysis reactor (PHPR) system developed for this project. The PHPR system overcomes transport limitations found in commercial pyroprobe systems used in milligram-scale biomass pyrolysis studies. We will use this system to identify major products and intermediates and validate the results obtained from the computational calculations. The computational and experimental findings will be used to identifying general reactivity trends between the major interunit linkages of lignin and propose and validate reaction mechanisms and kinetics for each model oligomer.

Table of Contents

CHAPTER 1 INTRODUCTION 1

1.1. Problem Statement 5

1.2. Research proposal and objectives 6

1.3. Organization of the Dissertation 9

References 12

CHAPTER 2 LITERATURE REVIEW – THE CURRENT STATE OF LIGNIN PYROLYSIS: EXPERIMENTAL AND THEORETICAL APPROACHES TO ELUCIDATE REACTION MECHANISMS 15

2.1. Introduction 16

2.2. Lignin structure and isolation 18

2.3. Reaction mechanisms and kinetics for lignin model compounds 20

2.3.1. Experimental determination of lignin reaction mechanisms 23

2.3.2. Computational investigation of lignin pyrolysis mechanisms 43

2.4. Pathways going forward 65

2.5. Conclusions 69

References 71

CHAPTER 3 COMPUTATIONAL INVESTIGATION INTO THE PYROLYSIS BOND DISSOCIATION ENTHALPIES (BDE) OF MODEL LIGNIN OLIGOMERS USING DENSITY FUNCTIONAL THEORY(DFT) 83

Abstract 84

3.1. Introduction 85

3.2. Materials and methods 89

3.2.1. Oligomer selection 89

3.2.2. Computational setup 93

3.3. Results and discussion 99

3.3.1. Conformational analysis 99

3.3.2. Bond dissociation enthalpies (BDEs) 103

3.4. Conclusions 118

References 120

Appendix III 125

CHAPTER 4 COMPUTATIONAL DETERMINATION OF REACTION MECHANISMS AND KINETICS OF LIGNIN OLIGOMER PYROLYSIS WITH A COMBINATION OF IMPORTANT LINKAGES, E.G., β-O-4, α-O-4, β-5, β-β', AND 4-O-5, THROUGH DENSITY FUNCTIONAL THEORY 210

Abstract 211

4.1. Introduction 212

4.2. Materials and methods 214

4.2.1. Oligomer and reaction class selection 214

4.2.2. Computational setup 216

4.3. Results and discussion 230

4.3.1. Reaction pathways for Model Compound 1 230

4.3.2. Reaction pathways for model compound 2 244

4.3.3. Reaction pathways for model compound 3 249

4.5. Conclusions 253

References 255

Appendix IV 258

CHAPTER 5 INVESTIGATION OF LIGNIN MODEL COMPOUNDS USING PULSE-HEATED PYROLYSIS EXPERIMENTS 307

Abstract 308

5.1. Introduction 308

5.2. Materials and methods 311

5.2.1. Materials 311

5.2.2. Experimental setup 312

5.2.3. Pulse -heated pyrolysis experiments 317

5.2.4. Data collection and analysis 320

5.3. Results and discussion 320

5.3.1. Evaluation of the PHPR system 321

5.3.2. Pulse-heated pyrolysis of PPE 323

5.3.3. Pulse-heated pyrolysis of DPE 329

5.3.4. Pulse-heated pyrolysis of BPE 333

5.4. Recommendations for future work 339

5.5. Conclusions 341

References 345

Appendix V 348

CHAPTER 6 CONCLUSIONS AND FUTURE RECOMMENDATIONS 351

6.1. Conclusions 351

6.2. Future recommendations 354

6.2.1. Further investigation into the concerted mechanisms associated with lignin pyrolysis through density functional theory 354

6.2.2. Implementation of a heating control loop that incorporates a feedback control loop to better control the temperature in the PHPR system 355

VITA 356

List of Tables

Table 2-1. Comparison of apparent kinetic rate parameters on isolated lignin from literature using various models. 30

Table 2-2. Comparison of estimated and experimental parameters for PPE pyrolysis. 48

Table 2-3. Comparison of bond dissociation enthalpies of model β-O-4 dimers. 66

Table 3-1. Relative enthalpy difference of optimized structure for each stereoisomer of the model tetramer at the M06-2X/6-311++G(d,p) level of theory at 298.15 K. ... 101

Table 3-2. Interatomic distances between aromatic rings of different stereoisomers of the model tetramer. 102

Table 3-3. Ring angles between the aromatic rings of different stereoisomers of the model tetramer. 104

Table 3-4. Relative enthalpy difference between stereoisomers for model compound 2 at the M06-2X/6-311++G(d,p) level of theory at 773.15 K 107

Table 3-5. Bond dissociation enthalpies, $\Delta H298$, (kcal/mol) for each stereoisomer conformation of MC1 at 298.15 K. 109

Table 3-6. Bond dissociation enthalpies, $\Delta H773$, (kcal/mol) for each stereoisomer conformation of MC1 at 773.15 K. 112

Table 3-7. Bond dissociation enthalpies, $\Delta H773$, (kcal mol^{-1}) for each stereoisomer of MC2 at 773.15 K. 114

Table 3-8. Bond dissociation enthalpies, $\Delta H773$, (kcal mol^{-1}) of MC2 at 773.15 K. .. 115

Table 5-1. Retention times for the primary products identified during online MS analysis of the pulse-heated pyrolysis experiments. 327

Table 5-2. Relative areas of the primary products identified during online GC/MS analysis of PPE at various temperatures. 330

Table 5-3. Retention times for the primary products identified during online MS analysis of the pulse-heated pyrolysis experiments. 332

Table 5-4. Relative areas of the primary products identified during online GC/MS analysis of PPE at various temperatures. 338

List of Figures

Figure 2-1. Chemical structures of the building blocks of native lignin. 21

Figure 2-2. Activation energy distributions from the DG-DAEM of four isolated lignin polymers. Figure taken from Wang et al.[74] 28

Figure 2-3. Proposed radical mechanism of PPE pyrolysis by Britt et al.[108] Adapted from Beste et al.[109] 37

Figure 2-4. Initial steps of the proposed PPE pyrolysis mechanisms. (1) α-position homolytic cleavage (2) β-position homolytic cleavage, (3) retro-ene fragmentation, and (4) Maccoll elimination[111]. 39

Figure 2-5. Proposed VGE pyrolysis pathways[116] 46

Figure 2-6. Median and range of BDEs for the classes of lignin model compounds investigated by Kim et al. [144] 49

Figure 2-7. Bond dissociation pathways of dibenzodioxocin model compound proposed by Elder[147] 50

Figure 2-8. Proposed reaction mechanism for guaiacol pyrolysis. Image used from Yerrayya et al.(2019)[136]. 55

Figure 2-9. Reaction energy profile for PPE pyrolysis[161]. 59

Figure 2-10. Activation energies for the initial step in each pathway. Step 1: β-O scission, Step 2: α -β scission, Steps 3-5: concerted pathways[166]. 60

Figure 2-11. Proposed pericyclic reaction mechanism for PPE[169]. 63

Figure 3-1. The structure of the lignin model oligomers used in our computational work. **a**. Model oligomer #1 is 4-(3-hydroxy-1-(4-[3-(hydroxymethyl)-5-[(1E)-3-

hydroxyprop-1-en-1-yl]-7-methoxy-2,3-dihydro-1-benzofuran-2-yl]-2-methoxyphenoxy)-2-(4-[(1E)-3-hydroxyprop-1-en-1-yl]-2-methoxyphenoxy) propyl)-2-methoxyphenol. It is a tetramer with four chiral centers (*) and β-O-4(blue), α-O-4 (red), and β-5 (green) linkages. **b**. Model oligomer #2 is hedyotisol, with eight chiral centers, two β-O-4(blue) linkages, and a β-β(pink) linkage. **c**. Model oligomer #3 is 4-(4-[4-(acetyloxy)-3-methoxyphenyl]-hexahydrofuro [3,4-c]furan-1-yl)-2-(4-(4-[4-(acetyloxy)-3-methoxyphenyl]-hexahydrofuro [3,4-c]furan-1-yl)-2-methoxyphenoxy) phenyl acetate. It has eight chiral centers, two β-β(pink) linkages, and one 4-O-5(orange) linkage. 91

Figure 3-2. Visualization of interatomic distances and ring angle calculations for MC1. 96

Figure 3-3. List of homolytic reactions investigated for the model lignin oligomer. . 97

Figure 3-4. List of homolytic bond scissions for each interunit linkage investigated for MC2 and MC3. 98

Figure 3-5. Optimized geometries for each stereoisomer of the MC1 at M06-2X/6-311++G(d,p). 105

Figure 3-6. Optimized geometries of each stereoisomer of MC2 (left) and MC3 (right) determined using M06-2X/6-311++G(d,p)..... 108

Figure 3-7. Spin density plots for the di-radical species formed from scission along the β-β′ linkage for the RRRSSRRR stereoisomer in MC1. 117

Figure 4-1. Structures of the three model oligomers investigated. Interunit linkages are color-coded, and relevant carbon positions have been highlighted in red. 217

Figure 4-2. The proposed reactions for a β-O-4 reaction class with three reaction pathways denoted by 1), 2), and 3). 220

Figure 4-3. The proposed class of reactions for the α-O-4 linkage. Pathway 1 is the homolytic cleavage and stabilization, and pathway 2 is the decomposition pathway. 222

Figure 4-4. The proposed class of reactions for the β-5 linkage with the C_α-O subclass. 224

Figure 4-5. The proposed class of reactions for the β-5 linkage with the C_α-C_β subclass. 225

Figure 4-6. The proposed class of reactions for the β-β′ linkage with the C_α-O subclass. 227

Figure 4-7. The proposed class of reactions for the β-β′ linkage with the C_α- C_β subclass. 228

Figure 4-8. The proposed class of reactions for the 4-O-5 linkage. 229

Figure 4-9. Schematic of the logic used in the development of the reaction mechanisms. 231

Figure 4-10. Reaction pathways for the lowest energy path associated with the four unique stabilization reactions of the β-5, C_α-O subclass. 235

Figure 4-11. Energy diagram for the four lowest energy pathways associated with the four unique stabilization reactions of the β-5, C_α-O subclass. 236

Figure 4-12. Reactions involved in the five lowest energy pathways of each secondary reaction path after resolving the C_α-C_β diradical of the β-5 interunit linkage. 238

Figure 4-13. Energy diagram for the five lowest energy pathways of each secondary reaction path after resolving the β-5 interunit linkage. Pathways that are similar in magnitude have been color coded for readability. 239

Figure 4-14. Reactions involved in the five lowest energy pathways of each secondary reaction path starting with the resolution of the β-O-4 interunit linkage. 240

Figure 4-15. Energy diagram for the five lowest energy pathways from distinct branches starting with the resolution of the β-O-4 interunit linkage. The species for the lowest energy pathway have been labeled for clarity. 241

Figure 4-16. Reactions involved in the three lowest energy pathways of each secondary reaction path starting with the resolution of the α-O-4 interunit linkage. 242

Figure 4-17. Energy diagram for the three lowest energy pathways of each secondary reaction path after resolving the α-O-4 interunit linkage. Pathways that are similar in magnitude have been color coded for readability. 243

Figure 4-18. Energy diagram for the lowest energy pathway associated with each type of initial reaction. 245

Figure 4-19. Energy diagram for the thermal deconstruction of MC2 with the lowest energy pathway associated with each type of initial reaction. 248

Figure 4-20. Energy diagram for the thermal deconstruction of MC3 with the lowest energy pathway associated with each type of initial reaction. 252

Figure 5-1. (Top) Mirror isometric views of the overall PHPR system. 1. Top block: 2. Bottom block: 3. Silicone rubber gasket, 4. Electric feedthrough, 5. pyrometer light pipe, 6. Back, top, and bottom cartridge heaters, 7. Front, top, and bottom cartridge

heaters, 8. Micro-channel cooling fluid inlet, 9. Micro-channel cooling fluid outlet, 10. carrier gas (He), 11. carrier gas and evolved gas outlet for online and offline analyses, 12. 1/16 in. thermocouple port, 13. 5/16 in. socket head screws. Note: Two additional thermocouple ports are included but not shown in this figure due to the angle. (Bottom) Images of the PHPR installed for offline (bottom, left) and online (bottom, right) analysis. The top insulation was removed to allow for visualization of the reactor. 314

Figure 5-2. Cross-sectional views of the PHPR's stacked thermal elements at increasing magnifications (1x, 6x, 12x, and 50x) to show the interfaces involved in heat transfer. 1. Copper brush, + lead; 2. Copper brush, - lead; 3. Micro-channel cooling block: 4. Aluminum nitride insulator: 5. Indium foil: 1008–1010 steel foil. 316

Figure 5-3. Overview of the two analytical analysis pathways used for evolved gas analysis. 319

Figure 5-4. Heating and cooling rates of model dimers for the 500 °C experimental condition. The time between data points is approximately 10 ms. There is a time-break between each run to allow for sufficient cooling to the initial temperature, which is not shown here. 324

Figure 5-5. Stacked total ion chromatogram (TIC) for pulse-heated pyrolysis of PPE at chosen pyrolysis temperatures. Primary products have been labeled: A: benzene, B: toluene, C: ethyl benzene, D: styrene, E: unknown #3, F: benzaldehyde, and G: phenol. 328

Figure 5-6. FID chromatogram for the offline analysis of PPE pyrolysis at various temperatures. Primary products have been labeled: 1: styrene, 2: tri-substituted benzene, 3: diethyl benzenes, and 4: polycyclic recombination products.....331

Figure 5-7. Stacked total ion chromatogram (TIC) for pulse-heated pyrolysis of DPE at chosen pyrolysis temperatures. Primary products have been labeled: A: benzene, D: styrene, E: unknown #3, and H: guaiacol. 334

Figure 5-8. FID chromatogram for the offline analysis of DPE pyrolysis at various temperatures. Primary products have been labeled: 1: styrene, 2: tri-substituted benzene, 3: diethyl benzenes, and 4: polycyclic recombination products.....335

Figure 5-9. Stacked total ion chromatogram (TIC) for pulse-heated pyrolysis of BPE at chosen pyrolysis temperatures. Primary products have been labeled: A: benzene, B: toluene, E: unknown #3, F: benzaldehyde, G: phenol, and H: guaiacol. 337

Figure 5-10. FID chromatogram for the offline analysis of BPE pyrolysis at various temperatures. Primary products have been labeled: 1: styrene, 2: tri-substituted benzene, 3: diethyl benzenes, and 4: polycyclic recombination products.....340

Figure 5-11. A simplified schematic of the heating control loop for pulse heating of the PHPR system. The blue dashed line represents the feedback provided by the optical pyrometer, while the red dashed line represents the actual heating loop. The pyrometer converts the infrared emission of the sample into a milliamp signal corresponding to a temperature. The milliamp signal is converted to a 0-10 V via a signal converter before being fed back to the power supply as the feedback control. 342

Nomenclature

Symbol	Meaning
DFT	Density functional theory
BDE	Bond dissociation enthalpy
PHPR	Pulse-heated pyrolysis reactor
k	Pre-exponential factor
E_a	Activation energy
R	Universal gas constant
T	Temperature
$(V^* - V)$	Remaining amount of volatiles
W	Weight
t	Time
$f(E_a)$	Distribution function of activation energy
TGA	Thermogravimetric analysis
DTA	Differential thermal analysis
DAEM	Distributed activation energy models
Py-FTIR	Pyrolysis- Fourier-transform infrared spectroscopy
PPE	Phenethyl phenyl ether
DPE	Diphenyl ether
BPE	Benzyl phenyl ether
ΔH_{298}	Bond dissociation enthalpy at 298.15 K
ΔH_{773}	Bond dissociation enthalpy at 773.15 K

CHAPTER 1 INTRODUCTION

The increasing concern over climate change has promoted more focus on reducing global greenhouse gas emissions and decreasing the dependence on fossil fuels. In this regard, lignocellulosic biomass is an attractive source of renewable fuels and a potential alternative to fossil fuels. It can be converted to a liquid fuel as an alternative to petroleum and can be a source of hydrogen for the future[1]. Lignocellulosic biomass comprises three main structural constituents: cellulose, hemicellulose, and lignin. Cellulose, the primary component of lignocellulosic biomass, is considered the most abundant naturally occurring polymeric material on earth[2, 3]. Cellulose is a primarily crystalline, unbranched polysaccharide made up of linear glucose monomers linked via β-1,4-glycosidic bonds and is responsible for maintaining the structural integrity of the cell wall[4]. Hemicellulose is a heteropolymer consisting of pentose and hexose sugars, such as xylose, galactose, mannose, glucose, and arabinose[5]. Unlike cellulose, the composition of hemicellulose varies by biomass type because pentose and hexose monomers are joined together through various linkages. Lignin is a more complicated structure than both cellulose and hemicellulose. Lignin is a more complicated polymer than both cellulose and hemicellulose and does not share their carbohydrate structure. Lignin is synthesized by the enzymatic dehydrogenation of various aromatic 4-hydroxycinnamyl alcohol monomers, mainly p-hydroxyphenyl (H), guaiacyl (G), and syringyl (S) units. The resulting radicals are then randomly polymerized to form a complex, non-repeating three-dimensional structure[6-8]. These units are primarily connected by the β-O-4 linkage, which represents 60% of

linkages in lignin. However, there are several other linkages in lignin, adding to the complexity of its structure[9]. The resulting aromatic nature of lignin, as well as higher carbon content and lower oxygen content, compared to cellulose and hemicellulose, makes it an attractive potential source for many platform chemicals (e.g., benzene, toluene, and xylene (BTX)[10]) and fuels[11]. However, despite making up approximately 30 wt. % of lignocellulosic biomass and accounting for upwards of 40% of the total energy content, lignin is currently underutilized in relation to its valorization potential[12]. In most industrial biorefineries, lignin is treated as a by-product waste to be used as a fuel for process heat. Developing efficient conversion technologies for lignin can significantly increase the efficiency and economic competitiveness of biorefineries.

Several technologies are currently considered for the conversion of lignocellulosic biomass into chemicals, biomaterials, and fuels, most of which can be classified as either biochemical or thermochemical techniques[13]. Biochemical conversion generally involves breaking down the hemicellulose and cellulose fraction of lignocellulosic biomass into monomeric carbohydrates, which can then be further converted into chemicals and fuels, such as ethanol, via fermentation and other biological transformations. Examples of biochemical conversion techniques are fermentation of enzymatically and chemically hydrolyzed C_5 and C_6 biomass sugars. In-depth reviews of biochemical conversion techniques can be found elsewhere[14, 15]. Thermochemical conversion techniques degrade lignocellulosic biomass using high temperatures with or without catalysts. Thermochemical conversion consists of four main technologies: pyrolysis, gasification, combustion, and thermal liquefaction[16].

Thermochemical conversion techniques typically differ in the operating temperature range and the amount of oxygen supplied to the system. Pyrolysis is carried out at moderate temperatures (400–600 °C) with little to no oxygen. Gasification is performed above 700 °C with a sub-stoichiometric oxygen supply relative to the amount of oxygen required for complete combustion to achieve partial oxidation. Combustion is carried out in the presence of excess oxygen to ensure complete oxidation at temperatures above 1000 °C[17]. The products from each process are also different. Combustion is primarily used to produce process heat and carbon dioxide (CO_2) rich flue gas, whereas the major product of gasification is producer gas, a gas mixture with several small-molecular weight non-condensable gases (CO, H_2, CO_2, and CH_4)[18]. This producer gas can be further converted into chemicals or liquid hydrocarbon fuels[19]. Pyrolysis produces three major products: solid biochar, light gases, and a condensable liquid referred to as bio-oil.

Fast pyrolysis of lignocellulosic biomass has become an attractive potential source of renewable fuels due to the ability to directly produce bio-oil, a liquid intermediate fuel that can be upgraded to fungible fuels and other specialty chemicals currently derived from petroleum. More detailed review papers discussing the entire body of work on fast pyrolysis can be found elsewhere[20-22]. However, generally, fast pyrolysis of lignocellulosic biomass produces approximately 75 wt. % liquid bio-oil, 13 wt. % light gases, and 12 wt. % solid char[23]. However, even with this high liquid bio-oil yield, there are still significant obstacles that must be overcome before fast pyrolysis is cost-competitive with fossil fuels at the commercial scale.

Bio-oil has high oxygen content and contains hundreds of organic molecules of varying reactivity, which makes the oil unstable and requires a significant amount of downstream upgrading[24]. Additionally, the chemical and physical properties of bio-oil can also vary greatly depending on the operating conditions and the biomass source. Understanding the fundamental degradation reactions of lignocellulosic biomass at a mechanistic level will be an important step in designing and optimizing conversion processes and, in turn, improving the overall economics of lignocellulosic biomass thermochemical conversion.

The fast pyrolysis reaction mechanisms of lignocellulosic biomass are generally understood in terms of the three major structural constituents: cellulose, hemicellulose, and lignin, which have different degradation temperature ranges and follow different reaction mechanisms[25, 26]. Cellulose has a degradation range of approximately 240–400 °C and proceeds via the initial random disassociation of the glycosidic linkage to glucose to produce lower molecular weight fragments of the cellulose. These fragments then also undergo subsequent and random disassociation of additional glycosidic linkages until low molecular weight cellulose oligomers and smaller organic molecules (e.g., levoglucosan, carbon monoxide, carbon dioxide, hydrogen) are produced as terminal products[21, 27, 28]. Hemicellulose has the lowest onset degradation temperature at 200–315 °C and has been postulated to follow a similar decomposition path to that of cellulose[29]. Concerted depolymerization of hemicellulose produces a wide variety of low molecular weight organics via active intermeditates[21, 26, 27, 30]. Lignin has a large variety of side chains and interunit linkages with different chemical

reactivities and therefore degrades over a much wider range of temperatures, from 280 °C to 900 °C [21, 27]. The variety of side chains and interunit linkages introduce significant complexity to lignin's polymeric structure compared to its carbohydrate counterparts. Therefore, the mechanistic work on the pyrolysis of lignin lags behind that of both cellulose and hemicellulose. This research seeks to begin bridging the current knowledge gap to improve our mechanistic understanding of the thermal deconstruction of lignin.

1.1. Problem Statement

Native lignin or even large lignin substructures have been the subject of only a few computational and experimental investigations. As a result, there is little information on the reaction mechanism of lignin or larger lignin oligomers. In contrast, we know a great deal about cellulose and hemicellulose fast pyrolysis reaction mechanisms based on density functional theory (DFT) calculations and experimental investigations. The well-defined structures of cellulose and hemicellulose lend them to investigation of model structures that are easily extrapolated to the respective polymer. For example, cellulose was mechanistically investigated using the disaccharide cellobiose as cellulose is a linear polymer containing a single type of interunit linkage[28, 31]. Unlike cellulose, native lignin does not contain only one type of linkage, and the linkages are not linearly repeating[32]. Therefore, in the case of lignin, investigation of larger oligomers with multiple interunit linkages is required to capture the structural complexity of native lignin.

Current mechanistic research on lignin pyrolysis has been limited to proposing mechanisms for model lignin dimers, such as phenethyl phenyl ether containing one major interunit linkage, primarily β-O-4[33-36]. The pyrolysis behavior of these model dimers is invaluable to understanding lignin pyrolysis mechanisms; however, they are not directly applicable to a native lignin mechanism. The few attempts at developing lignin fast pyrolysis reaction mechanisms and kinetics are not generalizable due to the oversimplification of the modeled lignin structures[26, 37-39], or if they are generalized, they do not contain detailed descriptions of the initial lignin[40].

1.2. Research proposal and objectives

This research aims to develop a deeper understanding of the underlying reaction mechanisms associated with the fast pyrolysis of lignin by investigating the pyrolysis behavior of representative model lignin oligomers. This will be accomplished using both pulse-heated pyrolysis as an advanced experimental technique and DFT calculations as an advanced computational technique. DFT simulations will allow us to identify reactivity trends for combinations of lignin interlinkages based on reaction energetics. The DFT calculations will then be supplemented using pulse-heated pyrolysis.

This dissertation project focuses on lignin oligomers to afford us the ability to simultaneously observe the fast pyrolysis behavior of multiple interunit linkages. By investigating multiple oligomers and interlinkages, coupled with the previously published kinetic information, I believe we will be able to propose reaction mechanisms for multiple model oligomers. The understanding of these proposed

mechanisms will lay the foundation for developing a set of general reaction rules and a hierarchy for the order of reactions that take place. These rules will be applicable to a wide variety of lignin structures. This project is broken down into three separate objectives, and each objective is supported by specific research questions and hypotheses that will help guide our research in investigating these objectives.

Objective 1: To computationally assess the bond dissociation enthalpies (BDE) of three lignin model oligomers with a combination of important linkages, e.g., β-O-4, α-O-4, β-5, β-β', and 4-O–5, through density functional theory (DFT) calculations to identify the initial points of reaction during thermal deconstruction. In this chapter, the homolytic cleavage of bonds along each interunit linkage will be investigated to determine which bonds were more likely to break during thermal deconstruction. Each model oligomer will be subject to a conformational analysis for possible stereoisomers to determine the lowest energy conformer. The low energy conformers, as well as the resulting radical products, will undergo geometric optimization and frequency analysis using a M06-2X/6–311++G(d,p) level of theory to determine the enthalpy of each species. The BDE for each bond will be compared against each other to identify the primary points of reaction during the thermal deconstruction of the chosen model oligomers. The central research question we seek to answer in this objective is as follows: Is it possible to deduce generalizable reaction trends for the primary decomposition of lignin using carefully selected oligomers that contain important interunit linkages and represent important lignin substructures through quantum chemical calculations? We hypothesize that density functional theory calculations will

allow for the determination of these trends, and based on the general rules of electronegativity and bond strength, the ether bonds are expected to be major points of reaction during lignin pyrolysis. However, the reactivity of ether-linking motifs in multi-linkage configuration is more challenging to deduce compared to ideal, isolated bonds.

Objective 2: To computationally investigate and propose reaction pathways for the thermal deconstruction of chosen model oligomers with a combination of β-O-4, α-O-4, β-5, β-β′, and 4-O-5 interunit linkages. In this chapter, the bonds with the lowest BDEs from the previous objective were chosen as the initial reaction points for the relevant oligomer. Reaction classes for each interunit linkage, containing all possible reactions along that interunit linkage, will be proposed based on chemical intuition and previously published reaction schemes. A systematic approach will be implemented to propose reaction pathways by applying relevant reaction classes until reaching the final monomeric products. The central research question we seek to answer in this objective is as follows: Is it possible to propose full reaction mechanisms for lignin substructures that capture generalizable behavior applicable to a variety of substructures? We hypothesize that given the variety of interunit linkages and differing adjacent units; these mechanisms will provide valuable information about how these linkages behave in various surroundings.

Objective 3: To experimentally identify primary pyrolysis products of model lignin dimers containing important interunit linkages via pulse-heated pyrolysis experiments coupled with online and offline product analysis. The model lignin dimers

contain similar linkages as our computational investigations. We will design and fabricate an advanced pulse-heated pyrolysis reactor system. The new pyrolysis system will be designed in a way to eliminate mass and transport limitations typically present in experimental pyrolysis. A thin sample of the model compounds will be heated up to the reaction temperature by resistive heating, using 50 ms pulses, and rapidly quenched via an inert carrier gas. Major products will be identified and quantified using online GC/MS analysis and offline GC/MS and GC/FID analysis. The central research question is as follows: Is it possible to experimentally validate the computationally determined reaction pathways and kinetics using pulse-heated pyrolysis experiments? We hypothesize that if heat transfer or diffusion limitations are eliminated and millisecond time resolution is achieved during the pulse-heated pyrolysis experiments of select lignin dimers, our experimentally observed products will closely match those determined through a similar density functional theory investigation as proposed in Objective 2.

1.3. Organization of the Dissertation

Organizationally, this dissertation consists of five chapters. The first chapter presents a brief introduction to determining the mechanisms of lignin fast pyrolysis and a quick summary of the state of the art of lignin fast pyrolysis. The first chapter also highlights the research proposal's overall goal and individual research objectives, and the specific research questions associated with each objective. The second chapter is a detailed literature review of the current state of lignin pyrolysis kinetics. The literature review addresses both the experimental and computational efforts to understand

lignin pyrolysis using isolated lignin and various smaller lignin compounds. Chapter 2 also presents a brief discussion of current techniques for mechanistically determining reaction kinetics for other complex polymeric systems and potential pathways forward in modeling lignin pyrolysis. The last three chapters are dedicated to their respective research objectives. Chapter 3 details the computational efforts to determine the bond dissociation enthalpies for the homolytic cleavage of bonds along the respective interunit linkages of three chosen model lignin oligomers through density function theory. Chapter 4 develops reaction classes for specific interunit linkages and applies them to the chosen model oligomers to propose full reaction mechanisms. Major pyrolysis pathways are identified, and general reactivity trends of various interunit linkages are developed to understand lignin pyrolysis more generally. Chapter 5 focuses on the experimental approach for elucidating reaction pathways using lignin model dimers. A pulse-heated pyrolysis reactor interfaced with online and offline analytical instruments is employed to identify significant pyrolysis products produced from select lignin model dimers. The observations from the experimental pyrolysis reactions were used to supplement the computationally derived reaction mechanisms and proposed reactivity trends.

This dissertation has adopted the American Chemical Society (ACS) reference style for in-text citations and bibliography sections. Mathematical equations will be referenced using parentheses and will contain the chapter number and the respective equation number separated by a hyphen. For example, in Chapter 2, the Arrhenius kinetic rate equation is shown by Eq. 2–1.

$$k = Ae^{-\frac{E_a}{RT}} \tag{2–1}$$

References

1. Catalán-Martínez, D.; Domine, M. E.; Serra, J. M., Liquid fuels from biomass: An energy self-sustained process integrating H2 recovery and liquid refining. *Fuel* **2018,** *212*, 353-363.
2. O'Sullivan, A. C., Cellulose: the structure slowly unravels. *Cellulose* **1997,** *4* (3), 173-207.
3. Krumm, C.; Pfaendtner, J.; Dauenhauer, P. J., Millisecond Pulsed Films Unify the Mechanisms of Cellulose Fragmentation. *Chemistry of Materials* **2016,** *28* (9), 3108-3114.
4. Mukarakate, C.; Mittal, A.; Ciesielski, P. N.; Budhi, S.; Thompson, L.; Iisa, K.; Nimlos, M. R.; Donohoe, B. S., Influence of Crystal Allomorph and Crystallinity on the Products and Behavior of Cellulose during Fast Pyrolysis. *ACS Sustainable Chemistry & Engineering* **2016,** *4* (9), 4662-4674.
5. Frassoldati, A.; Ranzi, E., Modeling of Thermochemical Conversion of Biomasses. In *Reference Module in Chemistry, Molecular Sciences and Chemical Engineering*, Elsevier: 2019.
6. Vanholme, R.; Morreel, K.; Ralph, J.; Boerjan, W., Lignin engineering. *Current Opinion in Plant Biology* **2008,** *11* (3), 278-285.
7. Glasser, W. G., About Making Lignin Great Again—Some Lessons From the Past. *Frontiers in Chemistry* **2019,** *7* (565).
8. Katahira, R.; Elder, T. J.; Beckham, G. T., A Brief Introduction to Lignin Structure. In *Lignin Valorization: Emerging Approaches*, Beckham, G. T., Ed. The Royal Society of Chemistry: 2018; p 0.
9. Lourenço, A.; Pereira, H., Compositional variability of lignin in biomass. *M. Poletto, Lignin-Trends and Aplications* **2018**, 65-98.
10. Grossman, A.; Vermerris, W., Lignin-based polymers and nanomaterials. *Current Opinion in Biotechnology* **2019,** *56*, 112-120.
11. Rinaldi, R.; Jastrzebski, R.; Clough, M. T.; Ralph, J.; Kennema, M.; Bruijnincx, P. C. A.; Weckhuysen, B. M., Paving the Way for Lignin Valorisation: Recent Advances in Bioengineering, Biorefining and Catalysis. *Angewandte Chemie International Edition* **2016,** *55* (29), 8164-8215.
12. Holladay, J. E.; White, J. F.; Bozell, J. J.; Johnson, D. *Top Value-Added Chemicals from Biomass - Volume II—Results of Screening for Potential Candidates from Biorefinery Lignin*; PNNL-16983; Other: BM0102070; TRN: US200805%%262 United States 10.2172/921839 Other: BM0102070; TRN: US200805%%262 PNNL English; ; Pacific Northwest National Lab. (PNNL), Richland, WA (United States): 2007; p Medium: ED; Size: PDFN.
13. Nanda, S.; Kozinski, J., A.; Dalai, A., K., Lignocellulosic Biomass: A Review of Conversion Technologies and Fuel Products. *Current Biochemical Engineering* **2016,** *3* (1), 24-36.
14. Brethauer, S.; Studer, M. H., Biochemical Conversion Processes of Lignocellulosic Biomass to Fuels and Chemicals – A Review. *CHIMIA International Journal for Chemistry* **2015,** *69* (10), 572-581.

15. Chen, H.; Wang, L., Chapter 1 - Introduction. In *Technologies for Biochemical Conversion of Biomass*, Chen, H.; Wang, L., Eds. Academic Press: Oxford, 2017; pp 1-10.
16. Pang, S., Advances in thermochemical conversion of woody biomass to energy, fuels and chemicals. *Biotechnology Advances* **2019,** *37* (4), 589-597.
17. Matsakas, L.; Gao, Q.; Jansson, S.; Rova, U.; Christakopoulos, P., Green conversion of municipal solid wastes into fuels and chemicals. *Electronic Journal of Biotechnology* **2017,** *26*, 69-83.
18. Oyedeji, O.; Abdoulmoumine, N., Computational fluid dynamics and discrete element simulation of the formation of inorganic syngas contaminants during lignocellulosic biomass gasification. *Sustainable Energy & Fuels* **2020,** *4* (8), 4219-4231.
19. Ail, S. S.; Dasappa, S., Biomass to liquid transportation fuel via Fischer Tropsch synthesis – Technology review and current scenario. *Renewable and Sustainable Energy Reviews* **2016,** *58*, 267-286.
20. Shen, D.; Jin, W.; Hu, J.; Xiao, R.; Luo, K., An overview on fast pyrolysis of the main constituents in lignocellulosic biomass to valued-added chemicals: Structures, pathways and interactions. *Renewable and Sustainable Energy Reviews* **2015,** *51*, 761-774.
21. Mohan, D.; Pittman, C. U.; Steele, P. H., Pyrolysis of Wood/Biomass for Bio-oil: A Critical Review. *Energy & Fuels* **2006,** *20* (3), 848-889.
22. Bridgwater, A. V., Review of fast pyrolysis of biomass and product upgrading. *Biomass and Bioenergy* **2012,** *38*, 68-94.
23. SriBala, G.; Carstensen, H.-H.; Van Geem, K. M.; Marin, G. B., Measuring biomass fast pyrolysis kinetics: State of the art. *WIREs Energy and Environment* **2019,** *8* (2), e326.
24. Hu, X.; Gholizadeh, M., Biomass pyrolysis: A review of the process development and challenges from initial researches up to the commercialisation stage. *Journal of Energy Chemistry* **2019,** *39*, 109-143.
25. Shafizadeh, F., Pyrolytic Reactions and Products of Biomass. In *Fundamentals of Thermochemical Biomass Conversion*, Overend, R. P.; Milne, T. A.; Mudge, L. K., Eds. Springer Netherlands: Dordrecht, 1985; pp 183-217.
26. Ranzi, E.; Cuoci, A.; Faravelli, T.; Frassoldati, A.; Migliavacca, G.; Pierucci, S.; Sommariva, S., Chemical kinetics of biomass pyrolysis. *Energy Fuels* **2008,** *22* (6), 4292-4300.
27. Yang, H.; Yan, R.; Chen, H.; Lee, D. H.; Zheng, C., Characteristics of hemicellulose, cellulose and lignin pyrolysis. *Fuel* **2007,** *86* (12–13), 1781-1788.
28. Vinu, R.; Broadbelt, L. J., A mechanistic model of fast pyrolysis of glucose-based carbohydrates to predict bio-oil composition. *Energy & Environmental Science* **2012,** *5* (12), 9808-9826.
29. Zhou, X.; Li, W.; Mabon, R.; Broadbelt, L. J., A Critical Review on Hemicellulose Pyrolysis. *Energy Technology* **2017,** *5* (1), 52-79.
30. Zhou, X.; Li, W.; Mabon, R.; Broadbelt, L. J., A mechanistic model of fast pyrolysis of hemicellulose. *Energy & Environmental Science* **2018,** *11* (5), 1240-1260.

31. Mayes, H. B.; Broadbelt, L. J., Unraveling the Reactions that Unravel Cellulose. *The Journal of Physical Chemistry A* **2012,** *116* (26), 7098-7106.
32. Sederoff, R. R.; MacKay, J. J.; Ralph, J.; Hatfield, R. D., Unexpected variation in lignin. *Current Opinion in Plant Biology* **1999,** *2* (2), 145-152.
33. Beste, A.; Buchanan, A. C., Kinetic simulation of the thermal degradation of phenethyl phenyl ether, a model compound for the β-O-4 linkage in lignin. *Chemical Physics Letters* **2012,** *550*, 19-24.
34. Chen, L.; Ye, X.; Luo, F.; Shao, J.; Lu, Q.; Fang, Y.; Wang, X.; Chen, H., Pyrolysis mechanism of βO4 type lignin model dimer. *Journal of Analytical and Applied Pyrolysis* **2015,** *115*, 103-111.
35. Choi, Y. S.; Singh, R.; Zhang, J.; Balasubramanian, G.; Sturgeon, M. R.; Katahira, R.; Chupka, G.; Beckham, G. T.; Shanks, B. H., Pyrolysis reaction networks for lignin model compounds: unraveling thermal deconstruction of β-O-4 and α-O-4 compounds. *Green Chemistry* **2016,** *18* (6), 1762-1773.
36. Elder, T.; Beste, A., Density Functional Theory Study of the Concerted Pyrolysis Mechanism for Lignin Models. *Energy & Fuels* **2014,** *28* (8), 5229-5235.
37. About the Author A2 - Klass, Donald L. In *Biomass for Renewable Energy, Fuels, and Chemicals*, Academic Press: San Diego, 1998; p ix.
38. Faravelli, T.; Frassoldati, A.; Migliavacca, G.; Ranzi, E., Detailed kinetic modeling of the thermal degradation of lignins. *Biomass and Bioenergy* **2010,** *34* (3), 290-301.
39. Hough, B. R.; Schwartz, D. T.; Pfaendtner, J., Detailed Kinetic Modeling of Lignin Pyrolysis for Process Optimization. *Industrial & Engineering Chemistry Research* **2016,** *55* (34), 9147-9153.
40. Klein, M. T.; Virk, P. S., Modeling of Lignin Thermolysis. *Energy & Fuels* **2008,** *22* (4), 2175-2182.

CHAPTER 2 LITERATURE REVIEW – THE CURRENT STATE OF LIGNIN PYROLYSIS: EXPERIMENTAL AND THEORETICAL APPROACHES TO ELUCIDATE REACTION MECHANISMS

2.1. Introduction

Lignocellulosic biomass is an attractive source for the production of renewable fuels, chemicals, and materials, due to its abundance, year-round availability, and renewable nature[1]. Lignocellulosic biomass biochemical or thermochemical deconstruction is necessary before its transformation to the aforementioned products. Fast pyrolysis is one of the more attractive thermochemical deconstruction techniques due to its ability to produce a biocrude, also known as bio-oil, as well as its favorable low energy requirement and high throughput[2-4]. In the context of lignocellulosic thermochemical processing, fast pyrolysis is the thermal degradation process that occurs at low vapor residence times (< 2 s), high heating rates, and moderate temperatures (400-600 °C) in the absence of oxygen to produce three major products in descending order by yield: solid biochar, light gases, e.g. (carbon monoxide, hydrogen, C_1-C_4 hydrocarbons, etc.), and bio-oil[5]. Deconstruction of lignocellulosic biomass through fast pyrolysis is complex for a variety of reasons. First, lignocellulosic biomass is compositionally complex and variable by location, seasons, and species[6]. These factors influence the conversion and, ultimately, the yield and product distribution. Second, the multiphase nature of fast pyrolysis conversion processes adds an additional layer of complexity. Finally, lignocellulosic biomass is thermochemically transformed through a complex network of reactions of thousands of species[7]. Understanding the reaction mechanisms of lignocellulosic biomass deconstruction via fast pyrolysis is a longstanding challenge that is actively investigated by the thermochemical conversion community.

Lignocellulosic biomass is comprised of three major components: cellulose, hemicellulose, and lignin, with a small amount of ash and extractives. Significant effort has been put forth to describe the pyrolysis of lignocellulosic biomass via mathematical models. Early work developed simple models assuming a single pyrolysis reaction[8-10]. The major component of lignocellulosic biomass is cellulose. Additionally, due to its linear, repeating structure, cellulose is easier to isolate and test experimentally than hemicellulose and lignin. Therefore, the fast pyrolysis of cellulose has been thoroughly investigated.

Broido and his colleagues spent a considerable amount of effort studying the behavior of cellulose pyrolysis and in 1975, they published a competitive reaction scheme showing two reaction pathways from cellulose to volatile tars or char and low molecular weight species[11, 12]. This model was further expounded upon to arrive at a multistep model including an active intermediate, known as "active cellulose"[13, 14]. This simple, general model for cellulose fast pyrolysis came to be known as the Broido-Shafizadeh model and would serve as the foundation for many future kinetic models for cellulose and biomass fast pyrolysis[15]. Recently, increased focus has been on the investigation of pyrolysis kinetics using computational chemistry to better determine the mechanism by which cellulose undergoes thermal decomposition. Comprehensive, critical reviews of the development of cellulose pyrolysis kinetics can be found elsewhere in literature[16-18].

In several models that attempt to present a global yet detailed scheme for biomass fast pyrolysis, the pyrolysis of hemicellulose and lignin are treated according

to the same methods as cellulose pyrolysis in which they initially decompose to an activated intermediate before being further converted into volatiles, light gases, and char[19].

Lignin is the second most abundant component of lignocellulosic biomass and one of the most abundant naturally occurring polymers in the world. Lignin is synthesized primarily via oxidative coupling of three 4-hydroxycinnamyl alcohol monomers: p-coumaryl, coniferyl, and sinapyl alcohol)[20]. Currently, the major use for lignin is burning for heat. However, due to the aromatic nature of lignin, there is potential for valorization to value-added products and intermediates through pyrolysis[21]. The purpose of this chapter is to present a critical review of the work on lignin pyrolysis kinetics up to this point and discuss potential pathways moving forward.

2.2. Lignin structure and isolation

Lignin is an integral component of the plant tissues, along with cellulose and hemicellulose, and presently the most abundant source of renewable aromatics[22]. Aromatic compounds are essential to modern life and have many product applications ranging from plastics to medicines. Thus, understanding the reactions that govern the conversion and transformation of lignin through thermochemical routes is important as we strive towards great independence from fossil fuels and fossil fuel-derived aromatics.

As previously stated, lignin is formed through the radical coupling of the primary lignin polymerization of 4-hydroxycinnamyl alcohol monomers, primarily through

endwise coupling[23]. The aromatic units of lignin are further classified into three groups: p-hydroxyphenyl (H), guaiacyl (G), and syringyl(S), depending on the level of methoxylation at the C3 and C5 positions[24]. This can be seen in Figure 0-1. The structure and composition of lignin varies depending on the source of biomass. Softwoods contain approximately 27-33 wt. % lignin, hardwoods contain 18-25 wt. %, and grasses 17-24 wt. %[25]. Softwood lignin is primarily made up of G units, while hardwood lignin consists of G and S units, and lignin from grass is built from H, G, and S units[26]. Additionally, delocalization of the radicals allows for linkages to be formed at multiple sites, leading to a variety of possible linkages[27]. These linkages can be either C-O or C-C linkages. The linkages include β-O-4, 5-5, β-5, 4-O-5, β-1, β- β, and several others with β-O-4 being the dominant linkage[28, 29]. Therefore, the exact structure of lignin remains unknown. However, significant research has been undertaken to better understand the structure of native lignin[23].

The lignocellulosic cell wall is comprised of a complex network of cellulose, hemicellulose, and lignin. Under gasification temperatures (800 °C), it has been shown there is a significant interaction effect between cellulose and lignin during wood pyrolysis[30]. Currently, there has not been significant progress in developing a kinetic model for lignocellulosic fast pyrolysis that accounts for the interactions of the individual biomass constituents[19]. To better understand lignin, it must be isolated from the lignocellulosic complex. Extraction of lignin remains a major challenge in understanding both the native structure and the pyrolysis behavior of lignin. Several methods have been investigated to either isolate or recover lignin, leading to various

types of isolated lignin, such as milled wood lignin (MWL), cellulase enzyme lignin (CEL), kraft lignin, Brauns' lignin, and Klason lignin. However, these methods either change the structure of the resulting lignin, have contaminating sugars, or are result in low isolation yields[31, 32].

2.3. Reaction mechanisms and kinetics for lignin model compounds

Due to the difficulty of isolating lignin in its native structure, researchers have looked to understand the pyrolysis mechanisms of lignin substructures, such as monomeric derivatives of the H, G, and S building blocks[33, 34], dimers containing ether or carbon-carbon linkages[35, 36], or larger oligomers representative of groups found in native lignin[37]. While it is not viable to assume the information gathered via these model compounds will be applicable to native lignin, these model compounds provide a method to develop a mechanistic understanding of the pyrolysis pathways for the building blocks of lignin.

The approaches for determining fast pyrolysis kinetics and proposing reaction schemes and mechanisms can be classified into two categories: empirical or mechanistic, and generally be thought of as experimental and computational, respectively. The empirical methods are the classic ways of determining reaction kinetics via experimental observation. However, experiments are limited by what products can be observed. Unless one has access to high-speed analytical techniques to measure on a femtosecond time scale, one cannot guarantee that all rapid-reacting intermediates will be observed[38]. Empirical kinetics depend on experimental

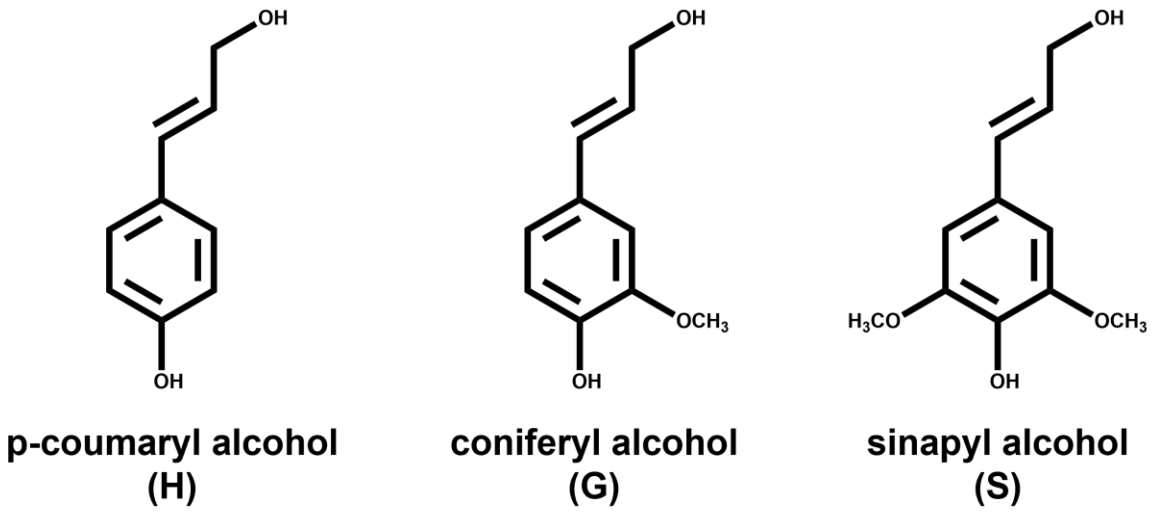

Figure 0-1. Chemical structures of the building blocks of native lignin.

conditions and do not provide insight into the underlying mechanism. Computational chemistry has recently gained popularity as a tool, paired with experimental observation, to understand the fundamental decomposition pathways of biomass pyrolysis. Computational chemistry has the advantage of predicting molecular processes by analyzing the energetics of a given system[39].

Experimental kinetic analysis of lignocellulosic biomass and lignin has primarily been performed via thermogravimetric analysis (TGA) experiments[40-45]. Researchers have proposed several different models for estimating kinetic parameters for biomass pyrolysis based on TGA mass loss data, such as first-order[40, 46, 47], distributed activation energy models (DAEM)[44, 48-50], and pseudo-component models[41, 51]. TGA provides valuable kinetic data for the total mass loss of the biomass sample during pyrolysis. However, this technique provides no information on the major volatile products released and, therefore, no mechanistic information as to which reaction pathways are present during pyrolysis. Pyrolysis has also been coupled with online spectroscopy systems to perform kinetic analysis while characterizing the volatile products[52-54]. However, even with a full characterization of the observable pyrolysis products, the analysis does not provide a time evolution of the pyrolysis system but consists of cumulative product yields[55]. Therefore, without very high-speed analytic techniques, experimental reaction analysis will necessarily be limited, requiring computational chemistry to determine the underlying mechanistic pathways and kinetic rate parameters of fast pyrolysis[56].

In the 1990s, density functional theory (DFT) gained popularity as the preferred method for electronic structure calculations[57]. In the last several years, DFT has become an invaluable tool for the kinetic analysis of pyrolysis. This is due to the reduced computation costs compared to traditional Hartree-Fock (HF) methods while maintaining comparable, or even improving, chemical accuracy. DFT is built from the Hohenberg-Kohn theorems that postulate all ground and excited-state properties for a given system can be determined from the ground state electron density[58, 59]. The energy of the system is broken down into four components: kinetic energy, electron-nuclear interaction, coulomb repulsion, and an exchange-correlation. The electron correlation is computed using generalized functionals of the election density[60]. The two most popular functionals for lignin pyrolysis calculations are the B3LYP[61, 62] and M06-2X[63]. Computational modeling using DFT has been shown to be helpful in determining reaction mechanisms for the complex reaction network of cellulose pyrolysis[55, 64]. The results from computational chemistry calculations are heavily dependent on the setup and design. Therefore, experimental validation is necessary for these models to be accepted. Both experimental and theoretical approaches are vital for completely understanding a complex mechanism such as that of lignin pyrolysis.

2.3.1. Experimental determination of lignin reaction mechanisms

2.3.1.1. Isolated lignin

The body of knowledge on lignin pyrolysis is less than that of cellulose and hemicellulose, arguably because of the historical significance of cellulose and the daunting complexity of lignin. Initial investigations of the kinetics of lignin pyrolysis

focused on lignin from various isolation techniques, such as Kraft[65, 66], Klason[67], Alkali[45, 68, 69], and Alcell[50]. Kinetic parameters for these investigations are shown in Table 0-1. Ramiah investigated the thermal decomposition of periodate and Klason lignin via TGA at temperatures up to 600 °C and found Klason to be more stable than periodate lignin[47]. The reactions were modeled as first-order reactions assuming the Arrhenius rate equation, and lignin was found to have a much lower activation energy than hemicellulose and cellulose, 13, 30 and 35 kcal/mol, respectively. The Arrhenius rate equation is shown below (0-1) :

$$k = Ae^{-\frac{E_a}{RT}} \qquad (0\text{-}1)$$

where k is the kinetic rate constant, A is the pre-exponential factor, E_a is the activation energy, R is the universal gas constant, and T is temperature. Domburg et al. further confirmed that isolation techniques had a larger effect on the thermal behavior of lignin than the biomass source[69]. Identical isolation techniques on different wood species provided very similar differential thermal analysis (DTA) curves. Activation energies for various lignin were calculated using the Freeman-Carrol method[70], and ranged from 17-33 kcal/mol, with one outlier of 54.8. Chan and Kreiger investigated the effects of an unusual heating rate, via microwave pyrolysis, on the pyrolysis of pinewood Kraft lignin and were able to overcome somewhat of the typical heat transfer limitation[71]. Analysis was performed using the general non-isothermal rate equation (0-2),

$$\frac{dV}{dt} = (V^* - V)Ae^{-\frac{E_a}{RT}} = -\frac{dW}{dt} \quad (0\text{-}2)$$

which can be rearranged (0-3) for simple estimation of the kinetic rate parameters:

$$\ln\left(\frac{1}{V^* - V}\frac{dW}{dt}\right) = \ln A - \frac{E_a}{RT} \quad (0\text{-}3)$$

where $(V^* - V)$ is the remaining amount of volatiles, W is the weight, and t is time. Nunn et al. aimed to expand the single reaction, first-order model by modeling the cumulative conversion of each major product in addition to the overall mass loss of milled wood lignin via an electric screen heater reactor[46]. The rate of formation was expressed in terms of conversion of the individual products, as described in (0-4.[46]

$$\frac{dV}{dt} = (V^* - V)Ae^{-\frac{E_a}{RT}} \quad (0\text{-}4)$$

Nunn notes that detailed pyrolysis mechanisms for lignin will be more complicated than a single-step model, but their simplified model can be used as a convenient correlation tool. Ojha et al. pyrolyzed alkali lignin using pyrolysis- Fourier-transform infrared spectroscopy (Py-FTIR) to better capture the high heating rates and time evolution of products. Apparent rate parameters were calculated using first-order, multi-dimensional diffusion, and contracting cylinder models. The first-order and the diffusion models provided the best fit to the experimental data over the full temperature range (400-700 ℃) with activation energies of 5.50, 5.50, and 2.14 kcal/mol for first-order, 1D-diffusion, and 2D-diffusion, respectively[68].

As opposed to the previously discussed single reaction models, distributed activation energy models (DAEM) have also been investigated to describe the kinetics

of lignin pyrolysis[44, 50]. For DAEM, pyrolysis is assumed to proceed via a set of irreversible first-order reactions with different activation energies. DAEM can be represented by the following (Eq. (*0-5*):

$$1 - \frac{V}{V^*} = \int_0^\infty exp\left(-A\int_0^t e^{-\frac{E_a}{RT}}dt\right) f(E_a)dE_a \qquad (0\text{-}5)$$

where $f(E_a)$ is the distribution function of activation energy. The distribution function satisfies the following equation (0-6):

$$\int_0^\infty f(E_a)\, dE_a = 1 \qquad (0\text{-}6)$$

A detailed explanation of the DAEM is published elsewhere[72, 73]. Ferdous et al. applied a DAEM approach to model the pyrolysis of Alcell and Kraft lignin[50]. Upon comparison, the range of frequency factors was significantly different for Alcell and Kraft lignin, which suggests that the kinetic parameters for pyrolysis are dependent upon the type of lignin and its origin. The activation energy ranges were 30.83-86.28 and 19.12-37.76 kcal/mol from Alcell and Kraft lignin, respectively[50]. The Gaussian function has been shown to accurately predict pyrolysis data; however, multiple Gaussian functions are required for lignin pyrolysis[73, 74]. Wang et al. used a double Gaussian DAEM (DG-DAEM) to model pyrolysis of alkali, klason, organosolv, and milled wood lignin from the same pine wood, and the results are shown in Figure 0-2[74]. The first function corresponded to the release of volatile species, while the second function was for char-forming reactions. The pyrolysis of alkali and milled wood lignin was characterized more by the release of volatiles, leading to a lower activation energy

than organosolv and klason lignin, due to the presence of more weak interunit linkages.

Zhang et al. proposed a multi-Gaussian-DAEM approach to investigate the effect of the surrounding atmosphere on lignin decomposition[44, 75]. Lignin decomposition was shown to occur in two stages. In the initial stage, the surrounding atmosphere did not have much of an effect on the mean activation energies; however, the mean activation energies were significantly larger for stage two under a CO_2 atmosphere, which was in agreement with previous literature[44].

As mentioned earlier, the complete, native structure of lignin has not been characterized, and attempts at isolation change the native lignin structure. An additional difficulty with understanding lignin pyrolysis is the sheer number of products observed during pyrolysis. Therefore, work on isolated lignin samples is unable to provide any mechanistic information as to the reaction pathways present during lignin pyrolysis. To circumvent these inherent issues with lignin, researchers began to focus on model compounds that contain fundamental structures and functional groups representative of native lignin[76-79]. Early work on pyrolysis model compounds did not provide much more mechanistic insight than that of isolated lignin. Kinetic parameters were reported; however, there was no concrete evidence for reaction pathways. Klein's thesis work provides a detailed overview of the early model compound works and addresses their limitations[80]. Klein investigated pyrolysis pathways of 20 model lignin compounds that could be classified as interunit linkages, methoxy phenols, carbonyl

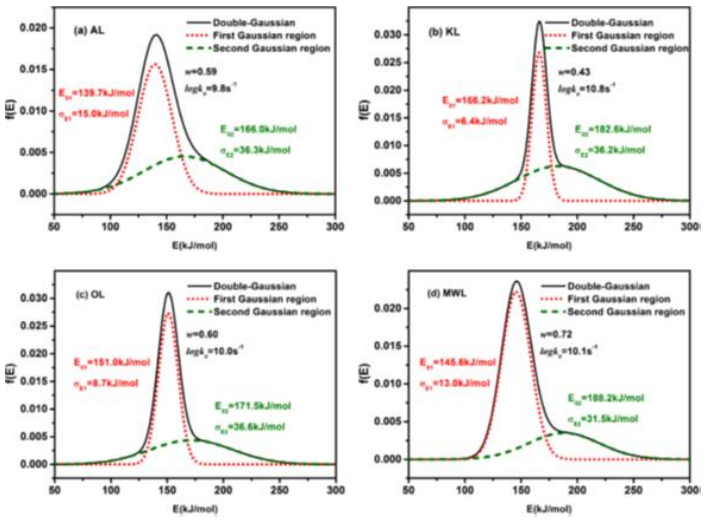

Figure 0-2. Activation energy distributions from the DG-DAEM of four isolated lignin polymers. Figure taken from Wang et al.[74]

units, propanoid side chains, or carbon dioxide precursors to create a superimposed model of whole lignin thermolysis. Due to the large scope of this project, there was still significant work to be done to completely understand the pyrolysis pathways of individual model compounds.

2.3.1.2. Model lignin monomers

Lignin is made up of three aromatic units: p-hydroxyphenyl(H), guaiacyl (G), and syringyl (S). Several of the major products observed during pyrolysis are believed to originate from the degradation of these methoxyphenol units. Most of the aromatic rings in lignin contain additional methoxy groups, which makes anisole a great initial model monomer for lignin pyrolysis[91-96]. Arends et al. modeled anisole pyrolysis in a hydrogen atmosphere and proposed a kinetic model consisting of 37 reactions and 23 species, and measured the activation energy for O-CH_3 bond scission to be 64 kcal/mol[92]. Pecullan performed pyrolysis and oxidation experiments for anisole using the Princeton atmospheric pressure flow reactor at 1000 K[93]. A new model for anisole pyrolysis containing 66 reversible reactions and 31 species was proposed and drew upon thermodynamic calculations and published literature for the kinetic rate parameters. Friderichesen et al. used a hyperthermal nozzle to study the formation of polynuclear aromatic hydrocarbons (PAHs) from the unimolecular decomposition of anisole[91]. The hyperthermal nozzle used with high temperatures and short residence times allowed for the observation of radical intermediates from pyrolysis. FTIR analysis suggested the phenoxy and cyclopentadienyl radicals, the two products from the scission of the O-CH_3 bond, play a large role in the formation of naphthalene[91].

Table 0-1. Comparison of apparent kinetic rate parameters on isolated lignin from literature using various models.

Study	Type	Method	Temperature (°C)	A (s^{-1})	E_a (kcal/mol)
Ramiah[47]	Periodate	TGA/DTA	244-330	-	13
	Klason	TGA/DTA	319-385	-	19
Domburg[69]	Various	TGA/DTA	20-600	-	17-33
Avni[81]	Various	Flash pyrolysis	150-1300	$1x10^{14}$	48
Caballero[67]	Klason	Pyroprobe	600-900	59.5	8.2
Caballero[82]	Kraft	TGA/DTA	200-700	-	17.3-41.6
Caballero[66, a]	Kraft	Pyroprobe	450-900	14.77+0.208(T_R-273)	52.64+0.173(T_R-273)
Chan[83]	Kraft	Microwave reactor	160-680	$4.7x10^{2}$	6.0
	Kraft		410-1890	$9.0x10^{1}$	7.3
Nunn[46]	Milled wood lignin	Microreactor	500-1000	$2.0x10^{7}$	19.6
Pasquali[84]	Klason	TGA/DTA	226-435	-	3.0, 9.4, 10.2

Table 2.1. Continued

Study	Type	Method	Temperature (°C)	A (s^{-1})	E_a (kcal/mol)
Rao[85]	Various	TGA/DTA	390-500	$1.26x10^7$	16.9
Tang[86]	Sulfuric acid	TGA/DTA	280-344	$9.86x10^5$	21.0
	spruce	TGA/DTA	344-435	5.6	9.0
	Bronwell	TGA/DTA	175-245	-	6.0 ± 8%
		TGA/DTA	175-310	-	6.7 ± 5%
	Björkman	TGA/DTA	185-245	-	8.0 ± 2%
		TGA/DTA	250-330	-	9.0 ± 4%
Beall[87]	Sulfuric acid	TGA/DTA	260-325	-	8.6 ± 0%
		TGA/DTA	235-325	-	11.1 ± 7%
		TGA/DTA	315-375	-	18.1 ± 2%
	Cellulase	TGA/DTA	178-239	-	10.7 ± 7%
		TGA/DTA	260-300	-	5.6 ± 8%
	DHP	TGA/DTA	220-340	-	2.0 ± 30%
		TGA/DTA	195-330	-	4.1 ± 2%
		TGA/DTA	170-337	-	9.3 ± 5%

Table 2.1. Continued

Study	Type	Method	Temperature (°C)	A (s^{-1})	E_a (kcal/mol)
Ferdous[50]	Alcell	TGA/DTA	257-542	$6.2x10^{11}$-$9.2x10^{22}$	30.8-86.3
	Kraft	TGA/DTA	217-537	$3.3x10^{7}$-$1.8x10^{9}$	19.1-37.8
Dominguez[88]	Organosolv	TGA/DTA	30-900	-	4.6-10.2
Liu[89]	Fir (SADF)	TGA/DTA	149-288	$1.14x10^{7}$	17.4
	Birch (SADF)	TGA/DTA	348-491	$8.76x10^{7}$	32.7
Jiang[40,b]	Alcell	TGA/DTA	105-900	28.5±0.1	38.1
	Asian (straw and grass)	TGA/DTA	105-900	23.9±0.2	32.0
	Organosolv	TGA/DTA	105-900	25.7±0.3	34.5
	Etek	TGA/DTA	105-900	27.4±0.4	36.3
	Klason (beech)	TGA/DTA	105-900	26.8±0.2	36.1

Table 2.1. Continued

Study	Type	Method	Temperature (°C)	A (s^{-1})	E_a (kcal/mol)
Jiang[40,b]	Alcell	TGA/DTA	105-900	28.5±0.1	38.1
	Klason (cassava stalk)	TGA/DTA	105-900	29.8±0.3	41.0
	Klason (mixed softwood)	TGA/DTA	105-900	24.8±0.1	34.7
	Klason (willow)	TGA/DTA	105-900	27.8±0.2	37.4
Chen[41]	Kraft	TGA/DTA	167-927	-	37.5
Damayanti[90]	Alkaline	TGA/DTA	300-350	-	28.7-34.2
Ohja[68]	Alkali	Py-FTIR	400-700	6.44	5.5

Note: A is the pre-exponential factor, and E_a is the activation energy

[a]= values report as ln(k) and E_a (kJ/mol)

[b]=k reported in min^{-1}

Scheer et al. confirmed the formation of the cyclopentadienyl radical and supported its role in the formation of naphthalene and suggested benzene is mostly formed through the decomposition of methylcyclopentadiene as opposed to propargyl radical recombination[94]. Nowakoska et al. performed pyrolysis and oxidation experiments of anisole in a jet-stirred reactor and proposed a detailed kinetic model adapted from a previous study on ethyl-benzene oxidation[95, 97]. While these numerous studies are helpful for better understanding anisole pyrolysis pathways, there is still a need to increase the quality of thermal control and product analysis in these experimental studies.

Guaiacol has been the most popular model monomer for lignin due to its methoxy group at the *ortho* position, which is representative of native lignin[98]. Vuori and Bredenberg studied the pyrolysis behavior of substituted anisoles, including guaiacol, and modeled the kinetics as first-order reactions[99, 100]. Guaiacol was shown to be more reactive than the other substituted anisoles due to the ortho-hydroxy group with an overall activation energy of 34.18±4.78 kcal/mol[99]. Suryan et al. performed very low-pressure pyrolysis on substituted anisoles and found good agreement with the previous work for guaiacol and the other methoxyanisoles[101]. Both works suggest a free-radical path dominates compared to a concerted reaction. Dorrestijn further investigated the radical mechanism associated with guaiacol pyrolysis using cumene as a radical scavenger and measured activation energies, noting the *ortho*-hydroxy group had a weakening effect on the BDE of the O-CH_3 bond of 6.45 kcal/mol[102]. The work on guaiacol agrees the homolysis of the O-CH_3 bond and *ipso*-substitution are

the major reaction pathways for both guaiacol and other methoxylated phenols[98-100, 102-104].

Another important yet less investigated model monomer is syringol (2,6-dimethoxyphenol)[105, 106]. Asmadi et al. compared the pyrolysis behavior of guaiacol and syringol to better understand the effect of the additional methoxyl group of syringol[106]. The homolysis of the O-CH_3 bond was found to be the rate-determining step at temperatures greater than 400 ℃. Additionally, syringol was found to produce significantly more coke than guaiacol in the initial stages of pyrolysis (80-120 s), which can be attributed to the additional methoxy group allowing for the formation of *o*-quinonemthide, an intermediate for coke formation[106].

2.3.1.3. Model lignin dimers

As β-O-4 linkages make up over half the linkages in native lignin, it stands to reason that model compounds containing a β-O-4 would be of great importance to understanding lignin pyrolysis. Phenethyl phenyl ether (PPE) has become the fundamental lignin β-O-4 model compound as it is the skeletal backbone devoid of side groups. Klein and Virk were the first group to provide quantitative information as to the kinetics and mechanism of PPE pyrolysis[36]. At 300 – 550 ℃, the major pyrolysis products were phenol, styrene, ethylbenzene, and toluene. Klein and Virk proposed the decomposition of PPE proceeds via a first-order reaction, initially producing one mole of phenol and styrene with first-order kinetic parameters of 11.1 ± 0.9 and 45.0 ± 2.7 for log A (s^{-1}) and E_a, respectively. Styrene then underwent secondary reactions to produce other hydrocarbon products. The mechanism by which pyrolysis of lignin and

representative model compounds occurs has not reached a consensus in the literature. In their work, Klein and Virk proposed both free-radical and concerted mechanisms and found their kinetic parameters to favor a concerted retro-ene reaction to form phenol and styrene (Table 0-2)[36]. Gilbert and Gajewski further investigated the pyrolysis of PPE and observed a reaction order (1.2-3) and radical initiator effects (addition of benzyl phenyl ether) that suggest PPE pyrolysis is more consistent with a free radical scheme[107]. Britt et al. attempted to resolve the discrepancies between the contradicting mechanisms by studying the thermolysis of PPE with or without a hydrogen donor in both the liquid and gas phase from 330-425 °C[108]. Britt calculated a fractional reaction order and observed rate acceleration due to free-radical initiators. Therefore, he also proposed two competitive free-radical mechanisms that differ by α/β selectivity, shown in Figure 0-3.

However, the estimated activation energy for the retro-ene reaction is comparable to the proposed free-radical mechanisms. A few years later, Britt performed flash vacuum pyrolysis (FVP) on PPE and other methoxy-substituted model compounds[110]. At 500 °C, he found evidence of both free-radical and concerted mechanisms for the production of phenol and styrene (1.4:1 free-radical:concerted). Estimation of the energetic barriers associated with the proposed free-radical and concerted mechanisms suggest that the retro-ene reaction should be dominant at temperatures less than 1250 °C[111]. To further elucidate the dominant mechanism of PPE pyrolysis, Jarvis used a hyperthermal nozzle to couple pyrolysis with

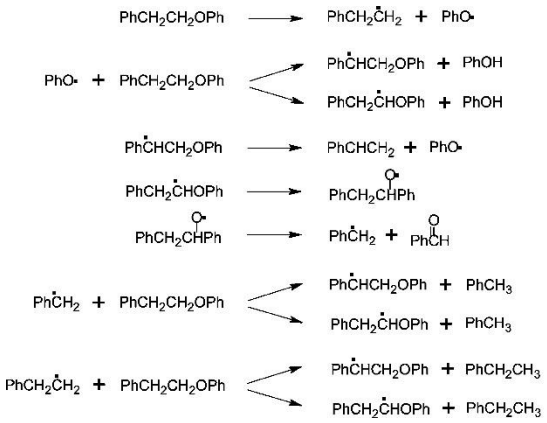

Figure 0-3. Proposed radical mechanism of PPE pyrolysis by Britt et al.[108] Adapted from Beste et al.[109]

photoionization mass spectrometry (PIMS), which is able to measure radicals and other unstable pyrolysis products[111]. The resulting mass spectra of PPE pyrolysis provided evidence for both mechanisms, but theoretical calculations suggested the concerted retro-ene pathway dominates at lower temperatures (<600 °C), Figure 0-4.

A caveat when working with PPE is the effect of side groups, especially at the α-position. Domburg et al. found that the functional group located at the α-position significantly affected the thermal stability of the dimer[112]. Evans et al. further discussed the inherent limitation of PPE as a model compound and specifically Klein's work on PPE due to the long pyrolysis timescale[113]. In addition to PPE, Britt also investigated the effect of methoxy and hydroxy substitutions on the pyrolysis of PPE[110, 114]. Under the operating conditions of 345 °C and an inert solvent, kinetic analysis suggested the substituted PPE compounds reacted via a free-radical mechanism[114]. Oxygen substitutions were found to have an additive effect on both the rate of pyrolysis as well as the product selectivity[110, 114, 115]. However, the complex interactions make it difficult to pinpoint the single factor causing the effect. McDermott and Klein looked to select a model compound that contained important structural aspects associated with β-ethers and subsequently chose α-[(o-methoxyphenoxy)methyl]veratryl alcohol (VGE) (Figure 0-5)[116]. VGE was pyrolyzed in a batch reactor from 250–380 °C at various reaction times. The primary pathway appeared to be dehydration to produce vinyl ethers. This pathway allows for the evolution of pyrolytic water from lignin.

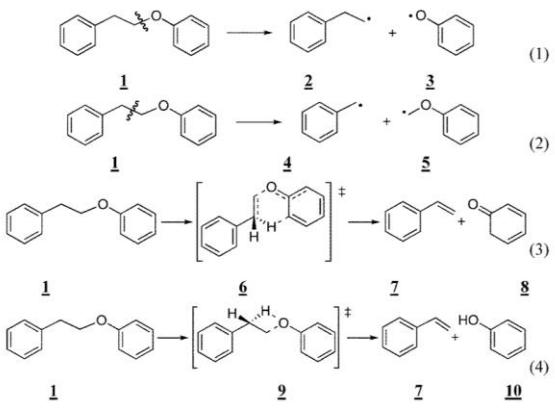

Figure 0-4. Initial steps of the proposed PPE pyrolysis mechanisms. (1) α-position homolytic cleavage (2) β-position homolytic cleavage, (3) retro-ene fragmentation, and (4) Maccoll elimination[111].

Kawamoto et al. performed pyrolysis experiments on eight model lignin dimers containing β-O-4, α-O-4, β-1, and biphenyl linkages[117]. For both sets of ether-linked dimers, the ether bond was shown to be easily cleaved above 400 ℃. The β-1 dimers were proposed to proceed through both C_α-C_β scission and C_γ-elimination with selectivity depending on the phenolic nature of the dimer. The biphenyl dimers do not play as large a role in the depolymerization of lignin but play a large part in the carbonization of lignin[117]. In a subsequent study on β-O-4 dimers, Kawamoto et al. determined that C_γ-OH changed the mechanism of C-O cleavage, with the presence of an OH group promoting the formation of quinone methide that facilitated the cleavage of the C-O bond[118, 119]. Due to the debate between free-radical and concerted mechanisms for β-O-4 pyrolysis, He et al. adopted synchrotron ultraviolet photoionization mass spectrometry (SVUV PIMS) to identify radical intermediates for β-O-4 (guaiacylglycerol-β-guaiacyl, GGGE) and α-O-4 dimers (4-(benzyloxy)phenol, BOP, and 4-(benzyloxy)anisole, BOA)[120]. For GGGE, no radicals were detected in the mass spectra, which suggests the agreement with Jarvis et al. that the concerted mechanism is dominant between 350-500 ℃[111, 120]. For both α-O-4 dimers, the major pyrolysis pathways were through the scission of the C_α-O; however, the *p*-methoxy present in BOA can significantly reduce the BDE of the $C_{aromatic}$- C_α and the O_{ether}- $C_{aromatic}$ bond, which supports the importance of these methoxy substitutions[110, 120]. The presence of a C_α-OH bond is common in native lignin, and that can be oxidized to a C_α ketone[121]. Jiang et al. investigated four β-O-4 dimers containing these substituents to understand

their role in lignin pyrolysis[122]. The presence of C_α-OH promoted cleavage of the C_β-O bond, while the C_α ketone increased the feasibility of C_α - C_β cleavage.

The β-5 linkage makes up approximately 6-16% of the interunit linkages in lignin[123]. Even so, the β-5 linkage has not been widely studied for pyrolysis[124-127]. Kuroda et al. studied product formation from β-5 model compounds in the presence of tetramethylammonium hydroxide (TAMH) pyrolysis gas chromatography mass spectrometry (Py-GCMS) at 500 °C. Under these conditions, the major pathways proceed through the opening of the β-5 ring[125].

2.3.1.4. Model lignin oligomers

Model lignin monomers and dimers have been extensively studied and have provided valuable insight into the major pathways of lignin decomposition. However, these model compounds do not account for the variety of interunit linkages present in native lignin. Trimers, tetramers, and other oligomeric model compounds introduce multiple interunit linkages and become more representative of lignin. Even so, the research on model oligomers is sparse compared to that of model monomers and dimers[37, 128-130]. Liu et al. performed TGA, Py-GC, and tube furnace experiments of two synthesized model oligomers comprised of H and G units with β-O-4 linkages[128]. Much like the previous work on β-O-4 dimers, the C_β-O and C_α-C_β are the easiest bonds to cleave to initiate the pyrolysis mechanism, with ArO-CH_3 being another secondary pathway. Another β-O-4 oligomer was synthesized by Chu et al. that had an average molecular weight of 1250 Da, and they proposed a free-radical reaction scheme for pyrolysis based on the observed products from Py-GCMS experiments[129]. The major

identified monomeric products were vanillin and 2-methoxy-4-methyl phenol suggesting the C_β-O bond throughout the oligomer is easily broken. The products accounted for via a C-C scission were only observed at higher temperatures (>500 °C), which is to be expected to be the difference in reported BDEs[129]. Sheng et al. examined the pyrolysis behavior of a β-O-4 trimer, tetramer, and a synthetic polymer made up of G-units[37]. Products were ionized using a negative ion mode atmospheric pressure chemical ionization ((-)APCI) and detected with a linear quadrupole ion trap (LQIT) mass spectrometer[131]. For all pyrolysis experiments, no free radical species were detected, which suggests the decomposition of these oligomers proceeds through concerted reactions compared to radical cleavage[37].

Dibenzodioxocins are recently discovered eight-member rings connected to phenylpropane by ether bonds. These substructures are considered important branching structures in lignin[132-134]. There has not been much experimental work done on the pyrolysis behavior of a dibenzodioxocin structure. Gardrat et al. studied the decomposition of dibenzodioxocin using TGA and mass spectrometry[130]. Dibenzodioxocin was shown to be thermally unstable even at low temperatures. For all temperatures, 200-400 ℃, 4-vinylguaiacol was the main product, which suggests two possible mechanisms: initial scission of the α-O-4 followed by scission of the β-O-4 or vice versa[130]. Theoretical calculations provided energetics for which bond would be broken first, and that will be discussed in a later section.

As these lignin model structures get larger, the possible degradation pathways quickly become more complicated. Therefore, it is more difficult to propose full

reaction mechanisms and determine individual reaction kinetics to produce major products. As will be discussed in the following sections, quantum chemistry can play a significant role in addressing the shortcoming associated with current experimental techniques.

2.3.2. Computational investigation of lignin pyrolysis mechanisms

Recently, kinetic analysis of lignin model compounds has coupled experimental observation with theoretical calculations to propose reaction mechanisms based on the observed products and the relative energetics associated with the pathways for the formation of the products. Density functional theory (DFT) allows for the determination of the energetics of a specific system and provides valuable information for proposing mechanistic reaction pathways. Bond dissociation energy, or more accurately, bond dissociation enthalpy (BDE), is a useful first step for understanding the probably major reaction pathways. It allows for the prediction of which bonds are most likely to break under certain conditions. Theoretical calculations can locate transition states that have the highest potential energy and represent the energy barrier for a given reaction. The rate constants for reactions can then be calculated via transition-state theory[135]. In the absence of a large energy barrier on the potential energy surface (PES) or transition state, the activation energy can be approximated as the BDE.

In literature, bond dissociation energy and bond dissociation enthalpy are sometimes used interchangeably. Since these reactions are investigated at reaction temperature, the term bond dissociation enthalpy (BDE) is more appropriate. For aromatic model lignin monomers, the general trend in BDE is CH_3-O < O-H < CH_3O-

$C_{aromatic}$ < CH_2-H < HO-$C_{aromatic}$ < $C_{aromatic}$-H[33, 136-139]. In 2009, Beste et al. investigated the BDE of substituted phenethyl phenyl ether (PPE) at 298 K to form initial radical species from the homolytic cleavage at either the α-(C-O) or β-position(C-C)[140]. For all PPEs investigated, using M06-2X/6-311++G**(** corresponds to (d,p)), the C-O bond was found to have a lower BDE than the C-C bond (7.6 – 17.1 kcal/mol lower). The individual BDE, as well as the BDE difference, is also affected by the type of substituents present on the aromatic ring. Wang et al. (2009) investigated 1-(4-hydroxyphenyl)-2-phenoxy-1,3 propylene glycol and further supported the claim that the C_β-O and C_α-C_β have the lowest BDE using a B3LYP/6-31G(d) setup[141]. In 2010, Thomas Elder calculated the BDEs for three fully substituted dilignols with a β-O-4 linkage at 298 K using both G3MP2 and CBS-4m methods. As previously reported, he found the BDE of the β-O cleavage is less than the α-β, but the difference decreases as the dilignol becomes more substituted[142]. Younker et al. used DFT at the M06-2X/6-311++G** level to determine the effect of substituents at the α- and β-positions of using substituted PPE dimers[143]. The M06-2X functional was shown to capture the effect of hydrogen bonding, which is important when dealing with aliphatic functional groups. The addition of functional groups to the aliphatic carbons also introduces chiral centers into the molecule, which must be accounted for via a conformational search for each enantiomer. The presence of hydrogen bonding stabilized both the radical and ground states, so the BDE increased by less than 3 kcal/mol compared to PPE[143]. It is now well-documented that the BDE of the C-O bond is lower than the C-C in the β-ether linkage regardless of the substituents[140-143].

PPE and other β-O-4 dimers have been the most heavily investigated; however, other major lignin linkages, such as β-5 (~10%) and α-O-4, have been the focus of only a few kinetic studies. Two of the most exhaustive investigations into the BDE of the homolytic cleavage of model lignin model compounds were performed by Kim et al.(69 model compounds)[144] and Parthasarathi et al. (65 model compounds)[145]. Parthasarathi selected 33 ether-linked compounds, subclassified as β-O-4, α-O-4, and 4-O-5, and 32 compounds consisting of C-C linkages, β-1, α-1, β-5, and 5-5. The BDEs for all compounds were calculated at the M06-2X/6-311++G(d,p) level at 298 K. In the ether compounds, except for 4-O-5 linkages, the C-O bond was weaker than the C-C bond. The weakest ether bond was found to be from the α-O-4 subgroup (48.31 kcal/mol), and the weakest C-C bond was a β-1 (64.7 kcal/mol)[145]. Kim et al.[144] selected compounds representing four common lignin linkages: β-O-4, α-O-4, β-5, and biphenyl. The purpose of this study was to determine the effect of various substituents on the aromatic rings and alkyl chains on BDEs. Oxidation of the primary or secondary alcohols on the alkyl chain led to reduced BDEs. A comparison of BDEs for each class of compound can be seen in Figure 0-6. Both studies provide results that are valuable to understanding the pyrolysis mechanism of lignin. Huang et al.[146] performed a computational DFT study on 63 C-O and C-C bonds for six major interunit linkages in lignin: β-O-4, α-O-4, 4-O-5, β-1, and β-5. At the B3P86/6-31G(d,p) level, on average, the trend of BDE follows C_α-O < C_β-O < C_α-C_β(β-1) < C_α-C_β(β-O-4) < C_4-O < O-C_5 < C_α-C_1 < C_5-C_5.

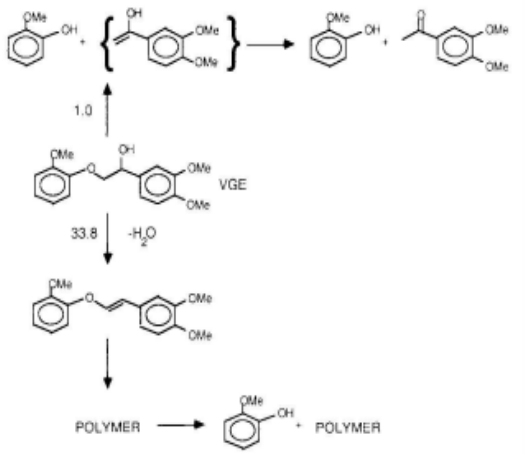

Figure 0-5. Proposed VGE pyrolysis pathways[116]

In addition to single C-C and C-O linkages, lignin also contains important fused ring structures, such as dibenzodioxocin, pinoresinol, phenylcoumaran, and spirodienone[147, 148]. Younker et al. calculated the BDEs of 15 substituted β-5 arylcoumaran model compounds with M06-2X/6-31++G**//G-31+G* level via homolytic cleavage. The C_{α}-O BDEs ranged from 40-44 kcal/mol while the C_{α}-C_{β} BDE was approximately 15 kcal/mol higher[149]. Thomas Elder and colleagues have been at the forefront of investigating some of the less understood lignin substructures[147, 148, 150].

Elder estimated the BDE of the linkages in a dibenzodioxocin model compound at M06-2X/6-311++G(d,p) level at 298 K. Dibenzodioxocin provides a unique opportunity compared to that of PPE. As shown in Figure 0-7, there are four possible bond dissociation products for the opening of the ring of dibenzodioxocin: 5-5′, α-O, α-β, and β-O. The BDEs were calculated to be 45.79, 57.13, 71.98, and 114.27 kcal/mol for α-O, β-O, α-β, and 5-5′, respectively.

The next step in proposed lignin pyrolysis pathways is identifying transition states and determining the energy barrier for each reaction. Kinetic rate constants are typically calculated using transition state theory[135]. For homolytic cleavages that have hard-to-identify transition states, the energy barrier can be assumed to be the BDE[151].

2.3.2.1. Model lignin monomers

Monomeric compounds, e.g., guaiacol, syringol, and coniferyl alcohol, are primary lignin pyrolysis products, and understanding their pyrolysis pathways can provide valuable insight into the secondary pyrolysis decomposition reactions.

Table 0-2. Comparison of estimated and experimental parameters for PPE pyrolysis.

	Mechanism	**Temperature (℃)**	**Reaction Order**	$\log A$ (s^{-1})	E_a **(kcal/mol)**
Klein[36]	Free-radical: Rice-Herzfeld chain	300-550	1	14 ±1	55±5
	Free-radical: Initial bond fission	300-550	1	15±1	70±5
	Concerted: Maccoll elimination	300-550	1	13±0.5	66±5
	Concerted: Retro-ene	300-550	1	11.5±1	45±5
	Experiment	300-550	1	11±1	45±3
Gilbert[107]	Free-radical	335-380	1.2	12.3	50.3
Britt[108]	Free-radical	330-425	1.29±0.02	11.4±0.1	46.4±1.0

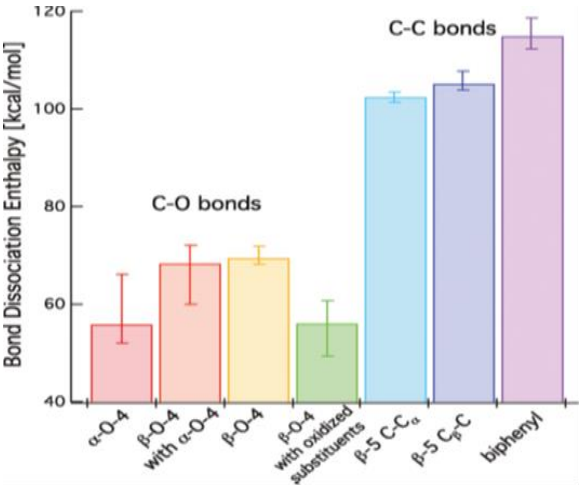

Figure 0-6. Median and range of BDEs for the classes of lignin model compounds investigated by Kim et al. [144]

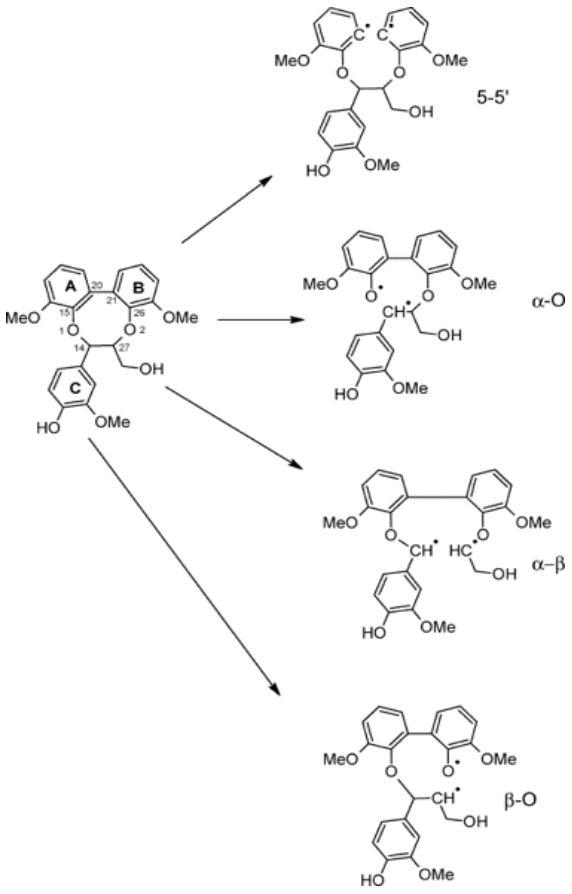

Figure 0-7. Bond dissociation pathways of dibenzodioxocin model compound proposed by Elder[147].

One of the most commonly selected model lignin monomers is guaiacol, as it has widely been used as a surrogate for lignin primary products[152, 153]. Huang et al. were one of the first groups to take a mechanistic approach to understanding the pyrolysis of guaiacol at the B3LYP/6-31++G(d,p) level at 298 K[34]. BDE calculations indicate that CH_3-O is the easiest bond to break, followed by the O-H bond. Three possible pathways were proposed, with the major pathway proceeding via cleavage of the methyl bond and hydrogenation to produce 1,2 dihydroxybenzene and methane with a total energy barrier of 74.78 kcal/mol with o-cresol and 2-hydroxybenzaldehyde as the main competitive products, which is in agreement with experimental observations[34]. As the methoxy group has been seen to play an important role in the pyrolysis of guaiacol, Liu et al. sought to better understand the influence of the methoxy functional group in guaiacol pyrolysis[137]. Five possible reaction mechanisms, all revolving around the methoxy group, were proposed using the same level of theory as Huang[34]. Each pathway was performed over a range representative of pyrolysis temperature (298-898 K), and it was found that the most reactive path was demethoxylation to form phenol and methane. The energy barrier was appreciably lowered upon coupling a hydrogen radical to the carbon atom at the position of the methoxy group[137]. Another finding of note was the proposed formation of o-quinonemethide. The proposed of this pathway may show methoxy groups are necessary to form o-quinonemethide intermediates, which supports the observations of Asmadi et al.[106] Verma and Kishore proposed reaction pathways that accounted for the formation of cyclopentanone and cyclohexanone as additional products of

guaiacol pyrolysis alongside phenol and anisole[139]. Thermochemistry calculations were carried out at the B3LYP/6-311++G(d,p) level of theory between 298-898 K. BDEs were calculated for each bond outside of the aromatic ring and showed close agreement with the work of Huang et al.[34] The formation of phenol was critical to the production of cyclohexanone from guaiacol. All of the proposed pathways were exothermic and spontaneous over the entire temperature range; however, the pathways for cyclopentanone and cyclohexanone formation showed a decrease in spontaneity as temperature increased[139]. Recently, Yerrayya et al. coupled experimental observation with DFT studies at the CBS-QB3 level of theory to investigate the fast pyrolysis of guaiacol to form four major phenols: phenol, catechol, o-hydroxybenzaldehyde, and o-cresol[136]. The full proposed mechanism consists of 19 elementary reactions with 17 different species, Figure 0-8. The o-hydroxyphenyl radical is a key intermediate for the formation of phenol and cresol, while o-hydroxybenzaldehyde was formed via an o-hydroxybenzyloxy radical[136]. Based on their findings, a kinetic model for the elementary reactions was developed and fit reasonably well with their experimental data. Nowakowska et al. proposed a detailed mechanism for guaiacol pyrolysis based of a previous model for anisole containing 1601 reactions with 233 species[152]. BDEs were calculated at the CBS-QB3 level of theory and showed good agreement with previously discussed work, with the CH_3-O (58.1 kcal/mol) being the easiest bond to break, followed by the O-H bond (87.1 kcal/mol). It was noted the presence of the phenolic O-H bond promotes the chain radical mechanism compared to that of anisole; however, the unimolecular decomposition dominates guaiacol pyrolysis[95, 152]. Most

work on guaiacol pyrolysis agrees, using both BDE calculations and experimental observations, that the proposed major pyrolysis pathways of guaiacol initiate with reactions involving the methoxy functional group.

Liu et al.[154] further modeled three types of guaiacyl-based model monomers: vanillin, vanillic acid, and vanillyl alcohol. Guaiacol was seen to be a common, major product for each monomer due to functional group removal. The formation of guaiacol was proposed to proceed via two routes: a synergy process with a cyclic transition state or a radical-induced process. The synergy pathway was shown to promote the release of gasses, and the pathways were consistent with experimental results[154]. Hu et al. calculated the bond strengths for various bonds in the vanillin molecule at the B3LYP/6-311g(d,p) level of theory[155]. The trend of bond strengths for vanillin was ArO-CH_3 < Ar-OCH_3 < Ar-CHO < Ar-OH < Ar-H. The bond strengths were also calculated by CBS-4M to get values closer to that of literature[155]. Wang et al. studied vanillin as a way to understand the secondary reactions of lignin pyrolysis[156]. As expected, the homolytic cleavage of the O-CH_3 bond was proposed to be the dominant initial step. All three functional groups, methoxy, hydroxy, and formyl, contribute to the formation of CO, which is shown to be the characteristic secondary pyrolysis product from vanillin[156].

Another popular lignin model monomer that is important to further understanding lignin pyrolysis is syringol. Like his work on guaiacol, Huang et al. investigated the pyrolysis mechanism of syringol at the B3LYP/6-31++G(d,p) level and found similar trends in regards to BDE: CH_3-O < O-H < CH_3O-$C_{aromatic}$ < CH_2-H < HO-$C_{aromatic}$ < $C_{aromatic}$-H[33]. Three possible pathways were proposed differing by the initial

bond breakage. The total energy barriers calculated implied the major proposed products to be guaiacol, 3-methoxycatechol, and 2-methoxy-6-methylphenol with total activation barriers of 5.11, 87.62, and 166.54 kcal/mol, respectively[33].

Catechol is another major component of lignin and pyrolysis oils[157]. Altarawneh et al. studied the unimolecular decomposition of catechol using a B3LYP/GTLarge level of theory and proposed a reaction scheme comprised of six possible pathways[158]. The migration of the hydroxyl H to an ortho carbon was shown to be the most feasible unimolecular route, followed by the self-expulsion of a hydroxyl H atom. However, based on high activation energies, it was suggested bimolecular reactions play a part in the formation of the major products of catechol pyrolysis[158]. The potential energy surface of catechol was examined at the CBS-QB3 and B3LYP/6-31G(d,p) level of theory by Khachatryan et al.[159] The *ipso*-catechol (70.4 kcal/mol) and α-catechol (68.7 kcal/mol) isomers were the most energetically favorable initial products. Based on further experimental work, the *para*- and *ortho*-semiquinone radicals (*p*-SQ and *o*-SQ) were the major radical products of catechol pyrolysis below 750 °C compared to the major product of *para*-benzoquinone (*p*-BQ) for hydroquninone[160].

2.3.2.2. Model lignin dimers

Lignin is comprised of a wide variety of interunit linkages of phenolic subunits. Investigating the pyrolysis of these interunit linkages is fundamental to understanding the major pathways of lignin pyrolysis. As mentioned earlier, the β-O-4 ether linkage makes up over half of the interunit linkages in native lignin. Therefore, a significant

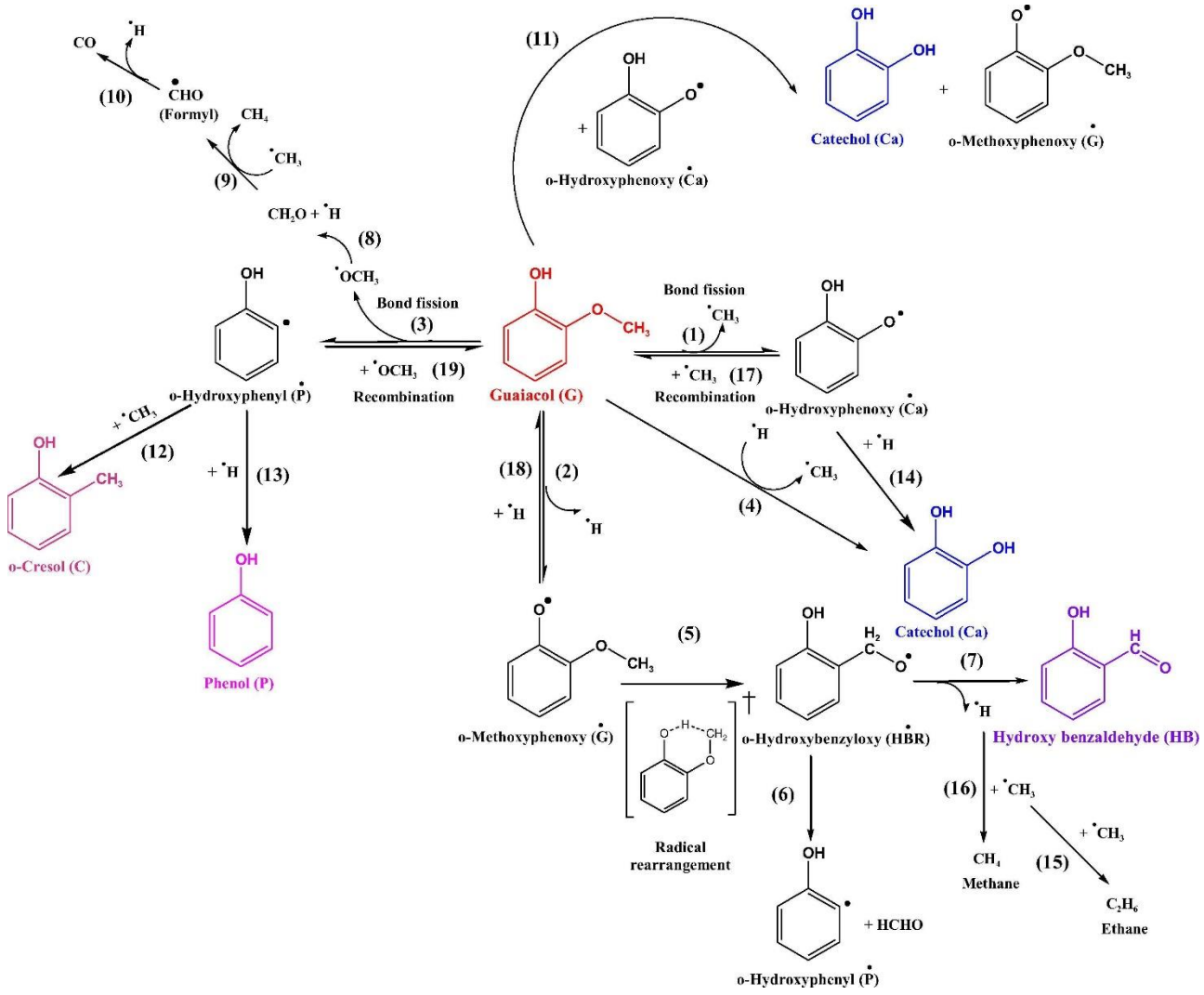

Figure 0-8. Proposed reaction mechanism for guaiacol pyrolysis. Image used from Yerrayya et al.(2019)[136].

amount of computational work has focused on studying β-O-4 model dimers, shown in Table 0-3. Phenethyl phenyl ether (PPE) is the simplest lignin model compound containing this linkage. Beste et al. have performed extensive work investigating the BDEs and homolytic pyrolysis reactions of PPE as well as the effect of various substituted PPEs that follow the scheme in Figure 0-3[35, 109, 140, 161-165]. Beste et al. developed a computational model for predicting the α/β selectivity for hydrogen abstraction by benzyl and phenoxyl radicals (reactions 2 and 6 in Figure 0-3) at the B3LYP/6-31++G(d,p) level[164]. For PPE to be more representative of native lignin, researchers need to account for substituents, commonly methoxy and hydroxy groups. Beste et al. built off their previous model for α/β selectivity and applied it to para-substituted PPE[165]. As substituents were introduced to the phenethyl ring, the α/β selectivity increased, with the general trend being PPE < p-hydroxy-PPE < p-methoxy-PPE. These simple selectivity models were shown to not be able to apply to PPE derivatives with methoxy groups on the ethyl-adjacent ring due to the strong endothermic nature of the resulting hydrogen abstraction reactions[109]. Like their previous work, the α-channel was favored over the β-channel, 11.5 to 13.5 kcal/mol for p-methoxy PPE abstraction by a benzyl radical, respectively. In addition to the hydrogen abstraction reaction, the phenyl shift (reaction 4 in Figure 0-3) was also studied by Beste et al. as it can significantly affect the selectivity of thermal decomposition[35]. Substituents on the phenethyl-side ring did not have a significant effect on the rate constant for the C-O phenyl shift; however, methoxy substituents on the ether-adjacent ring accelerated the rate of the C-O phenyl shift[35]. The less reported

C-C shift has a similar reaction profile as the C-O reaction and can only be differentiated by studying the subsequent β-scission. The C-C phenyl shift has an activation barrier of 15 kcal/mol compared to a virtually barrierless reaction for the C-O shift[162]. A sufficiently fast phenyl shift will limit the α/β selectivity by suppressing the interconversion from a β-radical to an α-radical. Beste et al. combined their previous work into a kinetic Monte Carlo simulation using calculated rate parameters for the hydrogen abstraction, phenyl shift, and β-scission reactions (Figure 0-3)[161]. The reaction profile for the α- and β-pathway is shown in Figure 0-9. The model predicted qualitatively accurate α/β-product selectivity but its values were overestimated compared to experimental observation. These simulations also confirmed the presence of the C-C phenyl shift reaction in the overall mechanism of PPE pyrolysis, which was previously unaccounted for[161]. One of the first studies to computationally investigate the pyrolysis of PPE via a concerted reaction was published by Huang et al.[151] Ten possible, eight free-radical and two concerted pyrolysis pathways were investigated at the B3LYP/6-31G(d) level from 298 to 1700 K. The two concerted pathways (retro-ene and Maccoll elimination reactions) were shown to have lower activation energies than all the free-radical pathways and are proposed to be the major pyrolysis pathways. The competitive free-radical pathways are initiated by the β -O scission and result in the formation of phenoxy, benzyl, and hydrogen radicals. which infer the major products are styrene, phenoxy, and compounds that can form from phenoxy, benzyl, phenyl, and hydrogen radicals[151]. These results are in line with the work of Jarvis suggesting concerted mechanisms dominate at moderate temperatures

(< 1000 K)[111]. Beste and Buchanan used DFT to investigate the effect of an aliphatic substituent (α-hydroxy PPE) at the M06-2X/6-311++G** level[163]. The aliphatic substitution was shown to lower the activation energy for the α-hydrogen abstraction while increasing the energy barrier for β-hydrogen abstraction, which results in a predicted larger α/β selectivity[163]. Huang et al. compared possible free-radical and concerted pyrolysis pathways for an aliphatic substituted model β-O-4 dimer, 1-phenyl-2-phenoxy-1,3-propanediol[166]. Over the range from 298-1900 K, the concerted pathways were shown to dominate at lower temperatures, with free-radical reactions becoming competitive at higher temperatures. The activation energies further support the findings of Jarvis et al., shown in Figure 0-10[111, 166]. Elder and Beste[167], based on the previous findings, performed DFT analysis to investigate possible concerted pathways for the pyrolysis of three fully substituted β-O-4 dimers, representing guaiacyl, syringyl, and para-hydroxy models.

All calculations were performed at the M06-2X/6-311++G(d,p) level with rate constants calculated by transition state theory and energy barriers calculated in terms of the Gibbs free energy of activation. The overall trend agrees with previous work on PPE, with the fully substituted dimers having slightly larger activation energies than PPE[111, 151]. For all the model dimers, the retro-ene fragmentation is favored over the Maccoll elimination, but both concerted pathways have lower activation energies than the BDEs associated with homolytic cleavage[167].

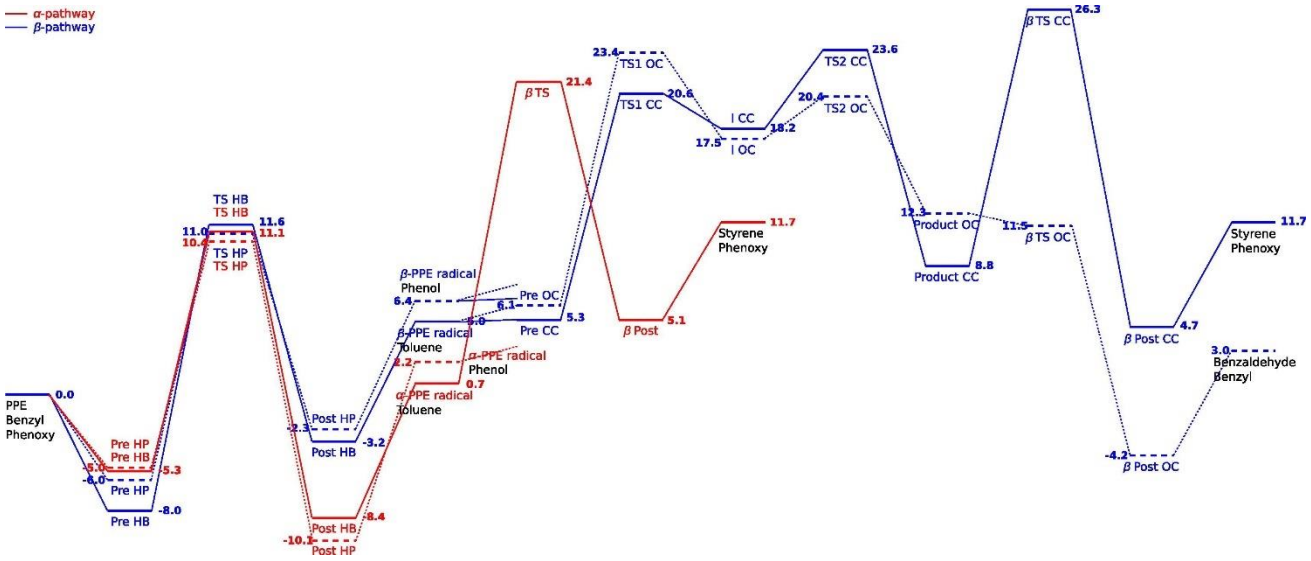

Figure 0-9. Reaction energy profile for PPE pyrolysis[161].

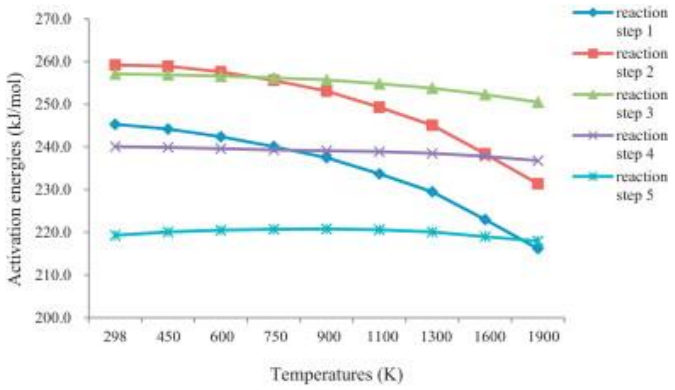

Figure 0-10. Activation energies for the initial step in each pathway. Step 1: β-O scission, Step 2: α -β scission, Steps 3-5: concerted pathways[166].

In addition to the β-O-4 linkage, the α-O-4 linkage also accounts for approximately 6-8% of total interunit linkages in lignin; therefore, it is imperative to study to understand lignin pyrolysis[168]. There have been significantly fewer computational studies on the pyrolysis model dimers involving the α-O-4 linkage. Huang et al. calculated the BDEs of the model dimer and proposed a pyrolysis pathway for the three lowest energy bond scissions, C_α-O, O-CH_3, and C_α-C_β. The C_α-O scission was the major pyrolysis pathway, and the major products of the model dimer pyrolysis were guaiacol, p-hydroxyphenyl-ethanol, p-hydroxyphenyl-acetaldehyde. 2-hydroxybenzaldehyde[168]. Choi et al. investigated both pericyclic concerted and free-radical reaction pathways for five β-O-4 and two α-O-4 dimers, PPE, 2-phenoxy-1,3-propanediol (PPPD), 1-(4-hydroxypheyl)-2-phenoxypropane-1,3-diol (HH), 1-(4-hydroxy-3-methoxyphenyl)-2-(2-methoxyphenoxy)propane-1,3-diol (GG), 2-(2,6-dimethoxyphenoxy)-1-(4-hydroxy-3,5-dimethoxyphenyl)propoane-1,3-diol (SS), benzylphenyl ether (BPE) and 1-(phenoxyethyl)benzene (PEB), at the B3LYP/6-31++G(d,p) level[169]. The proposed concerted pathway for PPE, the simplest of the β-O-4 dimers, is shown in Figure 0-11. Their experimental and computational results strongly support the pericyclic retro-ene reactions for β-O-4 dimers compared to the homolysis of the C_β-O bond[169].

However, the opposite was true for the α-O-4 dimers. The radicals formed by the homolysis of the C_α-O bonds were stabilized due to the delocalization of electrons, which implied pyrolysis would proceed via a homolysis mechanism[169].

The ether linkages have garnered the most attention in the use of model dimers, with little computational work done on the C-C interunit linkages. Huang et al. used a B3LYP/6-31G(d,p) level of theory to propose homolytic cleavage and concerted pathways for the pyrolysis of 1,2-p-hydroxy-phenyl-1,3-propanediol, a β-1 model lignin dimer[170]. The C_α-C_β cleavage and concerted C_γ-elimination mechanisms were calculated to be the predominant pyrolysis pathways. These proposed pathways agree with the experimental findings of Kawamoto et al.[117] As expected from previous results, the free-radical mechanism showed significant temperature dependence, which leads to the concerted mechanisms dominating at lower temperatures[170].

2.3.2.3. Model lignin oligomers

A limitation of using lignin model dimers to try and understand native lignin pyrolysis is only having one linkage. Lignin does not have a well-defined repeating structure like cellulose; therefore, lignin dimer pyrolysis schemes cannot be linearly extrapolated out to represent native lignin. Larger oligomeric (trimers, tetramers, hexamers, and on) model compounds are needed to bridge the knowledge gap between model dimers and native lignin. As these model compounds are more novel than heavily investigated dimers, e.g., PPE, these studies require a larger incorporation of experimental observations for validation.

Sheng et al. investigated pyrolysis pathways for a β-O-4 linked model trimer, tetramer, and a synthetic polymer[37]. The energy barriers were calculated using β-O-4 that were analogous to their oligomers of interest. No radical products were observed in their experimental analysis, and the energy barriers for Maccoll elimination and

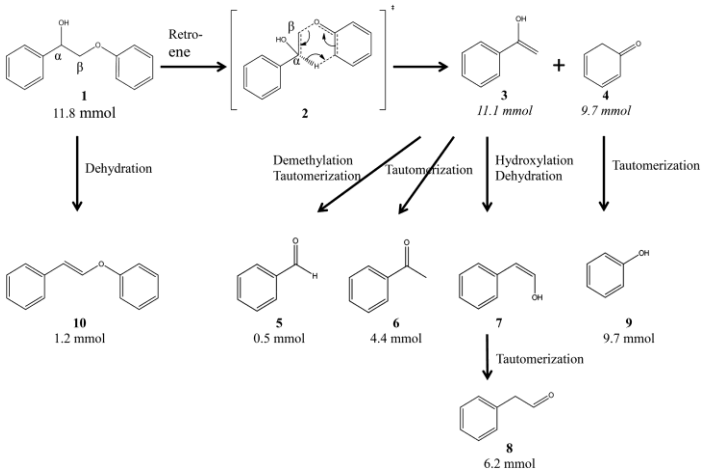

Figure 0-11. Proposed pericyclic reaction mechanism for PPE[169].

retro-ene fragmentation were calculated to be lower than the BDEs of homolytic cleavage at the M06-2X/6-311++G(d,p) level, 60.3, 56.8, and 72.1 kcal/mol, respectively[37].

Berstis et al. investigated the strength of the benzodioxane linkage found in C-lignin[171]. The BDEs for the dissociation for the benzodioxane linkage compared to a typical β-O-4 bond at the M06-2X/Def2-TZVPP level of theory. The α-bond of the benzodioxane linkage was found to be weaker than the standard β-O-4 linkage. This observation was extrapolated to projected linear benzodioxane-linked 24-mers. Stereochemistry can play a large part in lignin degradation; therefore, further analysis of lignin structure could help in understanding the structure-reactivity relationships of stereochemistry[171]. This paper was focused more on the lignin polymerization mechanisms; however, this information is just as useful for designing efficient lignin depolymerization.

Azad et al. published computational work on conformational and thermodynamic analysis of a 10-mer comprised of β-O-4 linked guaiacyl units[172]. BDEs were calculated as a function of temperature and bond cleaving position at the BLYP/DNP level of theory. The cleavage position along the oligomer was shown to have a larger effect on the BDE than the temperature. The approach taken to analyze a large model molecule compared to dimers can serve as a building block for more detailed lignin kinetic models.

Other special linkages, such as dibenzodioxocins and spirodienone, have been studied computationally to understand the BDEs associated with the initial scission reactions[147-150]. However, not much work has been done on proposing full pyrolysis pathways for these special substructures of lignin. Gardrat et al. took the computational investigation of a dibenzodioxocin model compound a step further using quantum chemistry, mass spectrometry, and thermal analysis[130]. The dibenzodioxocin compound contains both α and β ether linkages and is unstable at even low temperatures. The α-O-4 bond is expected to break before the β-O-4 due to lower energy. Experimental products show vinylguaicol and 3,3′-dimethoxy-5-5′-dipropylbiphenyl-2,2′-diol, indicating that both ether bonds break during decomposition[130].

2.4. Pathways going forward

This review has highlighted the current state-of-the-art research on lignin pyrolysis kinetics. Significant progress has been made on both the experimental and computational sides to understand the fundamental mechanisms involved in lignin pyrolysis. However, as mentioned by Maduskar et al., most current analytic techniques, such as TGA and Py-GCMS, are not adequate to accurately capture pyrolysis kinetics of pyrolysis at a mechanistic level[173]. Experimentally, techniques need to be developed to achieve the high heating rates representative of fast pyrolysis. Recently, it has been shown that the high heating rates published by commercial Py-GCMS systems (20,000 °C/s) are not reflected in the heating rate of the sample (~200 °C/s)[174]. In addition to faster heating rates, current techniques make it difficult to analyze products at the

Table 0-3. Comparison of bond dissociation enthalpies of model β-O-4 dimers.

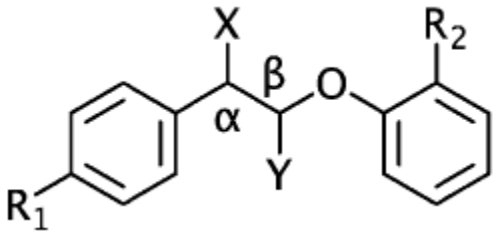

Compound	Method	Temperature (K)	C-O BDE (kcal/mol)	C-C BDE (kcal/mol)	Ref.
PPE	M06-2X/6-311++G**	298	69.5	77.1	140
pHO-PPE			69.6	76.6	
pCH3O-PPE			69.6	76.6	
PPE-pOCH3			64.1	76.7	
PPE-oOCH3			64.4	77.0	
PPE-dioOCH3			60.9	78.0	
PPE-oOCH3	G3MP2	298	66.6	68.3	142
	CBS-4m		68.3	79.6	
PPE	M06-2X/6-311++G** and M06-2X/31++G**	298	71.2	77.6	143
X = OH			72.3	75.1	
Y = CH2OH			71.8	78.1	
(αS, βS) X = OH, Y = CH2OH			72.9	75.3	

Table 2 3. Continued

Compound	**Method**	**Temperature (K)**	**C-O BDE (kcal/mol)**	**C-C BDE (kcal/mol)**	**Ref.**
(αS, βR) X = OH, Y = CH2OH	M06-2X/6-311++G** and M06-2X/31++G**	298	72.0	75.3	143
R1 = OH, R2 = OCH3			64.6	76.8	
R1 = OH, R2 = OCH3, X = OH			68.6	78.7	
R1 = OH, R2 = OCH3, X = =O			55.2	79.7	
R1 = OH, R2 = OCH3, Y = CH2OH			69.0	80.0	
(αS, βS) R1 = OH, R2 = OCH3, X = OH, Y = CH2OH			69.8	77.9	

Table 2 3. Continued

Compound	**Method**	**Temperature (K)**	**C-O BDE (kcal/mol)**	**C-C BDE (kcal/mol)**	**Ref.**
(αS, βR) R1 = OH, R2 = OCH3, X = OH, Y = CH2OH	M06-2X/6-311++G** and M06-2X/31++G**	298	68.6	78.0	143
Y = CH3			70.8	76.5	
PPE	B3LYP/6-31(d,p)	778	70.8	-	169
	B3LYP/6-31++(d,p)		69.4		
	B3LYP/6-311(d)		68.7		
	M06-2X/6-311++(d,p)		81.3		
PPE	M06-2X/6-311++G**	298	69.34	75.19	167
G			70.83	74.34	
H			68.32	79.35	
S			69.34	76.59	
X = OH, Y = CH2OH	B3LYP/6-31G(d,p)	298	58.63	61.95	166

pyrolysis time scale. Biomass pyrolysis reactions occur at the millisecond time scale; however, the residence time associated with TGA and Py-GCMS are on the scale of seconds, which only allows for cumulative product yields[55]. One of the most advanced pyrolysis systems was developed by Daunhauer and co-workers employed millisecond pulse heating and quenching of thin film samples connected to an online GC system[173, 175, 176]. The Pulse-heated Analysis of Solid Reaction (PHASR) system is a step in the right direction for gaining a mechanistic understanding of lignin pyrolysis through experimental techniques.

Computational investigation through quantum chemistry calculations has been extremely beneficial for understanding the mechanisms associated with model lignin pyrolysis. As computational power and availability of resources continue to increase, there is hope to be able to investigate larger model lignin substructures, such as octamers, 10-mers, and 20-mers, at the same level of scrutiny as the studies on guaiacol and PPE. Additionally, machine learning and artificial intelligence have been incorporated into understanding reaction schemes[177-179]. These advanced methods could play a large role in developing general rules for native pyrolysis or proposing a detailed reaction mechanism using a lignin structure.

2.5. Conclusions

In this review, the current knowledge of the mechanisms for lignin pyrolysis was discussed using both experimentally and computationally derived knowledge. Due to the lack of a well-defined repeating structure in lignin model monomers and dimers, along with isolated lignin, have been the focus of research trying to get a mechanistic

understanding of lignin pyrolysis. Most of the experimental work proposed simplified reaction schemes with reaction kinetics following a quasi-first-order reaction. On the computational side, the first step for several compounds was to determine the BDEs for each relevant bond breakage to determine the probable major reaction pathways. Afterward, the calculations followed through to determine the overall energy barriers for each pathway as well as activation energies associated with each possible reaction. Due to computational limitations, these works have largely been limited to monomers and dimers; however, with the increase in computational power and availability, there is room to build on to larger, more representative substructures in the future. There has been a lot of invaluable work on understanding lignin pyrolysis, but there is still a long way to go. Developing more advanced experimental techniques to increase the heating rate and analyze products at the millisecond time scale are vital next steps for understanding lignin pyrolysis pathways.

References

1. Tidball, R. B., J. ; Rodriguez, N.; Knoke, S. , Cost and Performance Assumptions for Modeling Electricity Generation Technologies. **2010**.
2. Yanez, A. J.; Natarajan, P.; Li, W.; Mabon, R.; Broadbelt, L. J., Coupled Structural and Kinetic Model of Lignin Fast Pyrolysis. *Energy & Fuels* **2018,** *32* (2), 1822-1830.
3. Jahirul, M. I.; Rasul, M. G.; Chowdhury, A. A.; Ashwath, N., Biofuels production through biomass pyrolysis—a technological review. *Energies* **2012,** *5* (12), 4952-5001.
4. Demirbaş, A., Partly chemical analysis of liquid fraction of flash pyrolysis products from biomass in the presence of sodium carbonate. *Energy Conversion and Management* **2002,** *43* (14), 1801-1809.
5. Bridgwater, A. V.; Meier, D.; Radlein, D., An overview of fast pyrolysis of biomass. *Org. Geochem.* **1999,** *30* (12), 1479-1493.
6. Williams, C. L.; Westover, T. L.; Emerson, R. M.; Tumuluru, J. S.; Li, C., Sources of Biomass Feedstock Variability and the Potential Impact on Biofuels Production. *BioEnergy Research* **2016,** *9* (1), 1-14.
7. Debiagi, P. E. A.; Gentile, G.; Pelucchi, M.; Frassoldati, A.; Cuoci, A.; Faravelli, T.; Ranzi, E., Detailed kinetic mechanism of gas-phase reactions of volatiles released from biomass pyrolysis. *Biomass and Bioenergy* **2016,** *93*, 60-71.
8. Kansa, E. J.; Perlee, H. E.; Chaiken, R. F., Mathematical model of wood pyrolysis including internal forced convection. *Combustion and Flame* **1977,** *29*, 311-324.
9. Kung, H.-C., A mathematical model of wood pyrolysis. *Combustion and Flame* **1972,** *18* (2), 185-195.
10. Villermaux, J.; Antoine, B.; Lede, J.; Soulignac, F., A new model for thermal volatilization of solid particles undergoing fast pyrolysis. *Chemical Engineering Science* **1986,** *41* (1), 151-157.
11. Broido, A.; Weinstein, M., Low Temperature Isothermal Pyrolysis of Cellulose. In *Thermal Analysis: Volume 3: Organic and Macromolecular Chemistry, Ceramics, Earth Science*, Wiedemann, H. G., Ed. Birkhäuser Basel: Basel, 1972; pp 285-296.
12. Broido, A.; Nelson, M. A., Char yield on pyrolysis of cellulose. *Combustion and Flame* **1975,** *24*, 263-268.
13. Shafizadeh, F., Introduction to pyrolysis of biomass. *Journal of Analytical and Applied Pyrolysis* **1982,** *3* (4), 283-305.
14. Broido, A., KINETICS OF SOLID-PHASE CELLULOSE PYROLYSIS. In *Thermal Uses and Properties of Carbohydrates and Lignins*, Shafizadeh, F.; Sarkanen, K. V.; Tillman, D. A., Eds. Academic Press: 1976; pp 19-36.
15. Bradbury, A. G. W.; Sakai, Y.; Shafizadeh, F., A kinetic model for pyrolysis of cellulose. *Journal of Applied Polymer Science* **1979,** *23* (11), 3271-3280.
16. Antal, M. J., Jr.; Varhegyi, G., Cellulose Pyrolysis Kinetics: The Current State of Knowledge. *Industrial & Engineering Chemistry Research* **1995,** *34* (3), 703-717.
17. Lédé, J., Cellulose pyrolysis kinetics: An historical review on the existence and role of intermediate active cellulose. *Journal of Analytical and Applied Pyrolysis* **2012,** *94*, 17-32.

18. Burnham, A. K.; Zhou, X.; Broadbelt, L. J., Critical Review of the Global Chemical Kinetics of Cellulose Thermal Decomposition. *Energy & Fuels* **2015,** *29* (5), 2906-2918.
19. Ranzi, E.; Cuoci, A.; Faravelli, T.; Frassoldati, A.; Migliavacca, G.; Pierucci, S.; Sommariva, S., Chemical kinetics of biomass pyrolysis. *Energy Fuels* **2008,** *22* (6), 4292-4300.
20. Lourenço, A.; Rencoret, J.; Chemetova, C.; Gominho, J.; Gutiérrez, A.; del Río, J. C.; Pereira, H., Lignin Composition and Structure Differs between Xylem, Phloem and Phellem in Quercus suber L. *Frontiers in Plant Science* **2016,** *7* (1612).
21. Kumar, A.; Anushree; Kumar, J.; Bhaskar, T., Utilization of lignin: A sustainable and eco-friendly approach. *Journal of the Energy Institute* **2020,** *93* (1), 235-271.
22. Liu, J.; Li, X.; Li, M.; Zheng, Y., Chapter Six - Lignin biorefinery: Lignin source, isolation, characterization, and bioconversion. In *Advances in Bioenergy*, Li, Y.; Zhou, Y., Eds. Elsevier: 2022; Vol. 7, pp 211-270.
23. Ralph, J.; Lapierre, C.; Boerjan, W., Lignin structure and its engineering. *Current Opinion in Biotechnology* **2019,** *56*, 240-249.
24. Lourenço, A.; Pereira, H., Compositional variability of lignin in biomass. *M. Poletto, Lignin-Trends and Aplications* **2018**, 65-98.
25. Holladay, J. E.; White, J. F.; Bozell, J. J.; Johnson, D. *Top Value-Added Chemicals from Biomass - Volume II—Results of Screening for Potential Candidates from Biorefinery Lignin*; PNNL-16983; Other: BM0102070; TRN: US200805%%262 United States 10.2172/921839 Other: BM0102070; TRN: US200805%%262 PNNL English; ; Pacific Northwest National Lab. (PNNL), Richland, WA (United States): 2007; p Medium: ED; Size: PDFN.
26. Dorrestijn, E.; Laarhoven, L. J. J.; Arends, I. W. C. E.; Mulder, P., The occurrence and reactivity of phenoxyl linkages in lignin and low rank coal. *Journal of Analytical and Applied Pyrolysis* **2000,** *54* (1), 153-192.
27. Ralph, J.; Lundquist, K.; Brunow, G.; Lu, F.; Kim, H.; Schatz, P. F.; Marita, J. M.; Hatfield, R. D.; Ralph, S. A.; Christensen, J. H.; Boerjan, W., Lignins: Natural polymers from oxidative coupling of 4-hydroxyphenyl- propanoids. *Phytochemistry Reviews* **2004,** *3* (1), 29-60.
28. Zakzeski, J.; Bruijnincx, P. C. A.; Jongerius, A. L.; Weckhuysen, B. M., The Catalytic Valorization of Lignin for the Production of Renewable Chemicals. *Chemical Reviews* **2010,** *110* (6), 3552-3599.
29. Chakar, F. S.; Ragauskas, A. J., Review of current and future softwood kraft lignin process chemistry. *Industrial Crops and Products* **2004,** *20* (2), 131-141.
30. Hosoya, T.; Kawamoto, H.; Saka, S., Cellulose–hemicellulose and cellulose–lignin interactions in wood pyrolysis at gasification temperature. *Journal of Analytical and Applied Pyrolysis* **2007,** *80* (1), 118-125.
31. Zhou, L.; Budarin, V.; Fan, J.; Sloan, R.; Macquarrie, D., Efficient Method of Lignin Isolation Using Microwave-Assisted Acidolysis and Characterization of the Residual Lignin. *ACS Sustainable Chemistry & Engineering* **2017,** *5* (5), 3768-3774.
32. Tuomela, M.; Vikman, M.; Hatakka, A.; Itävaara, M., Biodegradation of lignin in a compost environment: a review. *Bioresource Technology* **2000,** *72* (2), 169-183.

33. Huang, J.-b.; Liu, C.; Ren, L.-r.; Tong, H.; Li, W.-m.; Wu, D., Studies on pyrolysis mechanism of syringol as lignin model compound by quantum chemistry. *Journal of Fuel Chemistry and Technology* **2013,** *41* (6), 657-666.
34. Huang, J.; Li, X.; Wu, D.; Tong, H.; Li, W., Theoretical studies on pyrolysis mechanism of guaiacol as lignin model compound. *Journal of Renewable and Sustainable Energy* **2013,** *5* (4), 043112.
35. Beste, A.; Buchanan, A. C., Kinetic Analysis of the Phenyl-Shift Reaction in β-O-4 Lignin Model Compounds: A Computational Study. *The Journal of Organic Chemistry* **2011,** *76* (7), 2195-2203.
36. Klein, M. T.; Virk, P. S., Model pathways in lignin thermolysis. 1. Phenethyl phenyl ether. *Industrial & Engineering Chemistry Fundamentals* **1983,** *22* (1), 35-45.
37. Sheng, H.; Murria, P.; Degenstein, J. C.; Tang, W.; Riedeman, J. S.; Hurt, M. R.; Dow, A.; Klein, I.; Zhu, H.; Nash, J. J.; Abu-Omar, M.; Agrawal, R.; Delgass, W. N.; Ribeiro, F. H.; Kenttämaa, H. I., Initial Products and Reaction Mechanisms for Fast Pyrolysis of Synthetic G-Lignin Oligomers with β-O-4 Linkages via On-Line Mass Spectrometry and Quantum Chemical Calculations. *ChemistrySelect* **2017,** *2* (24), 7185-7193.
38. Buskirk, A.; Baradaran, H., Can Reaction Mechanisms Be Proven? *Journal of Chemical Education* **2009,** *86* (5), 551.
39. Young, D. C., Fundamental Principles. In *Computational Chemistry*, 2001; pp 5-18.
40. Jiang, G.; Nowakowski, D. J.; Bridgwater, A. V., A systematic study of the kinetics of lignin pyrolysis. *Thermochimica Acta* **2010,** *498* (1), 61-66.
41. Chen, T.; Li, L.; Zhao, R.; Wu, J., Pyrolysis kinetic analysis of the three pseudocomponents of biomass–cellulose, hemicellulose and lignin. *Journal of Thermal Analysis and Calorimetry* **2017,** *128* (3), 1825-1832.
42. Shafizadeh, F.; Chin, P. P. S., Thermal Deterioration of Wood. In *Wood Technology: Chemical Aspects*, American Chemical Society: 1977; Vol. 43, pp 57-81.
43. Grønli, M. G.; Várhegyi, G.; Di Blasi, C., Thermogravimetric Analysis and Devolatilization Kinetics of Wood. *Industrial & Engineering Chemistry Research* **2002,** *41* (17), 4201-4208.
44. Zhang, J.; Chen, T.; Wu, J.; Wu, J., Multi-Gaussian-DAEM-reaction model for thermal decompositions of cellulose, hemicellulose and lignin: Comparison of N2 and CO2 atmosphere. *Bioresource Technology* **2014,** *166*, 87-95.
45. Zhou, H.; Long, Y.; Meng, A.; Li, Q.; Zhang, Y., The pyrolysis simulation of five biomass species by hemi-cellulose, cellulose and lignin based on thermogravimetric curves. *Thermochimica Acta* **2013,** *566*, 36-43.
46. Nunn, T. R.; Howard, J. B.; Longwell, J. P.; Peters, W. A., Product compositions and kinetics in the rapid pyrolysis of milled wood lignin. *Industrial & Engineering Chemistry Process Design and Development* **1985,** *24* (3), 844-852.
47. Ramiah, M. V., Thermogravimetric and differential thermal analysis of cellulose, hemicellulose, and lignin. *Journal of Applied Polymer Science* **1970,** *14* (5), 1323-1337.

48. Radojević, M.; Janković, B.; Jovanović, V.; Stojiljković, D.; Manić, N., Comparative pyrolysis kinetics of various biomasses based on model-free and DAEM approaches improved with numerical optimization procedure. *PLOS ONE* **2018,** *13* (10), e0206657.
49. Cai, J.; Wu, W.; Liu, R., Sensitivity analysis of three-parallel-DAEM-reaction model for describing rice straw pyrolysis. *Bioresource Technology* **2013,** *132*, 423-426.
50. Ferdous, D.; Dalai, A. K.; Bej, S. K.; Thring, R. W., Pyrolysis of Lignins: Experimental and Kinetics Studies. *Energy & Fuels* **2002,** *16* (6), 1405-1412.
51. Li, Z.; Zhao, W.; Meng, B.; Liu, C.; Zhu, Q.; Zhao, G., Kinetic study of corn straw pyrolysis: Comparison of two different three-pseudocomponent models. *Bioresource Technology* **2008,** *99* (16), 7616-7622.
52. Bassilakis, R.; Carangelo, R. M.; Wójtowicz, M. A., TG-FTIR analysis of biomass pyrolysis. *Fuel* **2001,** *80* (12), 1765-1786.
53. de Jong, W.; Pirone, A.; Wójtowicz, M. A., Pyrolysis of Miscanthus Giganteus and wood pellets: TG-FTIR analysis and reaction kinetics☆. *Fuel* **2003,** *82* (9), 1139-1147.
54. Wójtowicz, M. A.; Bassilakis, R.; Smith, W. W.; Chen, Y.; Carangelo, R. M., Modeling the evolution of volatile species during tobacco pyrolysis. *Journal of Analytical and Applied Pyrolysis* **2003,** *66* (1), 235-261.
55. Vinu, R.; Broadbelt, L. J., A mechanistic model of fast pyrolysis of glucose-based carbohydrates to predict bio-oil composition. *Energy & Environmental Science* **2012,** *5* (12), 9808-9826.
56. Zhou, X.; Nolte, M. W.; Mayes, H. B.; Shanks, B. H.; Broadbelt, L. J., Experimental and Mechanistic Modeling of Fast Pyrolysis of Neat Glucose-Based Carbohydrates. 1. Experiments and Development of a Detailed Mechanistic Model. *Industrial & Engineering Chemistry Research* **2014,** *53* (34), 13274-13289.
57. Tanaka, A.; Maekawa, K.; Suzuki, K., Theoretical Calculations in Reaction Mechanism Studies. *Sumitomo Chemical Co, Ltd* **2013**, 1-10.
58. Hohenberg, P.; Kohn, W., Inhomogeneous Electron Gas. *Physical Review* **1964,** *136* (3B), B864-B871.
59. Sahni, V., The Hohenberg-Kohn Theorems and Kohn-Sham Density Functional Theory. In *Quantal Density Functional Theory*, Springer Berlin Heidelberg: Berlin, Heidelberg, 2004; pp 99-123.
60. Foresman, J. B.; Frisch, A., *Exploring chemistry with electronic structure methods*. 2nd ed.; Gaussian, Incorporated: 1996.
61. Becke, A. D., Density-functional thermochemistry. III. The role of exact exchange. *The Journal of Chemical Physics* **1993,** *98* (7), 5648-5652.
62. Lee, C.; Yang, W.; Parr, R. G., Development of the Colle-Salvetti correlation-energy formula into a functional of the electron density. *Physical Review B* **1988,** *37* (2), 785-789.
63. Zhao, Y.; Truhlar, D. G., Density Functionals with Broad Applicability in Chemistry. *Accounts of Chemical Research* **2008,** *41* (2), 157-167.
64. Mayes, H. B.; Broadbelt, L. J., Unraveling the Reactions that Unravel Cellulose. *The Journal of Physical Chemistry A* **2012,** *116* (26), 7098-7106.

65. Caballero, J. A.; Font, R.; Marcilla, A., Kinetic study of the secondary thermal decomposition of Kraft lignin. *Journal of Analytical and Applied Pyrolysis* **1996,** *38* (1), 131-152.
66. Caballero, J. A.; Font, R.; Marcilla, A., Study of the primary pyrolysis of Kraft lignin at high heating rates: yields and kinetics. *Journal of Analytical and Applied Pyrolysis* **1996,** *36* (2), 159-178.
67. Caballero, J. A.; Font, R.; Marcilla, A.; García, A. N., Flash pyrolysis of Klason lignin in a Pyroprobe 1000. *Journal of Analytical and Applied Pyrolysis* **1993,** *27* (2), 221-244.
68. Ojha, D. K.; Viju, D.; Vinu, R., Fast pyrolysis kinetics of alkali lignin: Evaluation of apparent rate parameters and product time evolution. *Bioresource Technology* **2017,** *241*, 142-151.
69. Domburg, G. E.; Sergeeva, V. N.; Kalninsh, A. I., Thermal Analysis of Lignin. In *Thermal Analysis: Volume 3: Organic and Macromolecular Chemistry, Ceramics, Earth Science*, Wiedemann, H. G., Ed. Birkhäuser Basel: Basel, 1972; pp 327-340.
70. Freeman, E. S.; Carroll, B., The Application of Thermoanalytical Techniques to Reaction Kinetics: The Thermogravimetric Evaluation of the Kinetics of the Decomposition of Calcium Oxalate Monohydrate. *The Journal of Physical Chemistry* **1958,** *62* (4), 394-397.
71. Chan, W.-C. R.; Kelbon, M.; Krieger, B. B., Modelling and experimental verification of physical and chemical processes during pyrolysis of a large biomass particle. *Fuel* **1985,** *64* (11), 1505-1513.
72. Miura, K., A New and Simple Method to Estimate f(E) and k0(E) in the Distributed Activation Energy Model from Three Sets of Experimental Data. *Energy & Fuels* **1995,** *9* (2), 302-307.
73. Cai, J.; Wu, W.; Liu, R., An overview of distributed activation energy model and its application in the pyrolysis of lignocellulosic biomass. *Renewable and Sustainable Energy Reviews* **2014,** *36*, 236-246.
74. Wang, S.; Ru, B.; Lin, H.; Sun, W.; Luo, Z., Pyrolysis behaviors of four lignin polymers isolated from the same pine wood. *Bioresource Technology* **2015,** *182*, 120-127.
75. Zhang, J.; Chen, T.; Wu, J.; Wu, J., A novel Gaussian-DAEM-reaction model for the pyrolysis of cellulose, hemicellulose and lignin. *RSC Advances* **2014,** *4* (34), 17513-17520.
76. Domburg, G. E.; Sergeeva, V. N.; Zheibe, G. A., Thermal analysis of some lignin model compounds. *Journal of thermal analysis* **1970,** *2* (4), 419-428.
77. Benjamin, B. M.; Raaen, V. F.; Maupin, P. H.; Brown, L. L.; Collins, C. J., Thermal cleavage of chemical bonds in selected coal-related structures. *Fuel* **1978,** *57* (5), 269-272.
78. Brower, K. R., Evidence for the involvement of quinone rings in reactions of some coals with tetralin. *Fuel* **1977,** *56* (3), 245-248.
79. Sprengling, G. R., The Reaction of a p-Substituted o-Methylolphenol with Oleic Acid. *Journal of the American Chemical Society* **1952,** *74* (11), 2937-2940.
80. Klein, M. T.; Virk, P. S., Model pathways in lignin thermolysis. **1981**.

81. Avni, E.; Coughlin, R. W.; Solomon, P. R.; King, H. H., Mathematical modelling of lignin pyrolysis. *Fuel* **1985,** *64* (11), 1495-1501.
82. Caballero, J. A.; Font, R.; Marcilla, A.; Conesa, J. A., New kinetic model for thermal decomposition of heterogeneous materials. *Industrial & Engineering Chemistry Research* **1995,** *34* (3), 806-812.
83. Chan, R. W.-C.; Krieger, B. B., Kinetics of dielectric-loss microwave degradation of polymers: Lignin. *Journal of Applied Polymer Science* **1981,** *26* (5), 1533-1553.
84. Pasquali, C. E. L.; Herrera, H., Pyrolysis of lignin and IR analysis of residues. *Thermochimica Acta* **1997,** *293* (1), 39-46.
85. Rao, T. R.; Sharma, A., Pyrolysis rates of biomass materials. *Energy* **1998,** *23* (11), 973-978.
86. Tang, W. K., *Effect of inorganic salts on pyrolysis of wood, alpha-cellulose, and lignin determined by dynamic thermogravimetry*. Forest Products Laboratory: 1967; Vol. 71.
87. Beall, F., Thermogravimetric analysis of wood lignin and hemicelluloses. *Wood and Fiber Science* **1969,** *1* (3), 215-226.
88. Domínguez, J. C.; Oliet, M.; Alonso, M. V.; Gilarranz, M. A.; Rodríguez, F., Thermal stability and pyrolysis kinetics of organosolv lignins obtained from Eucalyptus globulus. *Industrial Crops and Products* **2008,** *27* (2), 150-156.
89. Liu, Q.; Wang, S.; Zheng, Y.; Luo, Z.; Cen, K., Mechanism study of wood lignin pyrolysis by using TG–FTIR analysis. *Journal of Analytical and Applied Pyrolysis* **2008,** *82* (1), 170-177.
90. Damayanti; Wu, H. S., Pyrolysis kinetic of alkaline and dealkaline lignin using catalyst. *Journal of Polymer Research* **2017,** *25* (1), 7.
91. Friderichsen, A. V.; Shin, E.-J.; Evans, R. J.; Nimlos, M. R.; Dayton, D. C.; Ellison, G. B., The pyrolysis of anisole (C6H5OCH3) using a hyperthermal nozzle. *Fuel* **2001,** *80* (12), 1747-1755.
92. Arends, I. W. C. E.; Louw, R.; Mulder, P., Kinetic study of the thermolysis of anisole in a hydrogen atmosphere. *The Journal of Physical Chemistry* **1993,** *97* (30), 7914-7925.
93. Pecullan, M.; Brezinsky, K.; Glassman, I., Pyrolysis and Oxidation of Anisole near 1000 K. *The Journal of Physical Chemistry A* **1997,** *101* (18), 3305-3316.
94. Scheer, A. M.; Mukarakate, C.; Robichaud, D. J.; Ellison, G. B.; Nimlos, M. R., Radical Chemistry in the Thermal Decomposition of Anisole and Deuterated Anisoles: An Investigation of Aromatic Growth. *The Journal of Physical Chemistry A* **2010,** *114* (34), 9043-9056.
95. Nowakowska, M.; Herbinet, O.; Dufour, A.; Glaude, P.-A., Detailed kinetic study of anisole pyrolysis and oxidation to understand tar formation during biomass combustion and gasification. *Combustion and Flame* **2014,** *161* (6), 1474-1488.
96. Platonov, V. V.; Proskuryakov, V. A.; Ryl'tsova, S. V.; Popova, Y. N., Homogeneous Pyrolysis of Anisole. *Russian Journal of Applied Chemistry* **2001,** *74* (6), 1047-1052.

97. Husson, B.; Ferrari, M.; Herbinet, O.; Ahmed, S. S.; Glaude, P.-A.; Battin-Leclerc, F., New experimental evidence and modeling study of the ethylbenzene oxidation. *Proceedings of the Combustion Institute* **2013,** *34* (1), 325-333.
98. Lawson, J. R.; Klein, M. T., Influence of water on guaiacol pyrolysis. *Industrial & Engineering Chemistry Fundamentals* **1985,** *24* (2), 203-208.
99. Vuori, A. I.; Bredenberg, J. B. s., Thermal chemistry pathways of substituted anisoles. *Industrial & Engineering Chemistry Research* **1987,** *26* (2), 359-365.
100. Vuori, A., Pyrolysis studies of some simple coal related aromatic methyl ethers. *Fuel* **1986,** *65* (11), 1575-1583.
101. Suryan, M. M.; Kafafi, S. A.; Stein, S. E., The thermal decomposition of hydroxy- and methoxy-substituted anisoles. *Journal of the American Chemical Society* **1989,** *111* (4), 1423-1429.
102. Dorrestijn, E.; Mulder, P., The radical-induced decomposition of 2-methoxyphenol. *Journal of the Chemical Society, Perkin Transactions 2* **1999,** (4), 777-780.
103. About the Author A2 - Klass, Donald L. In *Biomass for Renewable Energy, Fuels, and Chemicals*, Academic Press: San Diego, 1998; p ix.
104. Hosoya, T.; Kawamoto, H.; Saka, S., Role of methoxyl group in char formation from lignin-related compounds. *Journal of Analytical and Applied Pyrolysis* **2009,** *84* (1), 79-83.
105. Vane, C. H.; Abbott, G. D., Proxies for land plant biomass: closed system pyrolysis of some methoxyphenols. *Organic Geochemistry* **1999,** *30* (12), 1535-1541.
106. Asmadi, M.; Kawamoto, H.; Saka, S., Thermal reactions of guaiacol and syringol as lignin model aromatic nuclei. *Journal of Analytical and Applied Pyrolysis* **2011,** *92* (1), 88-98.
107. Gilbert, K. E.; Gajewski, J. J., Coal liquefaction model studies: free radical chain decomposition of diphenylpropane, dibenzyl ether, and phenethyl phenyl ether via .beta.-scission reactions. *The Journal of Organic Chemistry* **1982,** *47* (25), 4899-4902.
108. Britt, P. F.; Buchanan, A. C., III; Malcolm, E. A., Thermolysis of Phenethyl Phenyl Ether: A Model for Ether Linkages in Lignin and Low Rank Coal. *The Journal of Organic Chemistry* **1995,** *60* (20), 6523-6536.
109. Beste, A.; Buchanan, A. C., Substituent Effects on the Reaction Rates of Hydrogen Abstraction in the Pyrolysis of Phenethyl Phenyl Ethers. *Energy & Fuels* **2010,** *24* (5), 2857-2867.
110. Britt, P. F.; Buchanan, A. C.; Cooney, M. J.; Martineau, D. R., Flash Vacuum Pyrolysis of Methoxy-Substituted Lignin Model Compounds. *The Journal of Organic Chemistry* **2000,** *65* (5), 1376-1389.
111. Jarvis, M. W.; Daily, J. W.; Carstensen, H.-H.; Dean, A. M.; Sharma, S.; Dayton, D. C.; Robichaud, D. J.; Nimlos, M. R., Direct Detection of Products from the Pyrolysis of 2-Phenethyl Phenyl Ether. *The Journal of Physical Chemistry A* **2011,** *115* (4), 428-438.
112. Domburg, G. E.; Rossinskaya, G.; Sergeeva, V., *Thermal Analysis*. 1974; Vol. 2.

113. Evans, R. J.; Milne, T. A.; Soltys, M. N., Direct mass-spectrometric studies of the pyrolysis of carbonaceous fuels: III. Primary pyrolysis of lignin. *Journal of Analytical and Applied Pyrolysis* **1986,** *9* (3), 207-236.
114. Britt, P. F.; Kidder, M. K.; Buchanan, A. C., Oxygen Substituent Effects in the Pyrolysis of Phenethyl Phenyl Ethers. *Energy & Fuels* **2007,** *21* (6), 3102-3108.
115. Li, P.; Chen, L.; Wang, X.; Yang, H.; Shao, J.; Chen, H., Effects of oxygen-containing substituents on pyrolysis characteristics of β-O-4 type model compounds. *Journal of Analytical and Applied Pyrolysis* **2016,** *120*, 52-59.
116. McDermott, J. B.; Klein, M. T.; Obst, J. R., Chemical modeling in the deduction of process concepts: a proposed novel process for lignin liquefaction. *Industrial & Engineering Chemistry Process Design and Development* **1986,** *25* (4), 885-889.
117. Kawamoto, H.; Horigoshi, S.; Saka, S., Pyrolysis reactions of various lignin model dimers. *Journal of Wood Science* **2007,** *53* (2), 168-174.
118. Kawamoto, H.; Ryoritani, M.; Saka, S., Different pyrolytic cleavage mechanisms of β-ether bond depending on the side-chain structure of lignin dimers. *Journal of Analytical and Applied Pyrolysis* **2008,** *81* (1), 88-94.
119. Kawamoto, H.; Horigoshi, S.; Saka, S., Effects of side-chain hydroxyl groups on pyrolytic β-ether cleavage of phenolic lignin model dimer. *Journal of Wood Science* **2007,** *53* (3), 268-271.
120. He, T.; Zhang, Y.; Zhu, Y.; Wen, W.; Pan, Y.; Wu, J.; Wu, J., Pyrolysis Mechanism Study of Lignin Model Compounds by Synchrotron Vacuum Ultraviolet Photoionization Mass Spectrometry. *Energy & Fuels* **2016,** *30* (3), 2204-2208.
121. Rahimi, A.; Ulbrich, A.; Coon, J. J.; Stahl, S. S., Formic-acid-induced depolymerization of oxidized lignin to aromatics. *Nature* **2014,** *515* (7526), 249-252.
122. Jiang, W.; Wu, S.; Lucia, L. A.; Chu, J., A comparison of the pyrolysis behavior of selected β-O-4 type lignin model compounds. *Journal of Analytical and Applied Pyrolysis* **2017,** *125*, 185-192.
123. Amen-Chen, C.; Pakdel, H.; Roy, C., Production of monomeric phenols by thermochemical conversion of biomass: a review. *Bioresource Technology* **2001,** *79* (3), 277-299.
124. Kuroda, K.-i.; Nakagawa-izumi, A., Analytical pyrolysis of lignin: Products stemming from β-5 substructures. *Organic Geochemistry* **2006,** *37* (6), 665-673.
125. Kuroda, K.-i.; Nakagawa-izumi, A.; Ashitani, T.; Fujita, K., Tetramethylammonium hydroxide (TMAH) thermochemolysis of 2-arylcoumaran lignin model compounds. *Journal of Analytical and Applied Pyrolysis* **2009,** *86* (1), 185-191.
126. Kuroda, K.-i.; Nakagawa-izumi, A.; Dimmel, D. R., Pyrolysis of Lignin in the Presence of Tetramethylammonium Hydroxide (TMAH): Products Stemming from β-5 Substructures. *Journal of Agricultural and Food Chemistry* **2002,** *50* (12), 3396-3400.
127. Daina, S.; Orlandi, M.; Bestetti, G.; Wiik, C.; Elegir, G., Degradation of β-5 lignin model dimers by Ceriporiopsis subvermispora. *Enzyme and Microbial Technology* **2002,** *30* (4), 499-505.
128. Liu, J.-Y.; Wu, S.-B.; Lou, R., CHEMICAL STRUCTURE AND PYROLYSIS RESPONSE OF BETA-O-4 LIGNIN MODEL POLYMER. *2011* **2011,** *6* (2), 15.

129. Chu, S.; Subrahmanyam, A. V.; Huber, G. W., The pyrolysis chemistry of a β-O-4 type oligomeric lignin model compound. *Green Chemistry* **2013,** *15* (1), 125-136.
130. Gardrat, C.; Ruggiero, R.; Rayez, M.-T.; Rayez, J.-C.; Castellan, A., Experimental and theoretical studies of the thermal degradation of a phenolic dibenzodioxocin lignin model. *Wood Science and Technology* **2013,** *47* (1), 27-41.
131. Hurt, M. R.; Degenstein, J. C.; Gawecki, P.; Borton Ii, D. J.; Vinueza, N. R.; Yang, L.; Agrawal, R.; Delgass, W. N.; Ribeiro, F. H.; Kenttämaa, H. I., On-Line Mass Spectrometric Methods for the Determination of the Primary Products of Fast Pyrolysis of Carbohydrates and for Their Gas-Phase Manipulation. *Analytical Chemistry* **2013,** *85* (22), 10927-10934.
132. Karhunen, P.; Rummakko, P.; Sipilä, J.; Brunow, G.; Kilpeläinen, I., Dibenzodioxocins; a novel type of linkage in softwood lignins. *Tetrahedron Letters* **1995,** *36* (1), 169-170.
133. Karhunen, P.; Rummakko, P.; Pajunen, A.; Brunow, G., Synthesis and crystal structure determination of model compounds for the dibenzodioxocine structure occurring in wood lignins. *Journal of the Chemical Society, Perkin Transactions 1* **1996,** (18), 2303-2308.
134. Argyropoulos, D. S.; Jurasek, L.; Krištofová, L.; Xia, Z.; Sun, Y.; Paluš, E., Abundance and Reactivity of Dibenzodioxocins in Softwood Lignin. *Journal of Agricultural and Food Chemistry* **2002,** *50* (4), 658-666.
135. McQuarrie, D. A., *Statistical Mechanics*. University Science Books: 2000.
136. Yerrayya, A.; Natarajan, U.; Vinu, R., Fast pyrolysis of guaiacol to simple phenols: Experiments, theory and kinetic model. *Chemical Engineering Science* **2019,** *207*, 619-630.
137. Liu, C.; Zhang, Y.; Huang, X., Study of guaiacol pyrolysis mechanism based on density function theory. *Fuel Processing Technology* **2014,** *123*, 159-165.
138. Pelucchi, M.; Cavallotti, C.; Cuoci, A.; Faravelli, T.; Frassoldati, A.; Ranzi, E., Detailed kinetics of substituted phenolic species in pyrolysis bio-oils. *Reaction Chemistry & Engineering* **2019,** *4* (3), 490-506.
139. Verma, A. M.; Kishore, N., DFT Analyses of Reaction Pathways and Temperature Effects on various Guaiacol Conversion Reactions in Gas Phase Environment. *ChemistrySelect* **2016,** *1* (19), 6196-6205.
140. Beste, A.; Buchanan, A. C., Computational Study of Bond Dissociation Enthalpies for Lignin Model Compounds. Substituent Effects in Phenethyl Phenyl Ethers. *The Journal of Organic Chemistry* **2009,** *74* (7), 2837-2841.
141. Wang, H.; Zhao, Y.; Wang, C.; Fu, Y.; Guo, Q., Theoretical study on the pyrolysis process of lignin dimer model compounds. *Acta Chim Sinica* **2009,** *67*, 893-900.
142. Elder, T., A computational study of pyrolysis reactions of lignin model compounds. *Holzforschung* **2010,** *64* (4), 435.
143. Younker, J. M.; Beste, A.; Buchanan III, A. C., Computational Study of Bond Dissociation Enthalpies for Substituted β-O-4 Lignin Model Compounds. *ChemPhysChem* **2011,** *12* (18), 3556-3565.
144. Kim, S.; Chmely, S. C.; Nimlos, M. R.; Bomble, Y. J.; Foust, T. D.; Paton, R. S.; Beckham, G. T., Computational Study of Bond Dissociation Enthalpies for a Large

Range of Native and Modified Lignins. *The Journal of Physical Chemistry Letters* **2011,** *2* (22), 2846-2852.
145. Parthasarathi, R.; Romero, R. A.; Redondo, A.; Gnanakaran, S., Theoretical Study of the Remarkably Diverse Linkages in Lignin. *The Journal of Physical Chemistry Letters* **2011,** *2* (20), 2660-2666.
146. Huang, J.-b.; Wu, S.-b.; Cheng, H.; Lei, M.; Liang, J.-j.; Tong, H., Theoretical study of bond dissociation energies for lignin model compounds. *Journal of Fuel Chemistry and Technology* **2015,** *43* (4), 429-436.
147. Elder, T., Bond Dissociation Enthalpies of a Dibenzodioxocin Lignin Model Compound. *Energy & Fuels* **2013,** *27* (8), 4785-4790.
148. Elder, T.; Berstis, L.; Beckham, G. T.; Crowley, M. F., Density Functional Theory Study of Spirodienone Stereoisomers in Lignin. *ACS Sustainable Chemistry & Engineering* **2017,** *5* (8), 7188-7194.
149. Younker, J. M.; Beste, A.; Buchanan, A. C., Computational study of bond dissociation enthalpies for lignin model compounds: β-5 Arylcoumaran. *Chemical Physics Letters* **2012,** *545*, 100-106.
150. Elder, T., Bond Dissociation Enthalpies of a Pinoresinol Lignin Model Compound. *Energy & Fuels* **2014,** *28* (2), 1175-1182.
151. Huang, X.; Liu, C.; Huang, J.; Li, H., Theory studies on pyrolysis mechanism of phenethyl phenyl ether. *Computational and Theoretical Chemistry* **2011,** *976* (1), 51-59.
152. Nowakowska, M.; Herbinet, O.; Dufour, A.; Glaude, P. A., Kinetic Study of the Pyrolysis and Oxidation of Guaiacol. *The Journal of Physical Chemistry A* **2018,** *122* (39), 7894-7909.
153. Olcese, R. N.; Bettahar, M.; Petitjean, D.; Malaman, B.; Giovanella, F.; Dufour, A., Gas-phase hydrodeoxygenation of guaiacol over Fe/SiO2 catalyst. *Applied Catalysis B: Environmental* **2012,** *115-116*, 63-73.
154. Liu, C.; Deng, Y.; Wu, S.; Mou, H.; Liang, J.; Lei, M., Study on the pyrolysis mechanism of three guaiacyl-type lignin monomeric model compounds. *Journal of Analytical and Applied Pyrolysis* **2016,** *118*, 123-129.
155. Hu, Y.; Zuo, L.; Liu, J.; Sun, J.; Wu, S., Chemical Simulation and Quantum Chemical Calculation of Lignin Model Compounds. *2015* **2015,** *11* (1), 17.
156. Wang, M.; Liu, C.; Xu, X.; Li, Q., Theoretical study of the pyrolysis of vanillin as a model of secondary lignin pyrolysis. *Chemical Physics Letters* **2016,** *654*, 41-45.
157. Ledesma, E. B.; Marsh, N. D.; Sandrowitz, A. K.; Wornat, M. J., An experimental study on the thermal decomposition of catechol. *Proceedings of the Combustion Institute* **2002,** *29* (2), 2299-2306.
158. Altarawneh, M.; Dlugogorski, B. Z.; Kennedy, E. M.; Mackie, J. C., Theoretical Study of Unimolecular Decomposition of Catechol. *The Journal of Physical Chemistry A* **2010,** *114* (2), 1060-1067.
159. Khachatryan, L.; Adounkpe, J.; Asatryan, R.; Dellinger, B., Radicals from the Gas-Phase Pyrolysis of Catechol: 1. o-Semiquinone and ipso-Catechol Radicals. *The Journal of Physical Chemistry A* **2010,** *114* (6), 2306-2312.

160. Khachatryan, L.; Asatryan, R.; McFerrin, C.; Adounkpe, J.; Dellinger, B., Radicals from the Gas-Phase Pyrolysis of Catechol. 2. Comparison of the Pyrolysis of Catechol and Hydroquinone. *The Journal of Physical Chemistry A* **2010,** *114* (37), 10110-10116.
161. Beste, A.; Buchanan, A. C., Kinetic simulation of the thermal degradation of phenethyl phenyl ether, a model compound for the β-O-4 linkage in lignin. *Chemical Physics Letters* **2012,** *550*, 19-24.
162. Beste, A.; Buchanan, A. C., Role of Carbon–Carbon Phenyl Migration in the Pyrolysis Mechanism of β-O-4 Lignin Model Compounds: Phenethyl Phenyl Ether and α-Hydroxy Phenethyl Phenyl Ether. *The Journal of Physical Chemistry A* **2012,** *116* (50), 12242-12248.
163. Beste, A.; Buchanan, A. C., Computational Investigation of the Pyrolysis Product Selectivity for α-Hydroxy Phenethyl Phenyl Ether and Phenethyl Phenyl Ether: Analysis of Substituent Effects and Reactant Conformer Selection. *The Journal of Physical Chemistry A* **2013,** *117* (15), 3235-3242.
164. Beste, A.; Buchanan, A. C.; Britt, P. F.; Hathorn, B. C.; Harrison, R. J., Kinetic Analysis of the Pyrolysis of Phenethyl Phenyl Ether: Computational Prediction of α/β-Selectivities. *The Journal of Physical Chemistry A* **2007,** *111* (48), 12118-12126.
165. Beste, A.; Buchanan, A. C.; Harrison, R. J., Computational Prediction of α/β Selectivities in the Pyrolysis of Oxygen-Substituted Phenethyl Phenyl Ethers. *The Journal of Physical Chemistry A* **2008,** *112* (22), 4982-4988.
166. Huang, J.; Liu, C.; Wu, D.; Tong, H.; Ren, L., Density functional theory studies on pyrolysis mechanism of β-O-4 type lignin dimer model compound. *Journal of Analytical and Applied Pyrolysis* **2014,** *109*, 98-108.
167. Elder, T.; Beste, A., Density Functional Theory Study of the Concerted Pyrolysis Mechanism for Lignin Models. *Energy & Fuels* **2014,** *28* (8), 5229-5235.
168. Huang, J.; He, C., Pyrolysis mechanism of α-O-4 linkage lignin dimer: A theoretical study. *Journal of Analytical and Applied Pyrolysis* **2015,** *113*, 655-664.
169. Choi, Y. S.; Singh, R.; Zhang, J.; Balasubramanian, G.; Sturgeon, M. R.; Katahira, R.; Chupka, G.; Beckham, G. T.; Shanks, B. H., Pyrolysis reaction networks for lignin model compounds: unraveling thermal deconstruction of β-O-4 and α-O-4 compounds. *Green Chemistry* **2016,** *18* (6), 1762-1773.
170. Huang, J.; He, C.; Liu, C.; Tong, H.; Wu, L.; Wu, S., A computational study on thermal decomposition mechanism of β-1 linkage lignin dimer. *Computational and Theoretical Chemistry* **2015,** *1054*, 80-87.
171. Berstis, L.; Elder, T.; Crowley, M.; Beckham, G. T., Radical Nature of C-Lignin. *ACS Sustainable Chemistry & Engineering* **2016,** *4* (10), 5327-5335.
172. Azad, T.; Schuler, J. D.; Auad, M. L.; Elder, T.; Adamczyk, A. J., Model Lignin Oligomer Pyrolysis: Coupled Conformational and Thermodynamic Analysis of β-O-4′ Bond Cleavage. *Energy & Fuels* **2020,** *34* (8), 9709-9724.
173. Maduskar, S.; Facas, G. G.; Papageorgiou, C.; Williams, C. L.; Dauenhauer, P. J., Five Rules for Measuring Biomass Pyrolysis Rates: Pulse-Heated Analysis of Solid Reaction Kinetics of Lignocellulosic Biomass. *ACS Sustainable Chemistry & Engineering* **2018,** *6* (1), 1387-1399.

174. Pecha, M. B.; Montoya, J. I.; Ivory, C.; Chejne, F.; Garcia-Perez, M., Modified Pyroprobe Captive Sample Reactor: Characterization of Reactor and Cellulose Pyrolysis at Vacuum and Atmospheric Pressures. *Industrial & Engineering Chemistry Research* **2017,** *56* (18), 5185-5200.
175. Krumm, C.; Pfaendtner, J.; Dauenhauer, P. J., Millisecond Pulsed Films Unify the Mechanisms of Cellulose Fragmentation. *Chemistry of Materials* **2016,** *28* (9), 3108-3114.
176. Maduskar, S.; Maliekkal, V.; Neurock, M.; Dauenhauer, P. J., On the Yield of Levoglucosan from Cellulose Pyrolysis. *ACS Sustainable Chemistry & Engineering* **2018,** *6* (5), 7017-7025.
177. Stocker, S.; Csányi, G.; Reuter, K.; Margraf, J. T., Machine learning in chemical reaction space. *Nature Communications* **2020,** *11* (1), 5505.
178. Fooshee, D.; Mood, A.; Gutman, E.; Tavakoli, M.; Urban, G.; Liu, F.; Huynh, N.; Van Vranken, D.; Baldi, P., Deep learning for chemical reaction prediction. *Molecular Systems Design & Engineering* **2018,** *3* (3), 442-452.
179. Cova, T. F. G. G.; Pais, A. A. C. C., Deep Learning for Deep Chemistry: Optimizing the Prediction of Chemical Patterns. *Frontiers in Chemistry* **2019,** *7* (809).

CHAPTER 3 COMPUTATIONAL INVESTIGATION INTO THE PYROLYSIS BOND DISSOCIATION ENTHALPIES (BDE) OF MODEL LIGNIN OLIGOMERS USING DENSITY FUNCTIONAL THEORY(DFT)

This chapter is composed of material that has previously been published in academic journals. I am the lead author of these manuscripts. I was responsible for designing the simulation plan and conducting the simulations. The other authors of this work are Dr. Abdoulmoumine and Dr. Elder.

1) Ross Houston, Thomas Elder, and Nourredine Abdoulmoumine. Investigation into the Pyrolysis Bond Dissociation Enthalpies (BDEs) of a Model Lignin Oligomer Using Density Functional Theory (DFT). Energy and Fuels 2022, 3, 1565–1573.
2) Ross Houston, and Nourredine Abdoulmoumine. Investigation of the thermal deconstruction of β-β' and 4-O-5 linkages in lignin model oligomers by density functional theory (DFT). RSC Advances 2023, 9, 6181-6190.

Abstract

Pyrolysis is a promising technology for converting lignocellulosic biomass into chemicals, materials, and fuels. Understanding the fundamental reactions and mechanisms during the fast pyrolysis of lignocellulosic biomass is essential for improving the efficiency of this technology. Investigations of lignin fast pyrolysis reactions and mechanisms have thus far lagged relative to cellulose and hemicellulose and have largely been focused on lignin model dimers and monomers. These studies provide valuable information about the reaction tendencies of individual linkages; however, the complex and varying nature of lignin interunit linkages does not allow direct extrapolation to larger lignin structures. In this chapter, we computationally investigate homolytic bond scission reactions of three larger, synthesizable model

lignin oligomers containing five major lignin linkages using density functional theory. The bond dissociation enthalpies of the model oligomers showed the trend that the C_α of the β-5 and the β-β′ interunit linkages exhibited the lowest BDE due to increased delocalization of the produced radicals. Comparing the ether interunit linkages, our findings showed the following trend in BDEs: C_α-O (α-O-4) < C_β-O (β-O-4) < C_4-O (4-O-5). Our results show the general trends identified in smaller dimer molecules are maintained while the magnitude of the BDEs is increased in the model oligomer. This work is an important first step in developing a library of reaction information for various lignin substructures.

3.1. Introduction

Fast pyrolysis of biomass is a thermochemical process that occurs at low gas residence times (< 2 s), high heating rates (200-12,000 °C s^{-1}), and moderate temperatures (400-600 °C) in the absence of oxygen[1-5]. It produces three major products in descending order by yield: solid biochar, light gases, e.g., carbon monoxide, carbon dioxide, hydrogen, and C_1-C_4 hydrocarbons, and bio-oil[6]. Fast pyrolysis has become an attractive technique for converting lignocellulosic biomass because of the promise of bio-oil, which can be upgraded to fuel, chemicals, and products. During the past three decades, there has been a notable increase in attempts to mechanistically understand the transformation of cellulose, hemicellulose, and lignin, the three main constituents of lignocellulosic biomass[7-12]. These efforts are producing the first detailed reaction mechanisms of biomass fast pyrolysis that could be incorporated into reactor models for optimization and scale-up investigations[8, 13-17].

While these mechanisms are far from perfect, they are nonetheless extremely valuable and provide a starting point for further improvements. The mechanism development studies take different approaches, but all rely on years of both experimental and computational studies on isolated cellulose, hemicellulose, and lignin, as well as model compounds thereof to collate data, propose, and evaluate mechanisms. For example, the cellulose branch of the Ranzi biomass pyrolysis mechanism, one of the leading biomass pyrolysis mechanisms, relies on findings on cellulose investigations that go back to the '70s to propose activated cellulose as the first intermediate and levoglucosan as a major product[18, 19]. Historically, cellulose, hemicellulose, and their model compounds have been the subject of more pyrolysis investigations in part because they are structurally less complex than lignin[17, 20]. However, as fast pyrolysis mechanisms are improved, it is imperative to investigate oligomeric lignin model compounds to provide mechanistic insights.

Lignin is one of the most abundant biopolymers in the world and constitutes up to 35 wt. % of lignocellulosic biomass[21-23]. Lignin provides strength, rigidity, and hydrophobicity to the secondary cell wall of plants[24]. Lignin synthesis is complex and consists of three steps: (1) biosynthesis of monomers, (2) transport, and (3) polymerization[25]. The monolignols are synthesized in the cytosol then transported to the secondary cell wall[26, 27]. There, lignin is synthesized via the radical polymerization of three major hydroxycinnamyl alcohol subunits (*p*-coumaryl, coniferyl, and sinapyl alcohol) by peroxidase and laccase, which results in lignin being an amorphous, racemic polymer with an aromatic nature[28]. The complexity and lack of a well-defined

structure presents challenges when investigating lignin fast pyrolysis, as discussed in the next sections.

Several researchers have investigated model lignin substructures that are representative of what can be found in native lignin[10, 29-36]. These model compounds range from the monomeric bases of major pyrolysis products, such as guaiacol and syringol, to model dimers and trimers that contain various critical interunit linkages (β-O-4, α-O-4, β-5, and others) and give rise to the complexity of the lignin structure. Bond dissociation enthalpies (BDE) and major pyrolysis pathways for these model compounds have been developed through computational and experimental investigation with the hope of better understanding the pyrolysis nature of native lignin.

Until recently, most computational mechanistic studies on lignin model compounds have been limited to monomers, dimers, and trimers, with most focusing on the β-O-4 linkage, which accounts for approximately 60% of all lignin linkages[17]. The kinetics and mechanisms of dimers and trimers, such as phenethyl phenyl ether (PPE)[36-38], offer valuable insights but because they contain limited interunit linkages, they are not directly applicable to native lignin. Therefore, the knowledge gap for lignin pyrolysis is how to get from model dimers to a native lignin structure. The authors believe it is possible to bridge that gap by increasing the size of the model compounds and beginning to investigate oligomers and other important lignin substructures. It is imperative to investigate larger oligomeric substructures that include multiple interunit

linkages and are more representative of lignin fractions that are observed during thermal degradation.

The recent advances in computational chemistry and continued improvements in access and power of high-performance computing infrastructures provide an opportunity to investigate the thermal degradation of model lignin oligomers to gain further mechanistic insight into the pathways involved in native lignin pyrolysis and their associated energetics[39]. Density functional theory (DFT) has been used extensively for simulating the pyrolysis of lignin model compounds due to its increased computational efficiency and comparable accuracy to other *ab initio* methods, such as Hartree-Fock methods[40]. Additionally, DFT explicitly addresses electron correlation, which otherwise would require more expensive post-Hartree-Fock methods. DFT calculations can identify the location of essential points on the potential energy surface (reactants, products, transition states) that allow for the determination of activation energetics and kinetics associated with specific reactions. Previous computational investigations of model lignin monomer, dimers, and trimers have identified trends between the relative strengths of several homolytic cleavage reactions, with the β-O bond having the lowest BDE. Additionally, DFT calculations have provided insight into the temperature dependence on the dominant reaction type during lignin pyrolysis, free-radical or concerted[10, 41]. DFT is already beginning to be used in this matter, with at least two studies that we are aware of exploring the lignin substructures up to decamers in some cases[27, 42, 43]. Larger oligomeric substructures of lignin allow for simultaneous investigation of the degradation behavior of multiple interunit linkages

as well as identification of any potential effects caused by adjacent linkages. The authors of the current work believe identifying reactivity trends over a variety of linkages can be leveraged to better understand the pyrolysis behavior of native lignin. The development of a mechanistic understanding of lignin's deconstruction during pyrolysis will bring us closer to developing a full mechanistic reaction scheme for whole biomass pyrolysis. The authors believe a promising way of developing a reaction mechanism that can account for the varying structure of lignin is to systematically investigate a variety of lignin substructures computationally and experimentally, identify reactivity trends, collate findings into a library of lignin reaction information, and postulate reaction rules, hierarchy, and mechanisms that can be applied to different lignin structures. The first step in identifying potential reaction mechanisms is the determination of BDEs for the initial cleavage positions along the interunit linkage. This chapter is a modest first step towards developing that library of reaction information by computationally investigating the BDEs of free-radical bond scissions using DFT for three chosen model lignin tetramers that contain five important interunit linkages (β-O-4, α-O-4, β-5, β-β', and 4-O-5) found in native lignin.

3.2. Materials and methods

3.2.1. Oligomer selection

The first step in this chapter is to choose appropriate lignin model oligomers. We had several considerations while selecting the model oligomers. Primarily, the model compound must be a representative substructure in native lignin with appropriate interunit linkages and side chains. Additionally, the combination of the

chosen interunit linkages needs to make up a large majority of the bonds found in native lignin. We have selected three model lignin oligomers, as shown in Figure 0-1, that contain β-O-4, α-O-4, β-5, β-β, and 4-O-5 interunit linkages. This collection of linkages makes up approximately 80% of the linkages found in lignin[44, 45].

Model compound 1 (MC1), *erythro*-guaiacylglycerol-α-dehydrodiconiferyl-β-coniferyl-bis-ether, is made up of coniferyl units, contains β-O-4, α-O-4, and β-5 linkages, and has been previously synthesized in appreciable yields[46, 47]. The structure of MC1 is shown in Figure 0-1 a. To the authors' knowledge, this work will be the first computational investigation into a model lignin oligomer with three different interunit linkage types, which captures three prevalent linkages found in native lignin. MC1 has several noteworthy characteristics. First, there are four chiral centers in this compound, identified by red stars in Figure 0-1 a, which produce 16 possible stereoisomers that must be appropriately treated in the following sections. In the results section, the investigated stereoisomers are presented using a specific naming nomenclature. Each chiral center is labeled by its carbon position (α, β, α', and β'), and each position is represented by its absolute configuration (*R* or *S*), depending on the spatial arrangement of atoms around the respective chiral center. The stereocenter labeling of *R* and *S* is used to differentiate between enantiomers of a chiral compound. The substituents of a chiral center are given priority by their atomic numbers. If the relative priority of the substituents follows a clockwise direction, the chiral center is labeled as *R* configuration. Likewise, if the relative direction is counterclockwise, the chiral center is in *S* configuration.

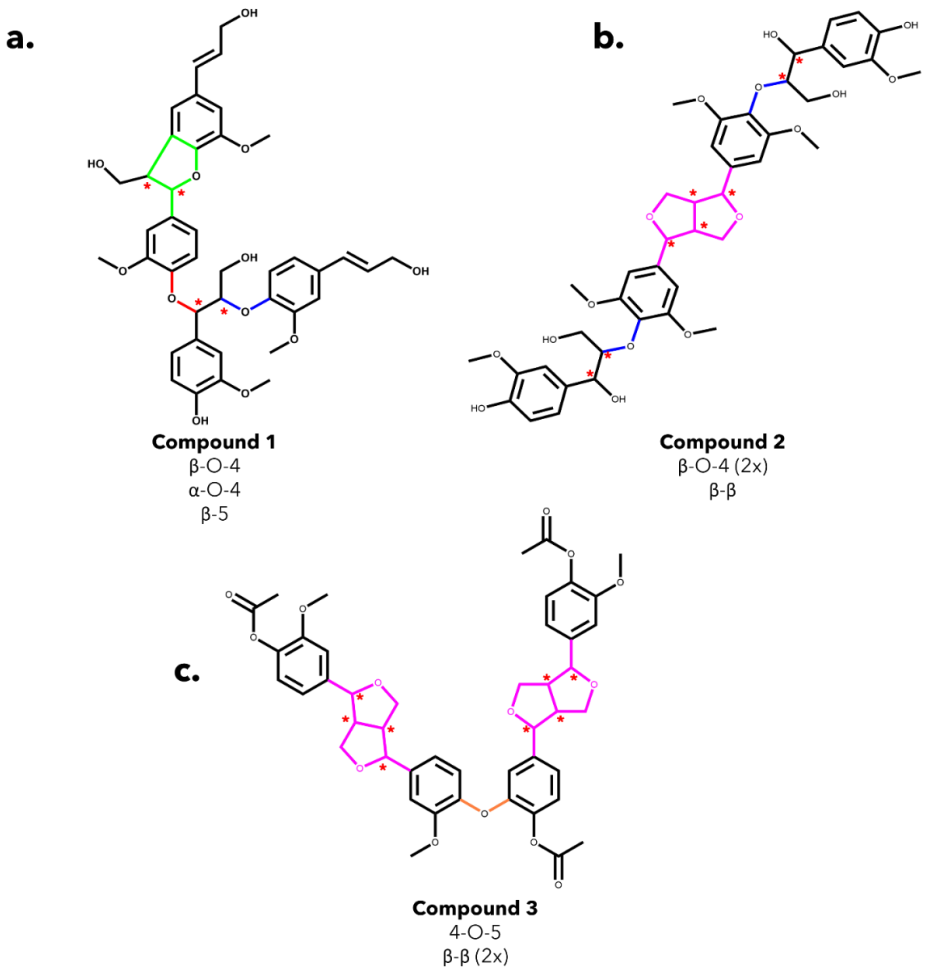

Figure 0-1. The structure of the lignin model oligomers used in our computational work. **a**. Model oligomer #1 is 4-(3-hydroxy-1-(4-[3-(hydroxymethyl)-5-[(1E)-3-hydroxyprop-1-en-1-yl]-7-methoxy-2,3-dihydro-1-benzofuran-2-yl]-2-methoxyphenoxy)-2-(4-[(1E)-3-hydroxyprop-1-en-1-yl]-2-methoxyphenoxy) propyl)-2-methoxyphenol. It is a tetramer with four chiral centers (*) and β-O-4(blue), α-O-4 (red), and β-5 (green) linkages. **b**. Model oligomer #2 is hedyotisol, with eight chiral centers, two β-O-4(blue) linkages, and a β-β(pink) linkage. **c**. Model oligomer #3 is 4-(4-[4-(acetyloxy)-3-methoxyphenyl]-hexahydrofuro [3,4-c]furan-1-yl)-2-(4-(4-[4-(acetyloxy)-3-methoxyphenyl]-hexahydrofuro [3,4-c]furan-1-yl)-2-methoxyphenoxy) phenyl acetate. It has eight chiral centers, two β-β(pink) linkages, and one 4-O-5(orange) linkage.

An example of the naming nomenclature of our model compound is as follows: if C_α and $C_{\beta'}$ are both *S* configurations while the other chiral centers are *R*, the resulting designation would be *SRRS*. The other notable characteristic is the presence of non-cyclic α-aryl ether linkage. This type of linkage has been identified in synthetic lignin oligomers; however, there is no experimental data to support the existence of this linkage in native lignin[28]. Even so, this combination of prevalent interunit linkages can provide valuable information on the behavior of this lignin substructure and will allow for the investigation into the effect of adjacent linkages on the bond dissociation enthalpies of specific linkages.

The second tetramer, hereafter referred to as model compound 2 (MC2), is commercially available as hedyotisol A/B. Hedyotisol has been previously identified in extracted poplar xylem and synthesized as part of an oligomeric mixture[48]. Hedyotisol is commercially available in two configurations: hedyotisol A (CAS# 95732-59-5) and hedyotisol B (CAS# 95839-45-5). Hedyotisol is formed from the oxidation of both coniferyl and sinapyl alcohol, contains two β-O-4 linkages as well as a β-β resinol linkage, and has eight chiral centers (Figure 0-1 b). These eight chiral centers produce 64 possible stereoisomers. However, in the initial identification of hedyotisol, Matsuda et al.[49] proposed a single absolute configuration of the four chiral centers of the β-β' linkage. Additionally, both β-O-4 linkages were reported as *erythro*, which further reduces the number of stereoisomers that should be considered. The reported configurations of each linkage reduce the number of possible stereoisomers from 64 to 4. A similar naming convention as previously discussed for model compound 1 will

also be used for MC2 and model compound 3 (MC3). The β-β linkage has only been the focus of a handful of studies; therefore, it provides an opportunity to gain new understanding of the thermal deconstruction behavior of an important lignin linkage.

MC3 is a previously identified model lignin oligomer that contains two β-β′ linkages and a 4-O-5 linkage[50]. Similar to MC2, MC3 has eight chiral centers located around both of the β-β′ linkages (Figure 0-1 c). Assuming the same configuration of the β-β′ in MC1, there is only one possible stereoisomer to account for, which is RSSRRSSR.

3.2.2. Computational setup

The computational work in this study was done using Spartan '18 (Wavefunction, Inc., Irvine, CA, 2018), GaussView 6, and Gaussian 16 (Gaussian, Inc., Wallingford, CT, 2016). The calculations in this project can be broken down into two categories that are discussed in the following sections: conformational analysis and bond dissociation enthalpy (BDE) calculations. The conformational analysis of each stereoisomer was performed using Spartan 18 on a local desktop using a single processor, while the density functional theory (DFT) calculations were performed using the Gaussian suite of software. The DFT simulations were carried out on the Infrastructure for Scientific Applications and Advanced Computing (ISAAC) high-performance computing resource at the University of Tennessee. Each DFT simulation was performed in parallel using eight processors.

3.2.2.1. Conformational analysis

Due to the radical polymerization of monomers at the β position during lignin synthesis, lignin oligomers have multiple chiral centers[28]. The stereochemistry of lignin

has the potential to play a role in reactivity and product formation[51]. Therefore, we must investigate each possible stereoisomer of the chosen oligomer. Fortunately, it has been reported that the enthalpies calculated via DFT for enantiomers are within "chemical accuracy," so we only need to consider one set of enantiomeric pairs[42, 51, 52]. For example, MC1 contains four chiral centers leading to 16 possible stereoisomers, which consist of eight enantiomeric pairs. We performed a Monte Carlo conformational analysis of eight stereoisomers in Spartan '18 to identify the lowest energy conformer to use in our DFT calculations. The search identified the 500 lowest energy conformers using the molecular mechanics force field MMFF94[53] and was further filtered down to the ten lowest energy conformers using a semi-empirical PM6 optimization method[54]. The ten remaining conformers were exported to Gaussian 16 and optimized using the M06-2X hybrid functional and the 6-31+G(d) basis set to identify the lowest energy conformer[55-58]. A geometry optimization and frequency analysis was performed on the lowest energy conformation for each stereoisomer at the M06-2X/6-311++G(d,p) level of theory[59]. The dispersion interactions were described using the GD3 empirical dispersion correction[60].

After completion of the conformation analysis and optimization, the structure of each stereoisomer of MC1 was investigated to identify any potential dimeric interactions, such as parallel or T-shaped conformations between the aromatic rings, indicative of π interactions. This analysis was accomplished via determination of the interatomic distances between aromatic rings and the calculation of the ring angles relative to each other. Each aromatic ring was labeled as A-D, Figure 0-2. The

interatomic distances were calculated as the distances between the centroid of the respective ring, and the angles were calculated as the angle between the planes of the respective rings.

3.2.2.2. Bond dissociation enthalpies and reaction energetics

The energetics associated with the homolytic cleavage of relevant bonds along each interunit linkage were determined via a two-step calculation procedure consisting of geometry optimization and frequency analysis at 773.15 K (500 °C). This is an established moderate temperature for biomass fast pyrolysis, and energetics determined for this temperature will be relevant for comparisons with experimental studies. For each stereoisomer, the starting oligomers, as well as the resulting products from each homolytic cleavage, were generated from the lowest energy conformer determined by conformational analysis. The products of the β-O-4, α-O-4, and 4-O-5 scissions consist of two separate, singlet radical species. These species are optimized and analyzed separately. However, for the β-5 and β-β' ring-opening scissions, the resulting product is a single molecule with two unpaired electrons. In the case of the di-radical species, special care was taken to ensure they did not immediately re-bond during geometry optimization. The molecules were optimized as triplets and given an initial interatomic distance of 2.5 Å, which has previously been successful in calculating ring-opening reactions[61]. The cleavage locations for every relevant bond along each interunit linkage are shown in Figure 0-3(MC1) and Figure 0-4(MC2).

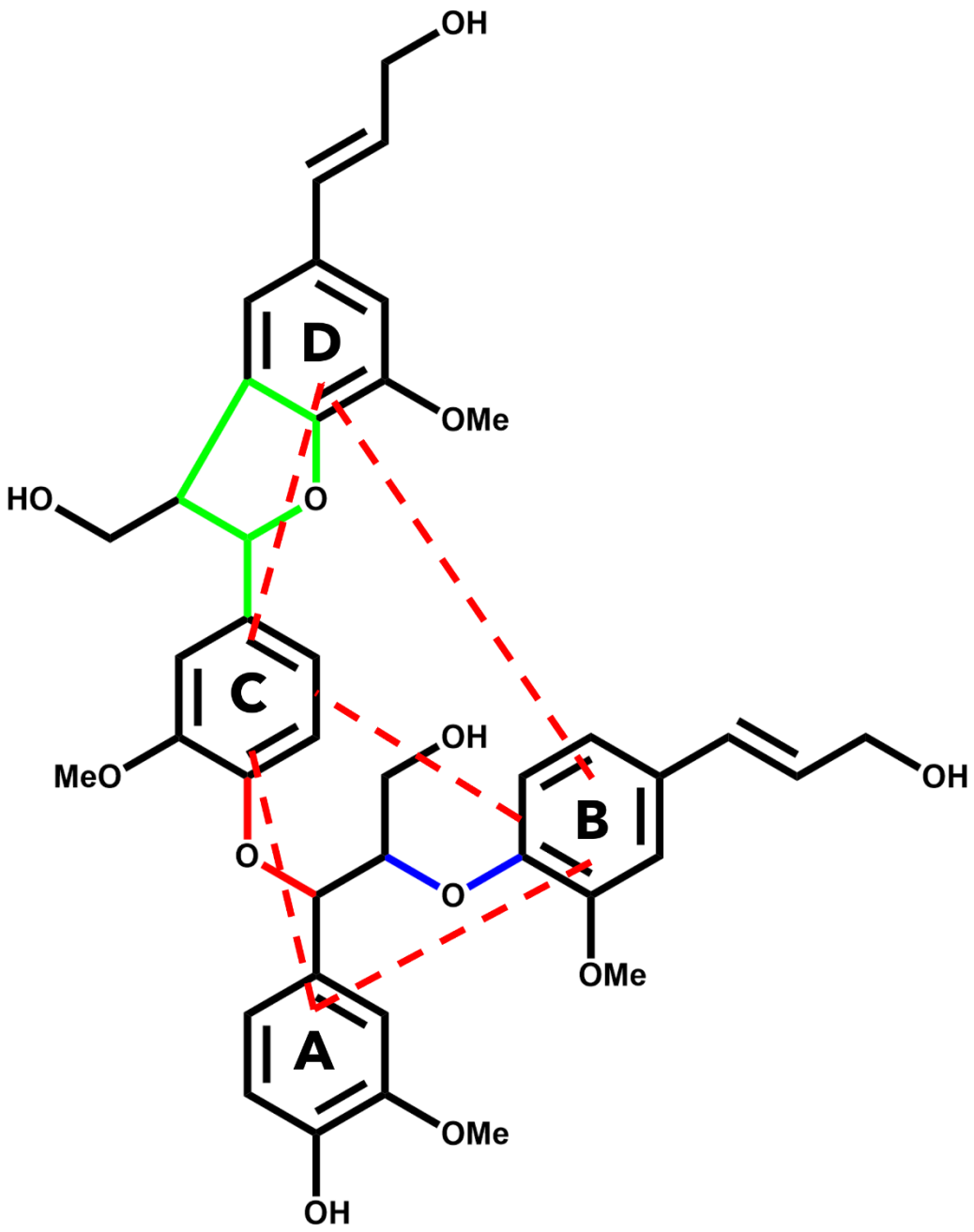

Figure 0-2. Visualization of interatomic distances and ring angle calculations for MC1.

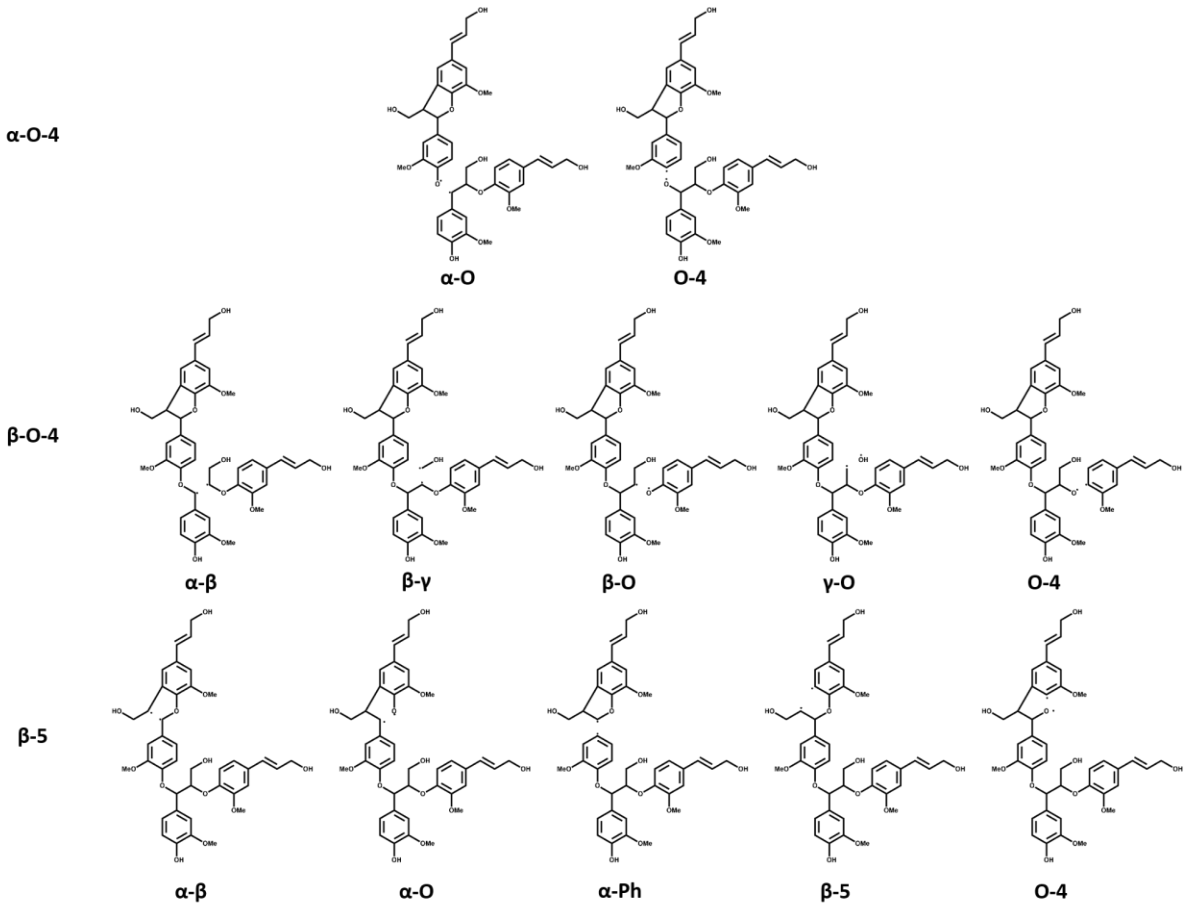

Figure 0-3. List of homolytic reactions investigated for the model lignin oligomer.

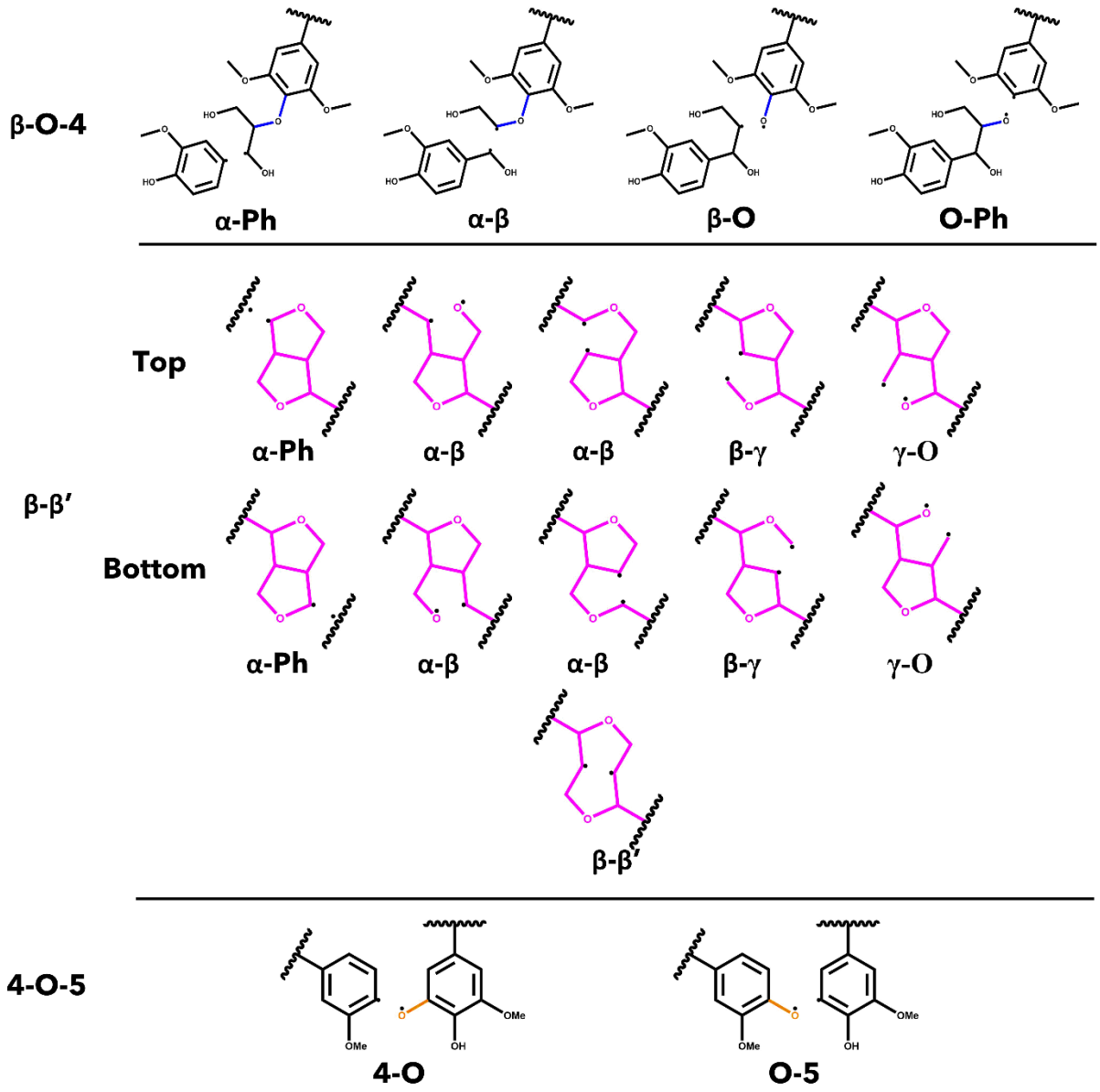

Figure 0-4. List of homolytic bond scissions for each interunit linkage investigated for MC2 and MC3.

Bond dissociation enthalpies (BDEs) were calculated for homolytic cleavage of major bonds by calculating the difference between the sum of electronic and thermal enthalpies for the products and the reactants, as shown in Eq. (0-1 and (*0-2*).

$$BDE = \sum (e_0 - H_{corr})_{products} - \sum (e_0 - H_{corr})_{reactants} \quad (0\text{-}1)$$

$$H_{corr} = E_{tot} + k_B T \quad (0\text{-}2)$$

where e_0 is the total electronic energy, H_{corr} is the thermal correction to enthalpy, E_{tot} is the total internal energy, and k_B is the Boltzmann constant. All the above energies are reported in Hartrees[62]. Bond dissociation enthalpies (BDE) were determined from calculations at 298-and 773.15 K and are referred to moving forward as ΔH_{298} and ΔH_{773}, respectively.

3.3. Results and discussion

3.3.1. Conformational analysis

3.3.1.1. Model Compound 1

The electronic energies of MC1, accounting for thermal correction to enthalpy, for each stereoisomer's ten lowest energy conformers were calculated at 298.15 K using the M06-2X/6-31+g(d) level of theory. Different configurations had a range of enthalpies of 3.79 to 16.28 kcal/mol, depending on the stereoisomer. The resulting lowest energy conformers were then optimized using M06-2X/6-311++G(d,p) to determine the initial tetramer for each stereoisomer, shown in Table 0-1. The range of enthalpies between stereoisomers was 5.30 kcal/mol. This range falls outside of the range of ± 1.00 kcal mol^{-1} of chemical accuracy, so several of the stereoisomers are

appreciably different[42]. *RSSR* and *RRSS* were the least stable isomers with indistinguishable differences in their enthalpies, while *RSSS* and *RSRS* were the most stable stereoisomers and indistinguishable from each other. This range of enthalpies is enough to conclude that stereochemistry can appreciably affect the energetics of a system. With additional investigation, it may provide some insight into the range of possible structures in a native oligomer.

The interatomic distances between aromatic rings were calculated from the centroids of the respective rings, labeled in Figure 0-2, and the measured ring angles were calculated as the angles formed between the planes of the respective rings. The calculated distances and angles are shown in Table 0-2 and Table 0-3, respectively. Equilibrium distances for specific conformations have been previously calculated by Tsuzuki et al. [63] Parallel configurations of aromatic rings had an equilibrium interatomic distance of approximately 3.80-4.00 Å. Additionally, the planes of the aromatic rings do not intersect in a parallel configuration. The other major configuration type is T-shaped or edge-to-face with equilibrium distances of 5.00-5.20 Å and perpendicular ring angles[63].

As evidenced by the values in Table 0-2 and Table 0-3, the most likely candidates for parallel or T-shaped configurations are the B-C rings, which correspond to the aromatic rings at the end of the β-O-4 and α-O-4 linkages. As the interatomic distances between B-C approach the previously mentioned equilibrium distances, we would expect an increased π/π interaction, which could give rise to increased stability of a specific stereoisomer. For example, the *RRSR* stereoisomer has a B-C interatomic

Table 0-1. Relative enthalpy difference of optimized structure for each stereoisomer of the model tetramer at the M06-2X/6-311++G(d,p) level of theory at 298.15 K.

Configuration	**Relative enthalpy difference (kcal mol^{-1})**
RRRR	1.26
RRRS	3.88
RRSR	4.07
RRSS	0.66
RSRR	3.48
RSRS	4.30
RSSR	0
RSSS	5.30

Table 0-2. Interatomic distances between aromatic rings of different stereoisomers of the model tetramer.

	Interatomic Distances (Å)					
	A-B	**A-C**	**A-D**	**B-C**	**B-D**	**C-D**
RRRR	6.51	6.30	10.92	4.79	6.38	5.50
RRRS	6.66	6.29	11.57	4.18	6.33	5.89
RRSR	6.72	6.30	11.50	3.89	5.40	5.90
RRSS	6.55	6.04	10.77	5.16	6.23	5.27
RSRR	7.16	6.26	9.83	5.00	5.26	5.01
RSRS	6.67	6.34	10.99	4.16	5.38	5.39
RSSR	6.41	5.63	10.77	4.01	6.43	5.19
RSSS	6.68	5.33	10.54	4.05	7.21	5.30

distance of 3.89 Å and an almost parallel angle (3.09°), suggesting a potential parallel configuration, which could explain the increase in stability of the *RRSR* compared to the least stable isomers of *RSSR* and *RRSS*. The optimized geometry of each stereoisomer is shown in Figure 0-5, and the three-dimensional cartesian coordinates of these stereoisomers are shown in Appendix III.

3.3.1.2. Model Compound 2

The conformers of stereoisomers for MC2 and MC3 were shown to have an appreciable difference in their enthalpies, ranging from 4.52 to 9.14 kcal mol^{-1} and 10.07 kcal mol^{-1}, respectively. The lowest energy conformer of each stereoisomer was then optimized using the same Minnesota 06 functional with a 6-311++G(d,p) basis set to determine the initial structure of each stereoisomer for MC2 and MC3. The relative enthalpy differences of stereoisomers for MC2 are shown in Table 0-4. The range of these enthalpies is 1.55 kcal mol^{-1}, which exceeds the accepted ± 1.00 kcal mol^{-1} threshold for chemical accuracy, so we are unable to say that these stereoisomers have the same total enthalpy[42]. Therefore, BDEs of relevant linkages will be calculated for all four stereoisomers of MC2. The optimized initial geometries of each stereoisomer for MC2 and MC3 are shown in Figure 0-6.

3.3.2. Bond dissociation enthalpies (BDEs)

3.3.2.1. Model Compound 1

The bond dissociation enthalpies were initially calculated for each relevant bond in the three interunit linkages found in MC1. The nomenclature for the reactions discussed in this section is based on the α and β positions of the relevant chiral carbons.

Table 0-3. Ring angles between the aromatic rings of different stereoisomers of the model tetramer.

	Ring Angle (°)					
	A-B	**A-C**	**A-D**	**B-C**	**B-D**	**C-D**
RRRR	61.77	59.42	89.66	25.29	49.36	74.05
RRRS	60.67	49.99	76.91	16.88	54.95	71.82
RRSR	55.61	53.86	80.57	3.09	45.78	48.80
RRSS	57.37	68.58	36.23	30.94	59.14	85.71
RSRR	63.10	33.63	82.49	64.00	31.67	85.88
RSRS	36.64	48.45	80.29	12.07	74.86	77.12
RSSR	54.15	78.80	14.16	30.41	64.77	85.22
RSSS	68.01	88.00	7.19	20.78	61.86	82.20

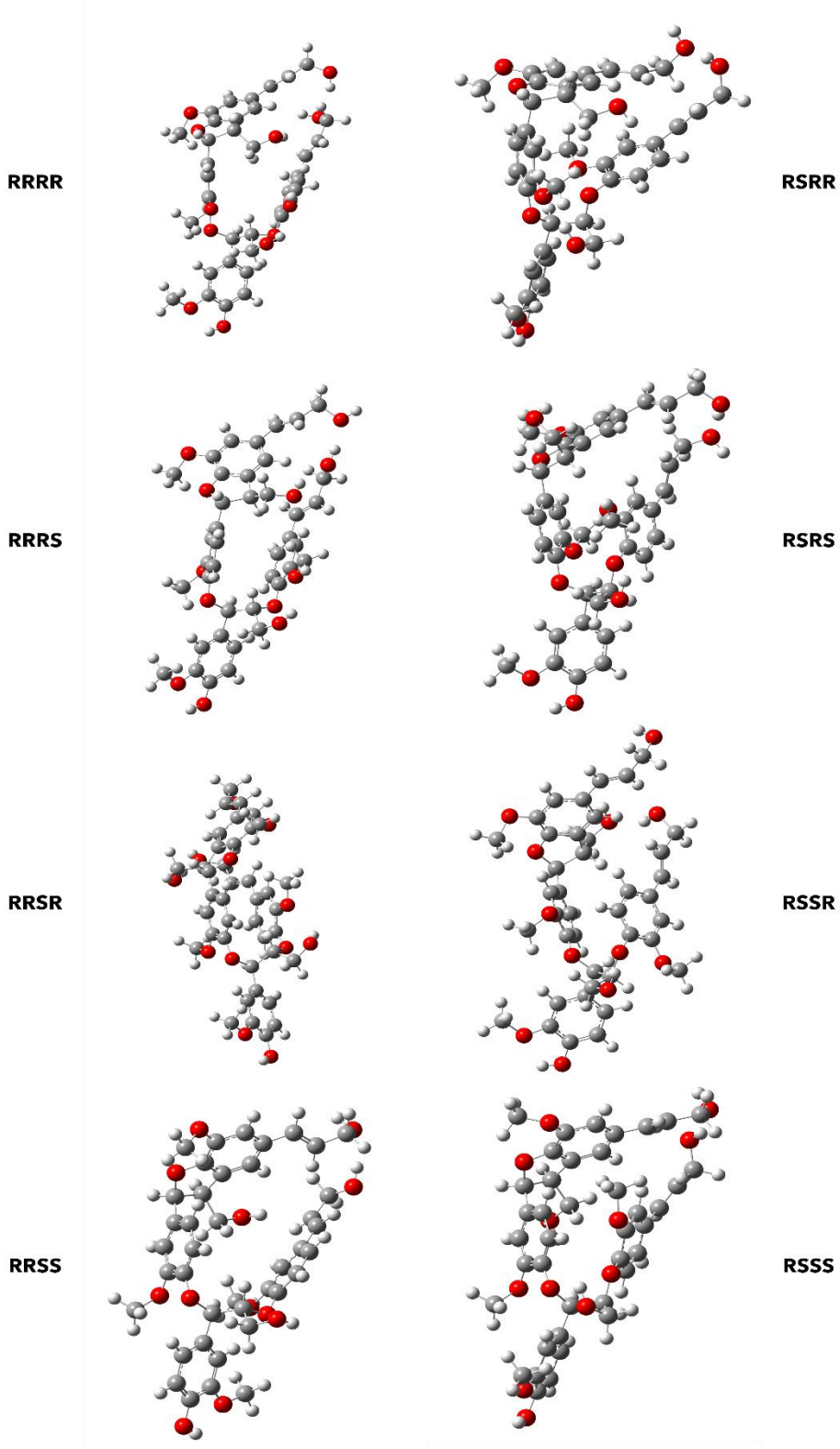

Figure 0-5. Optimized geometries for each stereoisomer of the MC1 at M06-2X/6-311++G(d,p).

The homolytic reactions investigated are shown in Figure 0-3. Upon convergence, the optimized geometries were subjected to a vibrational frequency analysis at 298.15 and 773.15 K to calculate the BDEs for room temperature and a relevant pyrolysis temperature. The BDEs for both temperatures can be seen in Table 0-5 and Table 0-6, respectively.

Upon comparison of the BDE calculations, several trends were identified. The magnitude of ΔH_{298} values are slightly different from that of ΔH_{773}, which is to be expected. However, the overall trends present at 298.15 K remain at the pyrolysis reaction temperature of 773.15 K. Overall, the carbon-oxygen bonds for a specific linkage are shown to be easier to break than the carbon-carbon bonds. The β-O and the C_α-O bonds in the ether linkages had ΔH_{773} with a range of 74.67-86.78 and 61.88-76.10 kcal mol^{-1}, respectively. Both the trend and overall magnitudes of these BDEs were expected and agreed with previous BDE investigations[64, 65]. The aromatic carbon-oxygen bonds in the ether linkages, *e.g.,* O-C_4 bond in a β-O-4 linkage, are the exception as they are harder to break than their non-aromatic counterparts (111.16-121.37 kcal/mol), which also agrees with the findings from Huang et al. [41]. The same general trend of C-O having a lower BDE than C-C can be seen in the C_α-O and C_α-C_β bonds for the β-5 ring-opening scission reactions, which are significantly easier to break than the aromatic C-O and C-C bonds. The C_α-O bond had a 46.25-55.75 kcal mol^{-1} range, and the C_α-C_β bond ranged from 57.76-71.49 kcal mol^{-1}, while the aromatic bonds had a much higher BDE, 86.06-118.13 kcal mol^{-1}. The lower BDE of the non-

Table 0-4. Relative enthalpy difference between stereoisomers for model compound 2 at the M06-2X/6-311++G(d,p) level of theory at 773.15 K

Configuration	Relative enthalpy difference (kcal mol^{-1})
RRRSSRRR	1.55
RRRSSRSS	0.43
SSRSSRRR	0.75
SSRSSRSS	0

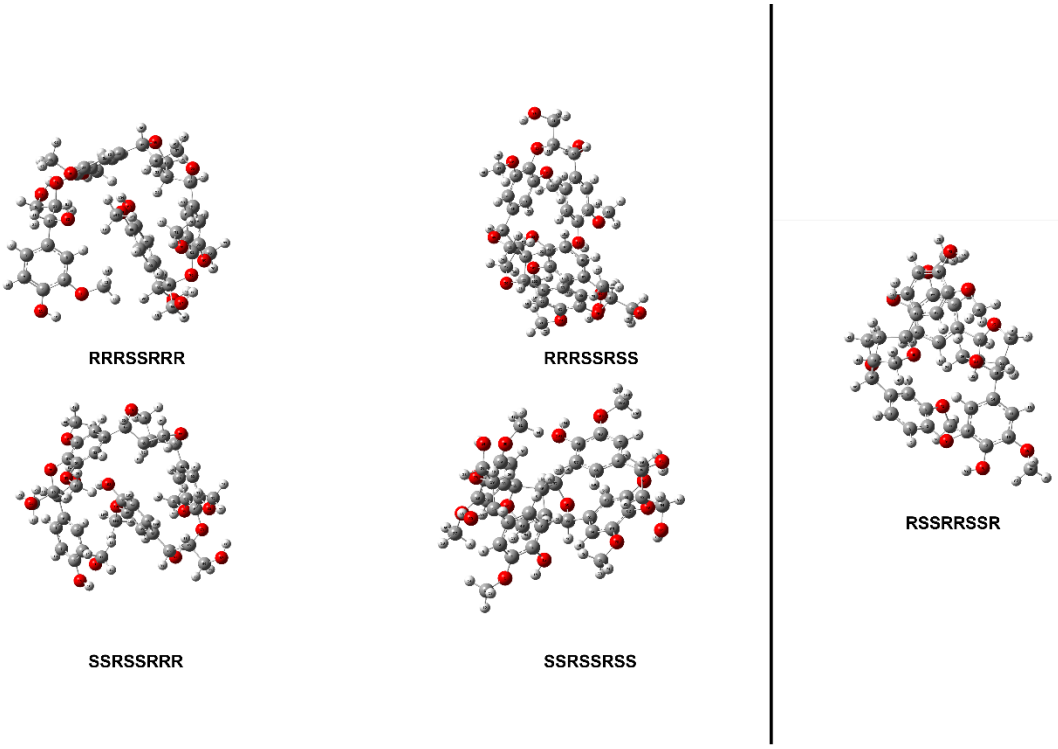

Figure 0-6. Optimized geometries of each stereoisomer of MC2 (left) and MC3 (right) determined using M06-2X/6-311++G(d,p).

Table 0-5. Bond dissociation enthalpies, ΔH_{298}, (kcal/mol) for each stereoisomer conformation of MC1 at 298.15 K.

Family	Bond	RRRR	RRRS	RRSR	RRSS	RSRR	RSRS	RSSR	RSSS
α-O-4	α-O	66.88	71.05	72.94	68.10	76.36	70.21	62.18	72.48
	O-4	113.18	117.72	119.58	112.73	119.06	116.29	110.64	117.50
β-O-4	1-α	104.88	101.62	100.26	105.20	106.45	101.00	102.96	111.47
	α-β	90.71	94.00	93.13	92.90	93.17	93.76	91.36	97.37
	β-O	78.14	84.33	81.40	77.77	79.07	77.72	74.70	86.74
	β-γ	88.65	89.58	87.83	91.47	91.96	86.26	87.00	88.36
	γ-O	100.03	103.22	96.45	97.48	96.91	96.06	96.39	96.88
	O-4	114.80	120.44	118.92	116.47	117.47	112.73	111.60	121.67
β-5	α-Ph	113.46	116.03	111.89	109.36	118.24	113.41	108.71	116.14
	β-5	100.00	99.18	96.29	95.05	97.52	98.82	93.81	101.22
	α-O	51.68	51.77	46.20	45.00	54.41	47.64	45.72	53.60
	α-β	66.66	64.17	64.77	65.34	67.55	69.96	69.11	56.97
	O-4	85.18	89.01	93.24	88.64	93.16	94.53	91.79	93.93

aromatic bonds can be attributed to the delocalization of electrons along the aromatic ring. Additionally, homolytic cleavage involving an aromatic ring would result in a radical on the carbon ring, which would disrupt the aromaticity. This trend was also reported by another BDE investigation of dimeric phenylcoumaran substructures[66]. The observed trend for the four lowest BDE scissions at both 298.15 K and 773.15 K is C_α-O (β-5) < C_α-C_β (β-5) < C_α-O (α-O-4) < C_β-O (β-O-4). While the trends were consistent, the magnitude of BDEs for individual bonds in the model tetramer were larger than their respective bonds in smaller, dimeric compounds. The BDEs for C_β-O bond of substituted β-O-4 dimers were calculated in the range of 68-71 kcal mol^{-1}, which is noticeable lower than the BDEs for the model tetramer[10]. The BDE for the C_α-O bond of the α-O-4 linkage is similarly larger than the BDE for the corresponding bond (42.4 kcal mol^{-1}) in an α-O-4 dimer studied by Huang and He[67]. The BDEs for the β-5 ring-opening reactions are closer to their dimer counterparts; however, they are still slightly larger than the BDEs calculated for smaller molecules[66].

Inspection of the spin density plots of the resulting radicals visualizes the delocalization of the unpaired electron around the molecule. The aromatic C-containing bonds exhibit a concentration of the spin density around the radical, whereas the products resulting from non-aromatic C-O bonds have a degree of delocalization of spin density around the neighboring aromatic ring. These observations agree with the trend of BDEs calculated as delocalization is expected to lower the BDE compared to a confined spin density. Spin density plots are reported in Appendix III.

It was observed that the least stable stereoisomer, RSSR, from the conformational analysis, was regularly on the lower end of the range of BDEs for each reaction. However, this trend did not always hold for the other indistinguishable lower stability stereoisomer, *RRSS*. This discrepancy can be partially attributed to the inherent error of 1.30 kcal mol^{-1} associated with M06-2X calculations[68]. Additionally, it can be assumed the stability trends for each conformation of the initial oligomer are not directly transferred to the resulting BDEs for individual reactions for a respective stereoisomer. The adjacent configuration may interact differently with the resulting radical fragments.

3.3.2.2. Model Compounds 2 and 3

The bond dissociation enthalpies (BDE) were calculated for each linkage along the β-β′ and 4-O-5 linkages. The three-dimensional coordinates for the investigated model oligomers are included in Appendix III. The linkages along the backbone of the β-O-4 linkages were also investigated; however, based on previous work, the branching linkages, such as the C_α-O and C_γ-O bonds, were not considered[69]. The BDEs of each homolytic cleavage were determined at 773.15 K (500 °C) to represent a well-accepted operating temperature for biomass fast pyrolysis. Upon determination of the BDEs for each relevant bond, trends were identified for each interunit linkage. Heat maps of the BDEs for MC2 and MC3 are shown in Table 0-7 and Table 0-8, respectively.

For the β-O-4 linkages of MC2, the C_β-O bond has a lower BDE than the other bonds along the β-O-4 linkage, ranging from 77.39-90.06 kcal mol^{-1}. The non-aromatic

Table 0-6. Bond dissociation enthalpies, ΔH_{773}, (kcal/mol) for each stereoisomer conformation of MC1 at 773.15 K.

Family	Bond	RRRR	RRRS	RRSR	RRSS	RSRR	RSRS	RSSR	RSSS
α-O-4	α-O	66.68	70.89	72.80	67.96	76.10	69.92	61.88	72.27
	O-4	112.83	117.48	119.31	112.45	118.66	115.89	110.42	117.00
β-O-4	1-α	104.50	101.23	99.87	104.83	106.18	100.49	102.68	110.97
	α-β	90.86	94.23	93.32	93.27	93.33	93.96	90.70	97.49
	β-O	78.12	84.42	81.34	77.81	78.97	77.67	74.67	86.78
	β-γ	89.01	89.72	88.02	91.81	92.23	86.37	87.27	88.48
	γ-O	101.10	104.44	97.46	98.50	98.06	97.08	97.43	97.87
	O-4	114.22	120.13	118.57	116.22	116.99	112.20	111.16	121.37
β-5	α-Ph	113.27	115.89	111.64	109.21	118.13	113.15	108.46	115.88
	β-5	101.26	100.44	97.47	96.33	98.83	100.12	95.00	102.38
	α-O	52.79	52.96	47.25	46.25	55.75	48.70	47.01	54.70
	α-β	68.48	65.56	66.43	66.95	69.18	71.49	70.65	57.76
	O-4	86.06	90.01	94.00	89.69	94.04	95.40	92.70	94.83

component of the ether bond has previously been shown to be the lowest BDE bond in the β-O-4 linkage; therefore, our trends are consistent with previous reports[30, 64, 65, 70]. The overall trends agree; however, the magnitudes of the BDEs are slightly higher than what has typically been reported for β-O-4 dimers (56-72 kcal mol^{-1})[64, 65, 71]. Inspection of the three-dimensional geometry shows MC2 is not necessarily linear and can fold in a way that brings the β-O-4 into closer proximity to other aromatics and linkages, which could serve to stabilize the bond. Further investigation into the cause of the magnitude discrepancy is needed; however, it is outside the scope of this study.

The ring-opening scissions in the β-β' linkage, for both MC2 and MC3, were shown to have the BDEs in the range of 70.29-87.06 kcal mol^{-1}. The reactions involving each C_α (excluding bonds to an aromatic ring) exhibited lower BDEs than the other β-β' ring-opening reactions. The C_α-O bond had a range of 70.29-80.04 kcal mol^{-1}, while the C_α-C_β had a range of 68.43-81.45 kcal mol^{-1}. This trend agrees with previous BDEs published for a pinoresinol dimer[72]. The magnitudes of the BDEs for these reactions are slightly larger than previously reported dimer values but have a much closer agreement than the BDEs for the β-O-4 linkage. Spin density plots for each di-radical produced from the β-β' ring opening scission of MC2 are shown in Figure 0-7. The spin density backs up what is seen from our BDE calculations. For the C_α-O and C_α-C_β scissions, there is significantly more delocalization of the unpaired electrons, which leads to more stable, di-radical products. The more stable the resulting product, the lower the BDE for the scission of that bond will be. The di-radical species produced from the scission of other bonds along the β-β' linkage do not possess similar levels of

Table 0-7. Bond dissociation enthalpies, ΔH_{773}, (kcal mol^{-1}) for each stereoisomer of MC2 at 773.15 K.

Side	Family	Bond	RRRSSRRR	RRRSSRSS	SSRSSRRR	SSRSSRSS
-	β-β'	β-β'	85.32	91.15	92.48	93.70
Bottom	β-β'	α-β	75.69	81.45	74.84	73.88
		α-O	74.03	70.29	77.60	76.48
		β-γ	83.54	84.34	84.48	84.09
		γ-O	82.58	82.77	82.52	81.88
		α-phenyl	112.74	111.20	113.73	111.63
	β-O-4	α-β	85.69	91.83	90.09	92.30
		α-phenyl	103.88	109.18	105.84	109.40
		β-O	77.39	79.67	82.60	80.11
		O-phenyl	108.60	118.35	117.83	118.68
Top	β-β'	α-β	71.52	71.56	74.72	73.88
		α-O	77.93	75.17	78.12	76.48
		β-γ	85.12	84.43	82.72	84.09
		γ-O	81.53	82.94	82.02	81.88
		α-phenyl	115.88	110.42	118.07	111.63
	β-O-4	α-β	97.83	92.76	97.47	92.30
		α-phenyl	117.31	107.14	116.74	109.55
		β-O	90.06	81.83	80.33	80.11
		O-phenyl	129.34	120.56	124.85	118.68

Table 0-8. Bond dissociation enthalpies, ΔH_{773}, (kcal mol^{-1}) of MC2 at 773.15 K.

Family	Bond	RSSRRSSR	Family	Bond	RSSRRSSR
4-O-5	4-O	87.12	**4-O-5**	O-5	93.89
β-β'	β-β'	82.78	**β''-β'''**	β''-β'''	87.06
	α-Ph	113.03		α-Ph	113.83
	α-β	68.43		α-β	73.18
	α-O	80.04		α-O	71.52
	β-γ	79.73		β-γ	83.38
	γ-O	84.26		γ-O	82.12
	α'-Ph'	106.25		α'-Ph'	106.89
	α'-β'	72.74		α'-β'	70.16
	α'-O'	72.62		α'-O'	67.60
	β'-γ'	81.45		β'-γ'	80.45
	γ'-O'	84.97		γ'-O'	79.55

electron delocalization. Instead, the spin density is centered around the remaining β-β' ring. This same trend and spin density phenomenon holds true for the linkages of MC3 as well.

The 4-O-5 linkage found in MC3 has similar BDEs for both the 4-O and the O-5 bond. The 4-O bond (87.12 kcal mol^{-1}) was shown to have a slightly lower BDE than the O-5 bond (93.89 kcal mol^{-1}). The 4-O-5 linkage is a strong ether linkage due to the proximity of the aromatic rings. The cleavage of these bonds is not favored compared to other ether linkages, such as the β-O-4, due to the fact scission would result in a radical on an aromatic carbon, which would disrupt the aromaticity. Additionally, the spin density is concentrated around the radical making the product unstable. Therefore, we see the 4-O-5 linkage has higher BDEs than other ether linkages.

The results obtained from BDE calculations in this study require comparison with experimentally observed products for validation. At this time, there has been no experimental investigation into these two model compounds; however, it is possible to use previous experimental work involving the linkages of interest for comparison. The formation of phenolic monomer compounds via the β-β' has been proposed to initiate via the homolytic cleavage of the C_α-O bond[73]. Additionally, experimental investigation of pinoresinol, a dimer containing a β-β' linkage, also proposed an initial cleavage of the C_α-O with the C_α-C_β being a secondary point of reaction[74]. In comparison with our BDEs from DFT, we would expect the C_α-O to be the primary point of reaction, followed by the C_α-C_β. For the 4-O-5 linkage, diphenyl ether has been experimentally investigated, with the primary point of reaction being homolytic

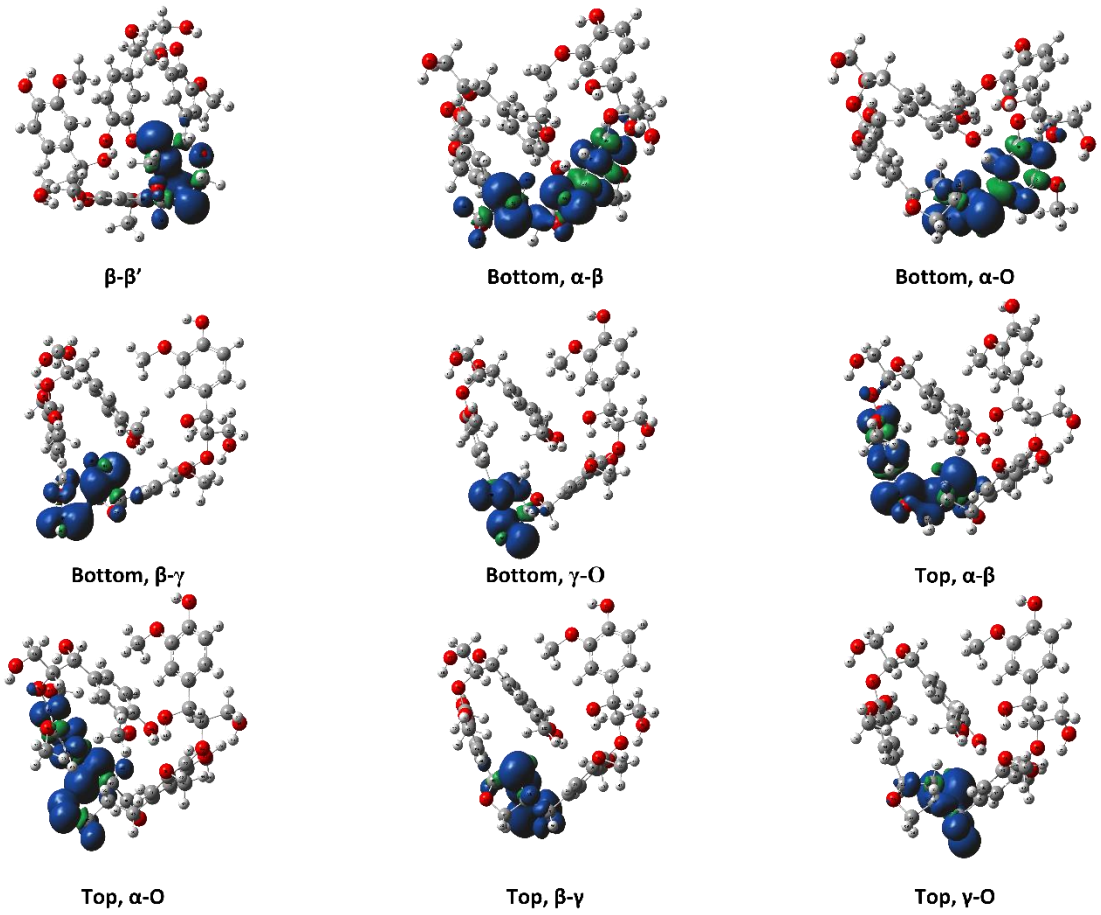

Figure 0-7. Spin density plots for the di-radical species formed from scission along the β-β′ linkage for the RRRSSRRR stereoisomer in MC1.

cleavage of the C-O bond leading to either stabilization or recombination[75]. The subsequent reaction pathways of the two linkages proposed by these previous studies will be further investigated in future DFT work.

The computational work on MC1, MC2, and MC3 has investigated the pyrolysis behavior of five interunit linkages in oligomer-sized model compounds. Additional investigation is still needed to incorporate more linkages as well as different combinations of linkages in each oligomer. The fast pyrolysis scientific community is gradually gaining a better mechanistic understanding of the pyrolytic deconstruction behavior of lignin. Investigation of larger model structures is another necessary step forward to bridge the current knowledge gap from monomers and dimers to native lignin.

3.4. Conclusions

The mechanistic understanding of lignin pyrolysis pathways is underdeveloped compared to both cellulose and hemicellulose. To narrow the gap, model lignin compounds have been studied to understand the pyrolysis of simpler lignin structures. In this work, the thermal behavior of three model lignin oligomers, containing β-O-4, α-O-4, β-5, β-β', and 4-O-5 interunit linkages, were investigated via density functional theory to determine the energetics associated with homolytic bond cleavage during biomass fast pyrolysis. The chiral complexity of MC1 and MC2 required consideration of multiple stereoisomers, which were found to have a range of enthalpy of 5.30 kcal mol^{-1}. The BDEs (ΔH_{298} and ΔH_{773}) of all three model oligomers followed the same trend in terms of relative bond strength as seen in smaller model lignin molecules. The bond

dissociation enthalpies of the model oligomers showed the trend that the C_α of the β-5 and the β-β′ interunit linkages exhibited the lowest BDE due to increased delocalization of the produced radicals. Comparing the ether interunit linkages, our findings showed the following trend in BDEs: C_α-O (α-O-4) < C_β-O (β-O-4) < C_4-O (4-O-5). The non-aromatic C-O bonds were shown to be the easiest to break in all three interunit linkages, which agrees with previous literature. The homolytic cleavages involving aromatic rings exhibited much higher BDEs due to the stability resulting from electron delocalization and disruption of aromaticity in the resulting products, which was confirmed when visualizing the spin density. This work provides an important first step in developing a library of reaction information for various lignin substructures that can be developed into generalized reaction rules for native lignin pyrolysis.

References

1. Maduskar, S.; Facas, G. G.; Papageorgiou, C.; Williams, C. L.; Dauenhauer, P. J., Five Rules for Measuring Biomass Pyrolysis Rates: Pulse-Heated Analysis of Solid Reaction Kinetics of Lignocellulosic Biomass. *ACS Sustainable Chemistry & Engineering* **2018,** *6* (1), 1387-1399.
2. Pecha, M. B.; Montoya, J. I.; Ivory, C.; Chejne, F.; Garcia-Perez, M., Modified Pyroprobe Captive Sample Reactor: Characterization of Reactor and Cellulose Pyrolysis at Vacuum and Atmospheric Pressures. *Industrial & Engineering Chemistry Research* **2017,** *56* (18), 5185-5200.
3. Hoekstra, E.; van Swaaij, W. P. M.; Kersten, S. R. A.; Hogendoorn, K. J. A., Fast pyrolysis in a novel wire-mesh reactor: Design and initial results. *Chemical Engineering Journal* **2012,** *191*, 45-58.
4. Dickerson, T.; Soria, J., Catalytic fast pyrolysis: A review. *Energies* **2013,** *6* (1), 514-538.
5. Balat, M.; Balat, M.; Kırtay, E.; Balat, H., Main routes for the thermo-conversion of biomass into fuels and chemicals. Part 1: Pyrolysis systems. *Energy Conversion and Management* **2009,** *50* (12), 3147-3157.
6. Bridgwater, A. V.; Meier, D.; Radlein, D., An overview of fast pyrolysis of biomass. *Org. Geochem.* **1999,** *30* (12), 1479-1493.
7. Mayes, H. B.; Broadbelt, L. J., Unraveling the Reactions that Unravel Cellulose. *The Journal of Physical Chemistry A* **2012,** *116* (26), 7098-7106.
8. Zhou, X.; Li, W.; Mabon, R.; Broadbelt, L. J., A mechanistic model of fast pyrolysis of hemicellulose. *Energy & Environmental Science* **2018,** *11* (5), 1240-1260.
9. Zhou, X.; Nolte, M. W.; Mayes, H. B.; Shanks, B. H.; Broadbelt, L. J., Experimental and Mechanistic Modeling of Fast Pyrolysis of Neat Glucose-Based Carbohydrates. 1. Experiments and Development of a Detailed Mechanistic Model. *Industrial & Engineering Chemistry Research* **2014,** *53* (34), 13274-13289.
10. Elder, T.; Beste, A., Density Functional Theory Study of the Concerted Pyrolysis Mechanism for Lignin Models. *Energy & Fuels* **2014,** *28* (8), 5229-5235.
11. Hosoya, T.; Sakaki, S., Levoglucosan Formation from Crystalline Cellulose: Importance of a Hydrogen Bonding Network in the Reaction. *ChemSusChem* **2013,** *6* (12), 2356-2368.
12. Faravelli, T.; Frassoldati, A.; Migliavacca, G.; Ranzi, E., Detailed kinetic modeling of the thermal degradation of lignins. *Biomass and Bioenergy* **2010,** *34* (3), 290-301.
13. Debiagi, P.; Gentile, G.; Cuoci, A.; Frassoldati, A.; Ranzi, E.; Faravelli, T., A predictive model of biochar formation and characterization. *Journal of Analytical and Applied Pyrolysis* **2018,** *134*, 326-335.
14. Ranzi, E.; Debiagi, P. E. A.; Frassoldati, A., Mathematical Modeling of Fast Biomass Pyrolysis and Bio-Oil Formation. Note I: Kinetic Mechanism of Biomass Pyrolysis. *ACS Sustainable Chemistry & Engineering* **2017,** *5* (4), 2867-2881.
15. Vinu, R.; Broadbelt, L. J., A mechanistic model of fast pyrolysis of glucose-based carbohydrates to predict bio-oil composition. *Energy & Environmental Science* **2012,** *5* (12), 9808-9826.

16. Klein, M. T.; Virk, P. S., Modeling of Lignin Thermolysis. *Energy & Fuels* **2008,** *22* (4), 2175-2182.
17. Hough, B. R.; Schwartz, D. T.; Pfaendtner, J., Detailed Kinetic Modeling of Lignin Pyrolysis for Process Optimization. *Industrial & Engineering Chemistry Research* **2016,** *55* (34), 9147-9153.
18. Bradbury, A. G. W.; Sakai, Y.; Shafizadeh, F., A kinetic model for pyrolysis of cellulose. *Journal of Applied Polymer Science* **1979,** *23* (11), 3271-3280.
19. Molton, P. M.; Demmitt, T. F. *Reaction mechanisms in cellulose pyrolysis: a literature review*; BNWL-2297 United States 10.2172/7298596 Dep. NTIS, PC A05/MF A01. PNNL English; ; Battelle Pacific Northwest Labs., Richland, WA (USA): 1977; p Medium: ED; Size: Pages: 90.
20. Chu, S.; Subrahmanyam, A. V.; Huber, G. W., The pyrolysis chemistry of a β-O-4 type oligomeric lignin model compound. *Green Chemistry* **2013,** *15* (1), 125-136.
21. Patwardhan, P. R.; Brown, R. C.; Shanks, B. H., Understanding the Fast Pyrolysis of Lignin. *ChemSusChem* **2011,** *4* (11), 1629-1636.
22. Glasser, W. G., About Making Lignin Great Again—Some Lessons From the Past. *Frontiers in Chemistry* **2019,** *7* (565).
23. Kawamoto, H., Lignin pyrolysis reactions. *Journal of Wood Science* **2017,** *63* (2), 117-132.
24. Bonawitz, N. D.; Chapple, C., The Genetics of Lignin Biosynthesis: Connecting Genotype to Phenotype. *Annual Review of Genetics* **2010,** *44* (1), 337-363.
25. Liu, Q.; Luo, L.; Zheng, L., Lignins: Biosynthesis and Biological Functions in Plants. *Int J Mol Sci* **2018,** *19* (2), 335.
26. Miao, Y.-C.; Liu, C.-J., ATP-binding cassette-like transporters are involved in the transport of lignin precursors across plasma and vacuolar membranes. *Proceedings of the National Academy of Sciences* **2010,** *107* (52), 22728-22733.
27. Azad, T.; Schuler, J. D.; Auad, M. L.; Elder, T.; Adamczyk, A. J., Model Lignin Oligomer Pyrolysis: Coupled Conformational and Thermodynamic Analysis of β-O-4′ Bond Cleavage. *Energy & Fuels* **2020,** *34* (8), 9709-9724.
28. Ralph, J.; Lapierre, C.; Boerjan, W., Lignin structure and its engineering. *Current Opinion in Biotechnology* **2019,** *56*, 240-249.
29. Zhu, X.; Lobban, L. L.; Mallinson, R. G.; Resasco, D. E., Bifunctional transalkylation and hydrodeoxygenation of anisole over a Pt/HBeta catalyst. *Journal of Catalysis* **2011,** *281* (1), 21-29.
30. Huang, X.; Liu, C.; Huang, J.; Li, H., Theory studies on pyrolysis mechanism of phenethyl phenyl ether. *Computational and Theoretical Chemistry* **2011,** *976* (1), 51-59.
31. Huang, J.-b.; Wu, S.-b.; Cheng, H.; Lei, M.; Liang, J.-j.; Tong, H., Theoretical study of bond dissociation energies for lignin model compounds. *Journal of Fuel Chemistry and Technology* **2015,** *43* (4), 429-436.
32. Huang, J.-b.; Liu, C.; Ren, L.-r.; Tong, H.; Li, W.-m.; Wu, D., Studies on pyrolysis mechanism of syringol as lignin model compound by quantum chemistry. *Journal of Fuel Chemistry and Technology* **2013,** *41* (6), 657-666.

33. Huang, J.; Li, X.; Wu, D.; Tong, H.; Li, W., Theoretical studies on pyrolysis mechanism of guaiacol as lignin model compound. *Journal of Renewable and Sustainable Energy* **2013,** *5* (4), 043112.
34. Elder, T., A computational study of pyrolysis reactions of lignin model compounds. *Holzforschung* **2010,** *64* (4), 435.
35. Beste, A.; Buchanan, A. C., Computational Study of Bond Dissociation Enthalpies for Lignin Model Compounds. Substituent Effects in Phenethyl Phenyl Ethers. *The Journal of Organic Chemistry* **2009,** *74* (7), 2837-2841.
36. Beste, A.; Buchanan, A. C., Kinetic simulation of the thermal degradation of phenethyl phenyl ether, a model compound for the β-O-4 linkage in lignin. *Chemical Physics Letters* **2012,** *550*, 19-24.
37. Beste, A.; Buchanan, A. C., Kinetic Analysis of the Phenyl-Shift Reaction in β-O-4 Lignin Model Compounds: A Computational Study. *The Journal of Organic Chemistry* **2011,** *76* (7), 2195-2203.
38. Klein, M. T.; Virk, P. S., Model pathways in lignin thermolysis. 1. Phenethyl phenyl ether. *Industrial & Engineering Chemistry Fundamentals* **1983,** *22* (1), 35-45.
39. Sangha, A. K.; Petridis, L.; Smith, J. C.; Ziebell, A.; Parks, J. M., Molecular simulation as a tool for studying lignin. *Environmental Progress & Sustainable Energy* **2012,** *31* (1), 47-54.
40. Tanaka, A.; Maekawa, K.; Suzuki, K., Theoretical Calculations in Reaction Mechanism Studies. *Sumitomo Chemical Co, Ltd* **2013**, 1-10.
41. Huang, J.; Liu, C.; Wu, D.; Tong, H.; Ren, L., Density functional theory studies on pyrolysis mechanism of β-O-4 type lignin dimer model compound. *Journal of Analytical and Applied Pyrolysis* **2014,** *109*, 98-108.
42. Elder, T.; Berstis, L.; Beckham, G. T.; Crowley, M. F., Density Functional Theory Study of Spirodienone Stereoisomers in Lignin. *ACS Sustainable Chemistry & Engineering* **2017,** *5* (8), 7188-7194.
43. Azad, T.; Torres, H. F.; Auad, M. L.; Elder, T.; Adamczyk, A. J., Isolating key reaction energetics and thermodynamic properties during hardwood model lignin pyrolysis. *Physical Chemistry Chemical Physics* **2021**.
44. Zakzeski, J.; Bruijnincx, P. C. A.; Jongerius, A. L.; Weckhuysen, B. M., The Catalytic Valorization of Lignin for the Production of Renewable Chemicals. *Chemical Reviews* **2010,** *110* (6), 3552-3599.
45. Chakar, F. S.; Ragauskas, A. J., Review of current and future softwood kraft lignin process chemistry. *Industrial Crops and Products* **2004,** *20* (2), 131-141.
46. Quideau, S.; Ralph, J., A Biomimetic Route to Lignin Model Compounds via Silver (I) Oxide Oxidation. 1. Synthesis of Dilignols and Non-cyclic Benzyl Aryl Ethers. *Holzforschung - International Journal of the Biology, Chemistry, Physics and Technology of Wood* **1994,** *48* (1), 12-22.
47. Freudenberg, K.; Friedmann, M., Oligomere Zwischenprodukte der Ligninbildung. *Chemische Berichte* **1960,** *93* (9), 2138-2148.
48. Morreel, K.; Ralph, J.; Kim, H.; Lu, F.; Goeminne, G.; Ralph, S.; Messens, E.; Boerjan, W., Profiling of Oligolignols Reveals Monolignol Coupling Conditions in Lignifying Poplar Xylem. *Plant Physiology* **2004,** *136* (3), 3537-3549.

49. Matsuda, S.; Kadota, S.; Tai, T.; Kikuchi, T., Isolation and Structures of Hedyotisol-A, -B, and -C Novel Dilignans From Hedyotis Lawsoniae. *Chemical & Pharmaceutical Bulletin* **1984,** *32* (12), 5066-5069.
50. Yue, F.; Lu, F.; Ralph, S.; Ralph, J., Identification of 4–O–5-Units in Softwood Lignins via Definitive Lignin Models and NMR. *Biomacromolecules* **2016,** *17* (6), 1909-1920.
51. Berstis, L.; Elder, T.; Crowley, M.; Beckham, G. T., Radical Nature of C-Lignin. *ACS Sustainable Chemistry & Engineering* **2016,** *4* (10), 5327-5335.
52. Elder, T.; Berstis, L.; Beckham, G. T.; Crowley, M. F., Coupling and Reactions of 5-Hydroxyconiferyl Alcohol in Lignin Formation. *Journal of Agricultural and Food Chemistry* **2016,** *64* (23), 4742-4750.
53. Halgren, T. A., Merck molecular force field. I. Basis, form, scope, parameterization, and performance of MMFF94. *Journal of Computational Chemistry* **1996,** *17* (5-6), 490-519.
54. Stewart, J. J. P., Optimization of parameters for semiempirical methods V: Modification of NDDO approximations and application to 70 elements. *Journal of Molecular Modeling* **2007,** *13* (12), 1173-1213.
55. Zhao, Y.; Truhlar, D. G., The M06 suite of density functionals for main group thermochemistry, thermochemical kinetics, noncovalent interactions, excited states, and transition elements: two new functionals and systematic testing of four M06-class functionals and 12 other functionals. *Theoretical Chemistry Accounts* **2008,** *120* (1), 215-241.
56. Hehre, W. J.; Ditchfield, R.; Pople, J. A., Self—Consistent Molecular Orbital Methods. XII. Further Extensions of Gaussian—Type Basis Sets for Use in Molecular Orbital Studies of Organic Molecules. *The Journal of Chemical Physics* **1972,** *56* (5), 2257-2261.
57. Hariharan, P. C.; Pople, J. A., The influence of polarization functions on molecular orbital hydrogenation energies. *Theoretica chimica acta* **1973,** *28* (3), 213-222.
58. Clark, T.; Chandrasekhar, J.; Spitznagel, G. W.; Schleyer, P. V. R., Efficient diffuse function-augmented basis sets for anion calculations. III. The 3-21+G basis set for first-row elements, Li–F. *Journal of Computational Chemistry* **1983,** *4* (3), 294-301.
59. Krishnan, R.; Binkley, J. S.; Seeger, R.; Pople, J. A., Self-consistent molecular orbital methods. XX. A basis set for correlated wave functions. *The Journal of Chemical Physics* **1980,** *72* (1), 650-654.
60. Grimme, S.; Antony, J.; Ehrlich, S.; Krieg, H., A consistent and accurate ab initio parametrization of density functional dispersion correction (DFT-D) for the 94 elements H-Pu. *The Journal of Chemical Physics* **2010,** *132* (15), 154104.
61. Elder, T., Bond Dissociation Enthalpies of a Dibenzodioxocin Lignin Model Compound. *Energy & Fuels* **2013,** *27* (8), 4785-4790.
62. Ochterski, J. W., Thermochemistry in gaussian. *Gaussian Inc* **2000,** *1*, 19.
63. Tsuzuki, S.; Honda, K.; Uchimaru, T.; Mikami, M.; Tanabe, K., Origin of Attraction and Directionality of the π/π Interaction: Model Chemistry Calculations of

Benzene Dimer Interaction. *Journal of the American Chemical Society* **2002,** *124* (1), 104-112.
64. Kim, S.; Chmely, S. C.; Nimlos, M. R.; Bomble, Y. J.; Foust, T. D.; Paton, R. S.; Beckham, G. T., Computational Study of Bond Dissociation Enthalpies for a Large Range of Native and Modified Lignins. *The Journal of Physical Chemistry Letters* **2011,** *2* (22), 2846-2852.
65. Parthasarathi, R.; Romero, R. A.; Redondo, A.; Gnanakaran, S., Theoretical Study of the Remarkably Diverse Linkages in Lignin. *The Journal of Physical Chemistry Letters* **2011,** *2* (20), 2660-2666.
66. Younker, J. M.; Beste, A.; Buchanan, A. C., Computational study of bond dissociation enthalpies for lignin model compounds: β-5 Arylcoumaran. *Chemical Physics Letters* **2012,** *545*, 100-106.
67. Huang, J.; He, C., Pyrolysis mechanism of α-O-4 linkage lignin dimer: A theoretical study. *Journal of Analytical and Applied Pyrolysis* **2015,** *113*, 655-664.
68. Zhao, Y.; Truhlar, D. G., Density Functionals with Broad Applicability in Chemistry. *Accounts of Chemical Research* **2008,** *41* (2), 157-167.
69. Houston, R. W.; Elder, T. J.; Abdoulmoumine, N. H., Investigation into the Pyrolysis Bond Dissociation Enthalpies (BDEs) of a Model Lignin Oligomer Using Density Functional Theory (DFT). *Energy & Fuels* **2022**.
70. Choi, Y. S.; Singh, R.; Zhang, J.; Balasubramanian, G.; Sturgeon, M. R.; Katahira, R.; Chupka, G.; Beckham, G. T.; Shanks, B. H., Pyrolysis reaction networks for lignin model compounds: unraveling thermal deconstruction of β-O-4 and α-O-4 compounds. *Green Chemistry* **2016,** *18* (6), 1762-1773.
71. Younker, J. M.; Beste, A.; Buchanan III, A. C., Computational Study of Bond Dissociation Enthalpies for Substituted β-O-4 Lignin Model Compounds. *ChemPhysChem* **2011,** *12* (18), 3556-3565.
72. Elder, T., Bond Dissociation Enthalpies of a Pinoresinol Lignin Model Compound. *Energy & Fuels* **2014,** *28* (2), 1175-1182.
73. Hu, J.; Shen, D.; Xiao, R.; Wu, S.; Zhang, H., Free-Radical Analysis on Thermochemical Transformation of Lignin to Phenolic Compounds. *Energy & Fuels* **2013,** *27* (1), 285-293.
74. Akazawa, M.; Kato, Y.; Kojima, Y., Application of two resinols as lignin dimer models to characterize reaction mechanisms during pyrolysis. *Journal of Analytical and Applied Pyrolysis* **2016,** *122*, 355-364.
75. Custodis, V. B. F.; Hemberger, P.; Ma, Z.; van Bokhoven, J. A., Mechanism of Fast Pyrolysis of Lignin: Studying Model Compounds. *The Journal of Physical Chemistry B* **2014,** *118* (29), 8524-8531.

Appendix III

Table AIII-1. Optimized geometries of the model lignin oligomer of MC1 (298 K).

RRRR

Atoms	XYZ Coordinates		
O	-8.46300	-0.91100	-2.92100
C	-7.25300	-0.70400	-2.34500
C	-4.76300	-0.26500	-1.16200
C	-7.07500	0.34800	-1.43500
C	-6.18300	-1.52400	-2.65700
C	-4.94000	-1.30400	-2.06700
C	-5.84000	0.56700	-0.84500
O	-8.20200	1.09000	-1.21600
C	-8.11600	2.15000	-0.28500
C	-3.42800	-0.08500	-0.48300
C	-3.14200	-1.13700	0.60300
O	-2.69700	-2.35100	-0.03300
C	-4.33600	-1.48800	1.46600
O	-3.95400	-2.24700	2.59100
O	-3.38000	1.21900	0.10600
C	-1.34500	-2.41100	-0.24000
C	1.42700	-2.57900	-0.61400
C	-0.49800	-2.69300	0.85000
C	-0.79900	-2.22400	-1.49600
C	0.58100	-2.29600	-1.68300
C	0.87100	-2.78300	0.65900
C	2.87800	-2.66100	-0.85800
C	3.79800	-3.15600	-0.02700
C	5.26300	-3.24500	-0.34300
O	5.61600	-2.69800	-1.59900
O	-1.12200	-2.85400	2.04300
C	-0.31600	-2.96500	3.20500
C	-2.12000	1.63600	0.45700
C	0.44600	2.43600	1.20900
C	-1.17300	1.95100	-0.51000

Table AIII-1. Continued

Atoms	XYZ Coordinates		
C	-1.79200	1.74300	1.81300
C	-0.51600	2.15600	2.17600
C	0.10700	2.34300	-0.13800
O	-2.67300	1.36800	2.78500
C	-3.82700	2.19400	2.91600
C	1.85800	2.76400	1.63900
O	2.48800	3.57000	0.62300
C	2.77700	1.51000	1.84700
C	3.75500	1.64900	0.70300
C	5.26800	2.42900	-1.46800
C	3.48800	2.84700	0.05200
C	4.81200	0.85000	0.30200
C	5.59400	1.25100	-0.79100
C	4.22300	3.25400	-1.05900
O	4.01800	4.42600	-1.72000
C	2.03200	0.17000	1.86800
O	2.92500	-0.90200	2.10800
C	2.67500	4.70700	-2.10200
C	6.75800	0.47000	-1.24800
C	7.46100	-0.40200	-0.51900
C	8.62300	-1.19100	-1.05400
O	8.42200	-2.58500	-0.91900
H	-9.07400	-0.25000	-2.57700
H	-6.33800	-2.33000	-3.36300
H	-4.11100	-1.96200	-2.30000
H	-5.69100	1.38200	-0.15000
H	-7.38500	2.89600	-0.61100
H	-7.84000	1.77500	0.70500
H	-9.10400	2.60000	-0.24300
H	-2.63000	-0.16500	-1.22900
H	-2.34300	-0.76500	1.25200
H	-5.07400	-2.02300	0.85700
H	-4.79000	-0.56100	1.82800

Table AIII-1. Continued

Atoms	XYZ Coordinates		
H	-3.25900	-2.85300	2.30700
H	-1.46500	-2.02300	-2.32700
H	1.00000	-2.14100	-2.67100
H	1.51600	-2.98100	1.50400
H	3.20700	-2.31300	-1.83400
H	3.51600	-3.56300	0.94300
H	5.56400	-4.29600	-0.37200
H	5.85100	-2.77800	0.46100
H	5.55800	-1.73600	-1.54100
H	0.23900	-3.90700	3.20400
H	0.38400	-2.12800	3.27300
H	-1.00400	-2.94300	4.04700
H	-1.45000	1.87600	-1.55500
H	-0.28600	2.22400	3.23500
H	0.84500	2.57500	-0.89700
H	-3.53300	3.21100	3.19100
H	-4.42300	1.75600	3.71400
H	-4.40200	2.21100	1.98800
H	1.82700	3.37000	2.54600
H	3.31000	1.59900	2.79800
H	5.85100	2.75100	-2.32400
H	5.05000	-0.05800	0.84500
H	1.48400	0.02000	0.93100
H	1.30200	0.16900	2.68100
H	3.22100	-1.24000	1.25600
H	2.04700	4.90900	-1.23300
H	2.26300	3.86800	-2.67200
H	2.72200	5.58700	-2.73900
H	7.07400	0.65400	-2.27400
H	7.20600	-0.58600	0.52300
H	9.52500	-0.96300	-0.48100
H	8.81000	-0.91200	-2.09900
H	7.61000	-2.81100	-1.39200

Table AIII-1. Continued

Atoms	XYZ Coordinates		
RRRS			
O	-9.14100	-0.10600	-2.02300
C	-7.85700	-0.08400	-1.58600
C	-5.21900	-0.02400	-0.68200
C	-7.52500	0.60600	-0.41000
C	-6.86600	-0.73500	-2.29900
C	-5.54800	-0.70200	-1.85000
C	-6.21500	0.63500	0.04300
O	-8.58900	1.21200	0.19700
C	-8.34400	1.89900	1.40900
C	-3.79500	-0.05600	-0.18800
C	-3.38400	-1.38700	0.47000
O	-2.84600	-2.26400	-0.53700
C	-4.49500	-2.14200	1.16800
O	-3.97600	-3.17500	1.97700
O	-3.60500	1.01800	0.74900
C	-1.50900	-2.07200	-0.78400
C	1.23000	-1.78000	-1.28000
C	-0.56700	-2.52800	0.15900
C	-1.07200	-1.45700	-1.94300
C	0.29200	-1.30100	-2.19000
C	0.78800	-2.37500	-0.08700
C	2.67500	-1.68000	-1.56300
C	3.58200	-2.55300	-1.12400
C	5.05000	-2.48200	-1.39600
O	5.72300	-2.66000	-0.15200
O	-1.08600	-3.10100	1.27600
C	-0.18400	-3.43600	2.31800
C	-2.28100	1.28400	1.00300
C	0.43300	1.65800	1.53500
C	-1.78300	1.08200	2.28300
C	-1.42400	1.74000	-0.01300

Table AIII-1. Continued

Atoms	XYZ Coordinates		
C	-0.07100	1.89300	0.25800
C	-0.43300	1.27900	2.55600
O	-1.85200	2.00000	-1.28100
C	-2.99800	2.84200	-1.41900
C	1.91400	1.74800	1.77300
O	2.46200	2.86100	1.03400
C	2.68100	0.48400	1.30300
C	3.88600	1.09900	0.64200
C	5.71800	2.69400	-0.66600
C	3.64500	2.45900	0.48500
C	5.05800	0.53300	0.18700
C	6.00100	1.34300	-0.46100
C	4.54400	3.28200	-0.19100
O	4.37400	4.61800	-0.38400
C	2.95700	-0.48700	2.45100
O	3.28100	-1.79500	2.02300
C	3.06100	5.05800	-0.71700
C	7.24300	0.72700	-0.96000
C	7.83800	-0.29700	-0.34800
C	8.97700	-1.08400	-0.90100
O	8.49500	-2.42800	-1.05400
H	-9.67800	0.39000	-1.39400
H	-7.14200	-1.26000	-3.20600
H	-4.77500	-1.22200	-2.40500
H	-5.94400	1.16900	0.94400
H	-7.94800	1.21800	2.16800
H	-9.30300	2.29200	1.73500
H	-7.64200	2.72300	1.25400
H	-3.12300	0.09600	-1.03800
H	-2.59900	-1.17900	1.20200
H	-5.19200	-2.53300	0.41800
H	-5.04300	-1.45400	1.81800
H	-3.22000	-3.55400	1.51100

Table AIII-1. Continued

Atoms	XYZ Coordinates		
H	-1.81000	-1.10600	-2.65400
H	0.62300	-0.82400	-3.10500
H	1.52200	-2.68200	0.64800
H	2.99500	-0.84600	-2.18700
H	3.27100	-3.40400	-0.52100
H	5.34200	-3.27900	-2.09000
H	5.31500	-1.51800	-1.85000
H	6.67100	-2.72400	-0.33600
H	0.39600	-2.56100	2.62500
H	-0.80000	-3.78300	3.14400
H	0.50100	-4.22800	2.00400
H	-2.47000	0.74400	3.05000
H	0.57900	2.22000	-0.54500
H	-0.05600	1.12300	3.56100
H	-3.01500	3.59500	-0.62700
H	-3.92500	2.26600	-1.39100
H	-2.89800	3.33000	-2.38700
H	2.11700	1.93400	2.83600
H	2.08000	-0.04800	0.55800
H	6.41900	3.33600	-1.18800
H	5.24700	-0.52900	0.28600
H	2.04500	-0.59500	3.04600
H	3.73800	-0.07600	3.10300
H	4.11100	-1.80600	1.52900
H	2.40600	5.05500	0.15400
H	2.63200	4.42100	-1.49700
H	3.17400	6.07200	-1.09800
H	7.65700	1.11500	-1.88900
H	7.44700	-0.65500	0.60200
H	9.82900	-1.07800	-0.21300
H	9.29700	-0.68100	-1.86700
H	9.23300	-3.02400	-1.20600

Table AIII-1. Continued

Atoms	XYZ Coordinates		
RRSR			
O	9.23800	-1.59400	-1.10600
C	7.94200	-1.27800	-0.85900
C	5.27900	-0.63200	-0.33500
C	7.60500	-0.51500	0.26800
C	6.94400	-1.71500	-1.71200
C	5.61400	-1.39500	-1.44700
C	6.28300	-0.19000	0.53000
O	8.67700	-0.15500	1.03600
C	8.42200	0.62300	2.18800
C	3.83700	-0.25400	-0.11300
C	3.31100	0.84000	-1.06900
O	2.59700	0.23200	-2.16400
C	4.34800	1.74600	-1.69700
O	3.72900	2.86100	-2.30400
O	3.67900	0.18500	1.24800
C	1.31600	-0.16300	-1.88300
C	-1.34200	-0.98000	-1.53500
C	0.30700	0.79700	-1.66800
C	0.98600	-1.50900	-1.90000
C	-0.33300	-1.92200	-1.73200
C	-1.00900	0.38100	-1.49800
C	-2.75900	-1.36300	-1.40000
C	-3.21000	-2.54000	-0.96400
C	-4.66500	-2.87500	-0.88800
O	-4.99500	-3.18500	0.47400
O	0.70800	2.09000	-1.69800
C	-0.25500	3.08400	-1.37900
C	2.36600	0.34300	1.60700
C	-0.34900	0.73500	2.10700
C	1.87200	1.61600	1.84600
C	1.50700	-0.76500	1.69700
C	0.15100	-0.55700	1.93900

Table AIII-1. Continued

Atoms	XYZ Coordinates		
C	0.52100	1.81900	2.10200
O	2.06500	-1.98300	1.50500
C	1.21100	-3.11200	1.56100
C	-1.83100	0.98100	2.24300
O	-2.19100	2.08000	1.35500
C	-2.73700	-0.19500	1.84600
C	-3.86300	0.51700	1.14500
C	-5.37400	2.14800	-0.47400
C	-3.41900	1.79900	0.83800
C	-5.07400	0.05100	0.68500
C	-5.85000	0.87400	-0.14700
C	-4.16000	2.63800	0.01200
O	-3.74000	3.86900	-0.39800
C	-3.09000	-1.15800	2.98700
O	-3.08000	-2.50700	2.57200
C	-3.23500	4.73400	0.61700
C	-7.12100	0.40800	-0.72300
C	-7.71500	-0.76200	-0.47300
C	-8.97100	-1.22200	-1.14500
O	-8.75200	-2.42200	-1.88000
H	9.77700	-1.20400	-0.40700
H	7.22200	-2.30800	-2.57400
H	4.83400	-1.73300	-2.12000
H	6.00700	0.38900	1.40100
H	7.77000	0.08600	2.88400
H	7.96100	1.57700	1.91800
H	9.38700	0.80200	2.65500
H	3.22000	-1.14200	-0.26500
H	2.61300	1.47400	-0.52200
H	4.94700	1.17900	-2.41900
H	5.01800	2.12200	-0.92000
H	2.93600	2.54100	-2.74900
H	1.77800	-2.22400	-2.08800

Table AIII-1. Continued

Atoms	XYZ Coordinates		
H	-0.57800	-2.97500	-1.80500
H	-1.79800	1.11100	-1.35100
H	-3.48400	-0.59100	-1.65600
H	-2.52300	-3.31300	-0.62800
H	-4.88600	-3.74300	-1.51700
H	-5.26800	-2.02800	-1.23500
H	-5.75000	-3.77800	0.49900
H	-0.69700	2.88900	-0.39800
H	0.28800	4.02700	-1.36700
H	-1.04300	3.12400	-2.13600
H	2.56300	2.44900	1.77800
H	-0.51600	-1.40800	1.97300
H	0.13800	2.82200	2.24300
H	0.74600	-3.20500	2.54600
H	1.84700	-3.97500	1.37500
H	0.43400	-3.05000	0.79300
H	-2.07800	1.31700	3.25900
H	-2.22200	-0.78900	1.08500
H	-5.94800	2.79900	-1.12300
H	-5.39000	-0.95600	0.93100
H	-4.05400	-0.87900	3.43000
H	-2.33200	-1.08500	3.77300
H	-3.76900	-2.66400	1.91000
H	-2.25400	4.40900	0.96400
H	-3.92700	4.77100	1.46300
H	-3.16400	5.72000	0.16200
H	-7.59700	1.09100	-1.42500
H	-7.27500	-1.47100	0.22400
H	-9.37100	-0.43100	-1.79000
H	-9.73700	-1.47500	-0.40800
H	-8.09100	-2.23600	-2.55200
RRSS			
O	-8.70100	-0.42900	-0.29500

Table AIII-1. Continued

Atoms	XYZ Coordinates		
C	-7.39100	-0.17000	-0.05500
C	-4.69500	0.35500	0.42400
C	-6.41200	-1.11500	-0.40300
C	-7.01100	1.02400	0.53000
C	-5.66200	1.28500	0.77500
C	-5.07300	-0.85500	-0.17100
O	-6.90900	-2.25400	-0.97100
C	-5.98100	-3.27300	-1.29200
C	-3.23100	0.56500	0.70700
C	-2.71800	-0.20100	1.93800
O	-2.52500	-1.58200	1.59800
C	-3.64700	-0.17100	3.13400
O	-3.05200	-0.81200	4.24400
O	-2.95200	1.96000	0.91600
C	-1.25400	-1.91900	1.20400
C	1.30200	-2.75500	0.41100
C	-0.98400	-2.16000	-0.15400
C	-0.24300	-2.06200	2.13900
C	1.02700	-2.47400	1.74900
C	0.28200	-2.58500	-0.53900
C	2.64800	-3.24600	0.06100
C	3.12800	-3.50400	-1.15700
C	4.50900	-4.03900	-1.40200
O	5.10400	-4.46200	-0.19900
O	-2.01800	-1.96200	-1.01500
C	-1.71700	-1.91800	-2.39900
C	-1.79500	2.35100	0.29400
C	0.60400	2.94000	-1.00200
C	-0.66100	2.65300	1.03200
C	-1.75100	2.40500	-1.10800
C	-0.55700	2.71100	-1.74100
C	0.53900	2.94300	0.38700
O	-2.84500	2.06700	-1.85100

Table AIII-1. Continued

Atoms	XYZ Coordinates		
C	-3.92600	3.00000	-1.78800
C	1.92200	3.03300	-1.73500
O	2.88300	3.75300	-0.93900
C	2.55800	1.62900	-2.01000
C	3.62500	1.57500	-0.94200
C	5.54000	2.10400	0.97200
C	3.74100	2.84700	-0.39300
C	4.47700	0.55900	-0.55100
C	5.44400	0.81900	0.43200
C	4.69600	3.14000	0.57600
O	4.88300	4.38100	1.10500
C	1.57000	0.45700	-1.99400
O	2.21400	-0.75800	-2.33300
C	3.72100	5.00500	1.64500
C	6.36700	-0.22800	0.89600
C	6.17700	-1.54200	0.76400
C	7.16700	-2.57000	1.21200
O	7.65000	-3.34700	0.10700
H	-8.76300	-1.30700	-0.69000
H	-7.78100	1.73800	0.79300
H	-5.36500	2.21900	1.23900
H	-4.30200	-1.57200	-0.42700
H	-5.26500	-2.92400	-2.04200
H	-6.56300	-4.09800	-1.69600
H	-5.44000	-3.60000	-0.40000
H	-2.65800	0.20800	-0.15200
H	-1.75100	0.22800	2.22700
H	-4.60100	-0.64000	2.87000
H	-3.84000	0.86600	3.41600
H	-2.94100	-1.73700	4.00400
H	-0.46900	-1.85000	3.17900
H	1.80700	-2.59500	2.49100
H	0.48300	-2.79200	-1.58100

Table AIII-1. Continued

Atoms	XYZ Coordinates		
H	3.30400	-3.44200	0.90500
H	2.53100	-3.34200	-2.05200
H	5.11400	-3.25600	-1.88700
H	4.44200	-4.87100	-2.11700
H	6.06000	-4.32900	-0.26000
H	-2.61900	-1.55800	-2.89000
H	-0.89100	-1.22700	-2.59500
H	-1.46000	-2.91100	-2.77900
H	-0.72400	2.62100	2.11400
H	-0.54400	2.72600	-2.82700
H	1.43100	3.13700	0.97000
H	-3.65400	3.91700	-2.31900
H	-4.18300	3.22600	-0.75200
H	-4.77400	2.52200	-2.27400
H	1.79300	3.59500	-2.66000
H	3.03700	1.63300	-2.99500
H	6.28700	2.33100	1.72400
H	4.44200	-0.41000	-1.03400
H	0.79600	0.62400	-2.74700
H	1.07800	0.37600	-1.01800
H	2.50000	-1.19100	-1.52100
H	3.26400	4.35900	2.40100
H	2.99400	5.23600	0.86500
H	4.06400	5.92400	2.11600
H	7.26600	0.12300	1.40100
H	5.27000	-1.93300	0.30800
H	6.69900	-3.29700	1.87900
H	8.00400	-2.10300	1.73900
H	8.04700	-2.74600	-0.53000
RSRR			
O	-8.01700	-1.73900	-3.04200
C	-6.85600	-1.36300	-2.45200
C	-4.48000	-0.58100	-1.22200

Table AIII-1. Continued

Atoms	XYZ Coordinates		
C	-6.86900	-0.83600	-1.14900
C	-5.65700	-1.49200	-3.12600
C	-4.46800	-1.09900	-2.50900
C	-5.69200	-0.44600	-0.53600
O	-8.11200	-0.76700	-0.58900
C	-8.19100	-0.30800	0.75000
C	-3.18700	-0.23000	-0.53600
C	-2.62100	-1.42500	0.25600
O	-1.47800	-0.97100	1.00800
C	-3.58500	-2.09300	1.22700
O	-4.19000	-1.21300	2.14800
O	-3.40500	0.89200	0.33200
C	-0.28400	-1.59300	0.77200
C	2.22500	-2.77800	0.35500
C	0.47400	-1.25700	-0.36700
C	0.22900	-2.49500	1.69200
C	1.47300	-3.09300	1.48800
C	1.71700	-1.84700	-0.56300
C	3.52100	-3.42700	0.07800
C	4.42700	-3.77800	0.99000
C	5.70900	-4.49200	0.66000
O	6.84800	-3.75500	1.05400
O	-0.08700	-0.35400	-1.20500
C	0.75800	0.27900	-2.15500
C	-2.30400	1.65500	0.60400
C	0.07300	2.95300	1.26000
C	-1.53500	2.23800	-0.38200
C	-1.94600	1.82100	1.95200
C	-0.77800	2.49400	2.27300
C	-0.33100	2.86300	-0.06200
O	-2.77300	1.22900	2.85500
C	-2.33100	1.15000	4.19800
C	1.47900	3.37400	1.63100

Table AIII-1. Continued

Atoms	XYZ Coordinates		
O	2.08400	4.10100	0.54000
C	2.42300	2.14900	1.86800
C	3.06800	2.02500	0.50900
C	4.07800	2.38200	-2.02500
C	2.82800	3.21200	-0.17800
C	3.81800	1.01200	-0.05100
C	4.33100	1.18600	-1.34700
C	3.33200	3.41800	-1.46000
O	3.19200	4.57800	-2.16200
C	1.75200	0.86500	2.34500
O	2.76500	-0.10900	2.52700
C	1.86200	5.06200	-2.31200
C	5.12700	0.14100	-2.00700
C	5.46000	-1.03900	-1.47500
C	6.29500	-2.06300	-2.17400
O	7.45600	-2.39500	-1.40800
H	-8.73400	-1.57700	-2.41600
H	-5.66800	-1.89400	-4.13200
H	-3.52900	-1.19800	-3.04400
H	-5.68100	-0.05600	0.47200
H	-9.24000	-0.36900	1.02900
H	-7.84800	0.72700	0.82500
H	-7.59100	-0.93900	1.41200
H	-2.43600	0.03400	-1.28200
H	-2.30100	-2.17700	-0.47500
H	-3.02100	-2.87400	1.75500
H	-4.38100	-2.58100	0.65900
H	-3.64800	-0.41800	2.25700
H	-0.37000	-2.72700	2.56500
H	1.83900	-3.83400	2.18800
H	2.32100	-1.57900	-1.42300
H	3.73200	-3.62300	-0.97300
H	4.27300	-3.53500	2.04000

Table AIII-1. Continued

Atoms	XYZ Coordinates		
H	5.73700	-4.72700	-0.41200
H	5.74000	-5.44100	1.20300
H	7.11700	-3.20800	0.30400
H	1.10400	-0.43000	-2.91300
H	0.14600	1.04300	-2.63200
H	1.61300	0.74800	-1.66100
H	-1.84700	2.14300	-1.41600
H	-0.47900	2.60100	3.30900
H	0.29900	3.25000	-0.85100
H	-2.26400	2.14300	4.64900
H	-3.07900	0.56100	4.72400
H	-1.36000	0.64800	4.25400
H	1.46900	4.04600	2.49000
H	3.18900	2.42300	2.60200
H	4.47000	2.54300	-3.02300
H	3.99700	0.11000	0.51700
H	1.01900	0.53800	1.60200
H	1.22500	1.03800	3.29100
H	2.36600	-0.98100	2.44000
H	1.24000	4.30600	-2.80300
H	1.93000	5.94100	-2.95000
H	1.42500	5.33500	-1.35000
H	5.46500	0.37200	-3.01600
H	5.15600	-1.30600	-0.46600
H	6.57900	-1.72200	-3.17500
H	5.75400	-3.00700	-2.28200
H	7.97000	-1.59100	-1.28200
RSRS			
O	-9.04600	-1.61100	-1.44300
C	-7.76200	-1.33700	-1.10500
C	-5.12000	-0.75900	-0.41200
C	-7.39600	-0.04000	-0.71400
C	-6.80200	-2.33100	-1.15200

Table AIII-1. Continued

Atoms	XYZ Coordinates		
C	-5.48400	-2.04000	-0.80700
C	-6.08600	0.24900	-0.36800
O	-8.42900	0.85300	-0.72200
C	-8.14400	2.18700	-0.34700
C	-3.69300	-0.48800	0.00500
C	-3.40200	-1.14500	1.36400
O	-2.04100	-0.95400	1.75600
C	-4.20700	-0.55300	2.51100
O	-3.90000	-1.19600	3.72900
O	-3.50300	0.92500	0.07000
C	-1.02300	-1.50900	1.04000
C	1.19200	-2.44400	-0.42200
C	0.25300	-0.95000	1.24400
C	-1.16700	-2.54800	0.12600
C	-0.07200	-3.00500	-0.60100
C	1.33100	-1.40900	0.50800
C	2.33800	-2.94200	-1.19700
C	3.62100	-2.78600	-0.86500
C	4.75300	-3.31800	-1.68500
O	5.48400	-4.32600	-0.98100
O	0.47800	0.10200	2.07900
C	-0.11600	0.11400	3.37200
C	-2.22800	1.43400	0.09200
C	0.28800	2.65100	0.16100
C	-1.92000	2.36900	1.07000
C	-1.27300	1.13200	-0.89400
C	-0.01700	1.72900	-0.83500
C	-0.67600	2.98700	1.10500
O	-1.64800	0.26600	-1.87100
C	-0.66200	-0.14000	-2.80600
C	1.67200	3.24700	0.25600
O	2.35700	3.10600	-1.00800
C	2.56000	2.54100	1.32200

Table AIII-1. Continued

Atoms	XYZ Coordinates		
C	3.51600	1.75900	0.45400
C	5.09500	0.72700	-1.54700
C	3.33900	2.17700	-0.86000
C	4.48300	0.82600	0.78500
C	5.28900	0.29100	-0.23200
C	4.12500	1.66500	-1.89300
O	3.98100	1.99000	-3.20500
C	3.30100	3.54000	2.21400
O	4.06300	4.46400	1.46700
C	3.75400	3.36500	-3.51000
C	6.34400	-0.70100	0.03600
C	6.42800	-1.50200	1.09900
C	7.52400	-2.50900	1.29400
O	7.01300	-3.82100	1.40300
H	-9.55800	-0.79700	-1.35400
H	-7.10000	-3.32400	-1.46600
H	-4.73600	-2.82500	-0.86200
H	-5.78800	1.24700	-0.07700
H	-7.40700	2.63100	-1.02200
H	-7.77200	2.23000	0.68100
H	-9.08200	2.73100	-0.42000
H	-3.02000	-0.91000	-0.74100
H	-3.62400	-2.21700	1.30200
H	-5.27000	-0.70300	2.32400
H	-4.00700	0.52400	2.56600
H	-2.94500	-1.15800	3.83600
H	-2.13900	-2.99300	-0.04100
H	-0.20800	-3.80900	-1.31500
H	2.28200	-0.90700	0.65100
H	2.09400	-3.49000	-2.10600
H	3.90300	-2.28300	0.05700
H	5.47900	-2.53100	-1.89600
H	4.38700	-3.71400	-2.63800

Table AIII-1. Continued

Atoms	XYZ Coordinates		
H	4.86400	-5.01800	-0.72900
H	-0.22100	-0.90200	3.76100
H	0.56500	0.67400	4.01300
H	-1.08800	0.60800	3.34500
H	-2.68700	2.61000	1.79800
H	0.73200	1.49500	-1.57900
H	-0.45600	3.72000	1.87400
H	0.19200	-0.59500	-2.29600
H	-0.32700	0.70600	-3.41300
H	-1.14500	-0.87700	-3.44400
H	1.61400	4.31900	0.45700
H	1.95100	1.87600	1.93900
H	5.71300	0.33600	-2.35000
H	4.63300	0.53300	1.81800
H	3.93000	2.99400	2.92800
H	2.58000	4.13200	2.78200
H	4.71900	3.97400	0.96000
H	4.44900	3.99900	-2.95000
H	2.73100	3.66000	-3.28000
H	3.94500	3.46800	-4.57600
H	7.11100	-0.78600	-0.73300
H	5.65900	-1.48800	1.87000
H	8.05600	-2.31100	2.22900
H	8.24900	-2.42600	0.47400
H	6.54200	-4.01700	0.58000
RSSR			
O	-8.47100	-0.71300	2.20100
C	-7.29200	-0.39100	1.61700
C	-4.86100	0.25900	0.41700
C	-6.61700	-1.33300	0.82400
C	-6.74100	0.86400	1.80600
C	-5.52500	1.18800	1.20900
C	-5.40900	-1.01100	0.22500

Table AIII-1. Continued

Atoms	XYZ Coordinates		
O	-7.25700	-2.53500	0.72400
C	-6.64400	-3.53900	-0.06200
C	-3.56200	0.64700	-0.25100
C	-3.78000	1.61100	-1.41800
O	-2.52900	2.01300	-2.00100
C	-4.56100	1.00500	-2.57100
O	-4.68400	1.93000	-3.63000
O	-2.86900	-0.48000	-0.77600
C	-1.46100	2.26700	-1.17800
C	0.77400	2.72300	0.45900
C	-1.53600	3.18500	-0.12500
C	-0.27200	1.57800	-1.40000
C	0.83300	1.79900	-0.59100
C	-0.43100	3.39100	0.68900
C	1.93800	3.05000	1.30000
C	3.21700	2.92800	0.94300
C	4.36700	3.34900	1.81200
O	5.27700	2.29100	2.05200
O	-2.70800	3.84200	0.15500
C	-3.06300	4.82800	-0.81400
C	-1.79200	-0.95100	-0.08700
C	0.55200	-1.84700	1.14200
C	-1.64700	-0.85100	1.29200
C	-0.78000	-1.55200	-0.84900
C	0.38100	-1.99000	-0.23300
C	-0.47400	-1.29200	1.89800
O	-0.87500	-1.62000	-2.21200
C	-1.87500	-2.50700	-2.70000
C	1.85200	-2.22200	1.81100
O	2.56200	-3.20800	1.02900
C	2.82200	-1.01800	1.94200
C	3.72100	-1.24200	0.75400
C	5.23200	-2.24800	-1.30900

Table AIII-1. Continued

Atoms	XYZ Coordinates		
C	3.52600	-2.55000	0.32100
C	4.67000	-0.42600	0.17100
C	5.45300	-0.93800	-0.87800
C	4.27400	-3.08000	-0.72600
O	4.15400	-4.36100	-1.17300
C	3.61700	-1.10400	3.25200
O	4.68800	-0.17800	3.30200
C	2.83700	-4.76800	-1.53300
C	6.49100	-0.12500	-1.53200
C	6.94300	1.06200	-1.11800
C	8.00100	1.82700	-1.85400
O	9.12300	2.11400	-1.03200
H	-8.68900	-1.62100	1.95700
H	-7.27300	1.57200	2.42900
H	-5.08800	2.16900	1.36800
H	-4.87500	-1.72800	-0.38500
H	-6.54100	-3.21000	-1.10000
H	-7.29900	-4.40500	-0.01600
H	-5.66000	-3.79900	0.34000
H	-2.92600	1.15300	0.48100
H	-4.31300	2.48900	-1.04100
H	-5.57000	0.76000	-2.23800
H	-4.05800	0.08800	-2.90000
H	-3.79100	2.18500	-3.88400
H	-0.25500	0.84000	-2.19500
H	1.74100	1.22900	-0.76200
H	-0.52400	4.10700	1.49900
H	1.71000	3.48500	2.27300
H	3.47800	2.53600	-0.03800
H	3.99100	3.77100	2.75200
H	4.94500	4.12800	1.30700
H	4.85900	1.63700	2.63100
H	-3.99600	5.27400	-0.47300

Table AIII-1. Continued

Atoms	XYZ Coordinates		
H	-2.28600	5.59500	-0.87100
H	-3.20700	4.37600	-1.80000
H	-2.44500	-0.42800	1.89000
H	1.15600	-2.42000	-0.85700
H	-0.36400	-1.19700	2.97300
H	-1.81900	-2.46600	-3.78600
H	-2.86900	-2.19600	-2.37200
H	-1.67300	-3.52800	-2.36100
H	1.65000	-2.68100	2.78200
H	2.29000	-0.06400	1.89000
H	5.81600	-2.66300	-2.12300
H	4.80800	0.59000	0.52100
H	3.99200	-2.12600	3.38100
H	2.96700	-0.86900	4.09700
H	5.37300	-0.47700	2.69200
H	2.43000	-4.09500	-2.29400
H	2.17700	-4.79000	-0.66500
H	2.93400	-5.76800	-1.95000
H	6.91800	-0.55500	-2.43700
H	6.57500	1.52000	-0.20100
H	7.62000	2.80200	-2.16700
H	8.30200	1.27900	-2.75500
H	9.42000	1.28900	-0.63700
RSSS			
O	8.88000	-1.08700	1.11000
C	7.56100	-0.99000	0.81500
C	4.85200	-0.77700	0.19100
C	7.15300	-0.38500	-0.38800
C	6.61100	-1.47700	1.69300
C	5.25500	-1.36500	1.38100
C	5.81000	-0.27900	-0.70000
O	8.18400	0.05500	-1.16700
C	7.84700	0.65800	-2.40400

Table AIII-1. Continued

Atoms	XYZ Coordinates		
C	3.38900	-0.65400	-0.14200
C	2.89000	-1.71500	-1.14100
O	1.53900	-1.42100	-1.49000
C	3.65000	-1.80400	-2.45700
O	3.80000	-0.57200	-3.13000
O	3.11500	0.64600	-0.69100
C	0.52700	-1.74400	-0.64200
C	-1.74600	-2.48600	0.84500
C	-0.76400	-1.33900	-1.05800
C	0.65900	-2.44300	0.55000
C	-0.47000	-2.80400	1.29100
C	-1.87500	-1.71900	-0.32400
C	-2.92900	-2.97400	1.57400
C	-4.12800	-3.19700	1.03500
C	-5.30100	-3.76600	1.78000
O	-6.48700	-3.01900	1.57500
O	-0.81900	-0.59800	-2.18900
C	-2.05000	0.04900	-2.46200
C	2.03800	1.29200	-0.13900
C	-0.20800	2.50400	0.98500
C	0.95700	1.62800	-0.93800
C	2.03100	1.62900	1.22200
C	0.91000	2.23000	1.77400
C	-0.16200	2.23500	-0.38000
O	3.09300	1.29900	2.02300
C	4.27200	2.07000	1.78400
C	-1.47700	2.98500	1.65000
O	-2.31700	3.64900	0.67600
C	-2.35800	1.82100	2.21500
C	-3.33900	1.63300	1.08500
C	-4.88800	1.79000	-1.18900
C	-3.24800	2.74300	0.25500
C	-4.20400	0.59700	0.79900

Table AIII-1. Continued

Atoms	XYZ Coordinates		
C	-4.97400	0.66100	-0.37200
C	-4.03000	2.85100	-0.89500
O	-3.97000	3.88500	-1.77600
C	-1.63200	0.54200	2.58900
O	-0.87000	0.80200	3.75900
C	-3.80700	5.19300	-1.23100
C	-5.82700	-0.49500	-0.69400
C	-6.14400	-0.91400	-1.92000
C	-6.99600	-2.12100	-2.19700
O	-7.61900	-2.66000	-1.04000
H	9.37700	-0.69600	0.38200
H	6.94400	-1.92900	2.61800
H	4.51100	-1.71800	2.08800
H	5.47700	0.18200	-1.62200
H	7.28400	-0.03600	-3.03500
H	7.25500	1.56300	-2.24400
H	8.78900	0.91400	-2.88300
H	2.81500	-0.76700	0.78100
H	2.96000	-2.70200	-0.66900
H	4.65400	-2.18800	-2.26000
H	3.12000	-2.52700	-3.08700
H	3.03000	-0.02700	-2.93500
H	1.63600	-2.73700	0.91000
H	-0.34400	-3.37500	2.20400
H	-2.86200	-1.41300	-0.64700
H	-2.77500	-3.21500	2.62500
H	-4.29300	-3.00300	-0.02500
H	-5.45700	-4.81000	1.47800
H	-5.10300	-3.76000	2.85400
H	-6.78000	-3.13800	0.66100
H	-2.82500	-0.67100	-2.74500
H	-1.86000	0.72300	-3.29500
H	-2.38900	0.61800	-1.59100

Table AIII-1. Continued

Atoms	XYZ Coordinates		
H	0.97900	1.35300	-1.98500
H	0.90700	2.44200	2.83700
H	-1.00500	2.48300	-1.01300
H	4.55500	2.03400	0.73000
H	4.10700	3.10600	2.09500
H	5.06200	1.62000	2.38400
H	-1.24600	3.71800	2.42100
H	-2.88400	2.18200	3.10600
H	-5.50100	1.88000	-2.07900
H	-4.27500	-0.27700	1.43900
H	-2.37300	-0.24300	2.78300
H	-0.99800	0.20600	1.76100
H	-0.22100	0.10100	3.86400
H	-4.48300	5.33900	-0.38400
H	-2.78000	5.36300	-0.90900
H	-4.06900	5.88300	-2.03100
H	-6.16500	-1.06700	0.16700
H	-5.76900	-0.39200	-2.79700
H	-6.38400	-2.92900	-2.60700
H	-7.75000	-1.88100	-2.95600
H	-8.23500	-2.00500	-0.69600

Table AIII-2. Optimized geometry for the RSSR scission products of MC1 (298 K).

α-O-4

α-O

Alpha_side

Atoms	XYZ Coordinates		
O	3.41700	-0.71200	1.50500
C	2.13500	-1.02900	1.19000
C	-0.51500	-1.65700	0.47200
C	1.87600	-2.06000	0.26300
C	1.07800	-0.35200	1.77800
C	-0.22700	-0.66000	1.43300
C	0.58200	-2.37700	-0.08100
O	3.00600	-2.65000	-0.22500
C	2.84600	-3.68000	-1.18100
C	-1.81800	-1.90900	-0.02100
C	-3.00200	-1.02400	0.17200
O	-3.07000	0.00600	-0.87100
C	-4.30900	-1.78700	0.02200
O	-5.42700	-0.93000	0.05300
C	-1.95000	0.80500	-0.90300
C	0.53800	2.07400	-0.72200
C	-1.73800	1.78600	0.07100
C	-0.96000	0.55300	-1.84800
C	0.27500	1.17500	-1.76300
C	-0.50000	2.41800	0.14200
C	1.89200	2.58200	-0.45100
C	3.01700	1.93800	-0.76600
C	4.38700	2.40800	-0.38500
O	5.08500	1.41700	0.35000
O	-2.63700	2.05800	1.05700
C	-4.00700	2.22600	0.69000
H	4.00400	-1.29200	1.00100
H	1.29800	0.43000	2.49400
H	-1.03100	-0.10200	1.89500
H	0.38000	-3.15000	-0.81200

Table AIII-2. Continued

Atoms	XYZ Coordinates		
H	2.27800	-4.51400	-0.76000
H	3.84800	-4.01200	-1.44000
H	2.34000	-3.30300	-2.07500
H	-1.93100	-2.70000	-0.75800
H	-2.98500	-0.50500	1.13700
H	-4.41400	-2.49000	0.84900
H	-4.27700	-2.35600	-0.91700
H	-5.30100	-0.28800	-0.65400
H	-1.16100	-0.19600	-2.60400
H	1.04700	0.94200	-2.48600
H	-0.34200	3.12500	0.94900
H	1.95800	3.51100	0.11200
H	2.97300	0.97500	-1.27200
H	4.31400	3.34500	0.18200
H	4.99300	2.60200	-1.27400
H	4.47600	1.03600	0.99400
H	-4.40900	2.99400	1.34900
H	-4.08800	2.55400	-0.34900
H	-4.56200	1.29600	0.82700
O_side			
O	-5.27000	-1.24500	-1.93400
C	-4.36100	-0.56700	-1.42100
C	-2.29000	1.01000	-0.25700
C	-4.01600	0.74700	-1.92800
C	-3.58100	-1.03300	-0.27200
C	-2.57300	-0.22800	0.27500
C	-3.02900	1.49700	-1.37400
O	-3.75800	-2.20500	0.32600
C	-4.71700	-3.17400	-0.11300
C	-1.18400	1.87800	0.29000
O	-0.68500	1.35400	1.53200
C	0.04000	1.93900	-0.65900
C	0.91600	0.87400	-0.04900

Table AIII-2. Continued

Atoms	XYZ Coordinates		
C	2.20100	-0.92700	1.57300
C	0.45000	0.64200	1.24200
C	2.01600	0.20600	-0.55000
C	2.67900	-0.71500	0.28000
C	1.08400	-0.26200	2.08700
O	0.68100	-0.58500	3.34000
C	0.72000	3.31300	-0.59100
O	1.93100	3.34900	-1.30900
C	0.04900	0.42900	4.11600
C	3.86300	-1.46800	-0.16500
C	4.59000	-1.23800	-1.26000
C	5.78500	-2.05800	-1.64000
O	6.95400	-1.26200	-1.77200
H	-4.59900	1.09200	-2.77400
H	-2.02700	-0.61000	1.13000
H	-2.79500	2.47900	-1.77500
H	-4.58400	-4.01100	0.56800
H	-4.51800	-3.47500	-1.14000
H	-5.72700	-2.77600	-0.04700
H	-1.57600	2.87700	0.50400
H	-0.23400	1.71500	-1.69200
H	2.69100	-1.63900	2.22800
H	2.33000	0.36300	-1.57500
H	0.87300	3.58400	0.46200
H	0.07100	4.06500	-1.04400
H	2.55800	2.76400	-0.87100
H	-0.98400	0.58000	3.80400
H	0.59500	1.37200	4.03200
H	0.08000	0.07700	5.14500
H	4.16200	-2.28700	0.48700
H	4.35600	-0.41300	-1.92900
H	5.63900	-2.51700	-2.62100
H	5.93400	-2.86300	-0.91100

Table AIII-2. Continued

Atoms	XYZ Coordinates		
H	7.08600	-0.79000	-0.94600
O-4			
O_side			
O	-5.44400	-2.16600	1.99700
C	-4.39200	-1.62600	1.33500
C	-2.23500	-0.51900	-0.04000
C	-4.46900	-1.40700	-0.05100
C	-3.23500	-1.29300	2.01700
C	-2.15800	-0.73800	1.33000
C	-3.39800	-0.85700	-0.73500
O	-5.65800	-1.78400	-0.60500
C	-5.81700	-1.59900	-1.99900
C	-1.06800	0.10800	-0.77700
C	-0.84900	1.58200	-0.31700
O	0.38000	2.10700	-0.81000
C	-1.92500	2.50300	-0.86400
O	-1.70700	3.83200	-0.44500
O	-1.12900	0.05700	-2.13200
C	1.53000	1.43800	-0.48000
C	3.91000	0.04800	0.06700
C	1.91700	1.20700	0.84600
C	2.34800	0.99700	-1.51700
C	3.52700	0.32000	-1.25200
C	3.09400	0.51200	1.10000
C	5.13200	-0.69900	0.40900
C	5.89600	-1.40200	-0.42900
C	7.12800	-2.13800	0.00300
O	7.06300	-3.51700	-0.32300
O	1.15400	1.60900	1.91000
C	1.04200	3.02400	2.06800
H	-6.14700	-2.33100	1.35700
H	-3.19400	-1.47700	3.08400
H	-1.25100	-0.48300	1.87000

Table AIII-2. Continued

Atoms	XYZ Coordinates		
H	-3.43400	-0.69400	-1.80500
H	-5.73100	-0.54100	-2.26200
H	-6.81400	-1.95700	-2.24200
H	-5.07200	-2.17600	-2.55400
H	-0.12800	-0.41200	-0.50000
H	-0.85700	1.59600	0.77500
H	-2.89700	2.19500	-0.47700
H	-1.93700	2.42700	-1.95900
H	-0.86000	4.10700	-0.81000
H	2.02200	1.19200	-2.53200
H	4.15000	0.00100	-2.07700
H	3.35900	0.33800	2.13800
H	5.41500	-0.66700	1.46000
H	5.63800	-1.49500	-1.48100
H	7.29600	-1.99000	1.07700
H	8.00400	-1.75900	-0.52800
H	6.26800	-3.88100	0.07600
H	0.54000	3.18500	3.01900
H	2.03600	3.47800	2.09300
H	0.45100	3.46800	1.26300
4_side			
C	-4.41000	-0.42400	-1.75300
C	-2.55000	0.92000	-0.28200
C	-4.23700	0.91400	-2.01300
C	-3.71300	-1.13400	-0.79900
C	-2.76000	-0.43200	-0.04900
C	-3.28600	1.59800	-1.26000
O	-3.88700	-2.44800	-0.54000
C	-4.85900	-3.10500	-1.33600
C	-1.49900	1.69400	0.48700
O	-1.04000	0.94400	1.62800
C	-0.23200	1.97900	-0.35600
C	0.65900	0.84500	0.08100

Table AIII-2. Continued

Atoms	XYZ Coordinates		
C	1.93900	-1.20000	1.38800
C	0.13700	0.34400	1.27100
C	1.81100	0.32600	-0.47700
C	2.47200	-0.71900	0.19200
C	0.76900	-0.68800	1.95700
O	0.32000	-1.26800	3.09700
C	0.38600	3.33200	0.02000
O	1.63000	3.55000	-0.60500
C	-0.41000	-0.45600	4.01200
C	3.70900	-1.32900	-0.32200
C	4.47700	-0.86800	-1.31100
C	5.72400	-1.55900	-1.77100
O	6.86300	-0.71500	-1.67800
H	-4.82000	1.42300	-2.77200
H	-2.20600	-0.96800	0.71300
H	-3.11900	2.65700	-1.43100
H	-4.87200	-4.14100	-1.00700
H	-4.59000	-3.05300	-2.39500
H	-5.84500	-2.65400	-1.19200
H	-1.93700	2.61600	0.87800
H	-0.44700	1.95800	-1.42600
H	2.42700	-2.01100	1.91800
H	2.16800	0.69500	-1.43100
H	0.47500	3.39300	1.11300
H	-0.27100	4.13900	-0.31200
H	2.25500	2.90400	-0.26200
H	-1.43200	-0.29300	3.67000
H	0.08600	0.50800	4.14700
H	-0.41400	-1.00200	4.95300
H	4.01200	-2.24800	0.17700
H	4.23900	0.06100	-1.82300
H	5.65000	-1.82200	-2.82900
H	5.87000	-2.48600	-1.20400

Table AIII-2. Continued

Atoms	XYZ Coordinates		
H	6.92900	-0.40500	-0.77100
β-O-4			
1-α			
1_side			
O	-0.20600	2.21200	-0.00000
C	-0.56500	0.90300	-0.00000
C	-1.28000	-1.71900	0.00000
C	0.42700	-0.09400	-0.00000
C	-1.90500	0.55600	-0.00000
C	-2.28600	-0.79200	0.00000
C	0.07000	-1.44100	-0.00000
O	1.70200	0.39200	0.00000
C	2.75800	-0.54900	0.00000
H	0.75700	2.25900	-0.00000
H	-2.64300	1.35000	0.00000
H	-3.33200	-1.07200	0.00000
H	0.81400	-2.22700	-0.00000
H	2.71800	-1.17700	0.89400
H	3.68000	0.02700	0.00000
H	2.71800	-1.17700	-0.89400
Alpha_side			
C	-4.89100	0.54500	-0.45700
C	-5.51400	-0.27300	0.60700
O	-4.51100	-0.96800	1.40000
C	-6.27200	0.55400	1.64300
O	-6.77900	-0.26500	2.67000
O	-3.95200	1.42000	-0.02100
C	-3.39800	-1.44400	0.75900
C	-1.06500	-2.41300	-0.47200
C	-3.48700	-2.31900	-0.32800
C	-2.14100	-1.04300	1.20800
C	-0.98700	-1.51900	0.60300
C	-2.32800	-2.78200	-0.93800

Table AIII-2. Continued

Atoms	XYZ Coordinates		
C	0.12300	-3.02100	-1.09700
C	1.32700	-3.15100	-0.53600
C	2.46800	-3.88900	-1.17400
O	3.65300	-3.11600	-1.23100
O	-4.70700	-2.70300	-0.82600
C	-5.42100	-3.59400	0.02900
C	-2.73700	1.52800	-0.64800
C	-0.13600	1.74500	-1.63500
C	-2.34200	0.75500	-1.73300
C	-1.83900	2.43000	-0.06600
C	-0.54800	2.52900	-0.56300
C	-1.04600	0.87000	-2.22100
O	-2.18400	3.15300	1.04000
C	-3.15100	4.17300	0.80800
C	1.28300	1.80500	-2.15900
O	2.05000	2.79800	-1.44700
C	2.04900	0.47400	-1.95800
C	2.77600	0.76100	-0.66900
C	4.13700	1.86800	1.43900
C	2.76000	2.14000	-0.48000
C	3.46200	-0.07900	0.18500
C	4.16700	0.48300	1.26200
C	3.44300	2.72500	0.58200
O	3.52600	4.06500	0.80600
C	3.04300	0.24800	-3.10400
O	3.94600	-0.81100	-2.84000
C	2.30500	4.79500	0.75600
C	4.93200	-0.34800	2.20500
C	5.19600	-1.65100	2.07900
C	5.98500	-2.42100	3.09400
O	7.13100	-3.03600	2.52500
H	-5.02600	0.38800	-1.51800
H	-6.18900	-1.00200	0.15200

Table AIII-2. Continued

Atoms	XYZ Coordinates		
H	-7.12500	1.03600	1.16300
H	-5.60000	1.32600	2.03600
H	-6.02800	-0.72700	3.05700
H	-2.09700	-0.32600	2.02000
H	-0.02100	-1.17100	0.95200
H	-2.43500	-3.46700	-1.77300
H	-0.03800	-3.46100	-2.08100
H	1.51700	-2.75700	0.46100
H	2.17500	-4.24500	-2.16900
H	2.71400	-4.76600	-0.57000
H	3.56900	-2.45300	-1.93200
H	-6.35300	-3.83200	-0.48200
H	-4.84300	-4.50900	0.18600
H	-5.63500	-3.12600	0.99400
H	-3.01100	0.02000	-2.15900
H	0.13200	3.22000	-0.08300
H	-0.74000	0.24100	-3.05100
H	-3.29800	4.67700	1.76200
H	-4.09700	3.75000	0.46700
H	-2.77500	4.88800	0.07000
H	1.28000	2.11400	-3.20700
H	1.37100	-0.37900	-1.87300
H	4.66700	2.32600	2.26700
H	3.45400	-1.15000	0.02100
H	3.59200	1.17700	-3.29800
H	2.50600	-0.02600	-4.01400
H	4.56500	-0.51700	-2.16100
H	1.56800	4.34600	1.43000
H	1.90600	4.83400	-0.25900
H	2.54200	5.80000	1.09900
H	5.31300	0.17400	3.08200
H	4.86500	-2.21400	1.20800
H	5.39000	-3.24300	3.49800

Table AIII-2. Continued

Atoms	XYZ Coordinates		
H	6.26200	-1.76600	3.92900
H	7.62900	-2.36000	2.05900
α-β			
Alpha_side			
O	8.96200	2.58200	-0.16700
C	7.81100	1.86900	-0.12500
C	5.43200	0.38100	-0.03900
C	7.84300	0.46500	-0.26600
C	6.59500	2.51100	0.05700
C	5.41500	1.78700	0.10000
C	6.68200	-0.27100	-0.22300
O	9.10200	-0.03700	-0.43800
C	9.23300	-1.43600	-0.58900
C	4.25400	-0.38400	-0.00500
O	3.08000	0.24000	0.28400
C	1.90500	-0.37200	-0.04800
C	-0.59000	-1.47800	-0.64500
C	1.77500	-1.26400	-1.10300
C	0.78100	-0.02400	0.71900
C	-0.45200	-0.57400	0.41200
C	0.53000	-1.81900	-1.39100
O	0.87700	0.88600	1.73000
C	1.57700	0.42400	2.88200
C	-1.94100	-2.04000	-1.01000
O	-2.68200	-2.39400	0.18200
C	-2.84400	-1.04200	-1.77900
C	-3.73900	-0.53900	-0.67500
C	-5.27200	-0.18700	1.57300
C	-3.61000	-1.41500	0.40000
C	-4.62500	0.52000	-0.64000
C	-5.42300	0.69600	0.50300
C	-4.36700	-1.25100	1.55600
O	-4.32200	-2.05300	2.65000

Table AIII-2. Continued

Atoms	XYZ Coordinates		
C	-3.66200	-1.77200	-2.85300
O	-4.60900	-0.93700	-3.47700
C	-3.06600	-2.63300	2.99200
C	-6.40400	1.78700	0.62400
C	-6.81400	2.60700	-0.34500
C	-7.82300	3.69300	-0.12900
O	-8.95100	3.54500	-0.98000
H	9.69100	1.96500	-0.30100
H	6.59600	3.58900	0.16200
H	4.46800	2.29100	0.23900
H	6.70400	-1.34900	-0.32800
H	8.86400	-1.95900	0.29800
H	10.29500	-1.63200	-0.71300
H	8.69000	-1.78300	-1.47300
H	4.23600	-1.46500	-0.07400
H	2.63800	-1.50400	-1.71200
H	-1.30200	-0.27700	1.01600
H	0.43900	-2.52000	-2.21400
H	1.54700	1.23700	3.60400
H	2.61500	0.18500	2.64300
H	1.07700	-0.45600	3.29800
H	-1.80700	-2.96700	-1.57400
H	-2.25800	-0.24700	-2.24200
H	-5.86100	-0.05900	2.47500
H	-4.67500	1.21500	-1.47000
H	-4.14500	-2.64900	-2.39900
H	-2.99400	-2.12400	-3.64200
H	-5.28100	-0.70700	-2.82800
H	-2.27000	-1.88500	2.93500
H	-2.82200	-3.46700	2.33500
H	-3.17100	-2.98000	4.01800
H	-6.83100	1.91400	1.61800
H	-6.44200	2.50700	-1.36200

Table AIII-2. Continued

Atoms	XYZ Coordinates		
H	-7.40000	4.66700	-0.38200
H	-8.12400	3.72000	0.92500
H	-9.31800	2.66900	-0.83700
Beta_side			
C	-3.21400	-0.53300	0.90000
O	-2.44300	-0.88600	-0.17800
C	-4.62600	-0.96400	0.74500
O	-5.21600	-0.44700	-0.43900
C	-1.12000	-0.51500	-0.17800
C	1.61300	0.11100	-0.23100
C	-0.70000	0.78200	0.14000
C	-0.18400	-1.47200	-0.55900
C	1.16500	-1.16500	-0.59300
C	0.66000	1.07000	0.11700
C	3.03700	0.48200	-0.21200
C	4.07600	-0.35300	-0.24500
C	5.50200	0.10500	-0.22100
O	6.22500	-0.46600	0.85900
O	-1.57200	1.76700	0.50500
C	-2.44500	2.20900	-0.53500
H	-2.71100	-0.41500	1.85100
H	-5.21200	-0.59000	1.58500
H	-4.70100	-2.06400	0.74500
H	-4.69900	-0.77100	-1.18300
H	-0.54400	-2.45900	-0.82300
H	1.87300	-1.92200	-0.90700
H	0.96000	2.07800	0.38300
H	3.23700	1.55100	-0.15100
H	3.92900	-1.43100	-0.26600
H	5.54300	1.20100	-0.19000
H	6.02600	-0.22400	-1.12100
H	5.76300	-0.25100	1.67400
H	-3.00800	3.04300	-0.12300

Table AIII-2. Continued

Atoms	XYZ Coordinates		
H	-1.86000	2.54600	-1.39600
H	-3.14000	1.42200	-0.83600
β-O			
Beta_side			
O	7.36800	-2.50200	-0.77500
C	6.52600	-1.44600	-0.87300
C	4.77200	0.71600	-1.07100
C	5.68000	-1.11700	0.19900
C	6.48100	-0.69400	-2.03400
C	5.60200	0.38300	-2.13300
C	4.81500	-0.04000	0.10400
O	5.79900	-1.94200	1.27800
C	4.93400	-1.70900	2.37500
C	3.85700	1.92900	-1.17100
C	4.58300	3.17700	-0.77500
C	4.64800	3.55600	0.66800
O	3.45600	4.18700	1.12900
O	2.76000	1.83600	-0.26100
C	1.80400	0.88100	-0.41600
C	-0.29700	-0.95800	-0.51400
C	1.75600	-0.06000	-1.43800
C	0.80200	0.89500	0.56600
C	-0.23800	-0.01700	0.51500
C	0.70400	-0.97200	-1.47700
O	0.83700	1.84900	1.54800
C	1.75800	1.57100	2.59700
C	-1.45300	-1.92400	-0.63400
O	-2.07700	-2.13000	0.65200
C	-2.58000	-1.40800	-1.56300
C	-3.53700	-0.82400	-0.55600
C	-5.01500	-0.16900	1.66400
C	-3.20100	-1.35200	0.68700
C	-4.59900	0.04700	-0.70300

Table AIII-2. Continued

Atoms	XYZ Coordinates		
C	-5.36100	0.38200	0.42900
C	-3.93800	-1.04300	1.82500
O	-3.64900	-1.48100	3.07900
C	-3.23600	-2.56600	-2.32800
O	-4.36900	-2.15700	-3.05800
C	-3.22600	-2.83500	3.20700
C	-6.51400	1.29400	0.36300
C	-7.13200	1.72100	-0.74000
C	-8.30200	2.65700	-0.71600
O	-9.43900	2.10200	-1.36100
H	7.24800	-2.90200	0.09400
H	7.13400	-0.96900	-2.85300
H	5.56900	0.96400	-3.04900
H	4.14800	0.20600	0.91900
H	5.11600	-0.72100	2.80900
H	5.16100	-2.47800	3.11000
H	3.88800	-1.78900	2.06700
H	3.47700	2.01300	-2.19600
H	5.07400	3.76100	-1.54100
H	5.45200	4.27200	0.83900
H	4.86000	2.66300	1.27600
H	2.71700	3.61300	0.89400
H	2.53700	-0.10100	-2.18600
H	-0.99700	0.02400	1.28800
H	0.67600	-1.70800	-2.27500
H	1.67900	2.39300	3.30600
H	2.78400	1.52800	2.21600
H	1.50100	0.62800	3.08800
H	-1.08400	-2.90000	-0.96000
H	-2.20600	-0.66500	-2.27100
H	-5.58300	0.08200	2.55300
H	-4.80900	0.49100	-1.66900
H	-3.48800	-3.36500	-1.61700

Table AIII-2. Continued

Atoms	XYZ Coordinates		
H	-2.52900	-2.97000	-3.05600
H	-5.04600	-1.88100	-2.43300
H	-2.19900	-2.96500	2.86600
H	-3.88600	-3.49500	2.63500
H	-3.30200	-3.07200	4.26600
H	-6.88700	1.63900	1.32600
H	-6.82200	1.38200	-1.72600
H	-8.07400	3.56900	-1.27300
H	-8.53200	2.94200	0.31700
H	-9.63700	1.26100	-0.94100
O_side			
O	-3.31800	1.38800	-0.10000
C	-2.16100	0.94800	-0.02900
C	0.53200	-0.02900	0.13400
C	-1.85600	-0.48800	-0.00300
C	-1.01100	1.83500	0.03300
C	0.26200	1.37500	0.11100
C	-0.53600	-0.92000	0.07500
C	1.88600	-0.56300	0.21300
C	3.02400	0.14000	0.28200
C	4.37900	-0.49600	0.35800
O	5.23300	-0.04000	-0.67900
O	-2.77600	-1.44900	-0.05200
C	-4.18100	-1.18400	-0.13300
H	-1.23900	2.89400	0.01400
H	1.08400	2.07900	0.15600
H	-0.36000	-1.98900	0.09200
H	1.95600	-1.65000	0.22000
H	3.02100	1.22600	0.26800
H	4.28400	-1.58800	0.34700
H	4.87800	-0.21300	1.28800
H	4.81700	-0.24200	-1.52100
H	-4.63900	-2.17000	-0.15400

Table AIII-2. Continued

Atoms	XYZ Coordinates		
H	-4.52000	-0.61900	0.73400
H	-4.41900	-0.62800	-1.03700
β-γ			
Beta_side			
O	-9.33300	1.34500	0.46400
C	-8.00300	1.12700	0.31700
C	-5.27000	0.66900	0.02500
C	-7.51700	-0.17800	0.15000
C	-7.11700	2.19000	0.33800
C	-5.75100	1.96100	0.19100
C	-6.15800	-0.40900	0.00200
O	-8.49000	-1.13800	0.15600
C	-8.08000	-2.48300	0.00700
C	-3.79400	0.44900	-0.19700
C	-3.48300	0.62200	-1.64300
O	-2.20400	0.71700	-2.11000
O	-3.45900	-0.89200	0.25000
C	-1.21800	1.31600	-1.36400
C	0.89900	2.43300	0.09000
C	-1.40400	2.52200	-0.67600
C	0.02700	0.69800	-1.35100
C	1.07700	1.25000	-0.63700
C	-0.35500	3.04600	0.06800
C	1.99800	3.05000	0.85400
C	3.29000	2.96300	0.53600
C	4.39500	3.58100	1.34200
O	5.31700	2.60600	1.80300
O	-2.60900	3.17500	-0.68400
C	-2.93500	3.77800	-1.93600
C	-2.16000	-1.10200	0.62200
C	0.47600	-1.65200	1.39400
C	-1.56700	-0.39100	1.66400
C	-1.42300	-2.08800	-0.04000

Table AIII-2. Continued

Atoms	XYZ Coordinates		
C	-0.11900	-2.36600	0.36000
C	-0.25900	-0.65600	2.03900
O	-1.94700	-2.76100	-1.10800
C	-2.96800	-3.69300	-0.77100
C	1.87000	-1.98700	1.88200
O	2.48100	-2.97600	1.02800
C	2.84600	-0.78200	1.91600
C	3.69900	-1.05400	0.70400
C	5.06500	-2.09500	-1.43900
C	3.42100	-2.34400	0.26400
C	4.66800	-0.27900	0.09700
C	5.37300	-0.80800	-0.99700
C	4.09300	-2.89100	-0.82600
O	3.90800	-4.14900	-1.30400
C	3.67900	-0.78500	3.20300
O	4.70800	0.18700	3.18600
C	2.56700	-4.61800	-1.38500
C	6.41200	-0.03300	-1.69400
C	6.89900	1.15400	-1.32200
C	7.95500	1.87700	-2.10300
O	9.10600	2.15200	-1.31900
H	-9.78000	0.49000	0.43100
H	-7.51200	3.18900	0.47600
H	-5.05100	2.78900	0.20700
H	-5.76800	-1.41100	-0.11300
H	-7.57600	-2.63200	-0.95300
H	-8.98500	-3.08400	0.04100
H	-7.41100	-2.77800	0.82100
H	-3.23200	1.16400	0.40500
H	-4.14100	0.19500	-2.38900
H	0.13700	-0.23600	-1.88900
H	2.03500	0.73900	-0.62100
H	-0.53200	3.97000	0.60800

Table AIII-2. Continued

Atoms	XYZ Coordinates		
H	1.70800	3.64300	1.72000
H	3.59400	2.41700	-0.35500
H	3.97700	4.15800	2.17500
H	4.97800	4.26600	0.72100
H	4.87000	2.01800	2.42900
H	-3.94100	4.18100	-1.83100
H	-2.23100	4.58400	-2.15800
H	-2.92200	3.04100	-2.74300
H	-2.14300	0.36800	2.18100
H	0.42400	-3.14600	-0.15700
H	0.18500	-0.09100	2.85200
H	-3.30200	-4.13600	-1.70800
H	-3.80300	-3.19200	-0.27700
H	-2.56600	-4.47400	-0.11800
H	1.79300	-2.45200	2.86900
H	2.31600	0.17100	1.82900
H	5.58400	-2.52300	-2.28900
H	4.87500	0.72100	0.45600
H	4.10000	-1.78500	3.36300
H	3.04100	-0.54500	4.05700
H	5.40300	-0.11800	2.59100
H	1.93300	-3.87100	-1.87300
H	2.16700	-4.85200	-0.39800
H	2.60100	-5.51800	-1.99500
H	6.80500	-0.49200	-2.60000
H	6.56400	1.64700	-0.41000
H	7.59000	2.85400	-2.42800
H	8.21700	1.30100	-3.00000
H	9.39600	1.32800	-0.91900
γ-O			
Gamma_side			
O	-8.60900	-0.47100	1.99100
C	-7.41600	-0.19100	1.41300

Table AIII-2. Continued

Atoms	XYZ Coordinates		
C	-4.95600	0.37100	0.22900
C	-6.76700	-1.16000	0.63100
C	-6.82700	1.04700	1.59800
C	-5.59500	1.32700	1.00800
C	-5.54600	-0.88200	0.03900
O	-7.44600	-2.34100	0.53400
C	-6.84600	-3.37800	-0.22000
C	-3.64300	0.70400	-0.43600
C	-3.83600	1.60500	-1.67300
O	-2.57100	1.96000	-2.25000
C	-4.62500	0.95500	-2.74800
O	-2.95900	-0.45200	-0.89200
C	-1.52200	2.24500	-1.41600
C	0.69000	2.76800	0.23800
C	-1.60000	3.22600	-0.42100
C	-0.33800	1.52900	-1.57100
C	0.75500	1.78300	-0.75400
C	-0.50900	3.46600	0.40300
C	1.84200	3.12900	1.08200
C	3.12600	2.96700	0.75900
C	4.26400	3.42700	1.62500
O	5.15400	2.37300	1.94900
O	-2.76700	3.91900	-0.20600
C	-3.06800	4.86000	-1.23500
C	-1.90700	-0.91600	-0.16000
C	0.39800	-1.76900	1.16400
C	-1.79300	-0.75600	1.21700
C	-0.88800	-1.56600	-0.87300
C	0.25600	-1.97900	-0.20400
C	-0.64000	-1.17300	1.87300
O	-0.91600	-1.72400	-2.22500
C	-2.11700	-2.20000	-2.83000
C	1.68100	-2.11600	1.87800

Table AIII-2. Continued

Atoms	XYZ Coordinates		
O	2.39800	-3.15000	1.16900
C	2.66000	-0.91400	1.96300
C	3.58500	-1.21400	0.81200
C	5.13400	-2.35100	-1.15200
C	3.38600	-2.54200	0.44900
C	4.55800	-0.44300	0.20800
C	5.36000	-1.02000	-0.79000
C	4.15200	-3.13800	-0.54800
O	4.02600	-4.44000	-0.92600
C	3.42100	-0.93000	3.29500
O	4.50100	-0.01300	3.31800
C	2.71300	-4.84800	-1.29900
C	6.42300	-0.25700	-1.46300
C	6.87700	0.94800	-1.10900
C	7.96100	1.65900	-1.86000
O	9.06500	1.98300	-1.02800
H	-8.85000	-1.37600	1.75800
H	-7.33900	1.77600	2.21300
H	-5.12800	2.29400	1.16400
H	-5.03000	-1.61600	-0.56700
H	-6.71500	-3.07400	-1.26200
H	-7.52700	-4.22400	-0.16800
H	-5.87800	-3.65700	0.20600
H	-3.01300	1.24700	0.27300
H	-4.34700	2.50900	-1.31200
H	-5.62300	0.59900	-2.53600
H	-4.26900	1.01200	-3.76600
H	-0.31300	0.74600	-2.32100
H	1.65700	1.19000	-0.87200
H	-0.60800	4.23000	1.16700
H	1.60200	3.62700	2.02000
H	3.40100	2.51100	-0.19000
H	3.87500	3.91100	2.52800

Table AIII-2. Continued

Atoms	XYZ Coordinates		
H	4.86300	4.16400	1.08500
H	4.71200	1.75800	2.55200
H	-4.01400	5.32500	-0.96300
H	-2.28600	5.62200	-1.28900
H	-3.16100	4.36300	-2.20500
H	-2.60300	-0.29700	1.77100
H	1.03800	-2.44900	-0.78700
H	-0.55500	-1.02900	2.94500
H	-1.81000	-2.71900	-3.73700
H	-2.78800	-1.37500	-3.07300
H	-2.62800	-2.90100	-2.16400
H	1.45600	-2.51800	2.86900
H	2.13800	0.03900	1.84200
H	5.73200	-2.81700	-1.92800
H	4.69900	0.59000	0.50300
H	3.78200	-1.94700	3.49400
H	2.75300	-0.64000	4.10900
H	5.19600	-0.35400	2.74300
H	2.33700	-4.21400	-2.10800
H	2.02900	-4.81000	-0.44900
H	2.80500	-5.87200	-1.65500
H	6.86900	-0.74400	-2.32900
H	6.49000	1.46400	-0.23100
H	7.59900	2.61600	-2.24200
H	8.28000	1.05400	-2.71900
H	9.33800	1.18300	-0.57200
O-4			
O_side			
O	5.71200	-3.86100	0.57400
C	5.35000	-2.59600	0.26000
C	4.58500	0.00900	-0.39300
C	4.27500	-1.98300	0.92600
C	6.02600	-1.90200	-0.72700

Table AIII-2. Continued

Atoms	XYZ Coordinates		
C	5.63900	-0.60300	-1.05600
C	3.90100	-0.68900	0.60700
O	3.67500	-2.77100	1.86200
C	2.54500	-2.24200	2.53100
C	4.20200	1.43600	-0.73300
C	5.14500	2.46200	-0.09200
O	4.99300	3.71500	-0.62000
C	5.06900	2.52700	1.44500
O	6.03900	3.41100	1.94400
O	2.90800	1.77800	-0.25800
C	1.81800	1.21200	-0.84400
C	-0.56500	0.18600	-1.91300
C	1.85500	0.34500	-1.93100
C	0.57800	1.56100	-0.28200
C	-0.59300	1.05300	-0.81700
C	0.66700	-0.15800	-2.45600
O	0.51200	2.43700	0.76400
C	0.91500	1.88900	2.01100
C	-1.82100	-0.45500	-2.44900
O	-2.10300	-1.65500	-1.67000
C	-3.10300	0.39600	-2.33500
C	-3.66700	-0.09900	-1.02600
C	-4.37000	-1.50400	1.22200
C	-3.03300	-1.30600	-0.73300
C	-4.65600	0.41500	-0.21100
C	-5.03100	-0.31100	0.93400
C	-3.35500	-2.02400	0.41400
O	-2.78500	-3.19300	0.80100
C	-4.06500	0.08500	-3.49100
O	-5.31600	0.71400	-3.33500
C	-1.42800	-3.41600	0.43100
C	-6.08400	0.14900	1.85400
C	-6.91000	1.18300	1.67800

Table AIII-2. Continued

Atoms	XYZ Coordinates		
C	-7.95900	1.57300	2.67400
O	-9.26000	1.56700	2.10400
H	5.12500	-4.17900	1.27200
H	6.84600	-2.39400	-1.23600
H	6.16700	-0.07400	-1.84300
H	3.06800	-0.21600	1.11100
H	2.81700	-1.35900	3.11700
H	2.19000	-3.02600	3.19700
H	1.76000	-1.98000	1.81600
H	4.24800	1.59500	-1.81700
H	6.18700	2.18400	-0.34100
H	5.27600	1.54100	1.86200
H	4.05600	2.83100	1.73000
H	5.91800	4.25500	1.49500
H	2.79900	0.04400	-2.36500
H	-1.52500	1.35800	-0.35300
H	0.71100	-0.83900	-3.29900
H	0.76500	2.66700	2.75700
H	1.97100	1.60600	1.99200
H	0.29800	1.01900	2.26100
H	-1.65100	-0.80300	-3.47000
H	-2.88400	1.46500	-2.32400
H	-4.62500	-2.06800	2.11300
H	-5.10800	1.37300	-0.44100
H	-4.17600	-1.00400	-3.58000
H	-3.64500	0.46200	-4.42600
H	-5.76000	0.31700	-2.57900
H	-0.83400	-2.51200	0.59300
H	-1.34500	-3.71200	-0.61400
H	-1.07300	-4.21700	1.07800
H	-6.18400	-0.43500	2.76800
H	-6.87300	1.78700	0.77500
H	-7.80200	2.59800	3.01600

Table AIII-2. Continued

Atoms	XYZ Coordinates		
H	-7.90700	0.91500	3.55000
H	-9.41600	0.69500	1.73100
4_side			
C	-2.31000	1.08400	-0.00600
C	0.22500	0.04400	0.01800
C	-2.18400	-0.28800	-0.02400
C	-1.25300	1.96300	0.01300
C	0.03400	1.43400	0.02300
C	-0.88300	-0.80200	-0.01600
C	1.56800	-0.56400	0.04100
C	2.70900	0.04200	0.37200
C	4.04000	-0.64700	0.35600
O	4.95400	-0.00900	-0.52400
O	-3.21900	-1.15700	-0.05000
C	-4.50800	-0.56900	-0.06000
H	-1.41200	3.03500	0.01100
H	0.88600	2.10300	0.01700
H	-0.76000	-1.88000	-0.02800
H	1.60300	-1.62100	-0.21800
H	2.72500	1.09000	0.65900
H	3.91200	-1.70500	0.09500
H	4.50900	-0.59800	1.34100
H	4.55400	0.01700	-1.39800
H	-5.21900	-1.39200	-0.08000
H	-4.66400	0.03600	0.83800
H	-4.64000	0.06000	-0.94500
β-5			
α-Ph			
Alpha_side			
C	-3.11100	1.32100	-0.54200
O	-3.05100	0.02800	-0.06600
C	-1.74500	1.93800	-0.59200
C	-0.88700	0.70700	-0.42100

Table AIII-2. Continued

Atoms	XYZ Coordinates		
C	0.15900	-1.76900	0.13400
C	-1.72800	-0.35000	-0.07700
C	0.48200	0.53800	-0.49900
C	1.02100	-0.72600	-0.20300
C	-1.22900	-1.61900	0.19900
O	-1.94800	-2.71100	0.54700
C	-1.52700	2.94100	0.56500
O	-0.21100	3.44400	0.60200
C	-3.32000	-2.76900	0.16800
C	2.46700	-0.99800	-0.24600
C	3.44700	-0.10000	-0.36600
C	4.89900	-0.46900	-0.39900
O	5.63200	0.17500	0.63400
H	-4.04200	1.82700	-0.32800
H	-1.54300	2.45700	-1.53400
H	0.55400	-2.75600	0.34900
H	1.11600	1.35400	-0.82300
H	-1.79600	2.45500	1.51100
H	-2.18500	3.80000	0.42300
H	0.37000	2.74400	0.91500
H	-3.43900	-2.50800	-0.88600
H	-3.92700	-2.10000	0.77700
H	-3.62400	-3.80100	0.33000
H	2.74200	-2.04900	-0.16400
H	3.23300	0.96400	-0.42400
H	5.36000	-0.13100	-1.33000
H	5.01100	-1.55800	-0.34400
H	5.22100	-0.04900	1.47300
Phenyl_side			
O	6.07000	-1.22800	-2.09300
C	4.88500	-0.77500	-1.61800
C	2.44400	0.14700	-0.63500
C	4.30400	-1.37200	-0.48800

Table AIII-2. Continued

Atoms	XYZ Coordinates		
C	4.23700	0.27200	-2.24900
C	3.01400	0.72900	-1.76000
C	3.09200	-0.91300	0.00300
O	5.03300	-2.40100	0.03300
C	4.51100	-3.06100	1.17100
C	1.13400	0.68200	-0.09700
C	1.32900	2.01500	0.63400
O	0.11000	2.54900	1.18700
C	2.27600	1.91600	1.82100
O	2.37300	3.15200	2.49300
O	0.51800	-0.22500	0.80900
C	-1.09300	2.16500	0.65600
C	-3.45100	1.08700	-0.40300
C	-1.38900	2.32800	-0.70000
C	-2.03200	1.57700	1.49500
C	-3.20200	1.05200	0.97400
C	-2.55000	1.77300	-1.22100
C	-4.56700	0.35700	-1.02500
C	-5.28300	-0.60600	-0.44300
C	-6.30000	-1.43900	-1.15900
O	-5.95000	-2.81600	-1.10600
O	-0.48700	2.92800	-1.54600
C	-0.29800	4.32100	-1.30000
C	-0.43400	-1.07000	0.30900
C	-2.48600	-2.65500	-0.53700
C	-0.54100	-1.41100	-1.03700
C	-1.35300	-1.58600	1.24300
C	-2.40400	-2.39100	0.80900
C	-1.59900	-2.21400	-1.48200
O	-1.27900	-1.24500	2.56200
C	-0.14800	-1.76500	3.25400
H	6.36100	-1.95500	-1.53000
H	4.69700	0.71200	-3.12500

Table AIII-2. Continued

Atoms	XYZ Coordinates		
H	2.50000	1.54000	-2.26700
H	2.62900	-1.36800	0.86900
H	4.41000	-2.36600	2.01000
H	5.22700	-3.83900	1.42600
H	3.54000	-3.51200	0.94700
H	0.46500	0.86100	-0.93900
H	1.72700	2.73400	-0.09200
H	3.27700	1.66000	1.47200
H	1.91900	1.12400	2.49200
H	1.47500	3.42300	2.71100
H	-1.78700	1.46800	2.54300
H	-3.89900	0.56300	1.64300
H	-2.71600	1.84900	-2.29100
H	-4.75800	0.58800	-2.07100
H	-5.08600	-0.89800	0.58600
H	-6.40500	-1.09700	-2.19500
H	-7.27800	-1.36900	-0.67800
H	-5.01900	-2.89500	-1.34100
H	0.42600	4.66800	-2.03400
H	-1.24200	4.85700	-1.43300
H	0.08300	4.49300	-0.29000
H	0.19300	-1.05300	-1.74900
H	-3.12100	-2.75700	1.53500
H	-1.69100	-2.46300	-2.53200
H	-0.25200	-1.44900	4.29100
H	0.78000	-1.36600	2.84000
H	-0.14400	-2.85700	3.20300
β-5			
O	-8.67400	0.49200	-2.23000
C	-7.46600	0.24900	-1.66600
C	-4.97800	-0.24000	-0.50800
C	-6.88600	1.19400	-0.80600
C	-6.79400	-0.92900	-1.94200

Table AIII-2. Continued

Atoms	XYZ Coordinates		
C	-5.55000	-1.17300	-1.36400
C	-5.64900	0.95200	-0.22800
O	-7.64200	2.31500	-0.62200
C	-7.13200	3.31400	0.24000
C	-3.64500	-0.54500	0.13700
C	-3.77100	-1.60600	1.23100
O	-2.48600	-1.95900	1.76900
C	-4.57300	-1.14600	2.43600
O	-4.62200	-2.15800	3.41900
O	-3.07000	0.61400	0.73300
C	-1.40900	-2.09600	0.93400
C	0.87800	-2.34300	-0.68500
C	-1.43500	-2.90500	-0.20700
C	-0.24200	-1.40300	1.24800
C	0.88500	-1.52100	0.44800
C	-0.30600	-3.00800	-1.00900
C	2.08100	-2.59100	-1.50000
C	3.34200	-2.47100	-1.08000
C	4.53600	-2.91300	-1.87600
O	5.63200	-2.02000	-1.78500
O	-2.58200	-3.56800	-0.57200
C	-2.89100	-4.67700	0.27000
C	-1.92500	1.12200	0.19300
C	0.53500	2.07300	-0.73000
C	-1.62200	1.06700	-1.16300
C	-1.01500	1.70600	1.08300
C	0.20100	2.18500	0.61600
C	-0.39100	1.52600	-1.61500
O	-1.25700	1.71300	2.42900
C	-2.32100	2.55900	2.84600
C	1.87700	2.52100	-1.26700
O	2.67800	3.16800	-0.23800
C	2.60300	1.40400	-1.95200

Table AIII-2. Continued

Atoms	XYZ Coordinates		
C	3.30000	1.18800	1.03100
C	5.91800	1.81600	0.78000
C	3.59300	2.37600	0.39500
C	4.20800	0.26900	1.47900
C	5.57100	0.55700	1.28300
C	4.95400	2.72400	0.33900
O	5.36500	3.86700	-0.27600
C	3.92100	1.60800	-2.62200
O	4.90000	0.66300	-2.18400
C	4.90400	5.07800	0.32400
C	6.62100	-0.46200	1.43800
C	6.39900	-1.77400	1.37500
C	7.47000	-2.81000	1.22700
O	7.27800	-3.52500	0.02000
H	-8.98000	1.35300	-1.92100
H	-7.25400	-1.64100	-2.61600
H	-5.01700	-2.09200	-1.59000
H	-5.18600	1.67400	0.43200
H	-6.99400	2.92000	1.25200
H	-7.87200	4.11000	0.25600
H	-6.18100	3.70300	-0.13500
H	-2.96900	-0.94000	-0.62500
H	-4.24800	-2.49000	0.79600
H	-5.60100	-0.94200	2.13300
H	-4.12500	-0.22800	2.83300
H	-3.71100	-2.37000	3.64700
H	-0.25700	-0.75100	2.11400
H	1.77200	-0.94900	0.69500
H	-0.36300	-3.64900	-1.88300
H	1.90100	-2.98500	-2.49900
H	3.55400	-2.11000	-0.07600
H	4.25100	-3.08600	-2.92000
H	4.90300	-3.86100	-1.46900

Table AIII-2. Continued

Atoms	XYZ Coordinates		
H	5.36100	-1.14500	-2.10400
H	-3.81900	-5.10400	-0.10600
H	-2.09300	-5.42300	0.21700
H	-3.02500	-4.35700	1.30800
H	-2.33800	0.65300	-1.86200
H	0.89200	2.61500	1.33100
H	-0.15100	1.45200	-2.67000
H	-2.37800	2.46900	3.93000
H	-3.26800	2.24600	2.40100
H	-2.10600	3.59700	2.57500
H	1.71600	3.34200	-1.97700
H	2.21500	0.39400	-1.87800
H	6.95900	2.08400	0.63700
H	3.89500	-0.65900	1.94600
H	4.28600	2.62900	-2.46200
H	3.83600	1.44800	-3.70200
H	5.13400	0.87100	-1.27100
H	5.26400	5.14400	1.35400
H	3.81500	5.13400	0.30200
H	5.33100	5.88700	-0.26500
H	7.64500	-0.09700	1.46400
H	5.38500	-2.15700	1.28200
H	7.42600	-3.54600	2.03300
H	8.45800	-2.33300	1.25700
H	6.99400	-2.89900	-0.66400
α-O			
O	-7.58800	3.60200	-0.81700
C	-6.68000	2.61700	-0.61300
C	-4.80100	0.60000	-0.19200
C	-5.67800	2.77200	0.35900
C	-6.72600	1.46000	-1.37000
C	-5.78400	0.45400	-1.16200
C	-4.74600	1.76900	0.57100

Table AIII-2. Continued

Atoms	XYZ Coordinates		
O	-5.73100	3.96100	1.02600
C	-4.74900	4.19700	2.01700
C	-3.80600	-0.51700	0.04700
C	-4.45400	-1.67600	0.80900
O	-3.56600	-2.77200	1.09900
C	-5.00600	-1.26400	2.16800
O	-5.54300	-2.37300	2.85300
O	-2.67000	-0.06800	0.78100
C	-2.37500	-2.92000	0.43800
C	0.12700	-3.09300	-0.82100
C	-2.29600	-3.03000	-0.95300
C	-1.20900	-2.97800	1.19300
C	0.02400	-3.06800	0.57500
C	-1.05100	-3.08100	-1.57100
C	1.43400	-3.09000	-1.50300
C	2.60400	-3.41200	-0.94900
C	3.91900	-3.37500	-1.66700
O	4.85800	-2.61500	-0.91300
O	-3.43800	-3.01500	-1.71900
C	-4.23200	-4.19200	-1.58200
C	-1.57000	0.26100	0.03600
C	0.78500	0.60400	-1.48400
C	-1.64200	0.71000	-1.28600
C	-0.30900	0.10100	0.63900
C	0.83900	0.24100	-0.11400
C	-0.49000	0.88700	-2.02600
O	-0.20100	-0.27200	1.95200
C	-0.69300	0.68800	2.87800
C	1.93500	0.67400	-2.30400
O	3.67900	3.01000	-2.18200
C	3.28900	0.20000	-1.87900
C	3.98000	1.07800	-0.85500
C	5.26200	2.71400	1.05200

Table AIII-2. Continued

Atoms	XYZ Coordinates		
C	4.07100	2.51400	-1.11400
C	4.55200	0.53000	0.25300
C	5.22500	1.33100	1.22400
C	4.68900	3.32300	-0.05600
O	4.79600	4.65000	-0.12000
C	4.18800	0.01000	-3.11000
O	5.45400	-0.55100	-2.77500
C	4.01800	5.44200	-1.02400
C	5.86100	0.74100	2.39400
C	5.99600	-0.56900	2.64700
C	6.66200	-1.09500	3.88200
O	7.70300	-2.00800	3.57600
H	-7.39200	4.32200	-0.20500
H	-7.49900	1.36600	-2.12300
H	-5.81400	-0.44500	-1.76900
H	-3.96500	1.87600	1.31300
H	-4.81600	3.45100	2.81500
H	-4.95700	5.18500	2.42200
H	-3.74600	4.18100	1.58200
H	-3.47700	-0.90000	-0.91900
H	-5.27000	-2.05900	0.18400
H	-5.81600	-0.54600	2.03500
H	-4.20000	-0.79100	2.74400
H	-4.86200	-3.05400	2.85800
H	-1.29000	-2.87100	2.26700
H	0.91800	-3.03300	1.18500
H	-1.02200	-3.10900	-2.65500
H	1.41500	-2.78800	-2.55000
H	2.65700	-3.73300	0.08800
H	3.78600	-2.94700	-2.66800
H	4.30700	-4.39300	-1.79000
H	5.27000	-1.98200	-1.51800
H	-5.09800	-4.05800	-2.22800

Table AIII-2. Continued

	Atoms	XYZ Coordinates		
	H	-3.66500	-5.06900	-1.90600
	H	-4.55600	-4.32600	-0.54700
	H	-2.60800	0.90500	-1.73600
	H	1.78500	0.04800	0.37900
	H	-0.56300	1.21600	-3.05700
	H	-0.49900	0.28600	3.87100
	H	-1.76600	0.84400	2.74900
	H	-0.16100	1.63700	2.75900
	H	1.82300	1.07000	-3.30800
	H	3.17300	-0.78100	-1.40400
	H	5.74400	3.35000	1.78600
	H	4.48100	-0.54500	0.39200
	H	4.31300	0.96400	-3.63000
	H	3.71600	-0.70000	-3.79300
	H	5.96700	0.11900	-2.31100
	H	2.97200	5.13400	-1.00500
	H	4.39700	5.35800	-2.04000
	H	4.12200	6.46000	-0.65500
	H	6.26500	1.45000	3.11500
	H	5.64100	-1.32300	1.94800
	H	5.94600	-1.66400	4.48000
	H	7.02800	-0.26400	4.49700
	H	8.32400	-1.57200	2.98700
α-β				
	O	8.08300	-1.78900	-1.62100
	C	6.94700	-1.22500	-1.14700
	C	4.60100	-0.07600	-0.17400
	C	6.03000	-1.99600	-0.41400
	C	6.67900	0.11000	-1.39000
	C	5.50400	0.68400	-0.90600
	C	4.86500	-1.42600	0.07300
	O	6.40300	-3.29900	-0.25400
	C	5.52700	-4.14600	0.46500

Table AIII-2. Continued

Atoms	XYZ Coordinates		
C	3.35100	0.57400	0.37400
C	3.65100	1.47200	1.57500
O	2.45000	2.06700	2.08900
C	4.24600	0.72800	2.75900
O	4.42900	1.59900	3.85400
O	2.39100	-0.37600	0.82000
C	1.49700	2.49800	1.20000
C	-0.51000	3.34100	-0.57000
C	1.78400	3.44600	0.21300
C	0.21700	1.96200	1.28400
C	-0.77700	2.37700	0.40900
C	0.78900	3.84800	-0.66700
C	-1.55200	3.86500	-1.47000
C	-2.85200	3.93700	-1.18300
C	-3.88400	4.53400	-2.09400
O	-4.93400	3.62900	-2.37300
O	3.05500	3.94300	0.06100
C	3.47000	4.81100	1.11500
C	1.44000	-0.78700	-0.06200
C	-0.69200	-1.60800	-1.73700
C	1.58400	-0.75200	-1.45000
C	0.23600	-1.26200	0.48900
C	-0.80700	-1.65500	-0.32000
C	0.54300	-1.14900	-2.26600
O	0.05900	-1.27900	1.84700
C	0.83800	-2.25400	2.53000
C	-1.66500	-2.00200	-2.67900
O	-2.93500	-2.45300	-2.46800
C	-3.70000	0.34400	-1.80600
C	-3.93100	-0.78800	-0.98100
C	-4.61900	-2.92800	0.72600
C	-3.61100	-2.13000	-1.31300
C	-4.53700	-0.57400	0.28200

Table AIII-2. Continued

Atoms	XYZ Coordinates		
C	-4.89400	-1.61400	1.12700
C	-3.98400	-3.18300	-0.48300
O	-3.72800	-4.47600	-0.84300
C	-3.36200	0.41300	-3.26000
O	-4.20900	1.36200	-3.92000
C	-2.37400	-4.87800	-0.66300
C	-5.56000	-1.38900	2.42200
C	-6.20700	-0.28400	2.79700
C	-6.85600	-0.12600	4.13800
O	-8.23500	0.19000	4.02600
H	8.09200	-2.71700	-1.35600
H	7.39400	0.68500	-1.96500
H	5.29000	1.72800	-1.10900
H	4.14700	-2.00900	0.63600
H	5.39700	-3.78900	1.49000
H	5.99300	-5.12800	0.47600
H	4.55300	-4.20600	-0.03000
H	2.90000	1.19600	-0.40600
H	4.34400	2.25500	1.25000
H	5.22900	0.33900	2.49000
H	3.58900	-0.10900	3.02200
H	3.57100	1.99400	4.04300
H	0.03600	1.18400	2.01700
H	-1.76000	1.92200	0.46700
H	1.04300	4.58400	-1.42200
H	-1.20300	4.27600	-2.41600
H	-3.22300	3.57100	-0.22700
H	-3.40600	4.89100	-3.01500
H	-4.35000	5.39500	-1.60700
H	-4.59000	2.93300	-2.95100
H	4.47200	5.15000	0.85800
H	2.79600	5.66900	1.18200
H	3.49200	4.28400	2.07300

Table AIII-2. Continued

Atoms	XYZ Coordinates		
H	2.51600	-0.41800	-1.89100
H	-1.70500	-1.98900	0.18100
H	0.67200	-1.11400	-3.34100
H	0.58300	-2.16900	3.58400
H	1.90600	-2.06700	2.39400
H	0.58500	-3.25700	2.17100
H	-1.41700	-2.03800	-3.73100
H	-3.91500	1.31100	-1.36100
H	-4.89100	-3.77300	1.35000
H	-4.73600	0.45200	0.57200
H	-3.44300	-0.55500	-3.75500
H	-2.34400	0.78900	-3.40400
H	-5.09500	0.99000	-3.96900
H	-2.07400	-4.74700	0.38200
H	-1.70000	-4.31200	-1.31000
H	-2.33000	-5.93300	-0.92600
H	-5.51700	-2.22500	3.11900
H	-6.31600	0.55900	2.11900
H	-6.41200	0.71200	4.68000
H	-6.70300	-1.03200	4.73700
H	-8.65500	-0.49100	3.49500
O-4			
O	-8.36500	1.45600	-1.57800
C	-7.18400	0.93200	-1.17400
C	-4.74700	-0.13500	-0.34200
C	-6.36800	1.64100	-0.27700
C	-6.77000	-0.30000	-1.65000
C	-5.55000	-0.83100	-1.23700
C	-5.15700	1.11000	0.13900
O	-6.88100	2.84500	0.10700
C	-6.11500	3.62500	1.00500
C	-3.44500	-0.74800	0.12000
C	-3.66400	-1.87600	1.13000

Table AIII-2. Continued

Atoms	XYZ Coordinates		
O	-2.42000	-2.44900	1.56900
C	-4.34700	-1.42000	2.41000
O	-4.46100	-2.48800	3.32400
O	-2.59200	0.20300	0.74700
C	-1.35800	-2.49800	0.70200
C	0.84200	-2.50000	-1.03800
C	-1.45600	-3.09800	-0.55800
C	-0.15600	-1.91700	1.09000
C	0.93500	-1.92100	0.23300
C	-0.37200	-3.07200	-1.42400
C	1.99500	-2.53500	-1.95800
C	3.26400	-2.66200	-1.57000
C	4.44800	-2.70900	-2.49300
O	5.43200	-1.75600	-2.13000
O	-2.64400	-3.64600	-0.97900
C	-2.99500	-4.85200	-0.30100
C	-1.60300	0.76600	0.00500
C	0.59700	1.82600	-1.35300
C	-1.60700	0.83200	-1.38400
C	-0.51300	1.29000	0.72100
C	0.57200	1.81700	0.04500
C	-0.50800	1.36100	-2.05500
O	-0.47300	1.20400	2.08500
C	-1.40100	2.04300	2.76300
C	1.81500	2.33300	-2.12600
O	1.95700	3.64400	-1.73300
C	3.08200	1.48100	-1.90900
C	3.67500	1.59100	-0.52600
C	4.79700	1.78200	2.04600
C	3.88700	2.80100	0.10300
C	4.09500	0.44900	0.15400
C	4.67100	0.53800	1.43100
C	4.40200	2.94600	1.37400

Table AIII-2. Continued

Atoms	XYZ Coordinates		
O	4.54600	4.13400	2.00200
C	4.13900	1.86000	-2.95300
O	5.28900	1.03700	-2.85600
C	4.09000	5.26400	1.27400
C	5.14000	-0.67500	2.12500
C	5.53400	-1.79600	1.51500
C	5.98000	-3.01700	2.26000
O	7.26500	-3.45700	1.85000
H	-8.47800	2.31100	-1.14500
H	-7.40900	-0.82500	-2.34800
H	-5.21900	-1.79100	-1.62200
H	-4.51700	1.64700	0.82600
H	-5.96800	3.09500	1.95100
H	-6.68500	4.53400	1.18100
H	-5.14400	3.87800	0.56900
H	-2.93500	-1.17700	-0.74400
H	-4.27100	-2.64900	0.64800
H	-5.35900	-1.08200	2.18200
H	-3.77800	-0.58700	2.83900
H	-3.57300	-2.83400	3.46300
H	-0.11800	-1.41000	2.04700
H	1.85300	-1.42900	0.53800
H	-0.48900	-3.52700	-2.40100
H	1.76700	-2.49100	-3.02300
H	3.49300	-2.76000	-0.51000
H	4.12300	-2.57900	-3.53200
H	4.93200	-3.68600	-2.41600
H	5.21500	-0.89200	-2.51000
H	-3.94600	-5.17600	-0.71800
H	-2.23400	-5.61700	-0.47800
H	-3.10000	-4.68100	0.77400
H	-2.46000	0.47500	-1.94600
H	1.40200	2.19200	0.63100

Table AIII-2. Continued

Atoms	XYZ Coordinates		
H	-0.51700	1.39800	-3.13800
H	-1.23300	1.89100	3.82700
H	-2.42900	1.77200	2.51200
H	-1.21800	3.09200	2.50900
H	1.54500	2.28900	-3.19200
H	2.80100	0.43400	-2.08000
H	5.21400	1.87600	3.04200
H	3.96500	-0.51800	-0.31300
H	4.40800	2.91800	-2.84000
H	3.74400	1.71000	-3.96000
H	5.73300	1.23500	-2.02200
H	3.02800	5.16600	1.03200
H	4.65500	5.37800	0.34400
H	4.25200	6.12500	1.91700
H	5.17400	-0.62400	3.21200
H	5.57500	-1.85300	0.42700
H	5.30900	-3.85500	2.05000
H	5.95100	-2.82900	3.34100
H	7.86400	-2.70700	1.88900

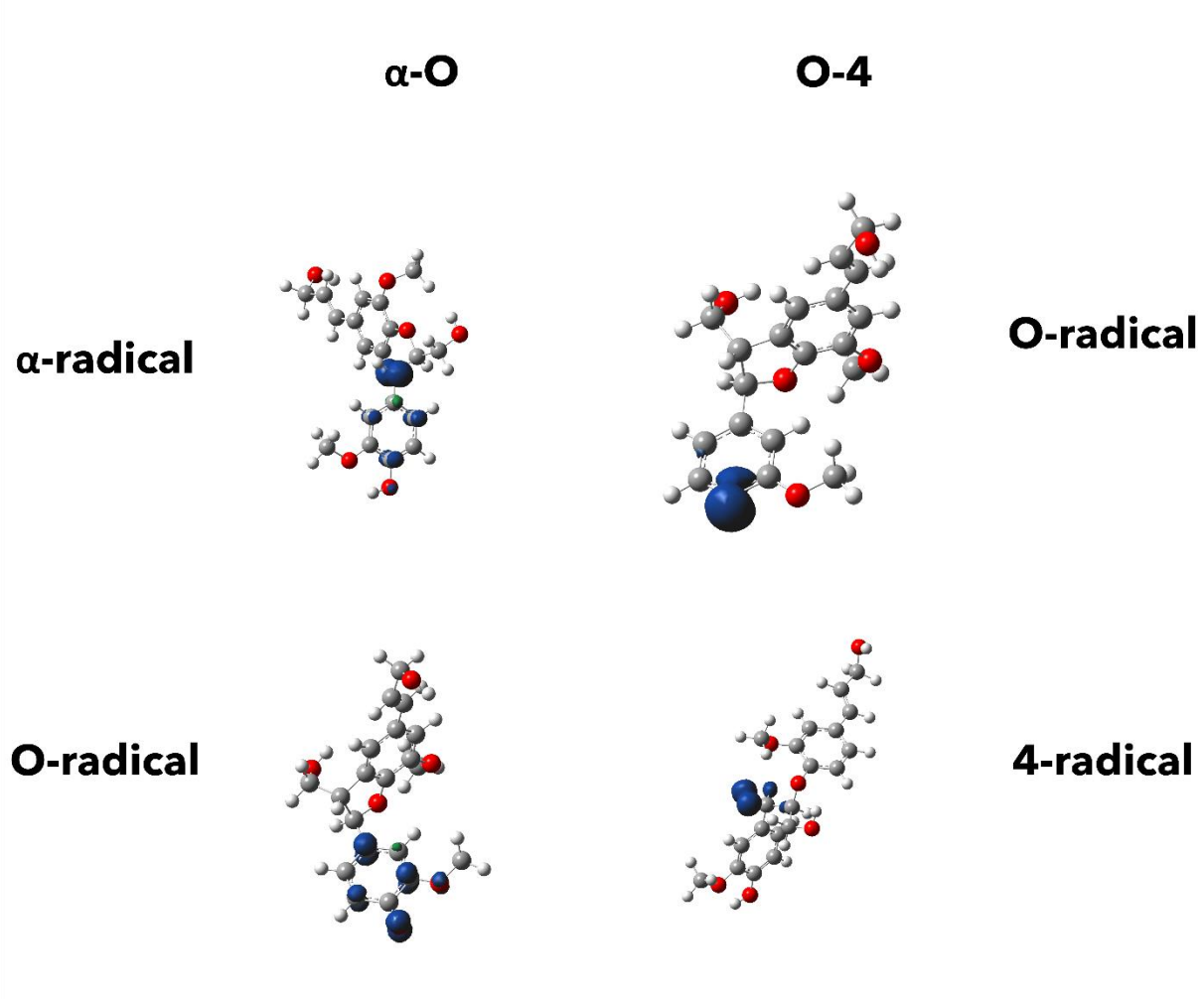

Figure AIII-1 Spin density plot for the α-O-4 bond scission products of the RSRS stereoisomer of MC1.

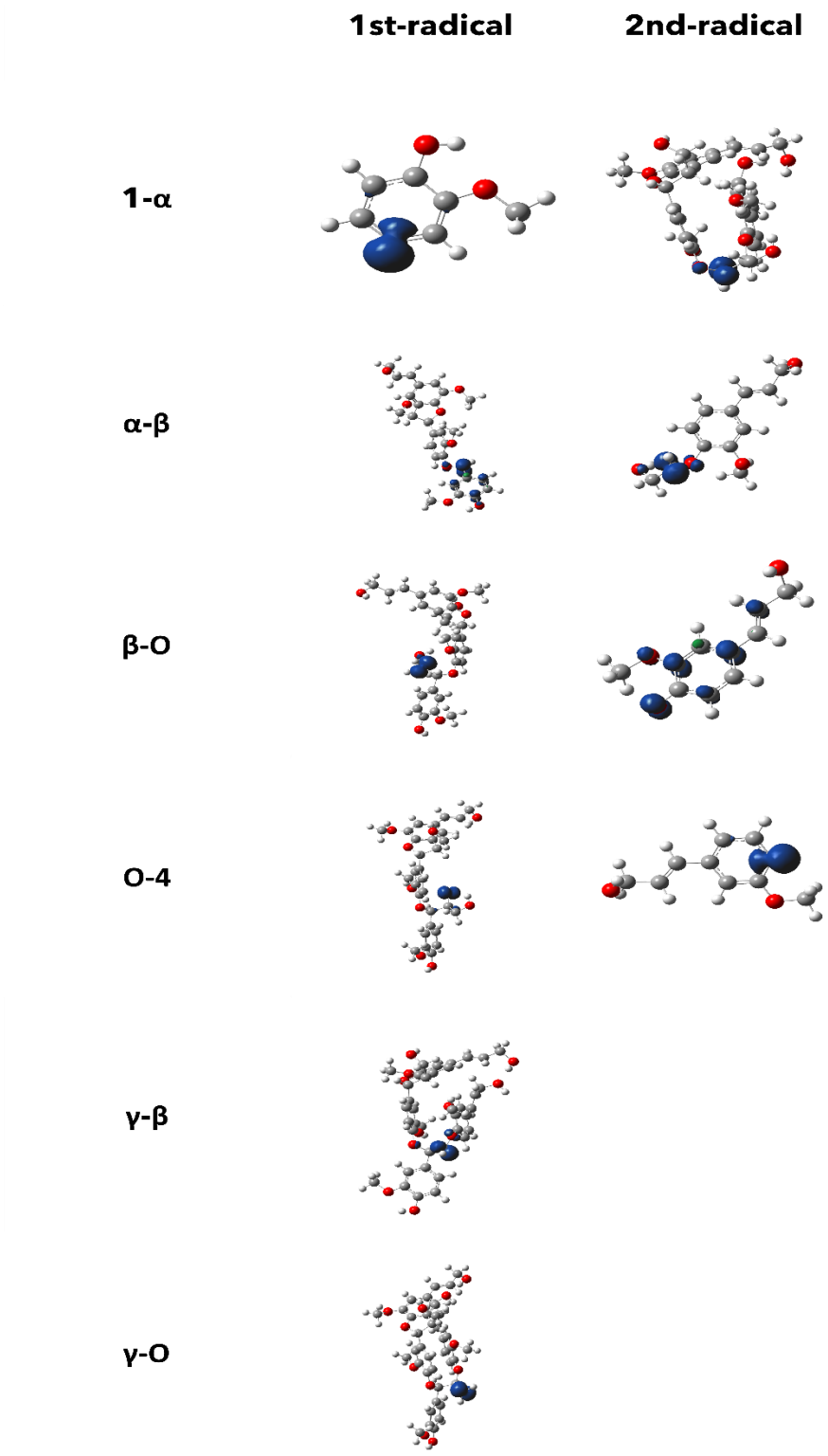

Figure AIII-2. Spin density plot for the β-O-4 bond scission products of the RSRS stereoisomer of MC1.

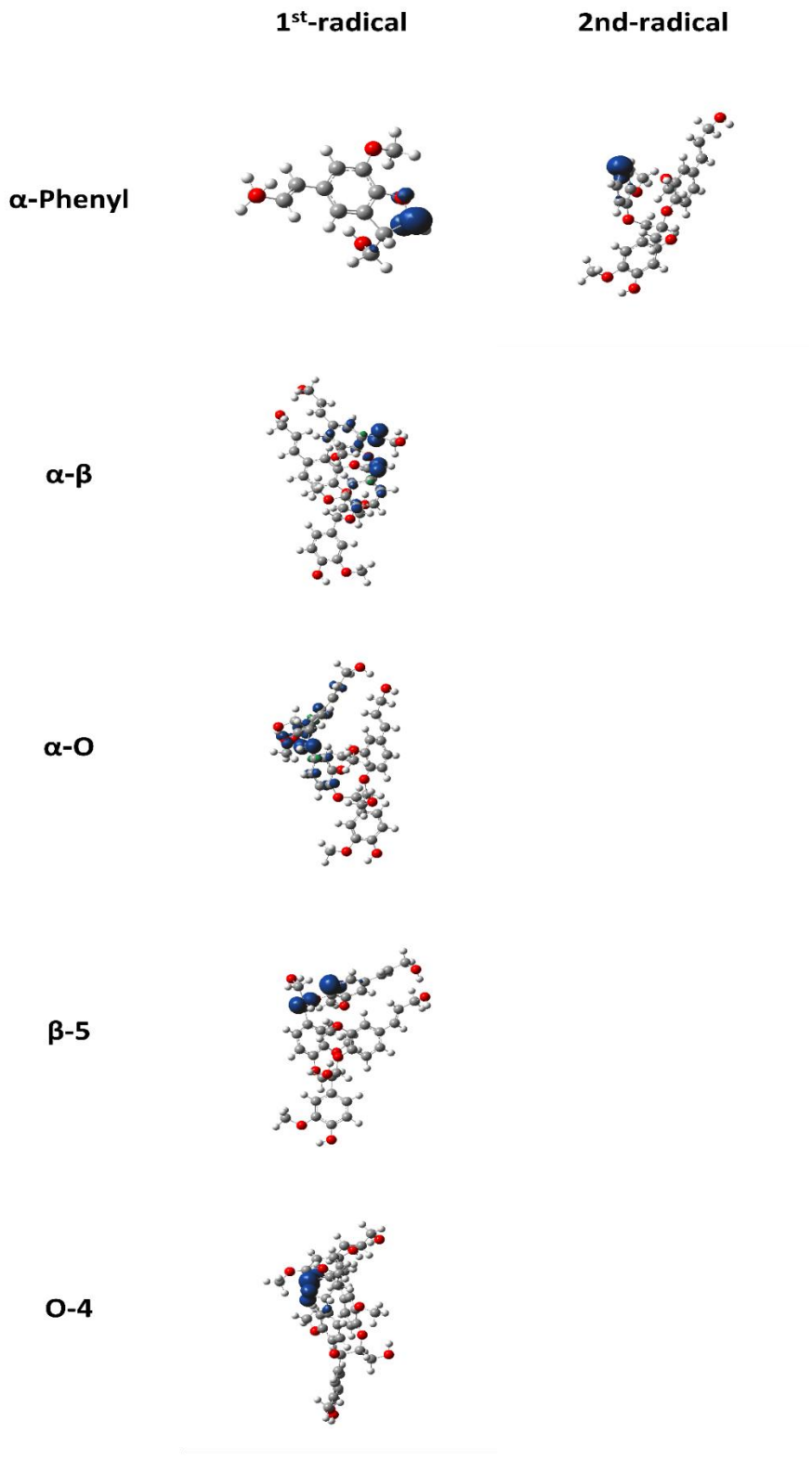

Figure AIII-3. Spin density plot for the β-5 bond scission products of the RSRS stereoisomer of MC1.

Table AIII-3. Optimized geometries of the initial stereoisomers of MC2.

RRRSSRRR

Atoms	XYZ Coordinates	
O	1.81714707	4.75311763	-0.83164502
C	2.86768026	4.16621231	-0.19099402
C	5.13923862	3.23738791	1.09943302
C	3.96153308	5.02610689	0.01132056
C	2.91855949	2.85208212	0.24506845
C	4.06888201	2.38097281	0.88932897
C	5.08959316	4.55990981	0.65900090
H	6.02742481	2.87639841	1.60675288
H	2.07646289	2.18227214	0.10996788
H	5.91576147	5.24183334	0.81710906
C	0.63722544	3.98078479	-0.96768191
H	-0.08829029	4.60638873	-1.48416352
H	0.25364721	3.69799059	0.01636398
H	0.82160484	3.07640180	-1.55421387
O	3.90027738	6.30961942	-0.41958165
H	3.03773421	6.44318545	-0.83112714
C	4.14693337	0.92823331	1.28373870
H	4.98542268	0.79290542	1.98065069
C	4.42001620	0.04009411	0.06004220
H	3.57654267	0.10209820	-0.63756878
C	5.72711598	0.39066358	-0.63404214
H	5.70262269	1.43698305	-0.93965458
H	6.54186447	0.26538051	0.09460078
O	5.96391264	-0.38001978	-1.78668221
H	5.59540852	-1.25815709	-1.63809541
O	4.55735491	-1.33404827	0.51272878
C	3.48449406	-2.16729491	0.38645025
C	1.29479930	-3.90339947	0.15959529
C	3.08588004	-2.65096183	-0.86945143

Table AIII-3. Continued

Atoms	XYZ Coordinates	
C	2.81060435	-2.62220479	1.51777429
C	1.72631029	-3.48286759	1.41180416
C	1.99147705	-3.50770413	-0.98074654
H	1.21917004	-3.78531942	2.32183330
H	1.67411165	-3.88081057	-1.94497233
O	3.82523826	-2.21554997	-1.91389587
O	3.16772907	-2.14410187	2.75730034
C	3.37017004	-2.49351197	-3.23186913
H	4.06042101	-1.97335857	-3.89201140
H	2.35749767	-2.10815750	-3.37363428
H	3.40226547	-3.56739541	-3.43345011
C	4.39949749	-2.67610592	3.25856467
H	4.56169051	-2.21137987	4.22908269
H	4.31082900	-3.75880643	3.37654641
H	5.22078775	-2.43524154	2.58187862
C	0.04893148	-4.76577052	0.04068534
C	-1.17871821	-4.04640922	0.60365263
C	-1.70054484	-3.23912436	-0.59787008
C	-1.11295668	-3.98647937	-1.81096645
O	-0.29363704	-5.04545089	-1.30339752
H	0.22233563	-5.72978705	0.52932576
H	-0.94963918	-3.40867175	1.45812101
H	-1.35054642	-2.20824190	-0.57894522
H	-0.51257103	-3.30815150	-2.42443400
H	-1.87821009	-4.44738017	-2.43896502
C	-3.24538100	-3.28807396	-0.43203379
O	-3.50436982	-4.12850352	0.68501508
C	-2.37216267	-4.95216975	0.89825439
H	-3.70740560	-3.72486254	-1.32657650
H	-2.37707693	-5.80711784	0.20811329

Table AIII-3. Continued

Atoms	XYZ Coordinates	
H	-2.41234674	-5.31874915	1.92417853
C	-3.81295239	-1.90950071	-0.19692880
C	-4.54846550	0.73991471	0.18426744
C	-4.07991282	-1.10515663	-1.30121889
C	-3.94845932	-1.41976932	1.09680187
C	-4.32916323	-0.09076322	1.28422710
C	-4.45072621	0.22373045	-1.10863943
H	-3.97229825	-1.51379302	-2.29797790
H	-3.76881595	-2.08467486	1.92980266
O	-4.71463624	1.10406439	-2.10914541
O	-4.48732098	0.50520499	2.49376968
C	-4.32587071	-0.29682126	3.64826536
H	-4.52447298	0.35637726	4.49462685
H	-3.30563043	-0.68668142	3.71829339
H	-5.03430207	-1.12973548	3.64830699
C	-4.56867903	0.64269092	-3.44046166
H	-4.78843448	1.49550194	-4.07941202
H	-5.27698419	-0.16335199	-3.65096538
H	-3.54598235	0.29969657	-3.62180851
O	-4.87582478	2.05727694	0.35797114
O	2.93044791	0.55886419	1.90456866
H	3.05094250	-0.30197112	2.32948677
C	-3.80973220	2.91068151	0.81474949
H	-3.27226744	2.40491151	1.62050779
C	-4.51563458	4.11995954	1.39959190
H	-3.77585034	4.84361387	1.74820848
H	-5.12447022	4.59036046	0.62006577
O	-5.29482955	3.74918030	2.51564959
H	-5.77938107	2.95414060	2.26639622
C	-2.87331588	3.27262682	-0.34714223

Table AIII-3. Continued

Atoms	XYZ Coordinates	
H	-2.24408767	4.10065188	0.00383891
O	-3.62049821	3.78956968	-1.42299373
H	-4.27085091	3.11012584	-1.65680943
C	-1.94976483	2.13373121	-0.78548754
C	-0.22684968	0.08637128	-1.62060595
C	-1.29700627	1.32809834	0.15969933
C	-1.70978111	1.91184775	-2.13417224
C	-0.85310930	0.89059749	-2.55309495
C	-0.45121863	0.30968128	-0.25016362
H	-1.45510250	1.48800421	1.21846401
H	-2.19544717	2.54439516	-2.86646000
H	-0.65814096	0.71493844	-3.60472356
O	0.20649840	-0.56044083	0.56477797
O	0.59786986	-0.92166336	-2.00886267
H	0.94219893	-1.35855026	-1.21403367
C	0.04649179	-0.38709149	1.96271707
H	0.64926765	-1.16008192	2.43492899
H	0.41676449	0.59305075	2.27183190
H	-1.00721528	-0.51132135	2.23732622
RRRSSRSS			
O	-0.10291281	-2.86870208	0.12065349
C	-1.29568747	-2.40743016	-0.36426268
C	-3.56794313	-1.38537694	-1.57601710
C	-1.17217295	-1.52460969	-1.44404166
C	-2.54958524	-2.74168144	0.12487766
C	-3.70214410	-2.22237786	-0.47267884
C	-2.30991984	-1.02369305	-2.04907380
H	-4.43835782	-0.97110202	-2.06938690
H	-2.65936859	-3.40208563	0.97505549
H	-2.19873986	-0.34874834	-2.88979883

Table AIII-3. Continued

Atoms	XYZ Coordinates	
C	-0.13467659	-3.71758015	1.25322982
H	-0.67389608	-4.64203264	1.03009812
H	0.90260698	-3.94265622	1.49246611
H	-0.60242949	-3.21500861	2.10484728
O	0.05580544	-1.16819636	-1.91432718
H	0.73542085	-1.48065908	-1.30174109
C	-5.06417601	-2.60717885	0.10972085
H	-5.46133517	-3.44610237	-0.47340703
C	-6.10328871	-1.48118592	0.04478244
H	-6.14043675	-1.02466484	-0.94618361
C	-7.50046937	-1.95252235	0.40360421
H	-7.80340922	-2.75111537	-0.27678701
H	-7.49413126	-2.34699250	1.42529100
O	-8.43318142	-0.90387663	0.25752888
H	-8.04455571	-0.12628219	0.67359677
O	-5.80894763	-0.46465645	1.02169998
C	-4.79316777	0.40468098	0.72453356
C	-2.70124215	2.14945295	0.14845231
C	-4.94409615	1.37844682	-0.26325631
C	-3.59523774	0.32301523	1.43575794
C	-2.54573237	1.19314833	1.15101416
C	-3.89454590	2.24821964	-0.55918243
H	-1.62528877	1.15032817	1.71876756
H	-3.99081119	3.01863883	-1.31183561
O	-6.14740728	1.37582105	-0.89394560
O	-3.54008871	-0.65824764	2.37781455
C	-6.36444383	2.35021167	-1.89661148
H	-7.37548898	2.18308344	-2.26051930
H	-5.65277859	2.23252395	-2.71950748
H	-6.28224429	3.36052183	-1.48636205

Table AIII-3. Continued

Atoms	XYZ Coordinates	
C	-2.31159414	-0.82965754	3.06120281
H	-2.45276034	-1.68116991	3.72461988
H	-1.50131076	-1.03764809	2.35549250
H	-2.05749863	0.05765201	3.64654931
C	-1.59803076	3.16957031	-0.09299297
C	-0.19287713	2.56866338	-0.21288964
C	-0.03624317	2.30063578	-1.72813703
C	-1.18372781	3.12113139	-2.35012604
O	-1.77124284	3.88590200	-1.30260650
H	-1.64460438	3.90939598	0.71177345
H	-0.06770663	1.66826427	0.38016186
H	-0.12375645	1.24179111	-1.96810442
H	-1.93551962	2.45246975	-2.78671088
H	-0.84486921	3.82527583	-3.11158192
C	1.36920290	2.84787961	-2.03287345
O	1.51838315	3.94387851	-1.15018547
C	0.91828017	3.58985222	0.09272075
H	1.43836940	3.24833750	-3.04841329
H	0.53791621	4.51088280	0.53679789
H	1.66432493	3.14781051	0.76457796
C	2.46041786	1.80397911	-1.83126147
C	4.40054008	-0.14037123	-1.38747490
C	2.41101033	0.60530511	-2.54013424
C	3.50515813	2.05985131	-0.95008862
C	4.47237533	1.08281341	-0.72554456
C	3.38857223	-0.36319743	-2.32542048
H	1.60078912	0.41709645	-3.23199102
H	3.54711837	3.01998378	-0.45717876
O	3.43312167	-1.57285566	-2.94258419
O	5.51431497	1.22120876	0.14148543

Table AIII-3. Continued

Atoms	XYZ Coordinates		
C	5.58014806	2.42398697	0.88382444
H	6.43419590	2.31902539	1.55112795
H	5.73610336	3.28226838	0.22468212
H	4.66534688	2.57173114	1.46779859
C	2.57535997	-1.77838169	-4.05610688
H	2.83591884	-2.75785627	-4.45056320
H	1.52580614	-1.76861611	-3.75408149
H	2.75079289	-1.01430636	-4.81897250
O	5.34241242	-1.10215589	-1.13630078
O	-4.95198192	-3.08141758	1.43387217
H	-4.72161510	-2.31397221	1.97968062
C	4.89460223	-2.24267469	-0.38142004
H	3.90952630	-2.54554928	-0.74479500
C	5.88701180	-3.33832329	-0.72326466
H	5.64731901	-4.24088391	-0.15682263
H	6.89359742	-3.00773201	-0.44444599
O	5.80926609	-3.67021419	-2.09179690
H	5.74229812	-2.84048203	-2.57837808
C	4.86472248	-1.90967186	1.11748922
H	4.78688043	-2.86057988	1.65733254
O	6.09610291	-1.34693635	1.50781913
H	6.24725742	-0.58816798	0.92374921
C	3.67735041	-1.03628914	1.53107071
C	1.53788198	0.57768518	2.34632611
C	3.87986192	-0.01508512	2.46342821
C	2.39425863	-1.24782480	1.03665307
C	1.32833380	-0.44089085	1.43363445
C	2.82282082	0.78812419	2.86241848
H	4.87605375	0.13624289	2.85778648
H	2.19706921	-2.05213309	0.33767204

Table AIII-3. Continued

Atoms	XYZ Coordinates	
H	0.32958479	-0.60098921	1.04001228
O	2.90297373	1.82164355	3.75553036
O	0.50016539	1.35990382	2.75948932
H	0.84319803	1.99025644	3.40594989
C	4.09752047	1.94246884	4.50854079
H	4.94352914	2.19777378	3.86492607
H	4.31291007	1.01196729	5.04052766
H	3.92815024	2.74671349	5.22051747
SSRSSRRR			
O	-1.29097099	-4.42193784	1.11766354
C	-2.31623324	-3.96672278	0.34474984
C	-4.42257771	-3.30851227	-1.33137756
C	-2.90251294	-4.95559631	-0.46440718
C	-2.77894233	-2.66188803	0.30072222
C	-3.84872168	-2.32255615	-0.53974890
C	-3.95107336	-4.62090007	-1.30100220
H	-5.25121095	-3.05480846	-1.98308417
H	-2.29737692	-1.90910302	0.91157653
H	-4.39383485	-5.39668463	-1.91336210
C	-0.76927057	-3.53866353	2.09913127
H	-1.55815242	-3.24023025	2.79658900
H	-0.32432306	-2.65660648	1.63533329
H	-0.00005697	-4.09732184	2.62781269
O	-2.43255190	-6.22516152	-0.42699171
H	-1.71594365	-6.25819355	0.21914405
C	-4.36945221	-0.90486727	-0.61434672
H	-5.38860981	-0.93209520	-1.02083290
C	-4.42814133	-0.22564709	0.75834204
H	-3.45384483	-0.27546786	1.24871042
C	-5.49563152	-0.84144750	1.64574304

Table AIII-3. Continued

Atoms	XYZ Coordinates	
H	-5.38004354	-1.92705576	1.65915276
H	-6.47513252	-0.60275135	1.20910445
O	-5.41395782	-0.39213320	2.97820618
H	-5.16586945	0.53953377	2.95293848
O	-4.78073350	1.16616079	0.59711668
C	-3.74268346	2.05880745	0.57920163
C	-1.57502718	3.81329407	0.50055875
C	-2.96067049	2.27429411	1.72042433
C	-3.47034336	2.79544199	-0.57146359
C	-2.39439483	3.68131695	-0.60982087
C	-1.86649762	3.12891613	1.67831666
H	-2.18110300	4.26627454	-1.49195047
H	-1.23905603	3.26639671	2.55089972
O	-3.35015999	1.57662149	2.81951726
O	-4.28252543	2.54291948	-1.64129568
C	-2.48890158	1.55644248	3.94205271
H	-1.49748835	1.18911542	3.66054828
H	-2.40279631	2.55030354	4.39002266
H	-2.94530877	0.87165069	4.65368278
C	-4.07441891	3.30526562	-2.81891943
H	-3.08309898	3.11380185	-3.24002426
H	-4.18970692	4.37225493	-2.61397701
H	-4.83926931	2.98316985	-3.52165924
C	-0.32247777	4.66679669	0.43207144
C	0.94662050	3.80349821	0.43346851
C	1.14031523	3.47365689	-1.05674731
C	0.46985831	4.66987570	-1.75853321
O	-0.23801384	5.41524462	-0.76694621
H	-0.32542466	5.38510279	1.25761112
H	0.83490865	2.90496824	1.03823665

Table AIII-3. Continued

Atoms	XYZ Coordinates	
H	0.68025141	2.52250738	-1.32625473
H	-0.22112062	4.33758022	-2.53948139
H	1.20773296	5.34168957	-2.20329047
C	2.66448136	3.47759702	-1.21867125
O	3.10611101	4.49547138	-0.33789567
C	2.22827048	4.58156125	0.78441230
H	2.95693177	3.78906150	-2.22637404
H	2.02870532	5.64117410	0.95990931
H	2.71581157	4.16094642	1.66989845
C	3.30161936	2.12997273	-0.93018197
C	4.47397660	-0.34685944	-0.46366294
C	4.18351566	1.98024408	0.13199129
C	3.02094336	1.06113980	-1.78117326
C	3.62360471	-0.17345077	-1.55905086
C	4.77086309	0.73478902	0.36277837
H	4.42868620	2.84105301	0.73763881
H	2.34450872	1.20398111	-2.61465327
O	5.63955122	0.46271371	1.37153223
O	3.44371718	-1.27358019	-2.33488955
C	2.55395614	-1.16045888	-3.43070655
H	2.52579893	-2.14434745	-3.89562834
H	2.92204068	-0.42759612	-4.15451722
H	1.55007044	-0.88119368	-3.09537488
C	5.98029988	1.51813353	2.25004118
H	6.47085777	2.33399930	1.71194787
H	6.66845864	1.09085591	2.97566031
H	5.09392707	1.90097265	2.76508610
O	5.03541921	-1.57293628	-0.22988866
O	-3.54408588	-0.16618006	-1.51195307
H	-3.98153131	0.68178700	-1.68578029

Table AIII-3. Continued

Atoms	XYZ Coordinates	
C	4.52624309	-2.29775864	0.90776286
H	4.36502720	-1.59923189	1.73184092
C	5.64988917	-3.24000302	1.29492220
H	5.32604180	-3.87804404	2.12012561
H	5.89477049	-3.87593460	0.43745012
O	6.77502028	-2.51532417	1.74297377
H	6.88757390	-1.77065065	1.14072990
C	3.23047441	-3.02575339	0.52709783
H	3.01366421	-3.74681239	1.32404855
O	3.44498283	-3.79414666	-0.63582057
H	3.76615847	-3.17890749	-1.31196162
C	2.03338363	-2.08478626	0.37793763
C	-0.13838705	-0.34487124	-0.01591123
C	1.13987449	-2.29357422	-0.67781803
C	1.80609925	-1.02098139	1.24624048
C	0.72656452	-0.15963674	1.05179793
C	0.07866612	-1.42575871	-0.88743165
H	1.30959480	-3.12504977	-1.34974192
H	2.46941437	-0.83498010	2.08259911
H	0.53699786	0.66694214	1.72736698
O	-0.80927254	-1.49819505	-1.91409285
O	-1.17853711	0.49494121	-0.19972551
H	-1.81257065	0.13692625	-0.85522336
C	-0.90497041	-2.71795987	-2.62699173
H	-0.98131951	-3.56394316	-1.93945575
H	-1.81451790	-2.64727583	-3.22005948
H	-0.04030309	-2.85792585	-3.28384777
SSRSSRSS			
O	-3.85358031	3.85960224	0.68167508
C	-3.39017848	2.82309933	-0.08366332

Table AIII-3. Continued

Atoms	XYZ Coordinates	
C	-2.21000506	0.76417547	-1.51032869
C	-2.02527369	2.55914953	0.07967198
C	-4.15349261	2.05868930	-0.94907504
C	-3.57262247	1.00456763	-1.65933056
C	-1.43583855	1.53463602	-0.64260822
H	-1.72551850	-0.03708834	-2.05627039
H	-5.21113538	2.24700629	-1.07591566
H	-0.37490667	1.34014981	-0.51597546
C	-5.16468957	4.32820561	0.41848558
H	-5.30984114	5.19901398	1.05339284
H	-5.26896439	4.61102972	-0.63238554
H	-5.90963164	3.56729348	0.66632069
O	-1.29230227	3.32307929	0.94055364
H	-1.88387770	3.98565440	1.32015219
C	-4.46672438	0.16946740	-2.57916930
H	-4.30609408	0.50364194	-3.61032319
C	-4.16401862	-1.33301412	-2.52917501
H	-3.09070867	-1.52723259	-2.58859898
C	-4.85250576	-2.11688214	-3.63052563
H	-4.56624455	-1.71151474	-4.60359345
H	-5.93727962	-2.01589735	-3.51556445
O	-4.45176138	-3.46929106	-3.60475089
H	-4.41187441	-3.73438060	-2.67823696
O	-4.67839766	-1.89223606	-1.30509860
C	-3.87175400	-1.76471161	-0.20556442
C	-2.20960332	-1.46057016	2.00085200
C	-4.22906322	-0.89594142	0.82237488
C	-2.70627593	-2.52837635	-0.09803773
C	-1.86398616	-2.36686639	0.99730092
C	-3.39540937	-0.74022670	1.93217227

Table AIII-3. Continued

Atoms	XYZ Coordinates	
H	-0.94742039	-2.93753165	1.07901038
H	-3.65417052	-0.08045051	2.74809144
O	-5.40510622	-0.23386110	0.64431025
O	-2.48562639	-3.38180400	-1.13062307
C	-5.78238150	0.69372912	1.64322843
H	-5.02553712	1.47751893	1.75624257
H	-6.72128969	1.13087025	1.30703421
H	-5.93816959	0.19347340	2.60302654
C	-1.33604377	-4.20992000	-1.06626766
H	-1.36492064	-4.82481114	-1.96286498
H	-1.36466687	-4.84593013	-0.17703191
H	-0.41915895	-3.61541113	-1.05387742
C	-1.26382317	-1.28769529	3.17932222
C	0.10321162	-0.76126098	2.73433990
C	-0.10320678	0.76143481	2.73430863
C	-1.23163060	0.96319193	3.75985490
O	-1.72366251	-0.33047782	4.11728321
H	-1.18114078	-2.23962920	3.71244577
H	0.39385148	-1.13889840	1.75851617
H	-0.39383953	1.13903371	1.75846706
H	-2.04055145	1.56455745	3.33015362
H	-0.87856406	1.44086370	4.67666583
C	1.26383193	1.28788264	3.17927068
O	1.72365603	0.33070916	4.11728283
C	1.23163966	-0.96297771	3.75989200
H	1.18116355	2.23984661	3.71234225
H	0.87858750	-1.44062745	4.67671932
H	2.04056231	-1.56434583	3.33019877
C	2.20961445	1.46069128	2.00079338
C	3.87175859	1.76470522	-0.20564681

Table AIII-3. Continued

Atoms	XYZ Coordinates	
C	3.39538606	0.74029048	1.93211572
C	1.86403438	2.36699006	0.99723290
C	2.70632230	2.52843457	-0.09811889
C	4.22903871	0.89594544	0.82231185
H	3.65412803	0.08051668	2.74804356
H	0.94750078	2.93770671	1.07894340
O	5.40504568	0.23380245	0.64425559
O	2.48571302	3.38187116	-1.13070518
C	1.33618866	4.21006804	-1.06633726
H	0.41926294	3.61562456	-1.05390697
H	1.36487882	4.84609543	-0.17711544
H	1.36508542	4.82493672	-1.96294907
C	5.78230414	-0.69373751	1.64322799
H	5.02543128	-1.47749068	1.75630533
H	5.93812699	-0.19342387	2.60298980
H	6.72118904	-1.13093628	1.30704416
O	4.67839316	1.89216211	-1.30519887
O	-5.83516857	0.38361984	-2.31284428
H	-6.01803138	-0.05477080	-1.46798751
C	4.16400043	1.33286301	-2.52923651
H	3.09069003	1.52707688	-2.58866346
C	4.85247238	2.11666986	-3.63064286
H	4.56620147	1.71124422	-4.60368322
H	5.93724813	2.01569798	-3.51568661
O	4.45172070	3.46907842	-3.60494427
H	4.41183690	3.73422069	-2.67844524
C	4.46671560	-0.16961943	-2.57915278
H	4.30610736	-0.50384196	-3.61029458
O	5.83516101	-0.38374680	-2.31280230
H	6.01800677	0.05466958	-1.46795532

Table AIII-3. Continued

Atoms	XYZ Coordinates	
C	3.57260930	-1.00468201	-1.65928362
C	2.02527194	-2.55916346	0.07982104
C	4.15347921	-2.05877076	-0.94898127
C	2.20999117	-0.76428094	-1.51028566
C	1.43583245	-1.53469063	-0.64251568
C	3.39017097	-2.82313079	-0.08351768
H	5.21111993	-2.24710031	-1.07581886
H	1.72550104	0.03695008	-2.05627169
H	0.37490032	-1.34019906	-0.51588680
O	3.85357954	-3.85959362	0.68187169
O	1.29230837	-3.32303088	0.94076347
H	1.88388172	-3.98559188	1.32038965
C	5.16467314	-4.32823559	0.41867097
H	5.90963683	-3.56732820	0.66645791
H	5.30982204	-5.19901979	1.05361198
H	5.26891881	-4.61110470	-0.63219072

Table AIII-4. Optimized geometries of the initial stereoisomers of MC3.

RSSRRSSR

Atoms	XYZ Coordinates	
C	1.88429498	4.02396804 -1.21780430
C	2.29284171	2.13306786 0.78668251
C	0.84277555	3.70341490 -0.34742435
C	3.09492240	3.34860292 -1.13857644
C	3.29194733	2.38251461 -0.16221359
C	1.06674181	2.77771029 0.66313307
H	3.89623043	3.53582834 -1.84309569
H	0.28361238	2.54177330 1.37311489
O	4.48644479	1.68258021 -0.16205294
C	4.41533988	0.30726543 -0.30634060
C	4.43990135	-2.44951590 -0.33730811
C	5.59423216	-0.36079738 0.01843531
C	3.27133813	-0.37793636 -0.67860661
C	3.26555323	-1.76774357 -0.64618559
C	5.60673445	-1.75797071 -0.02788811
H	4.47388999	-3.53362110 -0.30528913
H	2.38059426	0.16621997 -0.95868254
C	1.94805197	-2.51281362 -0.79394358
O	0.90969861	-1.67036993 -1.26300094
C	0.29002840	-1.01116113 -0.14513584
C	0.79716530	-1.70085361 1.13226049
C	1.45985497	-2.97410579 0.58872087
H	2.04881096	-3.33923487 -1.50402154
H	0.51136193	0.05868266 -0.16360571
H	-0.78749510	-1.13812875 -0.25215532
C	0.28722950	-3.98107137 0.57940483
O	-0.83411374	-3.34436289 1.19085416
C	-0.36469087	-2.24255023 1.95956299

Table AIII-4. Continued

Atoms	XYZ Coordinates	
H	0.54462777	-4.88693936	1.13750784
H	-0.00995044	-4.26437688	-0.43317919
H	0.00725556	-2.60811818	2.92878407
H	1.48139959	-1.06740698	1.69487566
H	2.28325479	-3.32265501	1.21149305
H	1.73843216	4.77530320	-1.98727015
C	-0.52099803	4.32968083	-0.53367662
O	-1.31191068	4.08477017	0.62367071
C	-2.64596040	3.78170976	0.24319767
C	-2.50290741	3.04729079	-1.07860706
C	-1.33813558	3.78545790	-1.75769005
H	-0.39300919	5.41232108	-0.65430440
H	-3.09857261	3.18710708	1.03937277
H	-3.22656509	4.70394803	0.11288469
H	-3.41459190	3.06634888	-1.67719978
H	-1.68092252	4.61388649	-2.37892385
C	-0.71156288	2.67277963	-2.58483029
O	-0.78326759	1.52533720	-1.75743032
C	-1.95346931	1.60671027	-0.94049045
H	0.33323181	2.82456904	-2.85324826
H	-1.29794455	2.52577650	-3.50162993
H	-1.61641651	1.44183303	0.09127718
C	-2.94889308	0.52107644	-1.28553097
C	-4.70256876	-1.60963946	-1.69691972
C	-4.25783293	0.58599931	-0.82385508
C	-2.51877682	-0.61115388	-1.98295139
C	-3.38417168	-1.67651443	-2.17057458
C	-5.13758383	-0.47316780	-1.03971254
H	-4.59910625	1.45314497	-0.26664297
H	-1.49840425	-0.64724729	-2.34218002

Table AIII-4. Continued

Atoms	XYZ Coordinates	
H	-6.15810253	-0.44075592	-0.67726352
C	-1.47007095	-1.23642609	2.17883736
C	-3.47543065	0.67414595	2.49685651
C	-2.80803747	-1.59888684	1.99835466
C	-1.14958338	0.06971793	2.53310347
C	-2.15213589	1.02713456	2.68981992
C	-3.80507682	-0.65088846	2.17139943
H	-3.04146592	-2.61352338	1.70517730
H	-0.11158487	0.36108810	2.66216826
H	-1.91542121	2.05432844	2.94565553
O	6.72720832	-2.45686878	0.31765854
O	6.69953600	0.32316026	0.41898818
O	2.42077561	1.21923572	1.79000584
O	-3.06718131	-2.84938915	-2.79120527
O	-5.54200956	-2.66766511	-1.86595686
O	-5.14424118	-0.87355208	2.04764214
O	-4.45922642	1.60904603	2.60787849
C	-5.56200580	-2.19756285	1.75779480
H	-5.24677564	-2.87943170	2.55272215
H	-5.16325824	-2.53224440	0.79722568
H	-6.64823508	-2.16810964	1.70748176
C	-1.70802732	-3.03391377	-3.15663370
H	-1.04805551	-2.89351087	-2.29553213
H	-1.63219021	-4.05204607	-3.53207608
H	-1.42069766	-2.33050133	-3.94311451
C	7.83246745	-2.28314001	-0.56484115
H	7.55990799	-2.60178027	-1.57557624
H	8.62898833	-2.91947102	-0.18404165
H	8.16496635	-1.24416883	-0.57825925
C	3.60914772	1.26583265	2.58064896

Table AIII-4. Continued

Atoms	XYZ Coordinates	
H	3.31787508	0.98012576	3.59064243
H	4.02288983	2.27653740	2.59309672
H	4.35439561	0.56127131	2.20633907
H	6.48770535	1.26439332	0.39692251
H	-5.30403945	1.15876208	2.48261988
H	-5.05621909	-3.35295111	-2.34131621

CHAPTER 4 COMPUTATIONAL DETERMINATION OF REACTION MECHANISMS AND KINETICS OF LIGNIN OLIGOMER PYROLYSIS WITH A COMBINATION OF IMPORTANT LINKAGES, E.G., β-O-4, α-O-4, β-5, β-β', AND 4-O-5, THROUGH DENSITY FUNCTIONAL THEORY

This chapter is composed of material that has previously been published in academic journals. I am the lead author of this manuscript. I was responsible for designing the simulation plan and conducting the simulations.

1) Ross Houston and Nourredine Abdoulmoumine. Computational Determination of Reaction Pathways of Lignin Oligomer Pyrolysis with a Combination of Important Linkages, e.g., β-O-4, α-O-4, β-5, β-β′, and 4-O-5, Through Density Functional Theory. ACS Sustainable Chemistry and Engineering (Submitted for Review)

Abstract

Lignin is a complex, aromatic polymer that is currently underutilized during the valorization of lignocellulosic biomass. The fundamental understanding of how to effectively convert lignin into valuable materials lags that of its carbohydrate counterparts: cellulose and hemicellulose. To develop a better understanding of the thermal deconstruction behavior of lignin, this work computationally investigates the reaction mechanism of three model lignin oligomers containing β-O-4, α-O-4, β-5, β-β′, and 4-O-5 interunit linkages using density functional theory (DFT) at the M06-2X/6-311++G(d,p) level. Reaction classes were proposed for each type of interunit linkage containing the possible reactions associated with the resolution of the relevant linkage. Reaction pathways were proposed by employing the appropriate reaction classes recursively until reaching monomeric products. Calculations indicate the β-5 interunit linkage being a primary initial reaction point, followed by the α-O-4 and β-O-4 ether linkages. The β-β′ has a similar structure to the β-5 linkage; however, it requires multiple steps to resolve, which puts it behind the non-aromatic ether linkages. This work

provides a valuable first step toward the development of a generalized reaction network that can be applied to a variety of lignin structures.

4.1. Introduction

The valorization of lignocellulosic biomass through pyrolysis commonly occurs in multiphase reactors (e.g., fluidized bed reactors) where lignocellulosic biomass particles simultaneously experience coupled processes, e.g., heat and mass transfer, as well as reaction processes, which govern the properties of the pyrolysis products, i.e., bio-oil, biochar, and pyrolysis gas, at a given operating condition. The optimization of these reactors requires knowledge of the degradation reaction mechanisms to enable process optimization in reactors towards producing bio-oil and pyrolysis gas intermediates for downstream processing to valuable products. Over the years, there have been significant advancements in understanding the underlying reaction mechanisms of cellulose and hemicellulose degradation pyrolysis using a mixture of experimental observations and quantum chemical calculations[1-4]. However, the reaction mechanism of lignin's pyrolytic degradation is less well-understood compared to its carbohydrate counterparts, with only a few mechanisms proposed currently. Yet, understanding lignin's degradation is important because it is a major component of lignocellulosic biomass materials and the most abundant source of renewable aromatics in the world[5].

Lignin is an aromatic polymer with diverse linking motifs that lead to a heterogenous, non-repeating structure, unlike cellulose and hemicellulose[6]. This heterogeneity complicates the determination of its pyrolysis reaction mechanisms,

which, unlike cellulose and hemicellulose, requires accounting for the cleavage of diverse interunit linkages, e.g., β-O-4, β-5, β-β, 5-5, and 4-O-5, dispersed throughout the native lignin structure[7-10]. Thus far, most of the work investigating the pyrolysis reaction mechanisms of lignin has used simple model compounds, monomers, and dimers, which represent important units found in native lignin and allow for the investigation of various types of interunit linkages[11-21]. However, the current knowledge of lignin's pyrolysis mechanisms from smaller model compounds is limited and cannot be directly extrapolated to native lignin. The increase in computational efficiency and availability of more computational resources has recently allowed for the investigation of increasingly larger lignin systems through DFT. Computational investigations on lignin model compounds have been performed on model oligomers, up to a 20-mer in size, containing linear β-O-4 interunit linkages[8, 22]. The increased size of these compounds allowed for the observation of the effect of neighboring groups and nonbonded interactions on the energetics; however, it serves as an investigation of a linear β-O-4 backbone. Therefore, it is imperative to investigate larger lignin substructures that are non-linear and contain a variety of interunit linkages found in lignin. The efforts in this study aim to bridge the knowledge gap between smaller model compounds and a lignin polymer by developing and proposing an approach to rationally derive pyrolysis reaction mechanisms for well-characterized lignin using Density Functional Theory (DFT) modeling. This approach is demonstrated on model lignin oligomers with important interunit linkages.

This work seeks to deepen the mechanistic understanding of the prevalent reaction pathways during the thermal deconstruction of lignin using density functional theory (DFT) by investigating model lignin compounds with important linkages found in lignin. Three model oligomers containing a variety of interunit linkages found in lignin, β-O-4, α-O-4, β-5, β-β′, and 4-O-5. Proposing a theoretical reaction mechanism for model lignin oligomers containing several different interunit linkages serves as a building block for the eventual development of a general reaction hierarchy that can be applied to various forms of lignin.

4.2. Materials and methods

4.2.1. Oligomer and reaction class selection

Three model oligomers were chosen for investigation in this work following our previous bond dissociation enthalpy (BDE) studies[23, 24]. The first model compound (MC1) is a tetramer formed from coniferyl units containing β-O-4, α-O-4, and β-5 interunit linkages. MC1 has previously been shown to be synthesizable by Quideau and Ralph[25]. This model tetramer contains a non-cyclic α-aryl ether linkage, which has only been found in synthetic lignin oligomers and not in native lignin[26]. However, the presence of an α-O-4 interunit linkage in close proximity to two other prominent interunit linkages in lignin can still provide valuable mechanistic information regarding the hierarchy of reactions during thermal deconstruction. The second tetramer, MC2, is commercially available as hedyotisol and contains two β-O-4 interunit linkages as well as a β-β′ interunit linkage[27]. The third model oligomer, MC3, is a tetramer containing two β-β′ interunit linkage and a 4-O-5 interunit linkage. MC3 has previously been used as a

model compound for the identification of 4-O-5 interunit linkages via NMR[28]. The combinations of interunit linkages in the three model oligomers make up approximately 80% of the interunit linkages found in native lignin[29, 30]. The stereochemistry of each model was adopted from the low energy configuration found in Chapter 3 using the same nomenclature as previously discussed. The configuration of MC1 was RSRS, MC2 was SSRSSRSS, and MC3 was RSSRRSSR.

In order to propose a reaction mechanism for these oligomer structures, we must first identify the logic that dictates the general order of how individual reactions are proposed. The primary type of reaction investigated for these specific interunit linkages is homolytic cleavage reactions, which generate products with at least one radical. In the case of these products, it is much more likely for the radical to stabilize rather than form another radical via a reaction at a separate interunit linkage. Therefore, the method employed in this work is to resolve one interunit linkage at a time. From that, we propose a set of possible reactions for each interunit linkage that we refer to as reaction classes. These reaction classes are deployed successively to convert the initial model compounds into monomeric products. The reactions studied in this chapter depend on the type of interlinkages in each oligomer. Model compound 1 has β-O-4, α-O-4, and β-5 linkages, model compound 2 has β-O-4 and β-β' linkages, and model compound 3 has β-β' and 4-O-5 linkages. Each linkage type is treated independently and allocated a class of reactions based on the potential reaction points along the interunit linkage, determined in our previous bond dissociation enthalpy

work[23, 24], as well as any previously published reactions for that specific linkage. The structures of the model compounds are shown in Figure 0-1.

4.2.2. Computational setup

The computational work in this chapter was performed using GaussView 6 and Gaussian 16 (Gaussian, Inc., Wallingford, CT, 2016) on the Infrastructure for Scientific Applications and Advanced Computing (ISAAC) high-performance computing resource at the University of Tennessee. Each DFT simulation was performed in parallel using various different processor configurations, primarily eight or sixteen processors. Additional discussion on the computational details employed in this work can be found in Houston et al.[24]

The energetics and kinetics were calculated for each proposed reaction. All relevant species (reactants, products, intermediates, and transition states) were subjected to geometry optimization and vibrational frequency analysis at 773 K (500 °C). DFT simulations were carried out using the M06-2X Minnesota functional[31] coupled with the 6-311++G(d,p) split-valence triple-zeta basis set[32-34]. Dispersion interactions were accounted for with the GD3 empirical dispersion correction[35]. The reactions investigated consisted of molecules with fully paired electrons and molecules with varying numbers of free radicals, one, two, and four. Non-radical and single-radical species were modeled as a singlet state and a doublet state, respectively. However, for the species with more than one free-radical, they were modeled as different spin states. Diradical species, as those seen from the initial ring-opening reactions of the β-5 and β-β′ interunit linkages, were modeled as triplet states, and the species with four radicals

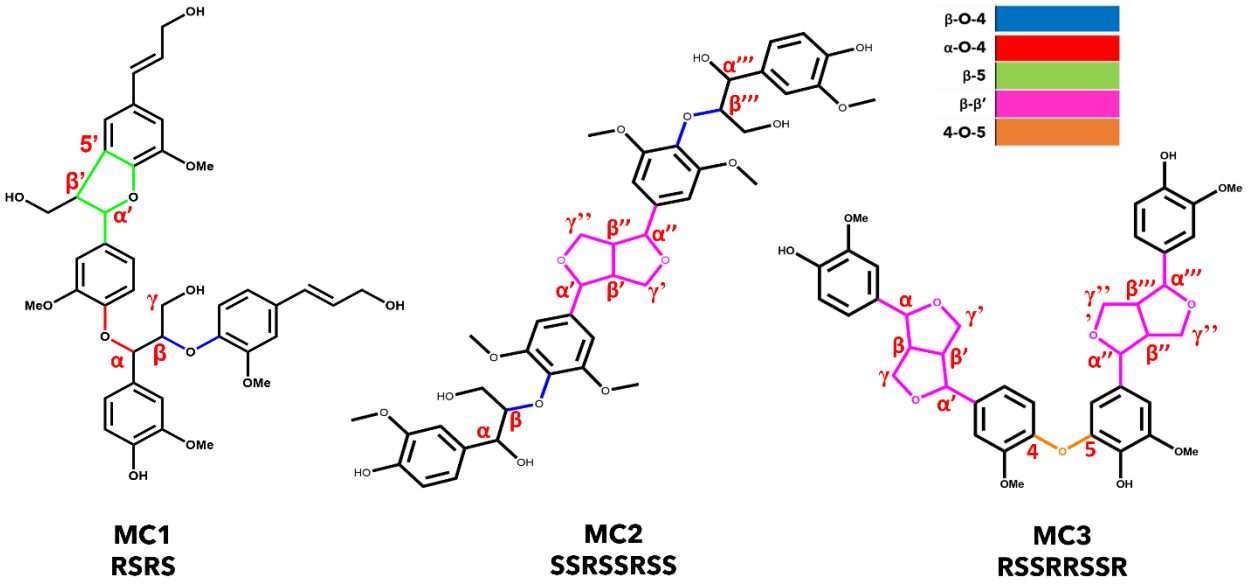

Figure 0-1. Structures of the three model oligomers investigated. Interunit linkages are color-coded, and relevant carbon positions have been highlighted in red.

are treated as quintets[11]. Special care was taken to ensure the radicals produced from ring-opening reactions do not re-bond into their original ring. The interatomic distance between the radicalized atoms was set to an initial length of 2.5 A to give sufficient distance to prevent re-bonding.

In addition to homolytic cleavage, the β-O-4 and α-O-4 ether linkages have been proposed to also undergo concerted reactions during thermal deconstruction[12, 15]. Transition state structures will be identified using transition state searching methods in Gaussian (Berny algorithm or Synchronous Transit-Guided Quasi-Newton methods) and confirmed by the presence of a single imaginary frequency upon frequency analysis and intrinsic reaction coordinate (IRC) calculations[12]. The kinetic rate parameters will be calculated using transition-state theory[36]. The activation energies for each reaction can be calculated as the relative energy difference between the products and the transition state. The activation energy can be assumed to be the BDE for radical reactions where transition states are either non-existent or hard to identify.

4.2.2.1. Reaction classes and reaction pathways

Each linkage type will have a set of reactions, or reaction class, and reaction pathways based on chemical intuition and previously published pyrolysis reactions, *e.g.,* β-O-4 reaction class reactions. These classes of reactions involve the initial homolytic cleavage reactions that have been determined to be the most favorable and any subsequent reactions that resolve the radicals produced. Stabilization is primarily achieved via radical rearrangement or the addition of hydrogen. In addition to the homolytic reactions, any previously proposed concerted reactions involving a specific

interunit linkage type are also included in the respective reaction class. In the free-radical reactions, we used the lowest bond dissociation enthalpies (BDE) from our previous studies[23, 24] to identify the bonds that serve as the primary points of reaction for homolytic cleavage, which will be further discussed in the following sections. Each interunit linkage type has its own reaction class; therefore, there are five reaction classes considered in total: β-O-4, α-O-4, β-5, β-β', and 4-O-5.

4.2.2.1.1. β-O-4 class of reactions

The β-O-4 reaction class has three major reaction pathways available, as shown in Figure 0-2. The first reaction pathway of the β-O-4 reaction class is the homolytic cleavage of the C_β-O found to be a prominent bond to be cleaved in our previous study as well as other works in literature[16, 20, 21, 24]. The second and third reaction pathways of the β-O-4 reaction class are concerted reactions proposed previously in literature[12]. In the first reaction pathway, the resulting radical species are subsequently stabilized by the addition of hydrogen. Additionally, the C_γ and oxygen can be potentially removed as formaldehyde via a transition state. The second reaction pathway is retro-ene fragmentation, which initially forms a quinone intermediate. This intermediate then undergoes tautomerization through a transition state before forming the phenolic product. The third reaction pathway is a Macoll elimination, which yields the same final products as the retro-ene fragmentation; however, it is a one-step concerted reaction that proceeds through a transition state without forming the quinone intermediate.

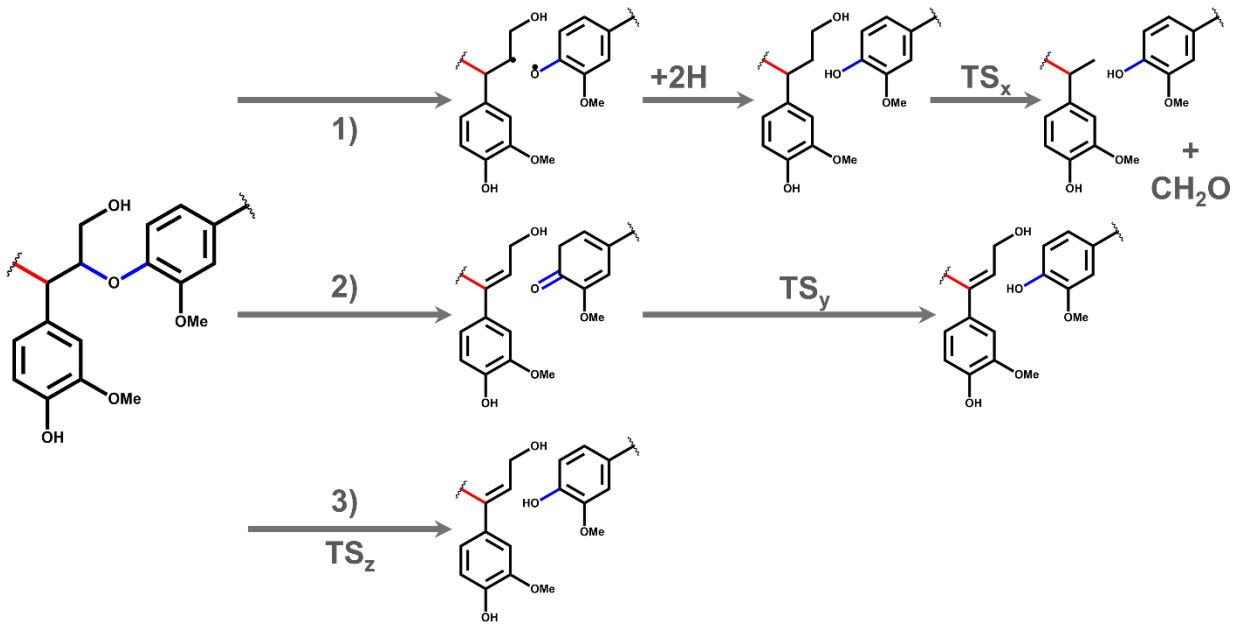

Figure 0-2. The proposed reactions for a β-O-4 reaction class with three reaction pathways denoted by 1), 2), and 3).

4.2.2.1.2. α-O-4 class of reactions

The α-O-4 is a simpler linkage than the β-O-4; therefore, its reaction class only contains two possible reaction pathways, as shown in Figure 0-3. The first pathway is the homolytic cleavage of the C_α-O bond of the ether linkage, which was previously shown to be a major point of reaction due to a low BDE[24]. The resulting radicals are then stabilized via hydrogen addition. The second reaction pathway involves a simple decomposition of the ether bond proceeding through a transition state previously suggested in a mechanism study of an α-O-4 model dimer[15].

4.2.2.1.3. β-5 class of reactions

The β-5 reaction class is subdivided into two reaction subclasses starting from either the C_α-O cleavage or the C_α-C_β cleavage. Both these initial homolytic cleavage reactions have been shown to have low BDEs compared to other ring-opening reactions as well as the other ether linkages found in MC1. The subsequent reactions proposed in the β-5 class of reactions come through chemical intuition and a previous study on the β-5 linkage[37]. The first reaction subclass, starting with the C_α-O cleavage, shown in Figure 0-4, has four possible reaction pathways. The first pathway involves the stabilization of the diradical via hydrogen addition before undergoing rearrangement, while the second, third, and fourth pathways contain rearrangement to eliminate the radical via the formation of a double bond.

The second subclass of the β-5 reaction class, shown in Figure 0-5, includes reactions starting from the initial homolytic cleavage of the C_α-C_β bond.

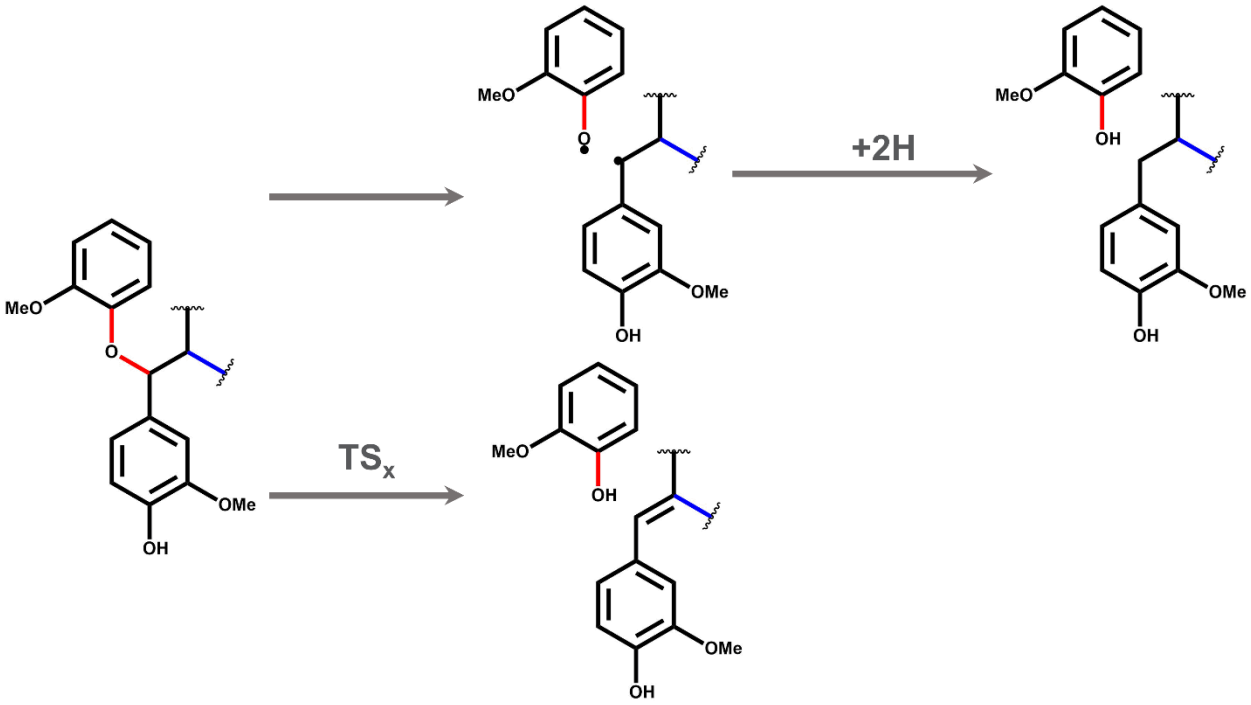

Figure 0-3. The proposed class of reactions for the α-O-4 linkage. Pathway 1 is the homolytic cleavage and stabilization, and pathway 2 is the decomposition pathway.

The diradical species formed from the homolytic cleavage can undergo rearrangement to stabilize via the formation of double bonds. In the first pathway, this results in the formation of two separate species, with the compound containing the three-membered cyclic ring being a monomeric final product. The second pathway results in stabilization while maintaining a single species.

4.2.2.1.4. β-β′ class of reactions

Similar to the β-5 reaction class, the β-β′ reaction class is broken into two subclasses that capture the chain of reactions after the cleavage of C_α-O and C_α-C_β bonds. The subsequent reactions and rearrangements that occur after the initial bond cleavage have previously been proposed in an investigation into the BDEs of pinoresinol by Elder et al.[11]. The reactions for both subclasses can be found in Figure 0-6 and Figure 0-7. The C_α-O reaction subclass has two reaction pathways, which both proceed from the same diradical intermediate. In the first reaction pathway, a quad-radical species is created by cleavage of the C_α-O bond on the opposite side of the β-β′ ring. In the second reaction pathway, a diradical intermediate is created by cleaving the C_β-$C_{\beta'}$ bond, followed by electron rearrangement to form a new double bond between the C_α-C_β on the side of the ring of the initial scission.

The second reaction subclass also has two reaction pathways. The first pathway in this subclass creates a quad-radical species by cleavage of the C_α-C_β on the opposite side of the β-β′ ring. This reaction is analogous to the first pathway of the C_α-O subclass. The quad-radical species then undergoes radical rearrangement to break the β-β′ bond and form three stable products: butadiene and two aromatic aldehydes. The

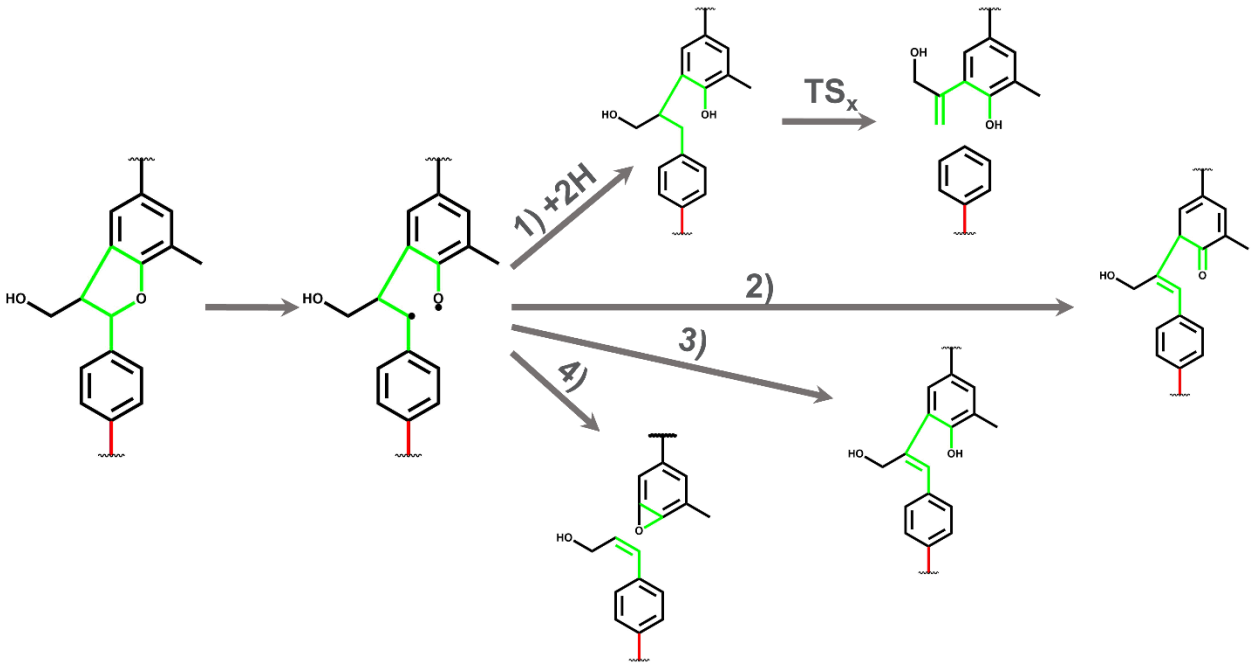

Figure 0-4. The proposed class of reactions for the β-5 linkage with the C_α-O subclass.

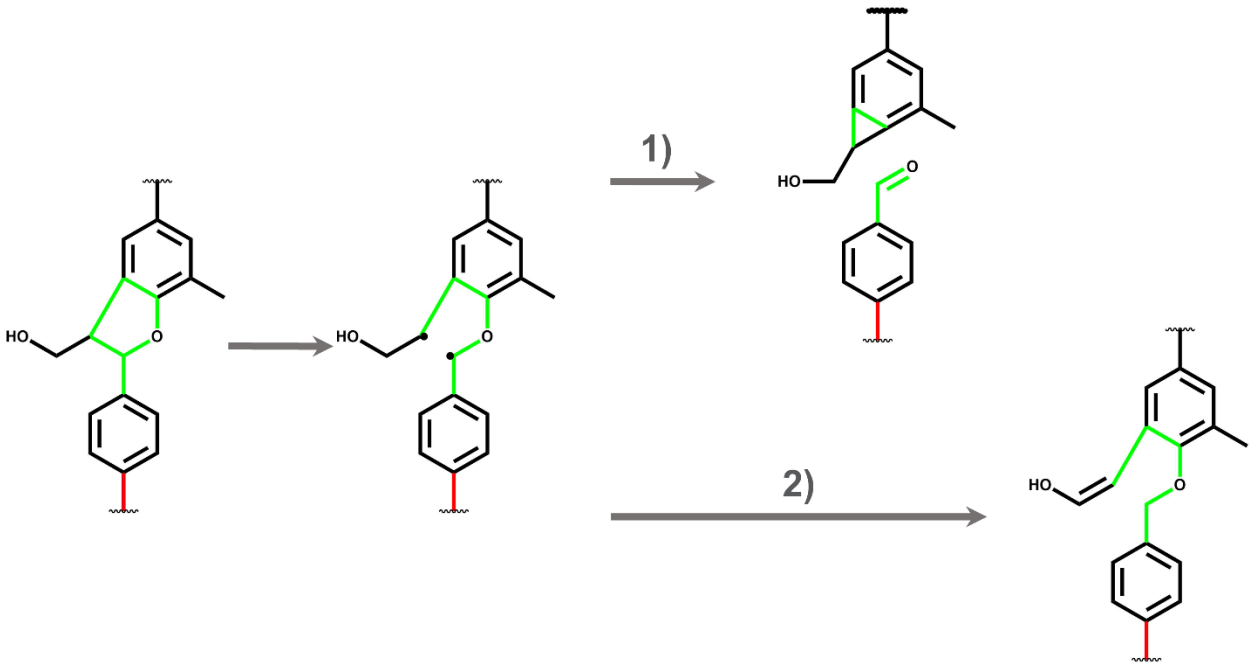

Figure 0-5. The proposed class of reactions for the β-5 linkage with the C_{α}-C_{β} subclass.

second reaction pathway instead undergoes immediate radical rearrangement to split into two species: an aromatic aldehyde and a five-membered cyclic diradical species. The resulting diradical rearranges once more to butadiene and another aromatic aldehyde. These two pathways result in the same three end products but take different steps to get there.

4.2.2.1.5. 4-O-5 class of reactions

The 4-O-5 class of reactions is the simplest of the ether interunit linkages investigated in this work. The class of reactions for this linkage, shown in Figure 0-8, includes the homolytic cleavage of the C_4-O and O-C_5 bonds. As the carbons involved in this linkage are aromatic and, therefore, unlikely to react, we do not consider any additional reactions involving the aromatic ring.

4.2.2.2. Development of complete reaction pathways

As discussed in the previous sections, the approach for proposing a reaction mechanism for these more complex lignin model compounds is to assume the resolution of a specific linkage before initiating deconstruction at another linkage in the oligomer. Once the linkage is stabilized and resolved, we then move onto any remaining linkages. The general logic for our mechanism generation is shown in Figure 0-9. We start with a model compound; that compound is subjected to a random class of reactions based on the types of interunit linkages present. Once that class of reactions has been applied and the resulting stabilized products are produced, the products are then examined for any additional interunit linkages. If there are none, the

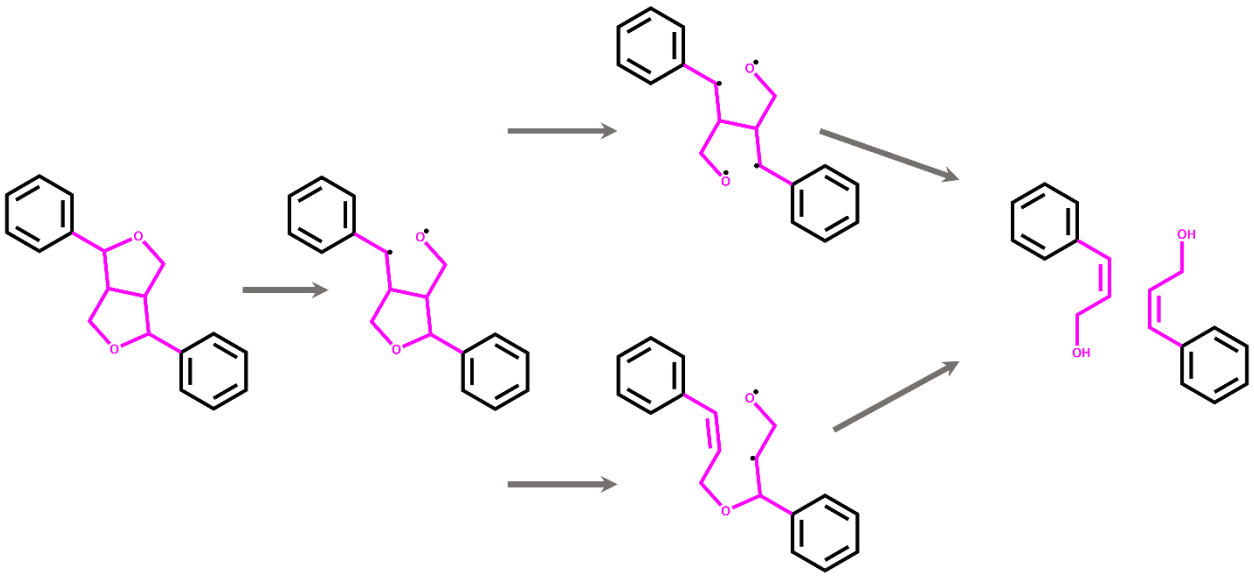

Figure 0-6. The proposed class of reactions for the β-β′ linkage with the C_{α}-O subclass.

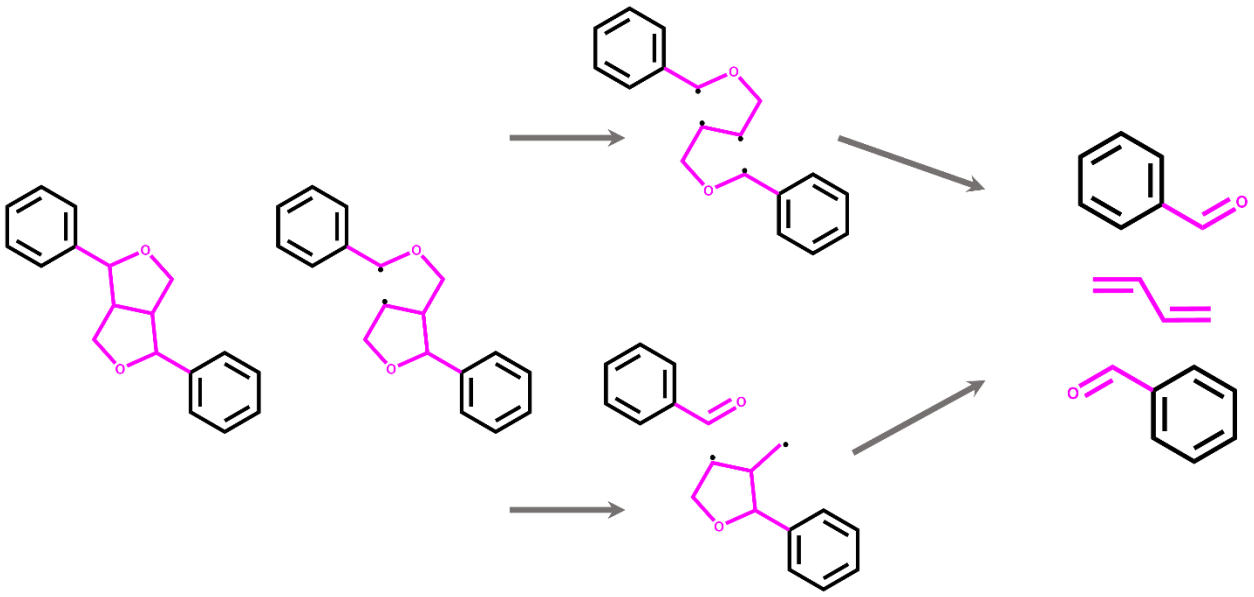

Figure 0-7. The proposed class of reactions for the β-β′ linkage with the C_{α}- C_{β} subclass.

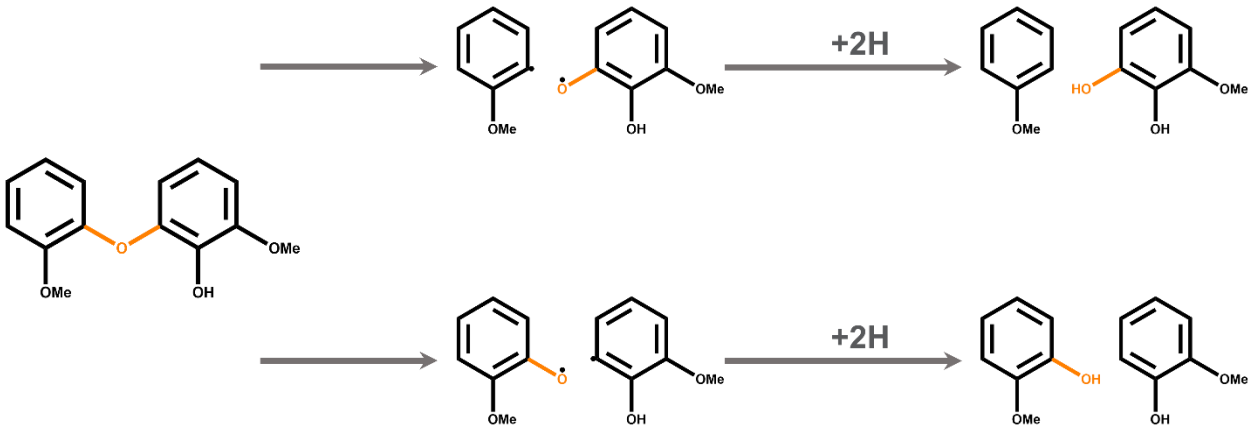

Figure 0-8. The proposed class of reactions for the 4-O-5 linkage.

product is monomeric and can be subjugated to monomeric pathways that are readily available in literature[17, 38, 39]. These monomeric reaction pathways are potentially responsible for the production of monomeric derivatives of the ones produced via our proposed pathways as well as the presence of light gases seen during pyrolysis. If there are still interunit linkages in the products, it is subjected to another class of reactions until the products are stable and the interunit linkage is resolved. This process repeats until we reach monomeric products without any interunit linkages.

4.3. Results and discussion

4.3.1. Reaction pathways for Model Compound 1

The reaction mechanism for MC1 was proposed by subjecting it and any resulting products to the β-O-4, α-O-4, and β-5 classes of reactions until reaching monomeric species. In total, 105 unique species were identified and simulated as a part of 132 unique individual reactions. These reactions were combined to form 155 unique reaction pathways for the thermal deconstruction of MC1. Additional information, such as the calculated thermodynamic values for all species, can be found in Appendix IV. In the following sections, reaction pathways will be discussed in terms of their initial reaction type, e.g., the scission of the C_α-O of the β-5 interunit linkage.

4.2.3.1. β-5 C_α-O reaction pathways

Assuming an initial scission of the C_α-O at the β-5 interunit linkage, there were 59 potential reaction pathways based on the available reaction classes. As shown in Figure 0-4, there are four proposed pathways to stabilize the diradical produced from the scission of the C_α-O bond.

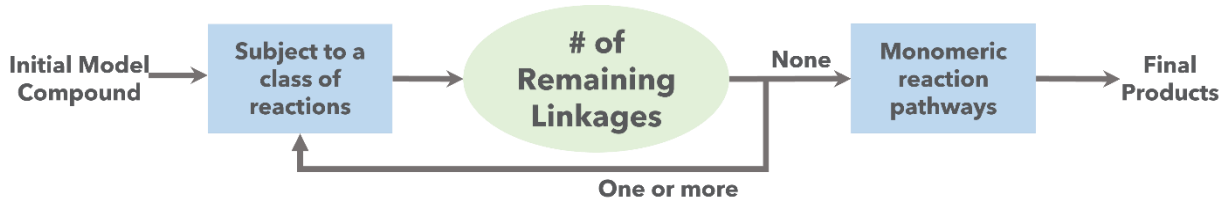

Figure 0-9. Schematic of the logic used in the development of the reaction mechanisms.

From there, the stabilized molecules underwent either β-O-4 or α-O-4 reaction classes. The lowest energy reaction pathways for each stabilization reaction are presented in Figure 0-10. A full list of all the relevant reaction pathways and individual species can be found in Appendix IV. To compare the pathways energetically, an energy diagram for each pathway is shown in Figure 0-11. In all cases of a C_α-O diradical, the stabilization via the addition of hydrogen was always found to be more energetically favorable. It is important to note that in the absence of available free hydrogen, the two rearrangement reactions that would dominate would be the ones in Pathway 1.1, -39.0 kcal/mol, and Pathway 1.14, -48.7 kcal/mol, which result in the formation of double bonds while maintaining a single compound. These simple species rearrangements were much more favorable than the rearrangement in Pathway 1.29, which results in an epoxide monomer, 78.5 kcal/mol. After the resolution of the β-5 interunit linkage, the resulting trimeric intermediate undergoes another homolytic cleavage at the C_α-O of the α-O-4 interunit linkage. The BDE of the C_α-O of the α-O-4 interunit linkage was shown to be lower than that of the C_β-O of the β-O-4 interunit linkage. This trend is evident regardless of how the β-5 linkage was resolved, which points to the second class of reactions applied to MC1 being the α-O-4 class. The homolytic cleavage of the ether bond followed by hydrogen stabilization was found to be more likely than the concerted decomposition reaction due to the lack of locating a viable transition state for the concerted reactions. Once the α-O-4 interunit linkage is resolved, only β-O-4 dimers remain. There were two prevalent reactions from the proposed class of reactions: homolytic cleavage of the C_β-O bond or a Maccoll elimination through a

transition state. These two reactions were relatively similar in their required energy barrier, so we would expect both reactions to occur during the thermal deconstruction of MC1.

4.2.3.2. β-5 C_α-C_β reaction pathways

The other subclass of the β-5 reaction class involves the homolytic cleavage of the C_α-C_β bond. Moving forward with thermal deconstructions mechanisms starting from the resulting diradical gives way to 25 potential reaction pathways. The five lowest energy pathways associated with unique secondary and tertiary reaction classes are shown in Figure 0-12. Similar to the stabilization behavior of the C_α-O diradical in the previous section, the rearrangement to form a single, stable species via double bonds is much more energetically favorable than splitting off an epoxide monomer, -57.8 and 5.51 kcal/mol, respectively. From the stable trimer, homolytic cleavage at both the α-O-4 and β-O-4 interunit linkages are likely as they have similar energy barriers of 83.0 and 89.7 kcal/mol. We would expect both respective pathways to be present during the thermal deconstruction of MC1. The radicals formed through the cleavage of the ether linkages are quickly stabilized via hydrogen addition, leaving stable monomeric and dimeric products. The energy diagram for the five low-energy pathways is shown in Figure 0-13.

4.2.3.3. β-O-4 C_β-O reaction pathways

The reaction pathways starting from the homolytic cleavage of the C_β-O bond of the β-O-4 interunit linkage had a wide variety of branching points due to possible reactions associated with the β-O-4 reaction class. There were 49 unique reaction pathways

considered for the thermal deconstruction of MC1, starting with the β-O-4 reaction class. The five lowest energy pathways with unique secondary and tertiary reaction classes are shown in Figure 0-14, and the respective energy diagram is in Figure 0-15. It was determined that both homolytic cleavage and Maccoll elimination at the β-O-4 interunit linkage had mild energy barriers for the initial reaction of 77.7 and 62.6 kcal/mol, respectively. The low-energy stabilization of the radicals produced in the homolytic cleavage lowers the energy barrier of their respective pathways compared to the Maccoll elimination. Therefore, we would expect the homolytic cleavage pathways to dominate even though their initial reaction has a higher energy barrier. After the resolution of the β-O-4 interunit linkage, the cleavage and stabilization of the β-5 interunit linkage is favored over the α-O-4. If sufficient reaction intensity is supplied for full depolymerization, a major product we would expect would be coniferyl alcohol and its derivatives, such as compound 1.53.

4.2.3.4. α-O-4 C_α-O reaction pathways

The final potential starting point for the thermal deconstruction of MC1 is through the α-O-4 class of reactions. This was achieved starting with the homolytic cleavage of the C_α-O bond of the α-O-4 interunit linkage of MC1. Carrying this out until reaching monomeric products yielded ten unique reaction pathways. The three lowest pathways and their respective energy diagrams are shown in Figure 0-16 and Figure 0-17. After the resolution of the α-O-4 interunit linkage, the resulting products are two dimeric species, a β-5 dimer, and a β-O-4 dimer. In the case of the β-O-4 dimer, the concerted Maccoll elimination, 55.2 kcal/mol, is slightly favored over the homolytic cleavage, 63.6

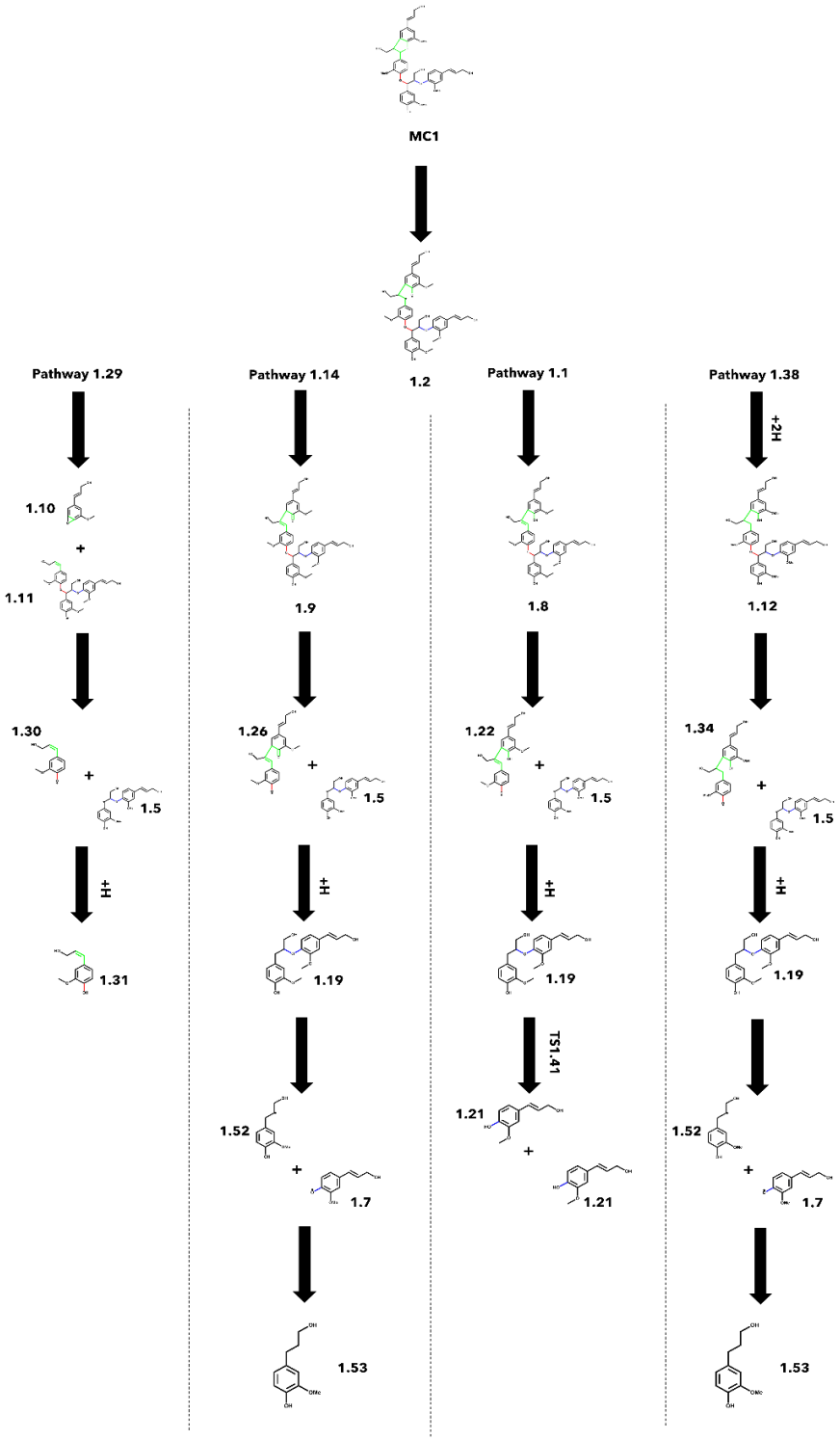

Figure 0-10. Reaction pathways for the lowest energy path associated with the four unique stabilization reactions of the β-5, C_{α}-O subclass.

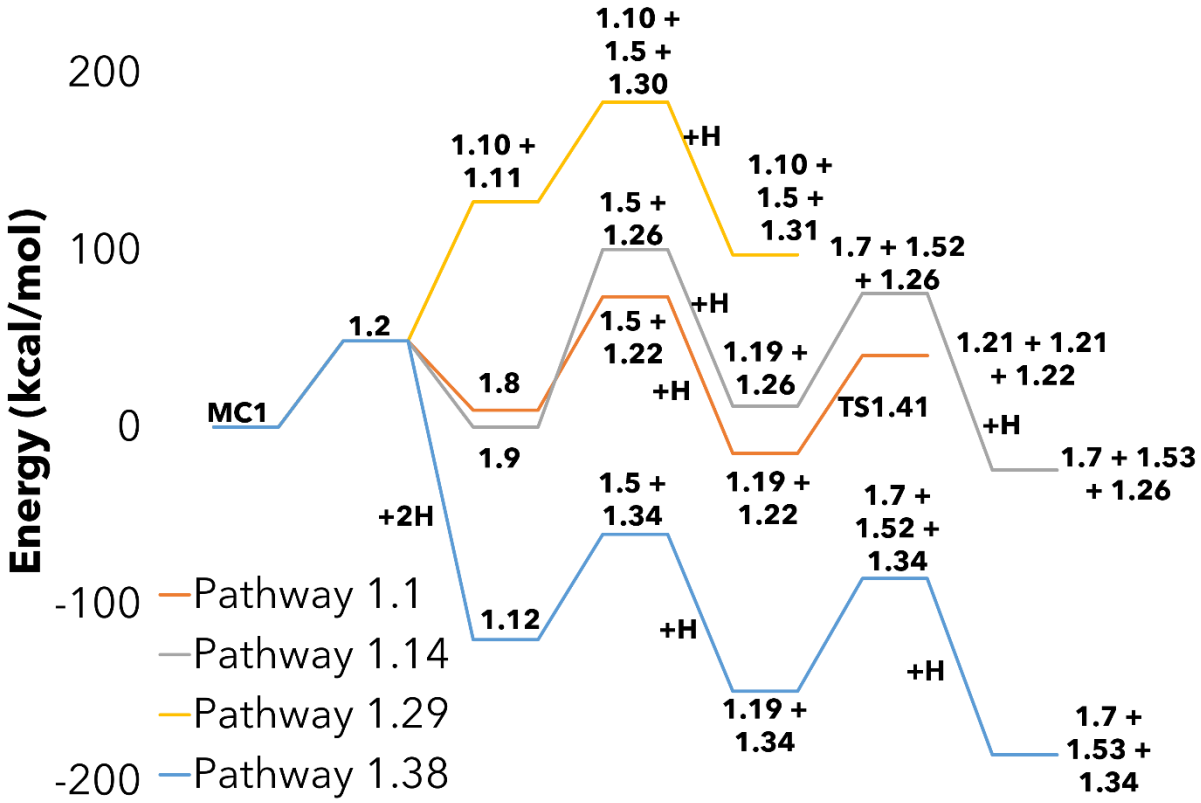

Figure 0-11. Energy diagram for the four lowest energy pathways associated with the four unique stabilization reactions of the β-5, C_α-O subclass.

kcal/mol, which follows a similar trend to the β-O-4 reaction class in other reaction pathways. The β-5 dimer underwent its relevant reaction class consisting of homolytic cleavage at either the C_α-O or C_α-C_β bond. In Pathways 1.138 and 1.140, the cleavage of the C_α-O bond (44.2 kcal/mol) and subsequent stabilization is much more favorable than rearrangement around the C_α-C_β diradical (69.6 kcal/mol). This results in a stable dimeric product; however, the interunit linkage is no longer a β-5 ring but instead an α-O-4 dimer. To take the pathway a step further, the α-O-4 reaction class could potentially be reapplied to these new stable dimers.

4.2.3.5. Overall reaction mechanism for model compound 1

After analyzing the pathways by the initial reaction type, we compared all the proposed pathways for the development of a general reaction mechanism for MC1 based on the lowest energy pathway for each type of initiation reaction. The lowest energy pathways for the thermal deconstruction of MC1 are shown in Figure 0-18. The pathways that involve creating a diradical at the C_α-O bond were shown to have much lower total energy barriers due to the highly favorable hydrogen addition reactions to stabilize. The pathway that proceeds through the diradical at the C_α-C_β position does not undergo hydrogen addition leading to a much higher energy barrier.

The pathways highlighted in Figure 0-18 are representative of the longer pathways that must account for the deconstruction of successive production of a trimer and dimer as opposed to the pathways that can be truncated by stabilizing the smaller fragment from a scission reaction. For example, in the β-O-4 pathway, the first reaction produces

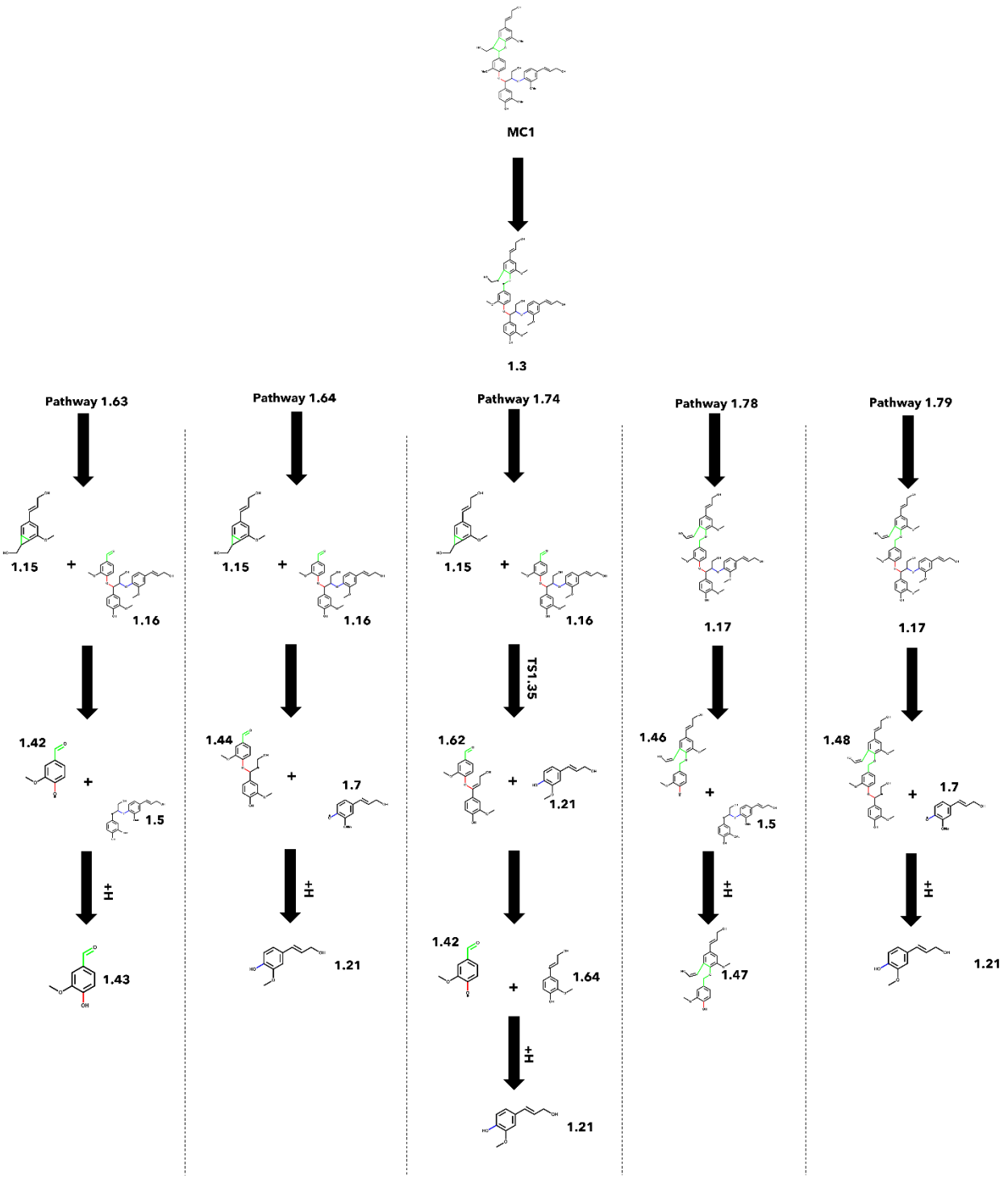

Figure 0-12. Reactions involved in the five lowest energy pathways of each secondary reaction path after resolving the C_{α}-C_{β} diradical of the β-5 interunit linkage.

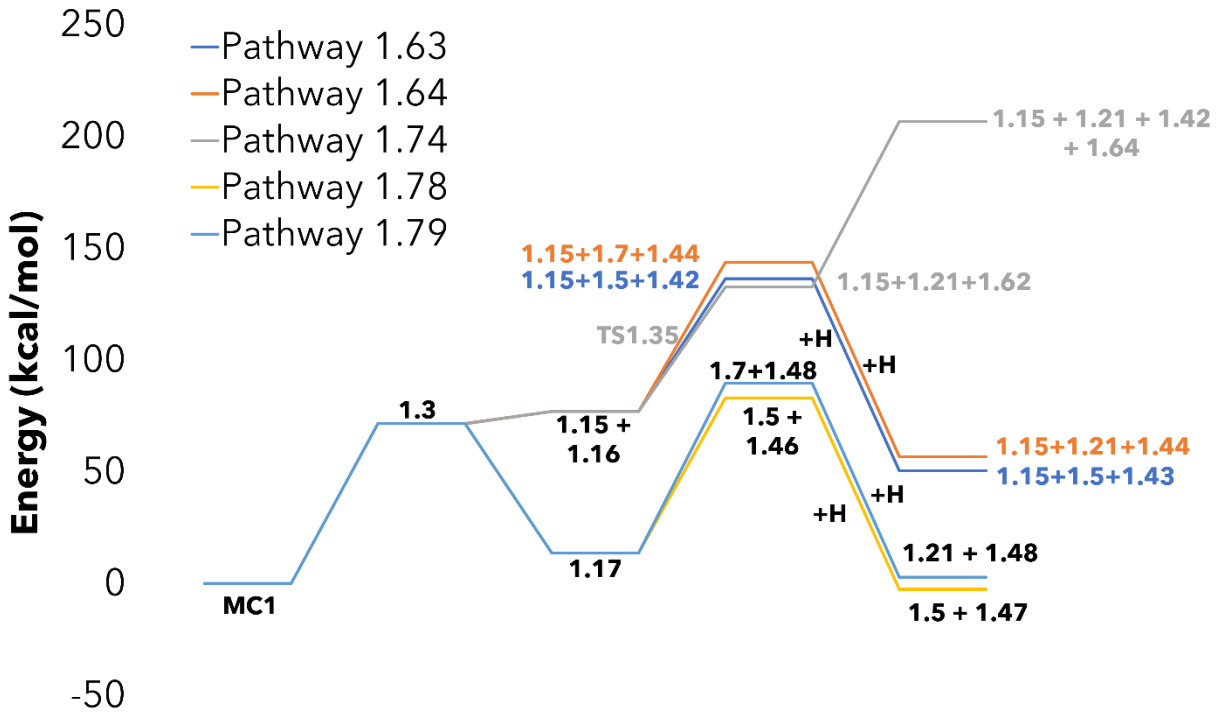

Figure 0-13. Energy diagram for the five lowest energy pathways of each secondary reaction path after resolving the β-5 interunit linkage. Pathways that are similar in magnitude have been color coded for readability.

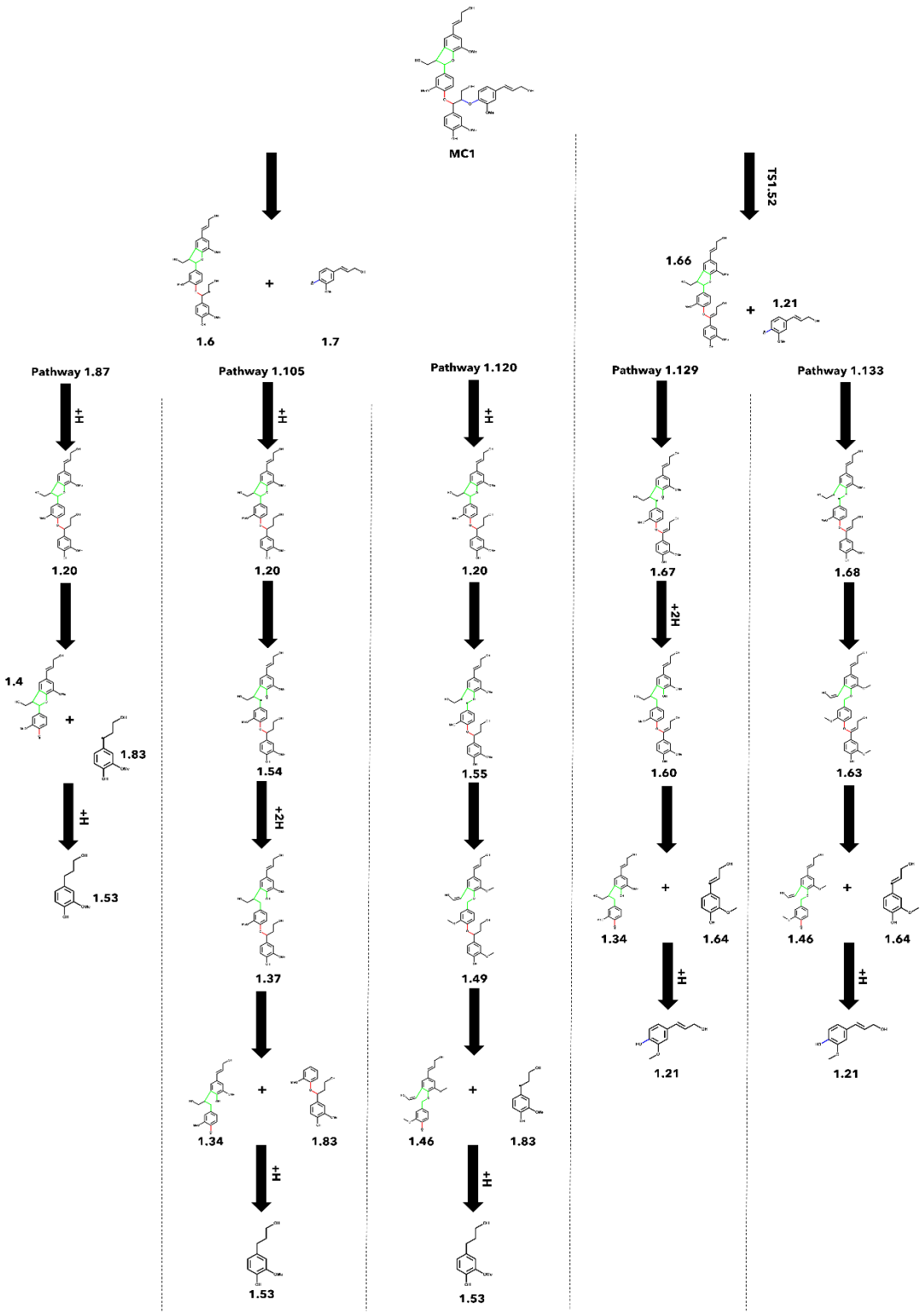

Figure 0-14. Reactions involved in the five lowest energy pathways of each secondary reaction path starting with the resolution of the β-O-4 interunit linkage.

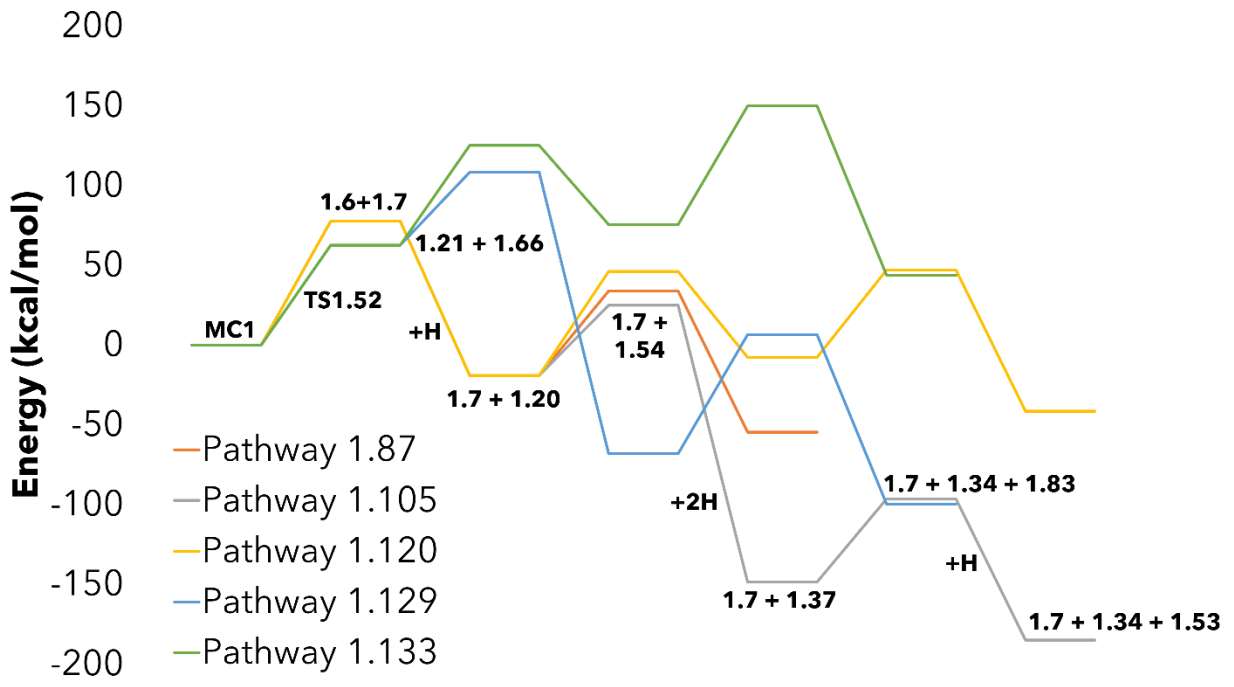

Figure 0-15. Energy diagram for the five lowest energy pathways from distinct branches starting with the resolution of the β-O-4 interunit linkage. The species for the lowest energy pathway have been labeled for clarity.

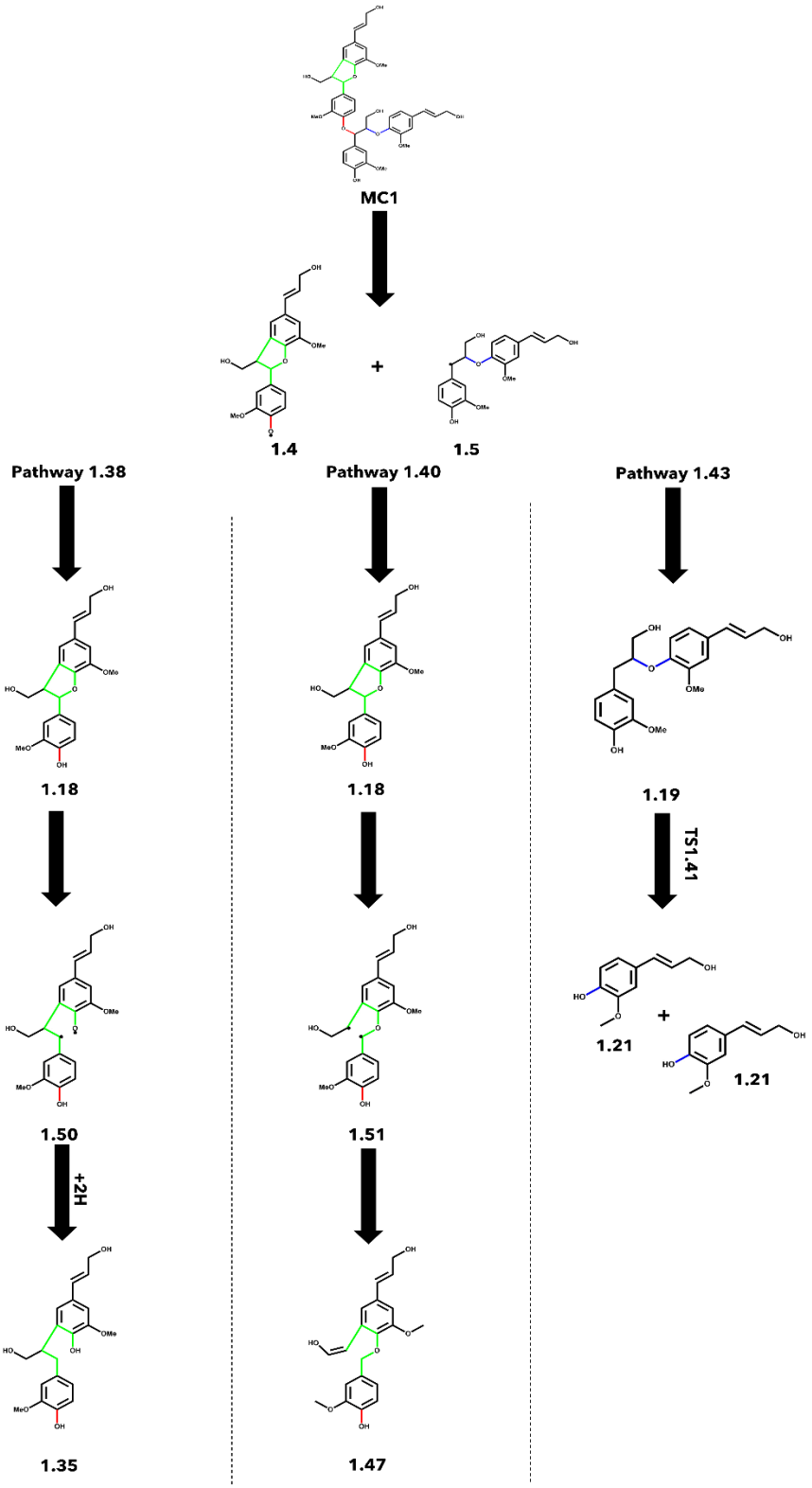

Figure 0-16. Reactions involved in the three lowest energy pathways of each secondary reaction path starting with the resolution of the α-O-4 interunit linkage.

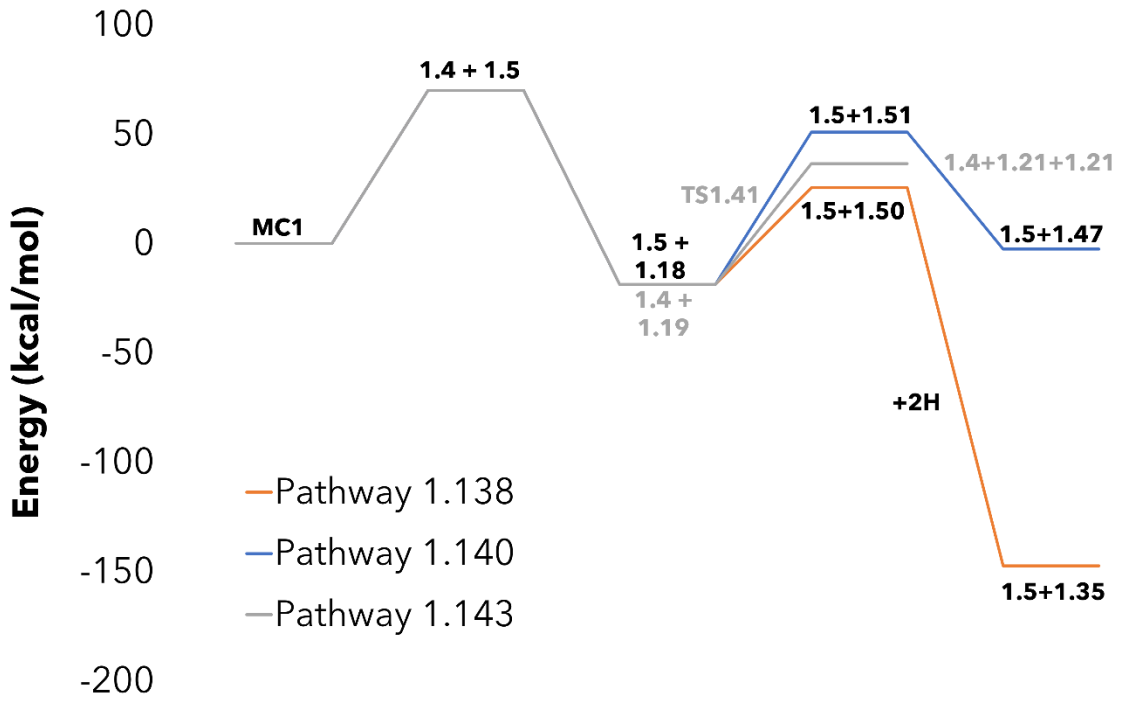

Figure 0-17. Energy diagram for the three lowest energy pathways of each secondary reaction path after resolving the α-O-4 interunit linkage. Pathways that are similar in magnitude have been color coded for readability.

compound 1.7, which can be stabilized via hydrogen addition to produce coniferyl alcohol. These pathways are also expected to be a prevalent source of monomeric products in addition to the pathways shown. Overall, we found the general rules for predicting the hierarchy of reactions for the thermal deconstruction of MC1 to most likely initially proceed through the β-5 class of reactions followed by the α-O-4 and β-O-4.

4.3.2. Reaction pathways for model compound 2

The reaction mechanism for MC2 was proposed by systematically applying the β-O-4 and β-β′ reaction classes to the initial tetramer and any resulting products until reaching stable, final products. In total, 67 species were identified and simulated as a part of 70 unique, individual reactions. These reactions were combined to form 50 distinct reaction pathways for the thermal deconstruction of MC2. Additional information, such as the calculated thermodynamic values for all species, can be found in Appendix IV. In the following sections, reaction pathways will be discussed in terms of the initially applied reaction class.

4.3.2.1. β-β′ C_α-O reaction pathways

In the cases where the initial reaction during the thermal deconstruction of MC2 was the homolytic cleavage of the C_α-O bond in the β-β′ interunit linkage, there were 12 possible reaction pathways. The next step to resolve the resulting diradical was the homolytic cleavage of the C_α-O bond on the opposite side of the β-β′ linkage to form a quad-radical species with an energy barrier of 68.2 kcal/mol.

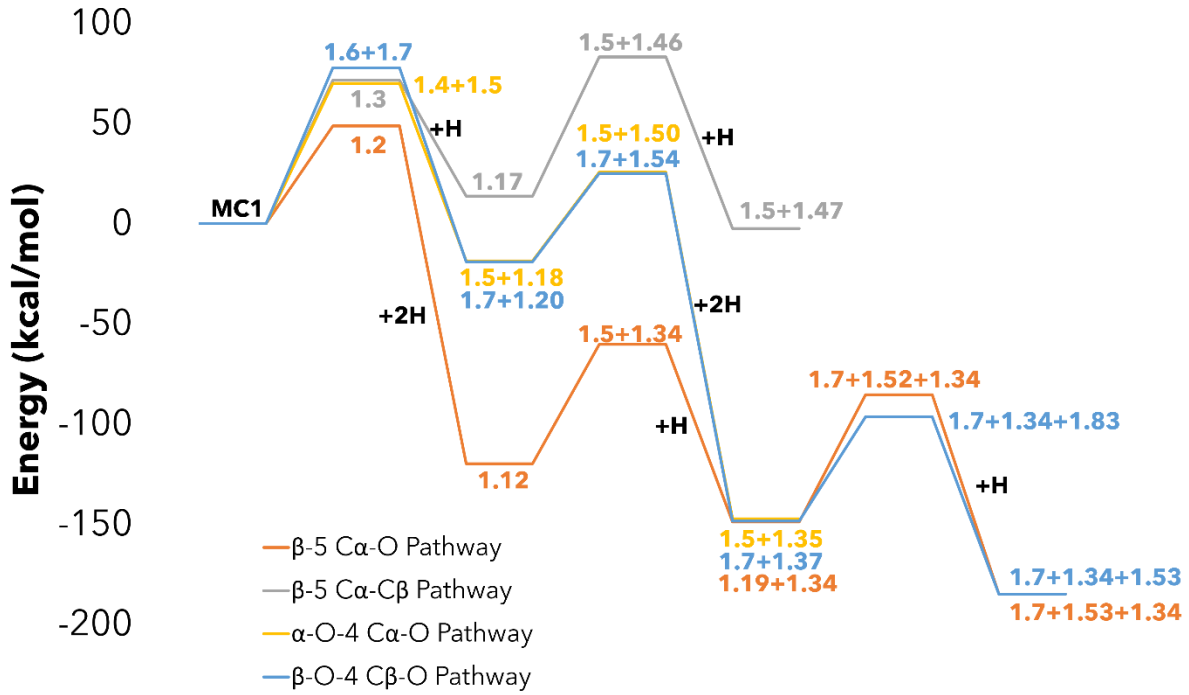

Figure 0-18. Energy diagram for the lowest energy pathway associated with each type of initial reaction.

The quad-radical then undergoes a low-energy barrier (-9.9 kcal/mol) rearrangement to split the β-β′ linkage and form two identical β-O-4 dimer radicals containing a double bond at each C_α-C_β bond, see Figure 0-6. The resulting dimers are cleaved at the C_β-O bond and stabilized via hydrogen addition to stable monomers of sinapyl alcohol and additional aromatic monomers. Due to the symmetry of MC2 along the β-β′ interunit linkage, many of the unique pathways do not differ significantly in their energy profile. The energy barriers associated with the resolution of the β-β′ linkage do not differ regardless of which C_α-O bond is cleaved first.

4.3.2.2. β-β′ C_α-C_β reaction pathways

There are 12 possible reaction pathways starting from the initial cleavage of the C_α-C_β of the β-β′ interunit linkage. However, unlike the C_α-O cleavage in the previous section, the β-β′ linkage can be resolved in two ways: formation of a quad-radical or rearrangement to produce a stable dimer capped with an aldehyde and another diradical dimer. For the initial tetramer, the rearrangement was significantly favored over the formation of the quad-radical species, 26.9 and 71.9 kcal/mol, respectively. The stable dimer produced was shown to undergo cleavage of the C_β-O of the β-O-4 interunit linkage and stabilized via hydrogen addition to form syringaldehyde with energy barriers of 72.1 and -85.7 kcal/mol, respectively.

4.3.2.3. β-O-4 C_β-O reaction pathways

When the initial reaction of MC2 was the homolytic cleavage along the β-O-4 interunit linkage instead of the β-β′ linkage, then there were 26 potential reaction pathways. The energy barrier associated with initiation at the C_β-O is 80.1 kcal/mol and

was found to be the same regardless of which β-O-4 interunit linkage is cleaved. Once the β-O-4 interunit linkage has been resolved, the remaining trimer was proposed to proceed through three possible pathways: cleavage of the remaining β-O-4 linkage (78.9 kcal/mol), ring opening of the β-β′ at the C_α-O bond (70.0-71.6 kcal/mol), or ring opening of the β-β′ at the C_α-C_β bond (70.4-74.6 kcal/mol). The energy barriers for each of the reactions were within 10 kcal/mol; therefore, we expect each pathway to be present during the thermal deconstruction in this scenario. However, the pathway with the lowest energy barrier undergoes resolution of the second β-O-4 interunit linkage via homolytic cleavage and hydrogen addition. The remaining β-β′ was resolved via cleavage of the C_α-C_β bond and stabilization via rearrangement to form two syringaldehyde monomers and butadiene.

4.3.2.4. Overall reaction mechanism for model compound 2

The lowest energy pathways from each type of initiation reaction for the thermal deconstruction of MC2 are shown in Figure 0-19. Unlike in MC1, the pathway originating from the cleavage of the β-O-4 interunit linkage was found to be favored over the pathways initiated by a ring-opening reaction. This can most likely be attributed to the additional step required to resolve the β-β′ interunit linkage compared to the single-ring β-5 linkage in MC1. The additional rearrangement introduces an extra energy barrier that is not present during the resolution of the β-5 interunit linkage.

The secondary β-O-4 interunit linkage had a lower energy barrier than initiating the β-β′ linkage. Even though the initial cleavage of either the C_α-O or C_α-C_β bond of the

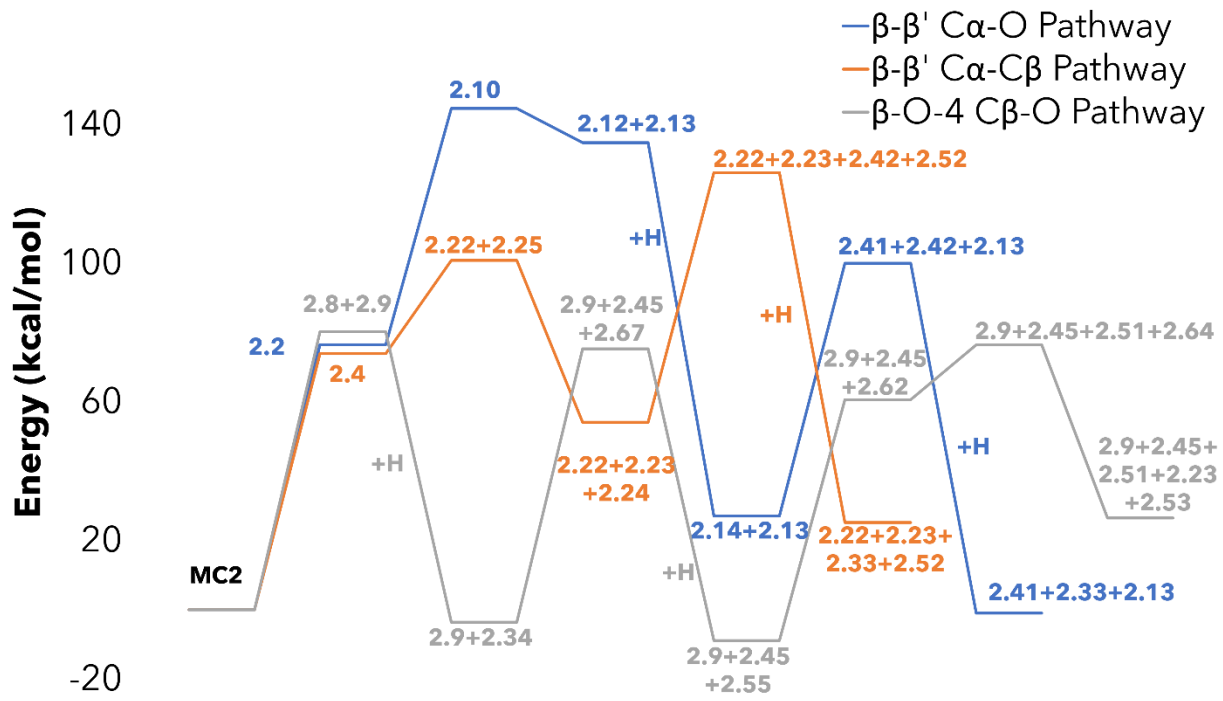

Figure 0-19. Energy diagram for the thermal deconstruction of MC2 with the lowest energy pathway associated with each type of initial reaction.

β-β′ linkage is more energetically favorable than the cleavage of the C_β-O of the β-O-4 interunit linkage (70.0, 74.6, and 78.9 kcal/mol, respectively), the rearrangement requires an additional 68.0 kcal/mol to begin to resolve. Therefore, we would expect the general order of reaction classes to be β-O-4, β-O-4, then β-β′ for MC2. The major monomeric products we expect from MC2 are 1-(4-Hydroxy-3-methoxyphenyl)-1,3-propanediol,sinapyl alcohol, syringaldehyde, and butadiene.

4.3.3. Reaction pathways for model compound 3

The reaction mechanism for MC3 was proposed by systematically applying the β-β′ and 4-O-5 reaction classes to the initial tetramer, and any resulting products, until reaching stable, final products. For the thermal deconstruction of MC3, 61 individual species were proposed, with 69 chemical reactions, leading to 68 unique reaction pathways. Additional information, such as the calculated thermodynamic values for all species, can be found in Appendix IV. In our previous work, it was found that initiation of the 4-O-5 is much less likely to happen compared to β-β′ interunit linkage due to high BDEs associated with homolytic cleavage at an aromatic carbon[23]. Therefore, the following discussions of possible reaction pathways will focus on pathways initiated by the β-β′ reaction class.

4.3.3.1. β-β′ C_α-O reaction pathways

For cases where thermal deconstruction was initiated via the homolytic cleavage of the C_α-O bond of the β-β′ interunit linkage, there were 23 possible reaction pathways. Even though the homolytic cleavage of the 4-O-5 interunit linkage (76.9-82.8 kcal/mol) was generally energetically unfavorable compared to the β-β′ linkage (65.3-

68.6 kcal/mol), the overall lowest energy barrier pathways involve cleavage of the 4-O-5 linkage as the second reaction class after resolution of the initial β-β′ linkage. The cleavage of the C_4-O bond was slightly more favorable than the cleavage of the O-C_5 bond, having energy barriers of 76.9 and 82.8 kcal/mol, respectively. However, the stabilization of the radical on the resulting β-β′ dimers via hydrogen addition is more favorable for the radical on the aromatic C_5 than on the oxygen leading to the lowest energy pathway involving the cleavage of the O-C_5 bond. The second iteration of the β-β′ reaction class lends itself to the production of syringaldehyde, vanillin, and butadiene, which are the primary monomeric products we expect to see.

4.3.3.2. β-β′ C_α- C_β reaction pathways

Initiating the deconstruction of MC3 via the C_α-C_β subclass of the β-β′ reaction class gave rise to 45 unique reaction pathways. Resolution of the diradical was achieved through the two pathways in Figure 0-7. The two-step resolution (33.3 kcal/mol), featuring a five-membered cyclic diradical intermediate, was energetically favorable compared to the single-step resolution (71.5 kcal/mol) to produce the stable trimer along with butadiene and vanillin. Like what was seen in MC2, the symmetrical nature of MC3 showed that it did not matter which β-β′ interunit linkage was resolved first as they effectively have the same energy barriers. The 4-O-5 reaction class was favored as the second reaction class over the remaining β-β′ class. The resolution of these linkages leads to the formation of a mixture of monomeric products, such as methoxybenzaldehyde, vanillin, butadiene, and syringaldehyde.

4.3.3.3. Overall reaction mechanism for model compound 3

The lowest energy pathway from each type of initiation reaction for the thermal deconstruction of MC3 is shown in Figure 0-20. MC3 contains similar interunit linkages to MC2, β-β′, and an ether linkage. However, the reaction behavior shown in MC3 did not follow the same trend shown in MC2. Instead, the β-β′ interunit linkage was more likely to be initially resolved before cleavage of the 4-O-5. This could possibly be attributed to the differences in the ether linkage. As found previously, the 4-O-5 interunit ether linkage is significantly harder to break than the other ether interunit linkages investigated in this work, β-O-4, and α-O-4[23, 24]. The aromatic nature of the carbons of the 4-O-5 significantly strengthens their respective C-O bonds leading to reaction pathways favoring the resolution of the β-β′ interunit linkages first. This is an important distinction in the investigation of these three oligomers. It provides evidence that the surrounding interunit linkages can have an effect on the thermal deconstruction behavior of lignin structures. In the low energy pathways shown in Figure 0-20, the pathways are shown to more favorably proceed through the cleavage of the O-C_5 bond rather than the C_4-O bond, which seems counterintuitive based on the BDEs for these specific reactions, 82.8 to 76.9 kcal/mol, respectively. However, the difference is due to the resulting β-β′ dimers produced from each cleavage. The dimer from the cleavage of the O-C_5 bond has one less hydroxy group than the dimer from

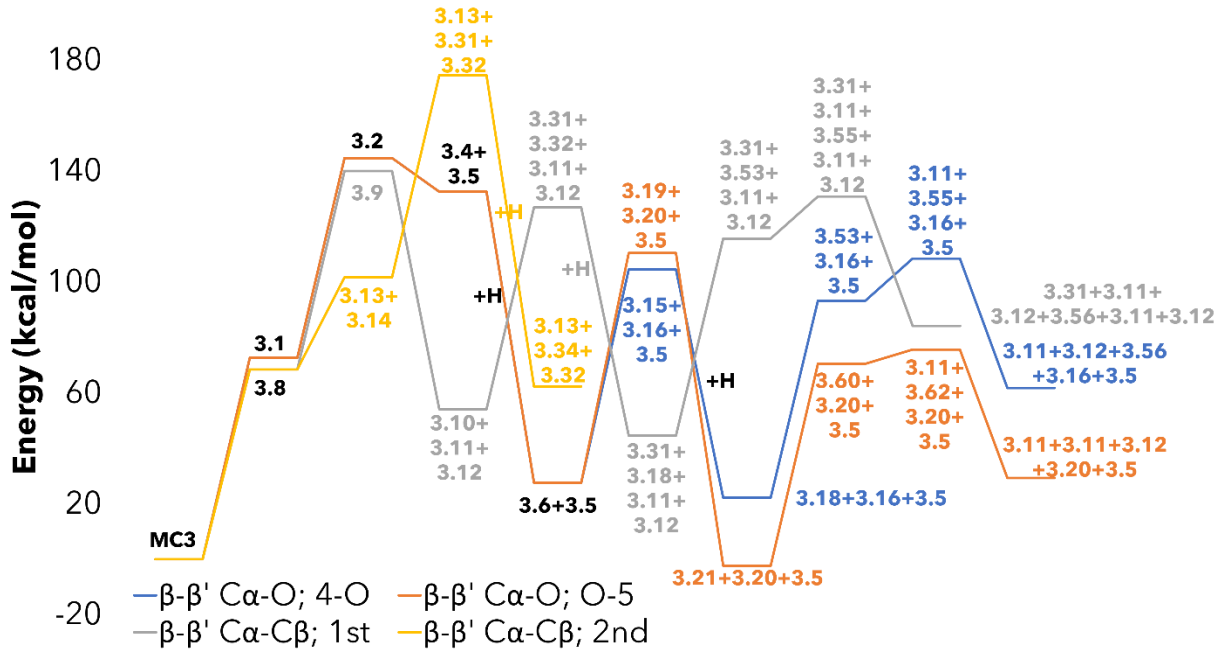

Figure 0-20. Energy diagram for the thermal deconstruction of MC3 with the lowest energy pathway associated with each type of initial reaction.

the C_4-O bond, leading to a lower energy barrier in the subsequent β-β′ class of reactions.

4.5. Conclusions

The diverse linking motifs and structural heterogeneity of lignin make it difficult to develop a mechanistic understanding of the prevalent reaction pathways during the thermal conversion of lignin. However, advancements in computational chemistry and the availability of computing resources create an opportunity to employ DFT-based approaches to probe the cleavage of multiple lignin interlinkages during pyrolysis, bringing us a step closer to developing mechanisms for well-characterized native lignin fragments. In this work, we investigated the reaction pathways of three model lignin oligomers containing several important interunit linkages, β-O-4, α-O-4, β-5, β-β′, and 4-O-5, during thermal deconstruction at 500 °C and proposed a rationale DFT-based approach to derive their reaction mechanisms. Reaction classes containing the possible relevant reactions for each interunit linkage were postulated and applied to each oligomer using recursive logic to find the prevalent reaction pathways for each model compound. For MC1, we found the β-5 interunit linkage to be a prevalent initial reaction point followed by the α-O-4 and β-O-4 linkages, which, if allowed to proceed to monomeric products, would yield coniferyl alcohol and its derivatives. MC2 introduced the β-β′ interunit linkage, and even though the structure is similar to the β-5 linkage in MC1, the need for a secondary rearrangement meant the β-O-4 linkages were the prevalent initial reaction point followed by both β-β′ linkage. The major monomeric products we expect from MC2 are 1-(4-hydroxy-3-methoxyphenyl)-1,3-

propanediol, sinapyl alcohol, syringaldehyde, and butadiene. The β-β′ linkages were also present in MC3; however, instead of a β-O-4 linkage, there was a 4-O-5 interunit linkage. This aromatic ether linkage is significantly harder to break than its β-O-4 ether counterpart; therefore, the β-β′ pathways were favored as initial reaction points compared to the ether linkage being predominant in MC2.

This work is an important first step and provides a valuable proof of concept for the development of a general reaction library and the generation of a reaction hierarchy. These rules can then be applied in a logical way to larger, more representative lignin structures to serve as a mechanistic foundation for the implementation of a detailed reaction mechanism closer to the level of cellulose and hemicellulose.

References

1. Zhou, X.; Li, W.; Mabon, R.; Broadbelt, L. J., A mechanistic model of fast pyrolysis of hemicellulose. *Energy & Environmental Science* **2018,** *11* (5), 1240-1260.
2. Zhou, X.; Nolte, M. W.; Mayes, H. B.; Shanks, B. H.; Broadbelt, L. J., Experimental and Mechanistic Modeling of Fast Pyrolysis of Neat Glucose-Based Carbohydrates. 1. Experiments and Development of a Detailed Mechanistic Model. *Industrial & Engineering Chemistry Research* **2014,** *53* (34), 13274-13289.
3. Vinu, R.; Broadbelt, L. J., A mechanistic model of fast pyrolysis of glucose-based carbohydrates to predict bio-oil composition. *Energy & Environmental Science* **2012,** *5* (12), 9808-9826.
4. Mayes, H. B.; Broadbelt, L. J., Unraveling the Reactions that Unravel Cellulose. *The Journal of Physical Chemistry A* **2012,** *116* (26), 7098-7106.
5. Nowakowski, D. J.; Bridgwater, A. V.; Elliott, D. C.; Meier, D.; de Wild, P., Lignin fast pyrolysis: Results from an international collaboration. *Journal of Analytical and Applied Pyrolysis* **2010,** *88* (1), 53-72.
6. Lahive, C. W.; Kamer, P. C. J.; Lancefield, C. S.; Deuss, P. J., An Introduction to Model Compounds of Lignin Linking Motifs; Synthesis and Selection Considerations for Reactivity Studies. *ChemSusChem* **2020,** *13* (17), 4238-4265.
7. Glasser, W. G., About Making Lignin Great Again—Some Lessons From the Past. *Frontiers in Chemistry* **2019,** *7* (565).
8. Azad, T.; Schuler, J. D.; Auad, M. L.; Elder, T.; Adamczyk, A. J., Model Lignin Oligomer Pyrolysis: Coupled Conformational and Thermodynamic Analysis of β-O-4′ Bond Cleavage. *Energy & Fuels* **2020,** *34* (8), 9709-9724.
9. Azad, T.; Torres, H. F.; Auad, M. L.; Elder, T.; Adamczyk, A. J., Isolating key reaction energetics and thermodynamic properties during hardwood model lignin pyrolysis. *Physical Chemistry Chemical Physics* **2021**.
10. Supriyanto; Usino, D. O.; Ylitervo, P.; Dou, J.; Sipponen, M. H.; Richards, T., Identifying the primary reactions and products of fast pyrolysis of alkali lignin. *Journal of Analytical and Applied Pyrolysis* **2020,** *151*, 104917.
11. Elder, T., Bond Dissociation Enthalpies of a Pinoresinol Lignin Model Compound. *Energy & Fuels* **2014,** *28* (2), 1175-1182.
12. Elder, T.; Beste, A., Density Functional Theory Study of the Concerted Pyrolysis Mechanism for Lignin Models. *Energy & Fuels* **2014,** *28* (8), 5229-5235.
13. Huang, J.; He, C.; Liu, C.; Tong, H.; Wu, L.; Wu, S., A computational study on thermal decomposition mechanism of β-1 linkage lignin dimer. *Computational and Theoretical Chemistry* **2015,** *1054*, 80-87.
14. Huang, J.-b.; Wu, S.-b.; Cheng, H.; Lei, M.; Liang, J.-j.; Tong, H., Theoretical study of bond dissociation energies for lignin model compounds. *Journal of Fuel Chemistry and Technology* **2015,** *43* (4), 429-436.
15. Huang, J.; He, C., Pyrolysis mechanism of α-O-4 linkage lignin dimer: A theoretical study. *Journal of Analytical and Applied Pyrolysis* **2015,** *113*, 655-664.

16. Huang, J.; Liu, C.; Wu, D.; Tong, H.; Ren, L., Density functional theory studies on pyrolysis mechanism of β-O-4 type lignin dimer model compound. *Journal of Analytical and Applied Pyrolysis* **2014,** *109*, 98-108.
17. Liu, C.; Zhang, Y.; Huang, X., Study of guaiacol pyrolysis mechanism based on density function theory. *Fuel Processing Technology* **2014,** *123*, 159-165.
18. Huang, J.-b.; Liu, C.; Ren, L.-r.; Tong, H.; Li, W.-m.; Wu, D., Studies on pyrolysis mechanism of syringol as lignin model compound by quantum chemistry. *Journal of Fuel Chemistry and Technology* **2013,** *41* (6), 657-666.
19. Huang, J.; Li, X.; Wu, D.; Tong, H.; Li, W., Theoretical studies on pyrolysis mechanism of guaiacol as lignin model compound. *Journal of Renewable and Sustainable Energy* **2013,** *5* (4), 043112.
20. Kim, S.; Chmely, S. C.; Nimlos, M. R.; Bomble, Y. J.; Foust, T. D.; Paton, R. S.; Beckham, G. T., Computational Study of Bond Dissociation Enthalpies for a Large Range of Native and Modified Lignins. *The Journal of Physical Chemistry Letters* **2011,** *2* (22), 2846-2852.
21. Parthasarathi, R.; Romero, R. A.; Redondo, A.; Gnanakaran, S., Theoretical Study of the Remarkably Diverse Linkages in Lignin. *The Journal of Physical Chemistry Letters* **2011,** *2* (20), 2660-2666.
22. Azad, T.; Auad, M. L.; Elder, T.; Adamczyk, A. J., Toward Native Hardwood Lignin Pyrolysis: Insights into Reaction Energetics from Density Functional Theory. *Energy & Fuels* **2023,** *37* (1), 401-423.
23. Houston, R. W.; Abdoulmoumine, N. H., Investigation of the thermal deconstruction of β-β' and 4-O-5 linkages in lignin model oligomers by density functional theory (DFT). *RSC Advances* **2023,** *13* (9), 6181-6190.
24. Houston, R. W.; Elder, T. J.; Abdoulmoumine, N. H., Investigation into the Pyrolysis Bond Dissociation Enthalpies (BDEs) of a Model Lignin Oligomer Using Density Functional Theory (DFT). *Energy & Fuels* **2022**.
25. Quideau, S.; Ralph, J., A Biomimetic Route to Lignin Model Compounds via Silver (I) Oxide Oxidation. 1. Synthesis of Dilignols and Non-cyclic Benzyl Aryl Ethers. *Holzforschung - International Journal of the Biology, Chemistry, Physics and Technology of Wood* **1994,** *48* (1), 12-22.
26. Ralph, J.; Lapierre, C.; Boerjan, W., Lignin structure and its engineering. *Current Opinion in Biotechnology* **2019,** *56*, 240-249.
27. Matsuda, S.; Kadota, S.; Tai, T.; Kikuchi, T., Isolation and Structures of Hedyotisol-A, -B, and -C Novel Dilignans From Hedyotis Lawsoniae. *Chemical & Pharmaceutical Bulletin* **1984,** *32* (12), 5066-5069.
28. Yue, F.; Lu, F.; Ralph, S.; Ralph, J., Identification of 4–O–5-Units in Softwood Lignins via Definitive Lignin Models and NMR. *Biomacromolecules* **2016,** *17* (6), 1909-1920.
29. Zakzeski, J.; Bruijnincx, P. C. A.; Jongerius, A. L.; Weckhuysen, B. M., The Catalytic Valorization of Lignin for the Production of Renewable Chemicals. *Chemical Reviews* **2010,** *110* (6), 3552-3599.
30. Chakar, F. S.; Ragauskas, A. J., Review of current and future softwood kraft lignin process chemistry. *Industrial Crops and Products* **2004,** *20* (2), 131-141.

31. Zhao, Y.; Truhlar, D. G., The M06 suite of density functionals for main group thermochemistry, thermochemical kinetics, noncovalent interactions, excited states, and transition elements: two new functionals and systematic testing of four M06-class functionals and 12 other functionals. *Theoretical Chemistry Accounts* **2008,** *120* (1), 215-241.
32. Hehre, W. J.; Ditchfield, R.; Pople, J. A., Self–Consistent Molecular Orbital Methods. XII. Further Extensions of Gaussian–Type Basis Sets for Use in Molecular Orbital Studies of Organic Molecules. *The Journal of Chemical Physics* **1972,** *56* (5), 2257-2261.
33. Hariharan, P. C.; Pople, J. A., The influence of polarization functions on molecular orbital hydrogenation energies. *Theoretica chimica acta* **1973,** *28* (3), 213-222.
34. Clark, T.; Chandrasekhar, J.; Spitznagel, G. W.; Schleyer, P. V. R., Efficient diffuse function-augmented basis sets for anion calculations. III. The 3-21+G basis set for first-row elements, Li–F. *Journal of Computational Chemistry* **1983,** *4* (3), 294-301.
35. Grimme, S.; Antony, J.; Ehrlich, S.; Krieg, H., A consistent and accurate ab initio parametrization of density functional dispersion correction (DFT-D) for the 94 elements H-Pu. *The Journal of Chemical Physics* **2010,** *132* (15), 154104.
36. McQuarrie, D. A., *Statistical Mechanics*. University Science Books: 2000.
37. Verdicchio, M.; Sirjean, B.; Tran, L. S.; Glaude, P.-A.; Battin-Leclerc, F., Unimolecular decomposition of tetrahydrofuran: Carbene vs. diradical pathways. *Proceedings of the Combustion Institute* **2015,** *35* (1), 533-541.
38. Kotake, T.; Kawamoto, H.; Saka, S., Pyrolysis reactions of coniferyl alcohol as a model of the primary structure formed during lignin pyrolysis. *Journal of Analytical and Applied Pyrolysis* **2013,** *104*, 573-584.
39. Yerrayya, A.; Natarajan, U.; Vinu, R., Fast pyrolysis of guaiacol to simple phenols: Experiments, theory and kinetic model. *Chemical Engineering Science* **2019,** *207*, 619-630.

Appendix IV

Table AIV-1. Thermal enthalpies and thermal free energies for each structure in the investigation of MC1.

Compound	Thermal Enthalpy (Hartrees)	Thermal Free Energy (Hartrees)
MC1	-2451.982252	-2452.681008
1.2	-2451.904637	-2452.610166
1.3	-2451.868321	-2452.576057
1.4	-1225.351695	-1225.740942
1.5	-1226.519138	-1226.920303
1.6	-1838.920657	-1839.481914
1.7	-612.937826	-613.165786
1.8	-2451.966756	-2452.671471
1.9	-2451.982251	-2452.681072
1.10	-612.232372	-612.45345
1.11	-1839.547171	-1840.100485
1.12	-2453.157522	-2453.86978
1.13	-805.37616	-805.662026
1.14	-1647.729327	-1648.226203
1.15	-690.826832	-691.08159
1.16	-1761.032705	-1761.550521
1.17	-2451.960471	-2452.654394
1.18	-1225.984856	-1226.372737
1.19	-1227.152378	-1227.555543
1.20	-1839.566994	-1840.124805
1.21	-613.568358	-613.795325
1.22	-1225.345487	-1225.733632
1.23	-1225.977186	-1226.367597
1.24	-1838.912212	-1839.477019
1.25	-1839.559643	-1840.120855
1.26	-1225.30295	-1225.694362
1.27	-1225.930747	-1226.324567
1.28	-1838.866294	-1839.432525
1.29	-1839.515288	-1840.081177
1.30	-612.938077	-613.161408

Table AIV-1. Continued

Compound	Thermal Enthalpy (Hartrees)	Thermal Free Energy (Hartrees)
1.31	-613.56771	-613.793193
1.32	-1226.502541	-1226.900976
1.33	-1227.149906	-1227.548766
1.34	-1226.543549	-1226.934511
1.35	-1227.174273	-1227.566464
1.36	-1840.110066	-1840.675618
1.37	-1840.757463	-1841.325827
1.38	-421.11836	-421.280826
1.39	-421.752426	-421.91639
1.40	-1034.687257	-1035.024782
1.41	-1035.334768	-1035.674
1.42	-534.419005	-534.604027
1.43	-535.047909	-535.234803
1.44	-1147.98859	-1148.34885
1.45	-1148.636521	-1148.995173
1.46	-1225.330769	-1225.716274
1.47	-1225.959307	-1226.343057
1.48	-1838.901488	-1839.458945
1.49	-1839.548935	-1840.10503
1.50	-1225.914501	-1226.303589
1.51	-1225.874027	-1226.270419
1.52	-614.113208	-614.350325
1.53	-614.764043	-614.996312
1.54	-1839.49679	-1840.05796
1.55	-1839.463054	-1840.01678
1.56	-1838.375876	-1838.919657
1.57	-1225.954079	-1226.347823
1.58	-1838.326566	-1838.878396
1.59	-1225.958724	-1226.346795
1.60	-1839.569578	-1840.110862
1.61	-1034.14339	-1034.471432
1.62	-1147.444348	-1147.793742
1.63	-1838.356533	-1838.911765
1.64	-612.907268	-613.137718
1.65	-612.902558	-613.129112
1.66	-1838.377128	-1838.925407
1.67	-1838.304385	-1838.861359
1.68	-1838.277409	-1838.818314

Table AIV-1. Continued

Compound	Thermal Enthalpy (Hartrees)	Thermal Free Energy (Hartrees)
1.70	-1725.093402	-1725.628388
1.71	-1725.023335	-1725.558895
1.72	-1724.982287	-1725.522438
1.73	-1725.092102	-1725.610913
1.74	-1725.048454	-1725.587935
1.75	-1112.673708	-1113.048453
1.76	-1726.291045	-1726.812892
1.77	-920.861002	-921.171336
1.78	-1034.162555	-1034.493241
1.79	-1725.083158	-1725.596691
1.80	-499.657484	-499.858772
1.81	-500.290229	-500.493108
1.82	-499.090872	-499.285986
1.83	-614.130871	-614.361602
IM1.1	-613.521081	-613.748125
CH2O	-114.448313	-114.524646
H	-0.492074	-0.531655
TS1.10	-1227.005425	-1227.403909
TS1.16	-1840.586577	-1840.158245
TS1.20	-2451.87649	-2452.579767
TS1.21	-613.438874	-613.665348
TS1.26	-1839.450503	-1840.004449
TS1.32	-1647.635627	-1648.130267
TS1.34	-1647.636709	-1648.130999
TS1.35	-1760.936626	-1761.461885
TS1.41	-1227.076532	-1227.467598
TS1.52	-2451.886354	-2452.581275
TS1.67	-1839.422401	-1839.982274
TS1.68	-1839.377836	-1839.941029
TS1.71	-1035.197279	-1035.532936
TS1.72	-1148.498923	-1148.854164
TS1.75	-1724.965506	-1725.504814
TS1.76	-1112.594524	-1112.969904
TS1.78	-920.777851	-921.085878
TS1.79	-1034.085044	-1034.420607

Table AIV-2. Thermal enthalpies and thermal free energies for each structure in the investigation of MC2.

Compound	Thermal Enthalpy (Hartrees)	Thermal Free Energy (Hartrees)
MC2	-2832.582844	-2833.331059
2.2	-2832.460963	-2833.217265
2.3	-2832.460962	-2833.217265
2.4	-2832.465104	-2833.229883
2.5	-2832.465104	-2833.229883
2.6	-2143.130041	-2143.712892
2.7	-689.325141	-689.568551
2.8	-2143.13004	-2143.712891
2.9	-689.325141	-689.568551
2.10	-2832.352363	-2833.120267
2.11	-2832.352622	-2833.126325
2.12	-1416.183828	-1416.608856
2.13	-1416.184268	-1416.608762
2.14	-1416.847642	-1417.263985
2.15	-1416.841330	-1417.268067
2.16	-2832.460908	-2833.218242
2.17	-1416.183828	-1416.608874
2.18	-1416.847642	-1417.263979
2.19	-1416.183828	-1416.608872
2.20	-1416.841224	-1417.268111
2.21	-2832.350554	-2833.131178
2.22	-1338.328830	-1338.716792
2.23	-155.839074	-155.952850
2.24	-1338.328831	-1338.716806
2.25	-1494.093448	-1494.544163
2.26	-2143.755517	-2144.342904
2.27	-2143.641366	-2144.241644
2.28	-2143.527298	-2144.130162
2.29	-727.371041	-727.626419
2.30	-728.030339	-728.287895
2.31	-1416.185657	-1416.608008
2.32	-1416.842536	-1417.267854
2.33	-689.978104	-690.218683
2.34	-2143.755517	-2144.342905

Table AIV-2. Continued

Compound	Thermal Enthalpy (Hartrees)	Thermal Free Energy (Hartrees)
2.35	-2143.644022	-2144.238297
2.36	-2143.535662	-2144.141758
2.37	-727.371041	-727.626416
2.38	-728.030339	-728.287895
2.39	-1416.185657	-1416.608008
2.40	-1416.842575	-1417.267662
2.41	-727.406270	-727.659387
2.42	-689.325141	-689.568554
2.43	-727.404445	-727.658725
2.44	-728.027990	-728.285466
2.45	-689.325141	-689.568564
2.46	-689.973208	-690.217824
2.48	-727.406270	-727.659387
2.49	-728.030339	-728.287879
2.50	-648.888843	-649.102724
2.51	-649.517759	-649.734045
2.52	-648.888843	-649.102724
2.53	-649.517758	-649.734056
2.54	-1454.304713	-1454.727981
2.55	-1454.930856	-1455.357220
2.56	-1454.818567	-1455.256391
2.57	-1454.713909	-1455.159594
2.58	-727.370966	-727.626897
2.59	-728.030282	-728.288203
2.60	-2143.643304	-2144.236134
2.61	-2143.541582	-2144.132892
2.62	-1454.820103	-1455.257287
2.63	-1454.726189	-1455.164643
2.64	-805.277175	-805.559720
2.65	-2143.636631	-2144.245797
2.66	-2143.52811	-2144.133116
2.67	-1454.304713	-1454.727984

Table AIV-3. Thermal enthalpies and thermal free energies for each structure in the investigation of MC3.

Compound	Thermal Enthalpy (Hartrees)	Thermal Free Energy (Hartrees)
MC3	-2450.850151	-2451.496834
3.1	-2450.734424	-2451.394237
3.2	-2450.619708	-2451.294318
3.4	-1837.729898	-1838.251002
3.5	-612.909102	-613.134268
3.6	-1838.389211	-1838.91322
3.7	-613.567634	-613.792483
3.8	-2450.741107	-2451.407171
3.9	-2450.627093	-2451.312029
3.10	-1759.873055	-1760.367012
3.11	-535.056121	-535.24211
3.12	-155.834736	-155.948811
3.13	-690.815032	-691.067736
3.14	-1759.873055	-1760.367012
3.15	-1300.593658	-1300.973105
3.16	-537.672972	-537.886793
3.17	-538.344103	-538.557278
3.18	-1301.216885	-1301.595995
3.19	-1225.32565	-1225.694966
3.20	-612.931581	-613.158763
3.21	-1225.997443	-1226.366218
3.22	-1838.279884	-1838.816218
3.23	-1838.285012	-1838.821045
3.24	-1838.165641	-1838.713431
3.25	-1225.285931	-1225.667486
3.26	-1225.946537	-1226.331926
3.28	-1838.175704	-1838.727834
3.29	-1147.427251	-1147.783696
3.30	-1303.192399	-1303.609251
3.31	-459.163447	-459.338685
3.32	-1300.593659	-1300.9731
3.33	-1301.222388	-1301.602696
3.34	-459.834253	-460.008872
3.35	-534.418392	-534.605372

Table AIV-3. Continued

Compound	Thermal Enthalpy (Hartrees)	Thermal Free Energy (Hartrees)
3.36	-1225.32565	-1225.694965
3.37	-1225.997442	-1226.366204
3.39	-1759.756222	-1760.271979
3.40	-1759.765032	-1760.269704
3.41	-1759.631936	-1760.150474
3.42	-1146.77167	-1147.128681
3.43	-1147.430815	-1147.789966
3.45	-1759.649704	-1760.166451
3.46	-1068.916434	-1069.234408
3.47	-1224.680086	-1225.062609
3.48	-1301.10066	-1301.498387
3.49	-1301.176762	-1301.176762
3.50	-688.116501	-688.357592
3.51	-688.773695	-689.016949
3.53	-1301.10367	-1301.508435
3.54	-1301.000257	-1301.398761
3.55	-766.023383	-766.291368
3.56	-610.26294	-610.464126
3.57	-1225.883235	-1226.269039
3.58	-1225.760736	-1226.154955
3.60	-1225.881338	-1226.271262
3.61	-1225.768055	-1226.173657
3.62	-690.817069	-691.070637
3.63	-688.151738	-688.389835
3.64	-612.883917	-613.113474
3.65	-609.636195	-609.83451
3.66	-534.372629	-534.560536

Table AIV-4. List of reactions involved in the investigation of MC1 and their respective energy barrier.

Reaction #	Reactant	Hydrogen	Product 1	Product 2	TS#	dH (kcal/mol)
1	1		2			48.70
2	1		3			71.49
3	1		4	5		69.92
4	1		6	7		77.67
5	2		8			-38.98
6	2		9			-48.70
7	2		10	11		78.50
8	2	2	12			-168.63
9	12		13	14		32.65
10	3		15	16		5.51
11	3		17			-57.82
12	4	1	18			-88.53
13	5	1	19			-88.58
14	6	1	20			-96.80
15	7	1	21			-86.88
16	8		22	5		64.09
17	22	1	23			-87.61
18	8		24	7		73.24
19	24	1	25			-97.49
20	9		26	5		100.50
21	26	1	27			-85.17
22	9		28	7		111.78
23	28	1	29			-98.47
24	11		30	5		56.45
25	30	1	31			-86.32
26	11		32	7		67.02
27	32	1	33			-97.45
28	12		34	5		59.51
29	34	1	35			-87.00
30	12		36	7		68.79
31	36	1	37			-97.47
32	14		38	5		57.62
33	38	1	39			-89.10
34	14		40	7		65.41
35	40	1	41			-97.54
36	16		42	5		59.34

Table AIV-4. Continued

Reaction #	Reactant	Hydrogen	Product 1	Product 2	TS#	dH (kcal/mol)
37	42	1	43			-85.86
38	16		44	7		66.70
39	44	1	45			-97.80
40	17		46	5		69.38
41	46	1	47			-85.63
42	17		48	7		76.03
43	48	1	49			-97.50
44	18		50			44.15
45	18		51			69.55
46	50		23			-39.33
47	50		27			-10.19
48	50		10	31		71.80
49	50	2	35			-172.95
50	35		13	39		28.67
51	51		15	43		-0.45
52	51		47			-53.51
53	19		52	7		63.59
54	52	1	53			-99.62
55	20		4	83		52.98
56	83	1	53			-88.54
57	20		54			44.05
58	20		55			65.22
59	54		25			-39.44
60	54		29			-11.61
61	54		10	33		71.86
62	54	2	37			-173.52
63	37		13	41	TS16	732.66
64	55		15	45		-0.19
65	55		49			-53.89
66	25		22	83		52.26
67	29		26	83		51.12
68	33		30	83		50.80
69	37		34	83		52.11
70	41		38	83		53.67
71	45		42	83		54.37
72	49		46	83		54.78

Table AIV-4. Continued

Reaction #	Reactant	Hydrogen	Product 1	Product 2	TS#	dH (kcal/mol)
73	8		56	IM1	TS20	57.54
74	IM1		21		TS21	51.94
75	11		59	21	TS26	60.26
76	14		61	21	TS32	60.20
77	14		39	57	TS34	59.74
78	16		62	21	TS35	55.62
79	19		21	21	TS41	55.19
80	56		22	64		77.26
81	64	1	21			-106.06
82	57		7	65		71.34
83	65	1	21			-109.01
84	58		26	64		73.01
85	59		30	64		71.15
86	60		34	64		74.52
87	61		38	64		73.90
88	62		42	64		74.09
89	63		46	64		74.36
90	1		66	21	TS52	62.58
91	66		67			45.65
92	66		68			62.57
93	67		56			-44.86
94	67		58			-13.92
95	67		59	10		71.09
96	67	2	60			-176.36
97	68		15	62		3.91
98	68		63			-49.65
99	6	-1	66			32.29
100	24	-1	56			27.77
101	28	-1	58			29.90
102	32	-1	59			32.47
103	36	-1	60			30.38
104	40	-1	61			32.50
105	44	-1	62			32.74
106	48	-1	63			33.18
107	70		71			43.97
108	70		72			69.72
109	71		73			-43.15
110	71		74			-15.76

Table AIV-4. Continued

Reaction #	Reactant	Hydrogen	Product 1	Product 2	TS#	dH (kcal/mol)
111	71		10	75		73.58
112	71	2	76			-177.94
113	72		15	78		-4.46
114	72		79			-63.30
115	25		73	ch2o	TS67	86.96
116	29		74	ch2o	TS68	87.94
117	41		77	ch2o	TS71	88.52
118	45		78	ch2o	TS72	88.48
119	73		22	80		55.93
120	80	1	81			-88.27
121	74		26	80		55.23
122	74		27	82	TS75	52.16
123	75		30	80		49.04
124	76		34	80		56.48
125	77		38	80		53.44
126	77		39	82	TS78	53.62
127	78		42	80		54.01
128	78		43	82	TS79	45.58
129	79		46	80		59.55
130	52	-1	21			33.12
131	80	-1	82			46.77
132	83	-1	21			44.20

Table AIV-5. List of reactions involved in the investigation of MC2 and their respective energy barrier.

Reaction #	Reactant	Hydrogen	Product 1	Product 2	Product 3	dH (kcal/mol)
1	1		2			76.48
2	1		3			76.48
3	1		4			73.88
4	1		5			73.88
5	1		6	7		80.11
6	1		8	9		80.11
7	2		10			68.15
8	2		16			0.03
9	16		17	19		58.52
10	17	1	18			-107.77
11	19	1	20			-103.74
12	3	0	11			67.98
13	10	0	13	12		-9.87
14	12	1	14			-107.77
15	13	1	15			-103.53
16	4	0	21			71.88
17	5	0	21			71.88
18	21	0	22	23	24	-91.73
19	4	0	22	25		26.87
20	25	0	23	24		-46.72
21	6	1	26			-83.71
22	26	0	27			71.63
23	27	0	28			71.58
24	28	0	29	31		-18.45
25	29	1	30			-104.93
26	31	1	32			-103.42
27	7	1	33			-100.96
28	8	1	34			-83.71
29	34	0	35			69.96
30	35	0	36			68.00
31	36	0	37	39		-13.20
32	37	1	38			-104.93
33	39	1	40			-103.44
34	14	0	41	42		72.93
35	41	1	38			-82.83
36	42	1	33			-100.96

Table AIV-5. Continued

Reaction #	Reactant	Hydrogen	Product 1	Product 2	Product 3	dH (kcal/mol)
37	15	0	43	45		70.12
38	43	1	44			-82.50
39	45	1	46			-97.89
40	18	0	42	41		72.93
41	42	1	33			-100.96
42	48	1	49			-82.83
43	22	0	45	50		72.07
44	50	1	51			-85.87
45	24	0	42	52		72.07
46	52	1	53			-85.87
47	26	0	42	54		78.85
48	54	1	55			-84.13
49	55	0	56			70.46
50	56	0	57			65.67
51	55	0	62			69.50
52	62	0	63			58.93
53	63	0	23	51	53	-93.12
54	62	0	51	64		15.79
55	64	0	23	53		-49.98
56	57	0	29	58		-17.63
57	58	1	59			-104.94
58	26	0	60			70.41
59	60	0	61			63.83
60	61	0	23	24	51	-90.41
61	60	0	25	51		20.14
62	32	0	42	41		69.73
63	34	0	67	45		78.85
64	67	1	55			-84.13
65	34	0	65			74.60
66	65	0	66			68.10
67	66	0	22	64		-48.88
68	64	0	23	53		-49.98
69	66	0	22	23	53	-98.86
70	40	0	43	45		70.90

Table AIV-6. List of reactions involved in the investigation of MC3 and their respective energy barrier.

Reaction #	Reactant	Hydrogen	Product 1	Product 2	Product #3	dH (kcal/mol)
1	MC3		1			72.62
2	MC3		8			68.43
3	1		2			71.98
4	2		4	5		-12.11
5	4	1	6			-104.94
6	5	1	7			-104.45
7	6		15	16		76.92
8	6		19	20		82.82
9	6		22			68.60
10	6		23			65.38
11	8		9			71.54
12	8		13	14		33.27
13	9		10	11	12	-85.85
14	10		31	32		72.76
15	10		35	36		80.96
16	10		39			73.31
17	10		40			67.78
18	13		11	12		-47.58
19	15	1	18			-82.30
20	16	1	17			-112.36
21	18		48			72.93
22	18		53			71.04
23	19	1	21			-112.77
24	20	1	7			-90.35
25	21		57			71.67
26	21		60			72.86
27	22		24			71.69
28	23		28			68.59
29	23		11	30		22.90
30	24		5	25		-18.44
31	25	1	26			-105.75
32	26		16	63		76.45
33	26		20	64		82.23
34	28		11	12	29	-89.36
35	29		16	65		74.10
36	29		20	66		77.21

Table AIV-6. Continued

Reaction #	Reactant	Hydrogen	Product 1	Product 2	Product 3	dH (kcal/mol)
37	30		12	29		-43.67
38	31	1	34			-112.15
39	32	1	18			-82.30
40	35	1	11			-91.40
41	36	1	21			-112.77
42	39		41			77.99
43	40		45			72.37
44	40		11	47		18.09
45	41		5	42		-30.64
46	42	1	43			-104.84
47	43		31	63		72.56
48	43		35	64		80.64
49	45		11	12	46	-98.89
50	46		31	65		73.29
51	46		35	66		78.70
52	47		12	46		-44.61
53	48		49			-47.75
54	49		5	50		94.85
55	50	1	51			-103.61
56	53		54			64.89
57	53		11	55		15.16
58	54		11	12	56	-96.35
59	55		12	56		-46.62
60	57		58			76.87
61	58		5	5		-36.06
62	60		61			71.09
63	60		11	62		5.11
64	61		11	11	12	-112.27
65	62		11	12		-46.30
66	63	1	51			-81.50
67	64	1	7			-120.26
68	65	1	56			-84.51
69	66	1	11			-120.11

Table AIV-7. List of reactions involved in each pathway for the thermal deconstruction of MC1.

Pathway #	Reaction Number							
	1st	2nd	3rd	4th	5th	6th	7th	8th
1	1	5	16	13	95	---		
2	1	5	16	13	53	54	---	
3	1	5	16	13	53	167	---	
4	1	5	16	17	---			
5	1	5	18	15	---			
6	1	5	18	19	66	56	---	
7	1	5	18	19	66	169	---	
8	1	5	18	19	145	152	153	---
9	1	5	18	19	145	152	168	---
10	1	5	18	128	105	17	---	
11	1	5	18	128	105	106	---	
12	1	5	74	75	---			
13	1	6	20	13	95	---		
14	1	6	20	13	53	54	---	
15	1	6	20	13	53	167	---	
16	1	6	20	21	---			
17	1	6	22	15	---			
18	1	6	22	23	67	21	---	
19	1	6	22	23	67	169	---	
20	1	6	22	23	67	56	---	
21	1	6	22	23	146	155	153	---
22	1	6	22	23	146	155	168	---
23	1	6	22	23	146	156	---	
24	1	6	22	129	109	106	---	
25	1	6	22	129	109	21	---	
26	1	7	24	13	95	---		
27	1	7	24	13	53	54	---	
28	1	7	24	13	53	167	---	
29	1	7	24	25	---			
30	1	7	26	15	---			
31	1	7	26	68	56	---		
32	1	7	26	68	169	---		
33	1	7	26	130	110	106	---	
34	1	7	26	130	110	25	---	
35	1	7	80	110	---			
36	1	8	28	29	---			

Table AIV-7. Continued

Pathway #	Reaction Number							
	1st	2nd	3rd	4th	5th	6th	7th	8th
37	1	8	28	13	95	---		
38	1	8	28	13	53	54	---	
39	1	8	28	13	53	167	---	
40	1	8	30	15	---			
41	1	8	30	31	63	56	---	
42	1	8	30	31	63	169	---	
43	1	8	30	131	111	29	---	
44	1	8	30	131	111	106	---	
45	1	8	9	32	33	---		
46	1	8	9	32	13	95	---	
47	1	8	9	32	13	53	54	---
48	1	8	9	32	13	53	167	---
49	1	8	9	34	15	---		
50	1	8	9	34	35	70	33	---
51	1	8	9	34	35	70	56	---
52	1	8	9	34	35	70	169	---
53	1	8	9	34	35	149	161	153
54	1	8	9	34	35	149	161	168
55	1	8	9	34	35	149	162	---
56	1	8	9	34	132	113	33	---
57	1	8	9	34	132	113	106	---
58	1	8	9	86	113	---		
59	1	8	9	88	107	108	---	
60	2	10	36	13	95	---		
61	2	10	36	13	53	54	---	
62	2	10	36	13	53	167	---	
63	2	10	36	37	---			
64	2	10	38	15				
65	2	10	38	39	71	37	---	
66	2	10	38	39	71	56	---	
67	2	10	38	39	71	169	---	
68	2	10	38	39	150	163	37	
69	2	10	38	39	150	163	153	
70	2	10	38	39	150	163	168	
71	2	10	38	39	150	164	---	
72	2	10	38	133	114	37	---	
73	2	10	38	133	114	106	---	
74	2	10	89	114	---			

Table AIV-7. Continued

Pathway #	Reaction Number							
	1st	2nd	3rd	4th	5th	6th	7th	8th
75	2	11	40	13	95	---		
76	2	11	40	13	53	54	---	
77	2	11	40	13	53	167	---	
78	2	11	40	41	---			
79	2	11	42	15	---			
80	2	11	42	43	72	41	---	
81	2	11	42	43	72	56	---	
82	2	11	42	43	72	169	---	
83	2	11	42	134	115	41	---	
84	2	11	42	134	115	106	---	

85	4	15	--					
86	4	14	55	12	---			
87	4	14	55	56	---			
88	4	14	55	169	---			
89	4	14	57	59	66	17	---	
90	4	14	57	59	66	56	---	
91	4	14	57	59	66	169	---	
92	4	14	57	59	145	152	17	---
93	4	14	57	59	145	152	153	---
94	4	14	57	59	145	152	168	---
95	4	14	57	60	67	21	---	
96	4	14	57	60	67	56	---	
97	4	14	57	60	67	169	---	
98	4	14	57	60	146	155	21	---
99	4	14	57	60	146	155	56	---
100	4	14	57	60	146	155	169	---
101	4	14	57	60	146	156	---	
102	4	14	57	61	68	25	---	
103	4	14	57	61	68	56	---	
104	4	14	57	61	68	169	---	
105	4	14	57	62	63	70	33	---
106	4	14	57	62	69	56		
107	4	14	57	62	63	70	56	---
108	4	14	57	62	63	70	169	---
109	4	14	57	62	63	149	161	33
110	4	14	57	62	63	149	161	153
111	4	14	57	62	63	149	161	168

Table AIV-7. Continued

Pathway #	Reaction Number							
	1st	2nd	3rd	4th	5th	6th	7th	8th
112	4	14	57	62	63	149	162	---
113	4	14	58	64	71	37	---	
114	4	14	58	64	71	56	---	
115	4	14	58	64	71	169	---	
116	4	14	58	64	150	163	37	---
117	4	14	58	64	150	163	153	---
118	4	14	58	64	150	163	168	---
119	4	14	58	64	150	164	---	
120	4	14	58	65	72	41	---	
121	4	14	58	65	72	56	---	
122	4	14	58	65	72	169	---	
123	116	119	121	105	17	---		
124	116	119	121	105	106	---		
125	116	119	122	109	21	---		
126	116	119	122	109	106	---		
127	116	119	123	110	25	---		
128	116	119	123	110	106	---		
129	116	119	124	111	29	---		
130	116	119	124	111	106	---		
131	116	120	125	114	37	---		
132	116	120	125	114	106	---		
133	116	120	126	115	41	---		
134	116	120	126	115	106	---		
135	3	13	53	15	---			
136	3	12	44	46	---			
137	3	12	44	47	---			
138	3	12	44	48	---			
139	3	12	44	49		---		
140	3	12	45	51	---			
141	3	12	45	52	---			
142	3	13	53	54	---			
143	3	13	53	167	---			
144	3	13	95	---				

Table AIV-8. List of reactions involved in each pathway for the thermal deconstruction of MC2.

Pathway #	Reaction Number							
	1st	**2nd**	**3rd**	**4th**	**5th**	**6th**	**7th**	**8th**
1	1	9	15	16	36	37	---	
2	1	9	15	16	36	38	---	
3	1	9	15	17	39	40	---	
4	1	9	15	17	39	41	---	
5	1	10	11	12	42	43	---	
6	1	10	11	12	42	37	---	
7	1	10	11	13	39	40	---	
8	1	10	11	13	39	41	---	
9	2	14	15	16	36	37	---	
10	2	14	15	16	36	38	---	
11	2	14	15	17	39	40	---	
12	2	14	15	17	39	41	---	
13	3	18	20	45	41	---		
14	3	18	20	45	46	---		
15	3	18	20	47	38	---		
16	3	18	20	47	48	---		
17	3	21	22	47	38	---		
18	3	21	22	47	48	---		

19	3	21	45	41	-			

20	3	21	45	46	-			
21	4	19	20	45	41	---		
22	4	19	20	45	46	---		
23	4	19	20	47	38	---		
24	4	19	20	47	48	---		
25	5	23	24	25	26	27	---	
26	5	23	24	25	26	28	64	38
27	5	23	24	25	26	28	64	37

28	5	23	49	38	-			
29	5	23	49	50	51	52	58	27
30	5	23	49	50	51	52	58	59
31	5	23	49	50	53	54	55	---
32	5	23	49	50	53	56	57	---
33	5	23	60	61	62	47	38	---
34	5	23	60	61	62	47	48	---

Table AIV-8. Continued

Pathway #	Reaction Number							
	1st	**2nd**	**3rd**	**4th**	**5th**	**6th**	**7th**	**8th**
35	5	23	60	63	22	47	38	---
36	5	23	60	63	22	47	48	---

37	5	29	--					
38	7	30	31	32	33	34	---	
39	7	30	31	32	33	35	72	40
40	7	30	31	32	33	35	72	41

41	7	30	65	41	-			
42	7	30	65	66	51	52	58	27
43	7	30	65	66	51	52	58	59
44	7	30	65	66	53	54	55	---
45	7	30	65	66	53	56	70	---
46	7	30	67	68	71	45	41	---
47	7	30	67	68	71	45	46	---
48	7	30	67	68	69	70	---	
49	7	30	67	68	69	45	41	---
50	7	30	67	68	69	45	46	---

Table AIV-9. List of reactions involved in each pathway for the thermal deconstruction of MC3.

Pathway #	Reaction Number									
	1st	2nd	3rd	4th	5th	6th	7th	8th	9th	10th
1	1	3	5	7	9	21	23	59	61	8
2	1	3	5	7	9	21	23	59	61	62
3	1	3	5	7	9	21	24	64	66	
4	1	3	5	7	9	21	24	65	67	
5	1	3	5	7	9	22				
6	1	3	5	7	10	25	27	68	70	
7	1	3	5	7	10	25	28	72	74	
8	1	3	5	7	10	25	28	73	75	
9	1	3	5	7	10	26				
10	1	3	5	7	11	29	33	8		
11	1	3	5	7	11	29	33	34	35	22
12	1	3	5	7	11	29	33	34	35	76
13	1	3	5	7	11	29	33	34	36	26
14	1	3	5	7	11	29	33	34	36	77
15	1	3	5	7	12	31	38	39	22	
16	1	3	5	7	12	31	38	39	78	
17	1	3	5	7	12	31	38	40	26	
18	1	3	5	7	12	31	38	40	79	
19	1	3	5	7	12	32	41	39	22	
20	1	3	5	7	12	32	41	39	78	
21	1	3	5	7	12	32	41	40	26	
22	1	3	5	7	12	32	41	40	79	
23	1	3	5	8						
24	2	13	15	16	42					
25	2	13	15	16	43	23	59	61	8	
26	2	13	15	16	43	23	59	61	62	
27	2	13	15	16	43	24	64	66		
28	2	13	15	16	43	24	65	67		
29	2	13	15	17	44					
30	2	13	15	17	45	27	68	70	8	
31	2	13	15	17	45	28	72	74		
32	2	13	15	17	45	28	73	75		
33	2	13	15	18	46	50	8			
34	2	13	15	18	46	50	51	52	42	
35	2	13	15	18	46	50	51	52	76	
36	2	13	15	18	46	50	51	53	44	
37	2	13	15	18	46	50	51	53	77	
38	2	13	15	19	48	55	56	42		

Table AIV-9. Continued

Pathway #	Reaction Number									
	1st	2nd	3rd	4th	5th	6th	7th	8th	9th	10th
39	2	13	15	19	48	55	56	78		
40	2	13	15	19	48	55	57	44		
41	2	13	15	19	48	55	57	79		
42	2	13	15	19	49	58	56	42		
43	2	13	15	19	49	58	56	78		
44	2	13	15	19	49	58	57	44		
45	2	13	15	19	49	58	57	79		
46	2	14	20							
47	2	14	16	42						
48	2	14	16	43	23	59	61	8		
49	2	14	16	43	23	59	61	62		
50	2	14	16	43	24	64	66			
51	2	14	16	43	24	65	67			
52	2	14	17	44						
53	2	14	17	45	27	68	70	8		
54	2	14	17	45	28	72	74			
55	2	14	17	45	28	73	75			
56	2	14	18	46	50	8				
57	2	14	18	46	50	51	52	42		
58	2	14	18	46	50	51	52	76		
59	2	14	18	46	50	51	53	44		
60	2	14	18	46	50	51	53	77		
61	2	14	19	48	55	56	42			
62	2	14	19	48	55	56	78			
63	2	14	19	48	55	57	44			
64	2	14	19	48	55	57	79			
65	2	14	19	49	58	56	42			
66	2	14	19	49	58	56	78			
67	2	14	19	49	58	57	44			
68	2	14	19	49	58	57	79			

Table AIV-10. Skeletal structures of the species involved in the investigation of MC1.

Compound	Skeletal Structure
MC1	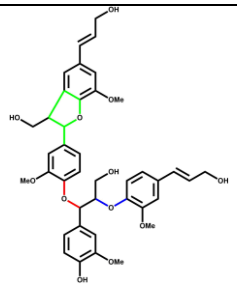
2	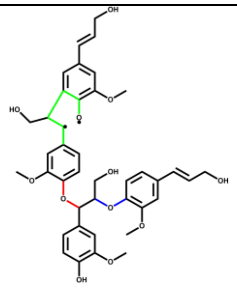
3	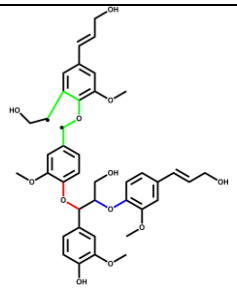
4	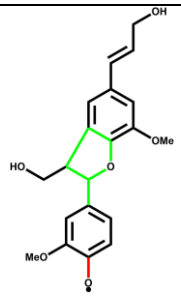

Table AIV-10. Continued

Compound	Skeletal Structure
5	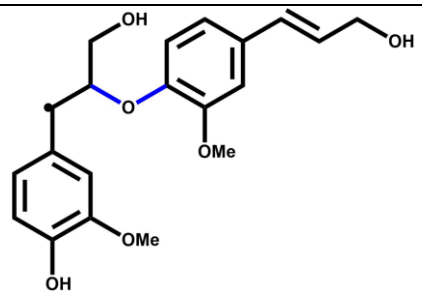
6	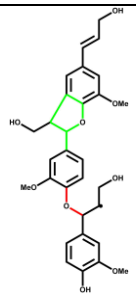
7	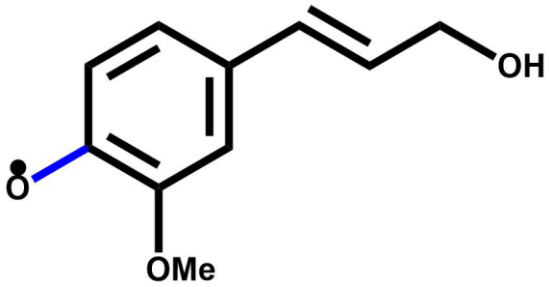
8	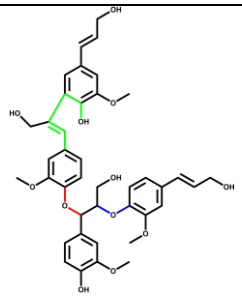

Table AIV-10. Continued

Compound	Skeletal Structure
9	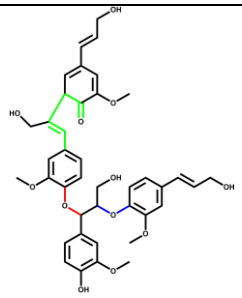
10	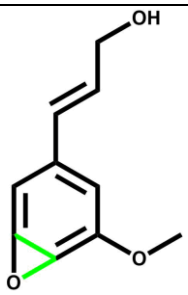
11	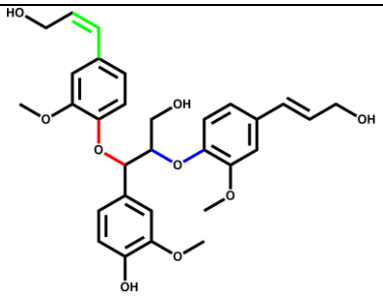
12	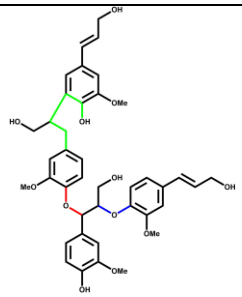

Table AIV-10. Continued

Compound	Skeletal Structure
13	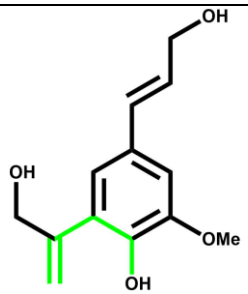
14	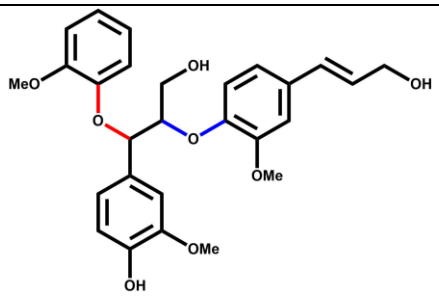
15	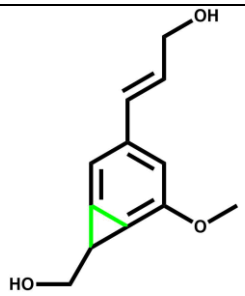
16	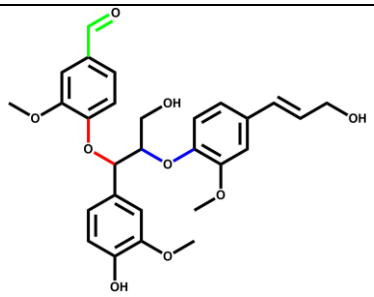

Table AIV-10. Continued

Compound	Skeletal Structure
17	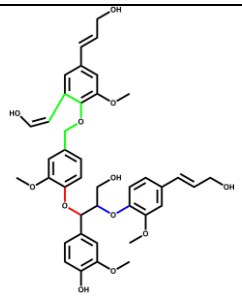
18	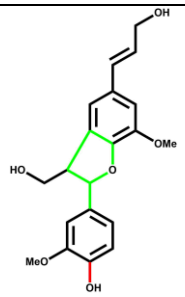
19	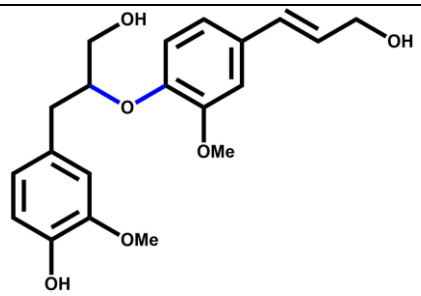
20	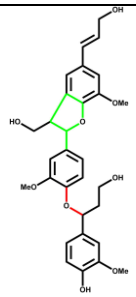

Table AIV-10. Continued

Compound	Skeletal Structure
21	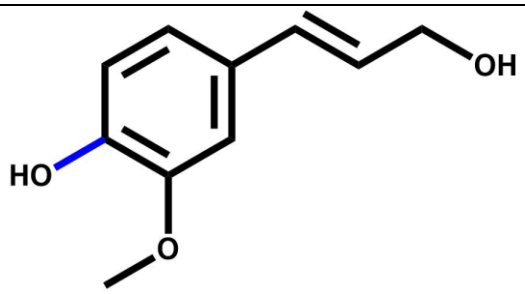
22	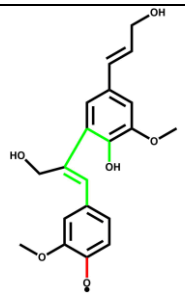
23	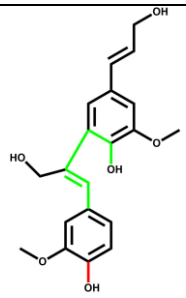
24	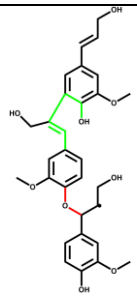

Table AIV-10. Continued

Compound	Skeletal Structure
25	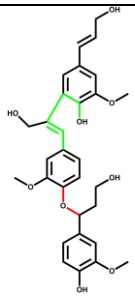
26	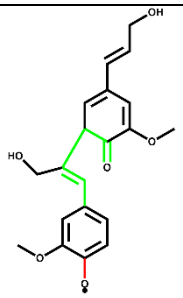
27	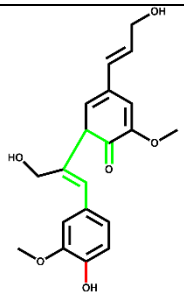
28	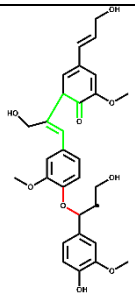

Table AIV-10. Continued

Compound	Skeletal Structure
29	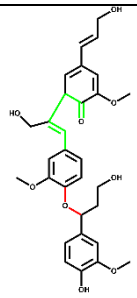
30	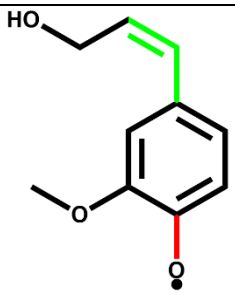
31	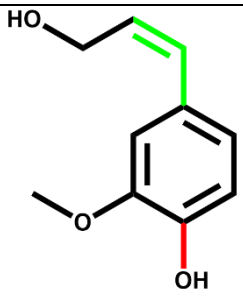
32	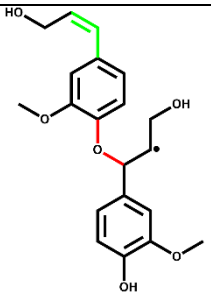

Table AIV-10. Continued

Compound	Skeletal Structure
33	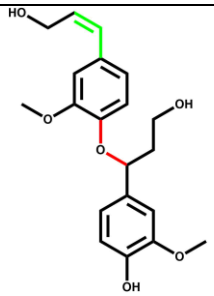
34	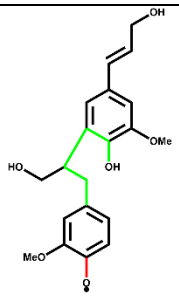
35	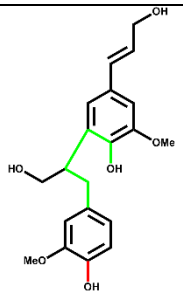
36	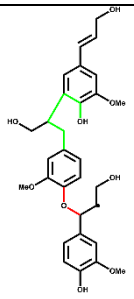

Table AIV-10. Continued

Compound	Skeletal Structure
37	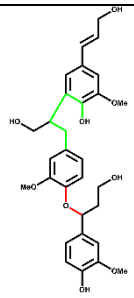
38	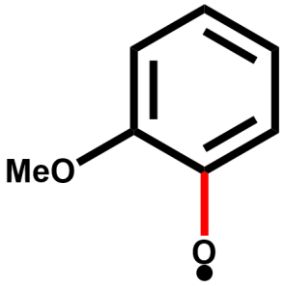
39	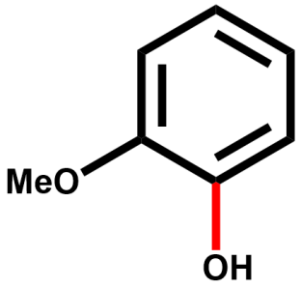
40	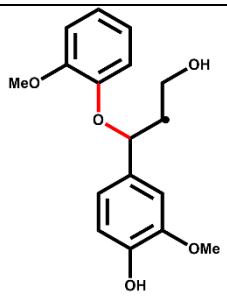

Table AIV-10. Continued

Compound	Skeletal Structure
41	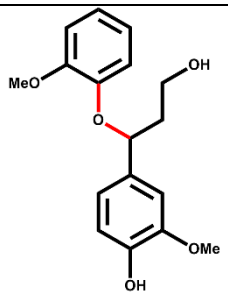
42	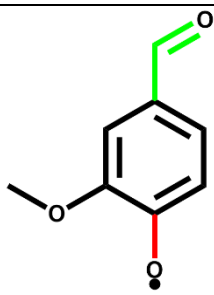
43	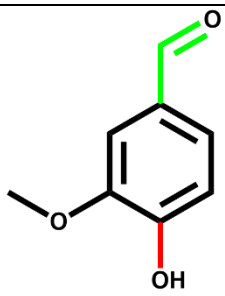
44	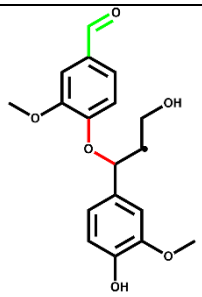

Table AIV-10. Continued

Compound	Skeletal Structure
45	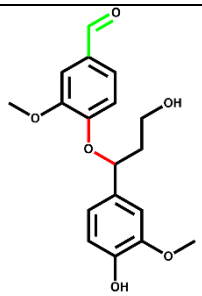
46	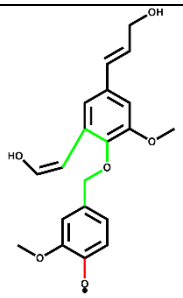
47	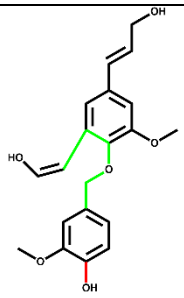
48	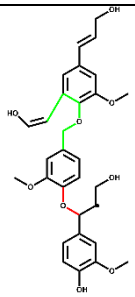

Table AIV-10. Continued

Compound	Skeletal Structure
49	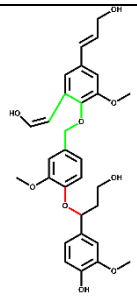
50	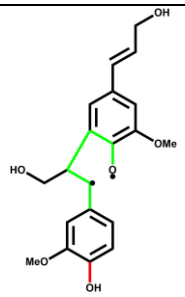
51	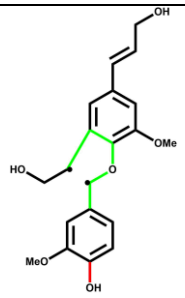
52	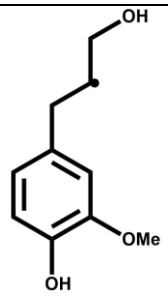

Table AIV-10. Continued

Compound	Skeletal Structure
53	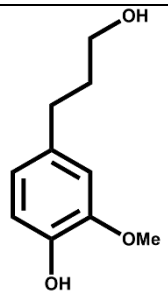
54	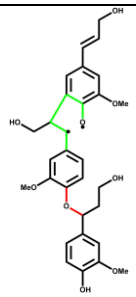
55	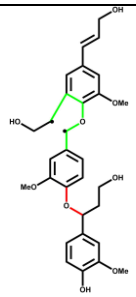
56	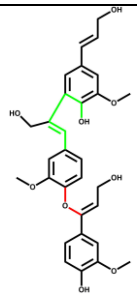

Table AIV-10. Continued

Compound	Skeletal Structure
57	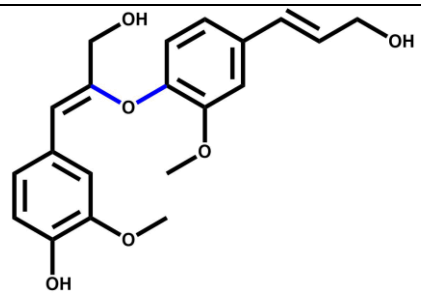
58	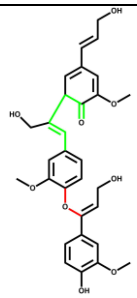
59	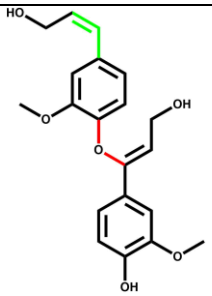
60	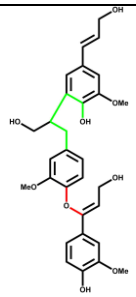

Table AIV-10. Continued

Compound	Skeletal Structure
61	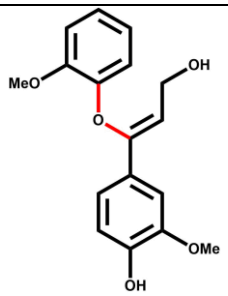
62	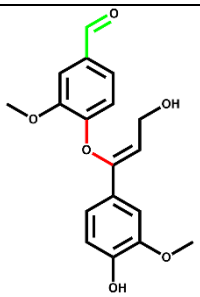
63	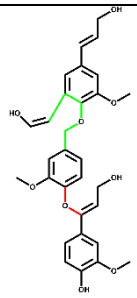
64	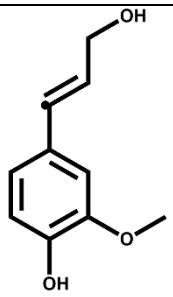

Table AIV-10. Continued

Compound	Skeletal Structure
65	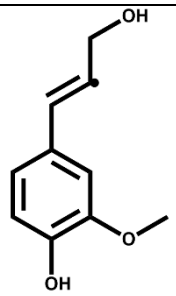
66	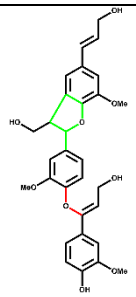
67	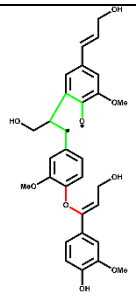
68	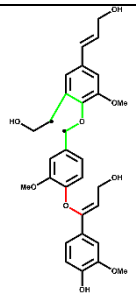

Table AIV-10. Continued

Compound	Skeletal Structure
70	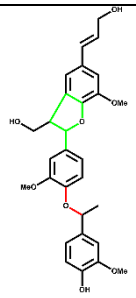
71	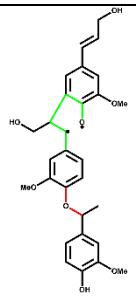
72	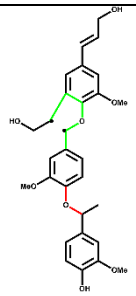
73	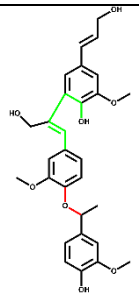

Table AIV-10. Continued

Compound	Skeletal Structure
74	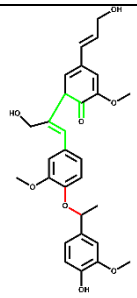
75	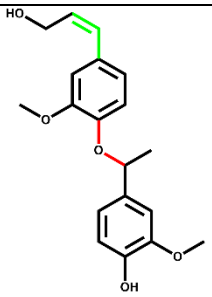
76	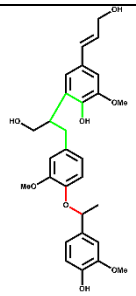
77	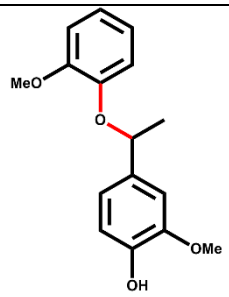

Table AIV-10. Continued

Compound	Skeletal Structure
78	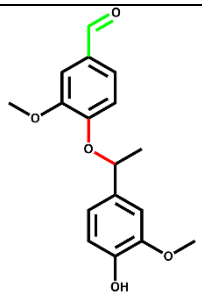
79	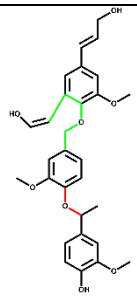
80	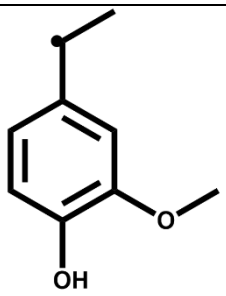
81	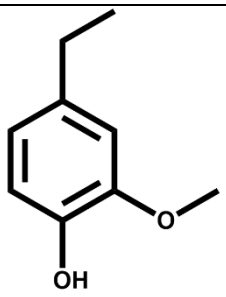

Table AIV-10. Continued

Compound	Skeletal Structure
82	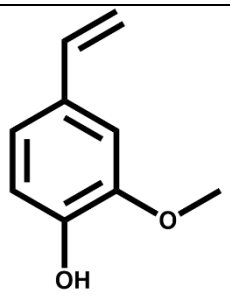
83	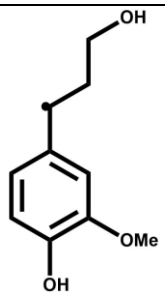
IM1	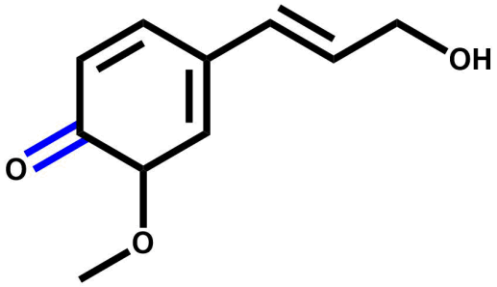
TS10	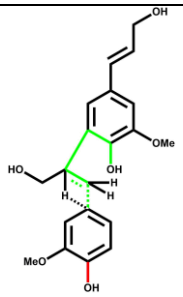

Table AIV-10. Continued

Compound	Skeletal Structure
TS16	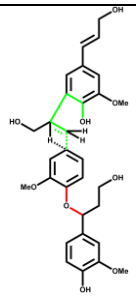
TS20	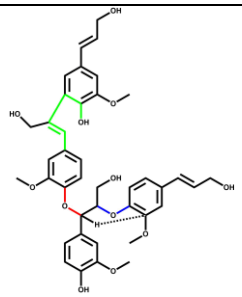
TS21	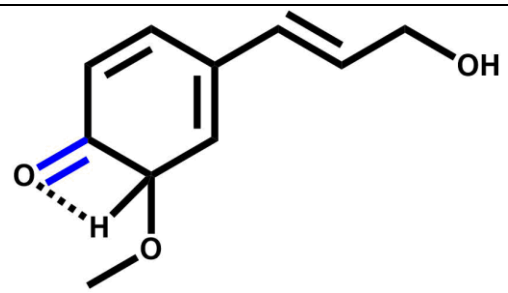
TS26	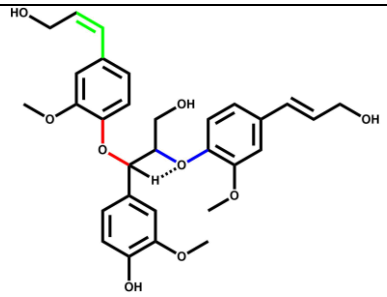

Table AIV-10. Continued

Compound	Skeletal Structure
TS32	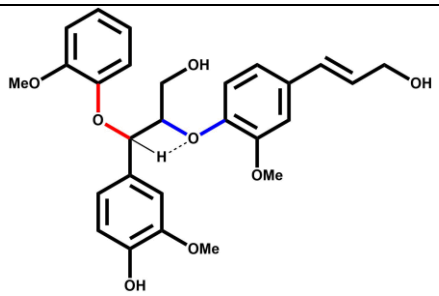
TS34	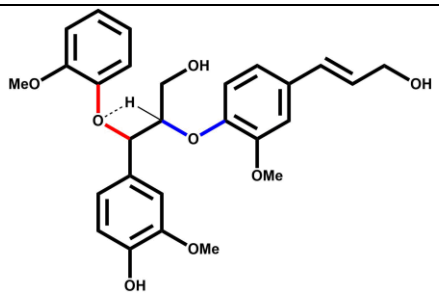
TS35	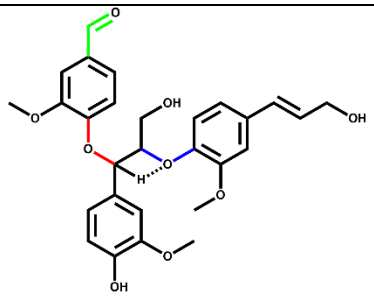
TS41	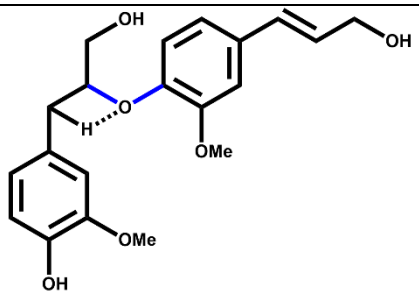

Table AIV-10. Continued

Compound	Skeletal Structure
TS52	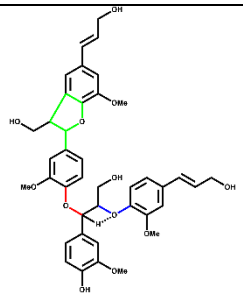
TS67	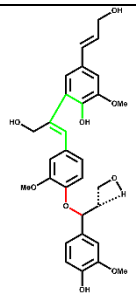
TS68	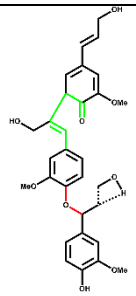
TS71	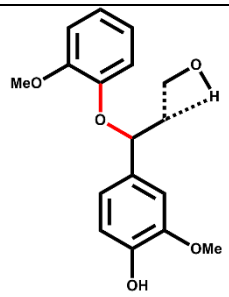

Table AIV-10. Continued

Compound	Skeletal Structure
TS72	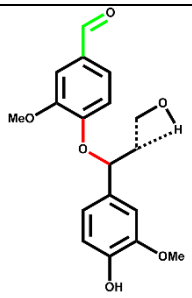
TS75	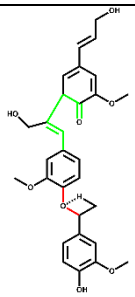
TS76	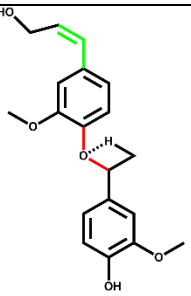
TS78	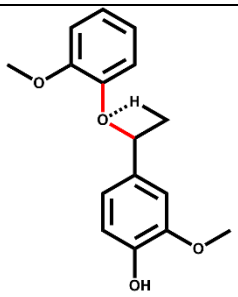

Table AIV-10. Continued

Compound	**Skeletal Structure**
TS79	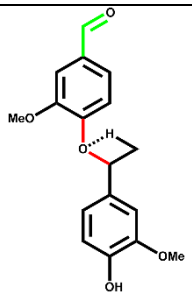
Note: Structures for MC2 and MC3 investigations are available upon contacting the authors.	

CHAPTER 5 INVESTIGATION OF LIGNIN MODEL COMPOUNDS USING PULSE-HEATED PYROLYSIS EXPERIMENTS

Abstract

It is imperative to couple the results from the computational determination of reaction mechanisms with high-fidelity experimental data. However, conventional pyrolysis techniques such as thermogravimetric analysis suffer from transport limitations that make it difficult to collect intrinsic reaction data useful for proposing fundamental reaction mechanisms. In this work, a pulse-heated pyrolysis reactor was designed and fabricated to overcome the mass and heat transport limitations for the pyrolysis of three model lignin dimers: phenethyl phenyl ether (PPE), diphenyl ether (DPE), and benzyl phenyl ether (BPE). The products of each dimer were subjected to online and offline analysis via GC/MS and GC/FID. The primary products of PPE were styrene and phenol as a result of homolytic cleavage at the C_β-O bond or a concerted reaction. Pyrolysis of DPE yielded guaiacol, benzene, styrene, and polycyclic recombination species as the primary products. BPE produced phenol and toluene as the primary products from the cleavage of the C_α-O bond. These pulse-heated pyrolysis experiments are a first step towards gaining valuable mechanistic information about the fundamentals of lignin pyrolysis.

5.1. Introduction

Experimental investigation into the kinetics of lignin pyrolysis is a necessary task to complement and validate theoretical and computational findings. However, experimental investigations must be conducted under kinetic control, i.e., isothermal reaction conditions, to generate quality data and accurate interpretations. Isothermal reaction conditions are characterized by a high pyrolysis number (Py^{I} and Py^{II}) and a

sufficiently small Biot number (Bi)[1]. Pyrolysis numbers provide a ratio of the heat transfer and reaction time scales; therefore, a large pyrolysis number indicates the reaction proceeds slowly in comparison to the heat transfer, while the Bi number relates the rate of thermal convection to conduction. Coupling a high Py number with a low Biot number, indicative that the internal heat transfer is sufficient, results in isothermal reaction conditions[2]. Five requirements are essential in conducting experimental pyrolysis reaction kinetics investigations in a kinetically controlled regime[3]. These requirements can be summarized as follows: (1) a small biomass length scale to eliminate temperature and reaction gradients in the sample. Samples with characteristic length scales of less than 70 μm are required to ensure the rates of heat transfer are sufficiently greater than the reaction rate, (2) accurate temperature measurement and control to eliminate the variation of reaction rates, (3) negligible conversion during heating and cooling to ensure the reactions do not occur outside of the isothermal region, (4) online millisecond scale product detection to achieve real-time product evolution, and (5) short vapor residence times to eliminate secondary reaction. At a thin-film length scale, the target heating and cooling rates, assuming elementary reactions, are 7,250 and 5,236 °C, respectively[3]. These values were determined based on a differential conversion approach for α-cyclodextrin, a cellulose model compound, using first-order reaction kinetics to limit the conversion to less than five percent. Over the years, several experimental investigations were carried out to investigate lignin's fast pyrolysis reactions and kinetics[4-6]. There have been several different reactor configurations used, at the lab scale, to try and understand the

mechanism and kinetics of biomass pyrolysis, such as the wire-mesh reactor[7], pyrolysis gas chromatography/mass spectrometry (Py-GC/MS)[8, 9], and microparticle microreactors[10]. However, the bulk of kinetic investigations used in lignin, or, for that matter, biomass, pyrolysis kinetics investigations are thermogravimetric analysis (TGA) and pyrolysis gas chromatography mass spectroscopy (Py-GCMS)[6, 11-19]. These reactor systems suffer from heat and mass transfer limitations, achieve lower than required heating and cooling rates for fast pyrolysis, and have poor time resolution that cumulatively results in sparse reaction data [20]. However, the heating and cooling rates achieved by commercial TGA and Py-GCMS systems are 3.34 and 0.31 °C/s and 216.4 and 0.31°C/s, respectively, significantly lower than the ideal 7,250°C/s and 5,236 °C/s required to heat the samples to the reaction temperatures with negligible conversion during heating and to rapidly quench the reaction upon completion[3, 21, 22]. Recently, a handful of studies have been able to achieve this high heating rate and approach the required cooling rate for thin-film pyrolysis[3, 23, 24]. Vapor residence times for an existing Frontier micropyrolyzer, another common commercial system employed for pyrolysis investigations, was found to be as high as 85 s[25]. However, at this residence time, vapor products in this reactor will undergo secondary reactions, which will mask the true nature of primary pyrolysis reactions that occurred, thereby complicating the interpretation of the findings. Therefore, it is important to shorten the vapor residence time during fundamental pyrolysis experiments (< 1 s) to reduce the occurrence of secondary reactions[26]. Most of the current reactor configurations and experimental techniques do not achieve one or more of the five aforementioned requirements. A

novel pulse-heated reactor meets all these requirements and achieves kinetically controlled experiments[23, 24, 27]. When coupled with intensive computational chemistry calculations, the results of pyrolysis from this pulse-heated reactor system can more accurately validate and propose reaction mechanisms for lignin pyrolysis.

In this chapter, we conducted fast pyrolysis experiments on three lignin model compounds, 2-phenethyl phenyl ether (PPE), benzyl phenyl ether (BPE), and diphenyl ether(DPE), using a pulse-heated pyrolysis reactor system that overcomes the limitations of existing analytical tools. The model compounds in this chapter were selected based on their commercial availability and the presence of important interunit linkages computationally investigated in the previous chapters. The goal of this chapter is to (i) design and fabricate a reactor system that can overcome the transport limitations of conventional pyrolysis analyses, (ii) discover and identify the products of pulse-heated pyrolysis of the model compounds, and (iii) compare the experiment results with previous computational chemistry calculation and previously published pyrolysis pathways.

5.2. Materials and methods

5.2.1. Materials

We purchased model dimers with β-O-4, α-O-4, and 4-O-5 interunit linkages. 2-phenethyl phenyl ether (PPE) (CAS No. 40515-89-7) was selected as the β-O-4 linkage and was purchased from Ambeed Inc. (Arlington Heights, IL, USA). PPE is the simplest model dimer that contains the β-O-4 ether linkage and has been used as a model compound to study lignin since the early 1980s[28, 29]. The lack of substitutions along the

backbone of the linkage allowed for the investigation of only the linkage reactions, which better reflect our computational work. Additionally, PPE has received a significant amount of experimental and computational investigation that will be helpful for comparison with our pulse-heated experiments. Benzyl phenyl ether (BPE) (CAS No. 946-80-5) was selected as the α-O-4 linkage model compound and was purchased from Sigma-Aldrich (St. Louis, MO, USA). Much like PPE, BPE is the simplest form of an α-O-4 dimer without any additional substitutions. Diphenyl ether (DPE) (CAS No. 101-84-8) was selected as the 4-O-5 linkage model and was purchased from Sigma-Aldrich. In total, we investigated three model lignin dimers: PPE (β-O-4), BPE (α-O-5), and DPE (4-O-5).

5.2.2. Experimental setup

The pulse-heated pyrolysis experimental setup consists of an integrated system with two subsystems: a Pulse-Heated Pyrolysis Reactor (PHPR) subsystem and the high-frequency power supply subsystem.

The Pulse-Heated Pyrolysis Reactor (PHPR) subsystem was designed and assembled in-house based on a similar system initially designed by reported by Dauenhauer and colleagues[27]. The PHPR subsystem is illustrated in Figure 0-1.

It consists of the top (Figure 0-1, 1) and bottom (Figure 0-1; 2) blocks machined from rectangular 316 stainless steel stocks joined together by 18 plastic socket screws (5/16 in. size) with a silicone rubber gasket between (Figure 0-1; 3). Detailed annotated schematics of the top and bottom blocks are shown in Appendix V: Figure AV-1 and

Figure AV-2. It has dimensions of 1.49, 3.34, and 0.70 in. for length, width, and height, respectively. On its top face, it has 18 bored-through holes on its perimeter to enable it to be bolted to the bottom block in a full assembly (Figure 0-1, 13). Additionally, the top block has a through hole on its top face located near its center of mass fitted with a Swagelok feed for the pyrometer (Figure 0-1, 5) and two adjacent through holes, each weld-fitted with an electric feedthrough (Figure 0-1, 4) that is externally connected to positive and negative lead wires carrying high amperage current. Copper brushes (Figure 0-2, 1. and 2.) are connected to the electrical feedthroughs on one end and to the sample holder on the other end, thereby completing the electrical circuit that enables pulse heating. The sample holder is made of a thin sheet (McMaster Carr, 1008–1010 steel foil, 0.007 in. thickness) and is resistively heated via electrical pulses, as described later. Finally, the top block has two slots for potential cartridge heaters slots on the front and back to heat the areas of the block that will be in contact with the carrier gas and evolved gases and decrease potential undesirable condensation on surfaces, if necessary (Figure 0-1, 6, and 7). The bottom block has identical length and width dimensions as the top block. However, it has a height of 1.49 in. to enable it to house a micro-channel cooling block on which rests the ceramic insulator, resistive heating element, and thin-film sample, as illustrated in Figure 0-2. The left and right sides of the bottom block have 3/8" fittings (Figure 0-1, 8, and 9) that serve as an inlet and outlet of the cooling fluid through the micro-channel cooling block if additional cooling is required. Like the top block, it has two slots for heating

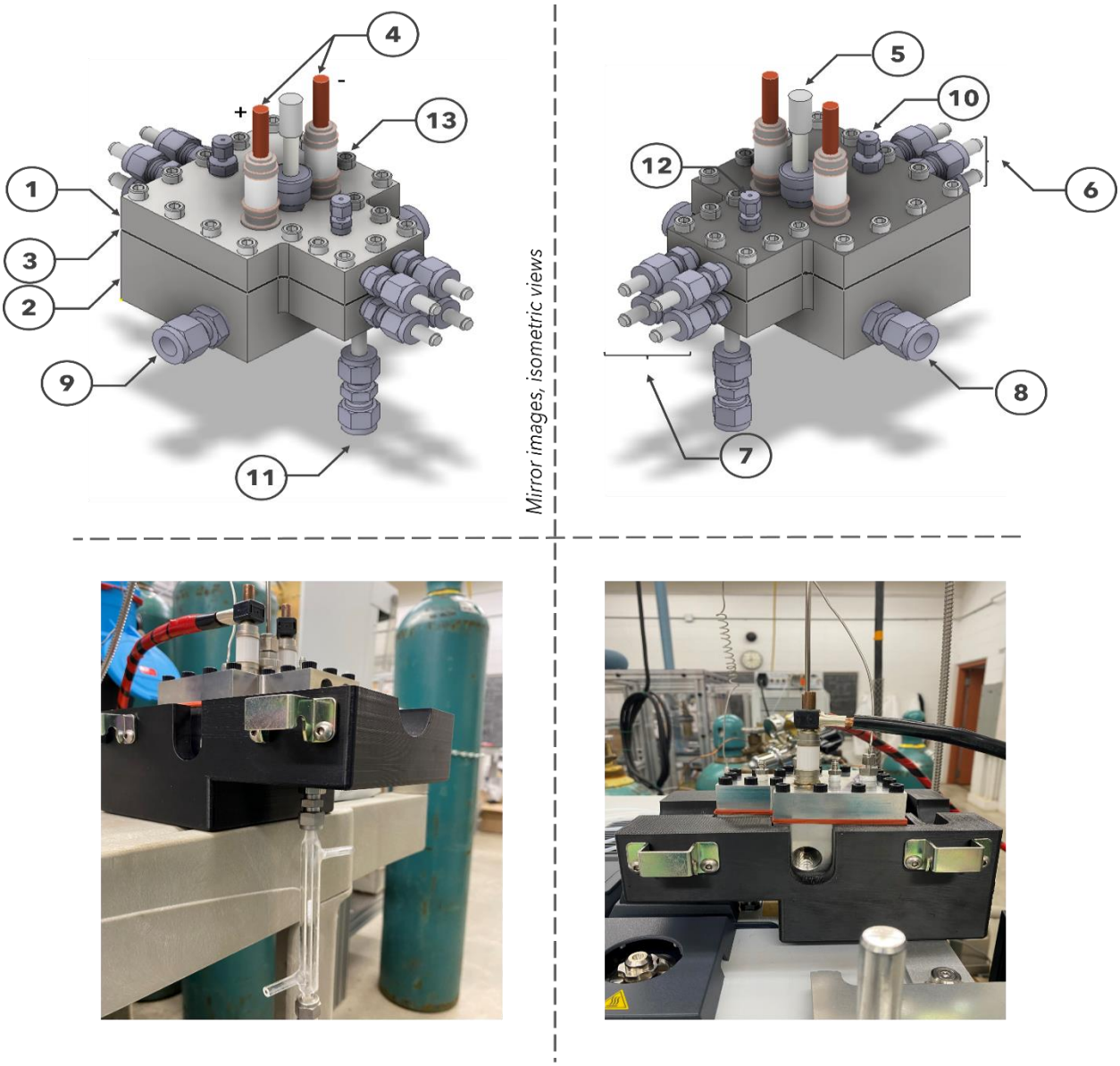

Figure 0-1. (Top) Mirror isometric views of the overall PHPR system. 1. Top block: 2. Bottom block: 3. Silicone rubber gasket, 4. Electric feedthrough, 5. pyrometer light pipe, 6. Back, top, and bottom cartridge heaters, 7. Front, top, and bottom cartridge heaters, 8. Micro-channel cooling fluid inlet, 9. Micro-channel cooling fluid outlet, 10. carrier gas (He), 11. carrier gas and evolved gas outlet for online and offline analyses, 12. 1/16 in. thermocouple port, 13. 5/16 in. socket head screws. Note: Two additional thermocouple ports are included but not shown in this figure due to the angle. (Bottom) Images of the PHPR installed for offline (bottom, left) and online (bottom, right) analysis. The top insulation was removed to allow for visualization of the reactor.

cartridges on the front and back to heat the block to decrease potential undesirable condensation on surfaces, if necessary. The bottom block has an outlet to enable the carrier gas and the evolved gases to be carried out of the PHPR system for online analysis. The outlet consists of a 1/16 in. VICI tube adapter (Valco Instruments Co., Part # ZLTA41) welded on one end to the bottom block (Figure 0-1, 11). The tube adapter is depicted in Figure 0-1 with a 1/8" Swagelok union to connect directly to the gas sampling valve (GSV) module of the gas chromatography (GC) system for online analysis.

The pulse heating is enabled by the high -frequency power supply subsystem. This subsystem produces millisecond-scale electrical pulses generated by a 2000 Hz, 460 V, 30A power supply (Miyachi-Unitek, HF-2) that run through the electrical feedthroughs, the copper brushes, and the sample holder. The high voltage and moderate amperage current from the power supply are turned down by a transformer (Miyachi-Unitek, IT1140-T) to a low voltage, high amperage (~ 13 V, 400-600 A) direct current that resistively heats the sample holder onto which a thin layer of a model compound. As the sample is heated, an optical pyrometer, with a response time of 1 ms (LumaSense Technologies, IGA 50-LO), monitors the temperature of the thin layer to generate a temperature-time profile from which the fast pyrolysis heating rate is determined. The reactor system is also outfitted to handle up to eight additional cartridge heaters: four inlet gas pre-heaters and four outlet gas heaters. The inclusion of these outlet cartridge heaters is to provide additional pre- and post-heating of the process gas, if necessary.

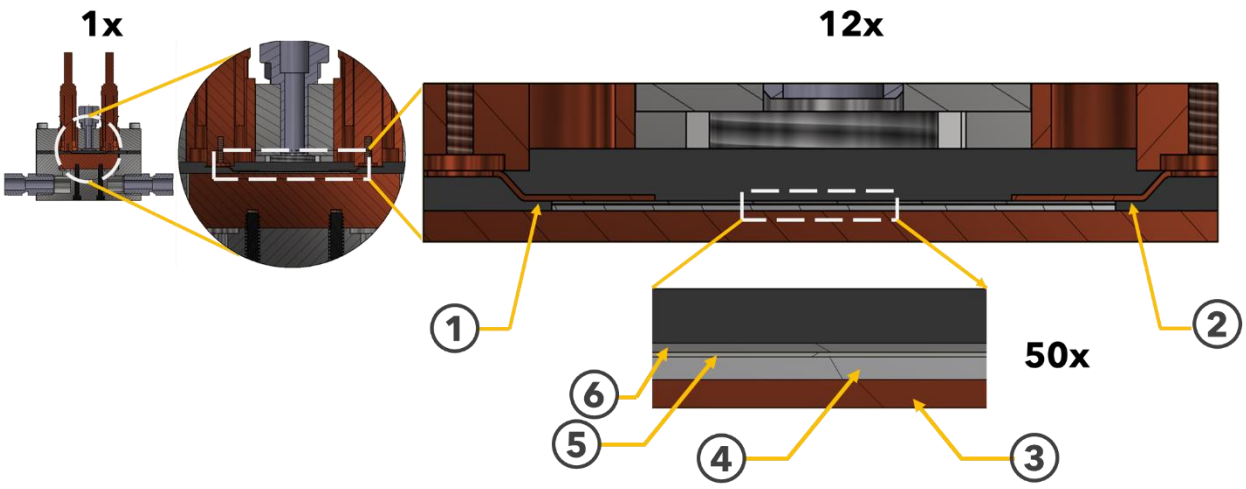

Figure 0-2. Cross-sectional views of the PHPR's stacked thermal elements at increasing magnifications (1x, 6x, 12x, and 50x) to show the interfaces involved in heat transfer. 1. Copper brush, + lead; 2. Copper brush, - lead; 3. Micro-channel cooling block: 4. Aluminum nitride insulator: 5. Indium foil: 1008–1010 steel foil.

5.2.3. Pulse -heated pyrolysis experiments

The pulse-heated pyrolysis experiments were carried out in two phases: sample preparation and pulse-heated pyrolysis experiments. Thin samples are necessary to reduce the Biot number to eliminate temperature gradients in the sample and ensure rapid heating[1, 30]. Before each experiment, the carbon steel sample holders were sonicated in acetone and dried in a vacuum oven overnight to ensure their surface was clean. The model dimers in this work are a mixture of both liquid and solid. For the liquid compounds, PPE and DPE, we applied a two µl droplet of the sample using a micropipette onto the previously weighed sample holder. The crystalline BPE dimer was weighed to approximately 0.015 mg and placed on the sample holder. Both the solid and liquid samples were positioned in the center of the sample holder to ensure their temperature was captured by the optical pyrometer.

After they had been applied to the sample holder, the samples were subjected to pulse-heated pyrolysis using the PHPR system at 450, 500, and 550 °C. The experiment begins with placing the carbon steel sheet with the thin model dimer sample on the aluminum nitride insulator, which sits on top of the micro-channel cooling block under a constant flow of nitrogen (N_2) carrier gas before pulse heating at predetermined times (50–1500 ms). The heating profiles were varied to accommodate the slight differences in the total weigh of the sample holder, but they were generally classified into two phases: pre-heating and the pyrolysis pulse. The optical pyrometer could measure temperatures as low as 249 °C; therefore, the preheat was implemented to bring the temperature of the sample close to that lower

threshold to ensure the pyrolysis pulse was captured by the pyrometer. The preheat section of the program supplied a 100 A pulse for 1000-1400 ms. After the preheating, the program began the pyrolysis pulse. The purpose of the pyrolysis pulse is to rapidly heat the sample to pyrolysis conditions for the experiment. The current of the pulse varied between 500-600 A and pulsed for 50 ms. After the pulse heating cycle, the pyrolyzed sample was then rapidly cooled by the flow of carrier gas sweeping the products out of the PHPR. The resulting evolved pyrolysis gases were analyzed through one of two analytical pathways illustrated in Figure 0-3.

In the online analysis mode, the evolved vapors were directly transferred onto the column (VF-1701ms; 30 m length, 0.25 mm diameter, and 0.25 μm film thickness) of the gas chromatograph (GC) (Thermo Fisher Scientific Inc., Model Trace 1310) using a gas sampling valve (GSV) module connected to the outlet on the PHPR. For the online experiments, the GC was equipped with an ISQ7000 mass spectrometer (MS) to enable immediate identification of individual species leaving the PHPR. The inlet temperature was maintained at 250 °C, and the analysis was carried out using the following temperature program: the oven was initially held at 40 °C for 2 min, ramped to 250 °C at a rate of 10 °C /min, and held for 10 min. Helium acted as the GC carrier gas. The sample flow was constant with a flow rate of 2 ml/min. The pyrolysis products were injected into the GC with a 5 ml/min split. Similar programs have been successful at characterizing various species present in pyrolysis oil[27, 31, 32]. The GC method was kept constant for both the online and offline analyses.

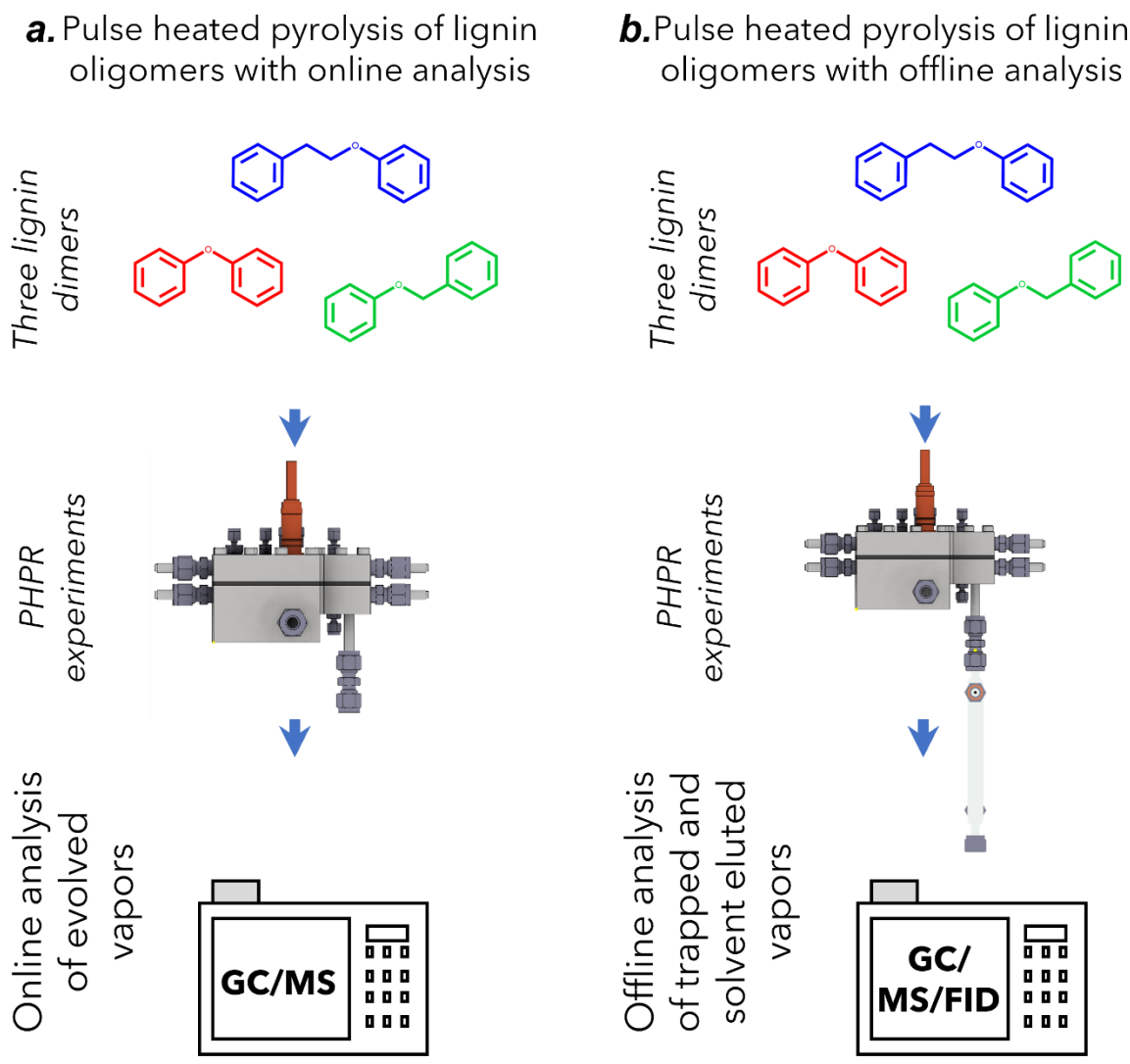

Figure 0-3. Overview of the two analytical analysis pathways used for evolved gas analysis.

For the offline analyses, the PHPR was disconnected from the GSV of the GC and was instead connected to a ¼" glass condenser packed with a bed of adsorbent (Amberlite XAD-2, Sigma Aldrich), shown in Figure AV-3. Before each run, the packed bed was chilled in a freezer to aid in condensation and trapping of the evolved species from the PHPR. After the experiment, the carrier gas continued to flow products through the condenser for two minutes to ensure all the products had been transferred to the bed. Afterward, the adsorbent bed was rinsed with dichloromethane (DCM) to elute the condensed and trapped species. The resulting DCM solution was then analyzed by both GC/MS and GC/FID.

5.2.4. Data collection and analysis

Gaseous products, from online experiments, and liquid products, from offline experiments, were identified via mass spectrometry. After identification, the offline products were quantified using GC/FID analysis. The peaks were integrated, and the peak area was used to determine the relative yield of the products. Due to the limitations of our characterization capabilities, we were unable to get an accurate reading on the sample weight after pyrolysis. Therefore, we assume the entire sample was volatilized, and both the products and unreacted dimers were transferred onto the column.

5.3. Results and discussion

The rationale for selecting the specific model dimers to compare and validate our computational work is based partially on the abundance of computational work on these chosen dimers compared to our chosen oligomers[9, 33-37]. Additionally, we have

previously performed density functional theory (DFT) simulations on model oligomers with similar interunit linkages. We have proposed a full reaction mechanism from each oligomer all the way down to the monomers. The energetics and kinetics of each individual reaction are independent of the rest of the mechanism. Therefore, it is possible to compare the results of our pulse-heated pyrolysis experiments to the computational mechanism from the previous chapter, starting at the dimer stage. If we confirm that the mechanism holds for the final stages for compounds up to the dimer level, we can assume that the mechanism also holds for the trimer and tetramer stages. Another point of confirmation is that the additional possible reactions gained from increasing to a trimer or tetramer have already been validated by the other model dimers. If we can validate the mechanism for each of our dimers, then adding another linkage to a dimer will not add any non-validated reactions to the mechanism.

5.3.1. Evaluation of the PHPR system

The primary goal of the pulse-heated pyrolysis reactor (PHPR) was to ensure reactions were happening inside the kinetically controlled regime to allow for identifying intrinsic reaction behavior not affected by mass or heat transport limitations. This was primarily accounted for by rapid heating and cooling of the samples during pyrolysis. Therefore, it is imperative to evaluate the performance of the PHPR to achieve these high heating and cooling rates. Pulse-heated pyrolysis was performed on each model lignin dimer at 450, 500, and 550 °C. The sample holders were shown to have the potential to exhibit different heating behavior with even milligram differences in weight. Therefore, each temperature condition was given a window of ±25 °C. In the

testing phase, each sample holder was subjected to multiple pulses, with adequate time to cool back to their original temperature between pulses, and there was good reproducibility of temperature on the same heating element. The heating and cooling rates were also measured for each replicate run for a given sample at each condition, an example of which is shown in Figure 0-4. The heating rate was calculated from the region of linear increase in temperature from 249 °C to the maximum temperature. This distinction is due to certain runs for PPE and DPE had a non-linear "pre-heating" region, most likely caused by poor contact of the firing switch in the pre-heating phase of the temperature program, causing it to restart, which increased the length of the pre-heat phase. This did not have an appreciable effect on the experiments, as the pyrolysis pulse began while the sample temperature was still below the threshold for pyrolysis reactions to begin to occur.

The heating and cooling rates are reported by the initial phase of the sample: liquid and solid. For the liquid samples, PPE and DPE, during pyrolysis at 500 °C, the heating rate was found to range from 3,952 – 5,026 °C/s, while the solid BPE sample heating rate ranged from 4,346 – 6,516 °C/s. These sample heating rates are significantly higher than the heating rates reported for both TGA and Py-GCMS, 3.34 and 216.4 °C/s, respectively. However, the heating rates were still below the ideal target of 7,250 °C/s proposed by Maduskar et al. to ensure less than 5% conversion happens during the heating and cooling phase[3]. The high heating rates show that the PHPR system was much more effective at heating the biomass samples compared to conventional experimental techniques. We believe that the development of a process-

control loop to better adjust the current output would allow for a more rapid and repeatable heating rate closer to that of the ideal system. The HF-2 power supply has the potential for integration into a feedback loop that uses the output from the optical pyrometer to adjust the current supplied to the PHPR on a millisecond scale.

The cooling rates for both the liquid and solid samples were 152 °C/s with standard deviations of 36 and 32 °C/s for solid and liquid samples, respectively. The cooling was done via the constant flow of carrier gas and outperformed the cooling of TGA and Py-GCMS; however, it is much lower than the required 5,236 °C/s for adequate quenching[3]. The PHPR is equipped with a microchannel cooling system that can serve as a heat-exchanger in future iterations to drastically reduce the time required to completely quench the pyrolysis reaction. Overall, we found the PHPR was a significant improvement over conventional techniques for acquiring intrinsic reaction information during pyrolysis.

5.3.2. Pulse-heated pyrolysis of PPE

PHPR experiments were first subjected to online pyrolysis for analysis via GC/MS to capture the produced volatiles directly from the outlet of the PHPR system. Each temperature was run in triplicate to ensure reproducibility, and the GC/MS were consistent over each replicate. The species identified, and their retention times, via online GC/MS analysis, are shown in Table 0-1, and the representative chromatograms are shown in Figure 0-5. Due to current library limitations, we were unable to identify several species with a reasonable degree of confidence; therefore, they have been assigned as unknowns. Throughout each temperature condition for PPE, we found

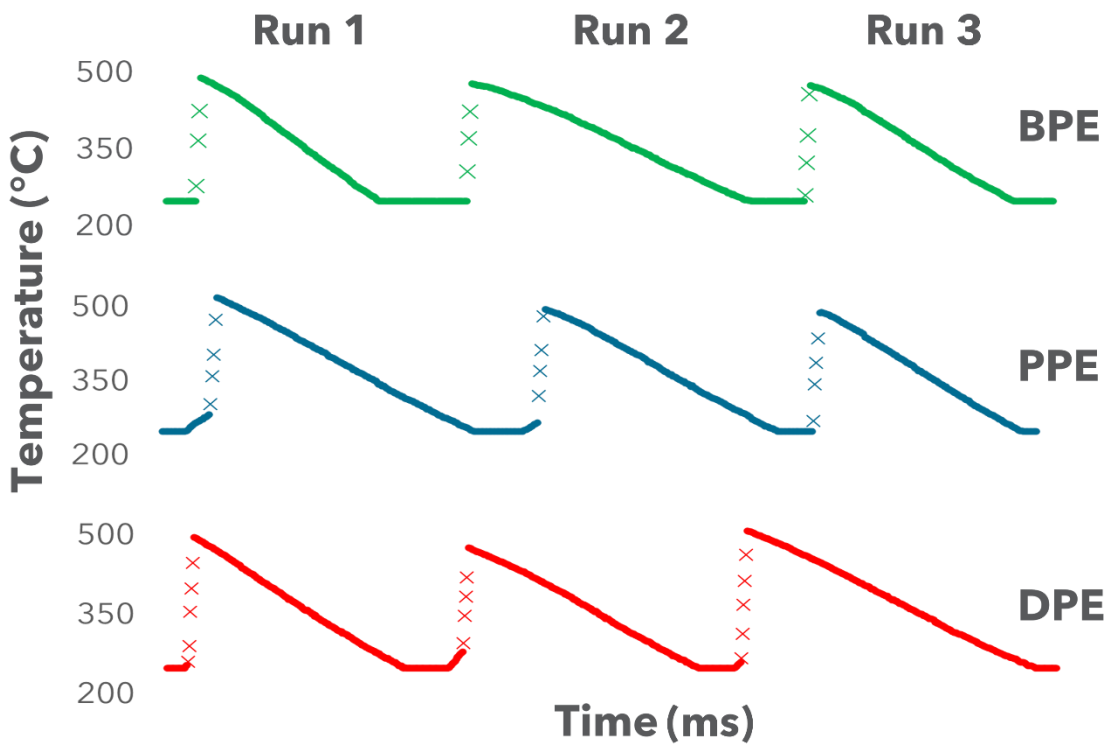

Figure 0-4. Heating and cooling rates of model dimers for the 500 °C experimental condition. The time between data points is approximately 10 ms. There is a time-break between each run to allow for sufficient cooling to the initial temperature, which is not shown here.

many of the same species present, with a majority of the products being aromatic monomers.

During online analysis, the primary species identified were aromatic monomers, such as benzene, styrene, and phenol. The relative areas for the primary products are shown in Table 0-2. The presence of these monomers indicated bond breakage is occurring along the β-O-4 interunit linkage, which agrees with previous mechanisms reported for the pyrolysis of PPE[33-35]. Two of the primary results from PPE pyrolysis we observed were styrene and phenol, with relative areas of 12-36 and 10-35%, respectively. The formation of these products can be through either the homolytic cleavage or a concerted reaction at the C_β-O bond of the β-O-4 linkage, which we have previously identified as the primary reaction point for the β-O-4 linkage in the previous chapters[38]. The other major products identified in the offline analysis are benzene, toluene, and phenylethyl alcohol. These products indicate that, albeit in lesser amounts, there are reactions at different places along the interunit linkage. Cleavage at the C_α- C_β bond forms radicals that lead to the formation of toluene, while phenylethyl alcohol and benzene can be produced via cleavage of the C_4-O bond. These specific bonds have higher BDEs but were still in a range possible to occur under these conditions. There is a primary unknown peak (peak E) that elutes shortly after styrene. Unlike other unknowns where we have some insight into the general nature of the species, there is no valuable information gleaned from the MS analysis. Due to the length of its retention time and the disappearance of styrene in several pyrolysis runs, the authors believe this peak to be similar in nature to styrene as a substituted aromatic

monomer. Further analysis utilizing a more comprehensive identification system is required to understand the nature of this prominent peak.

In the offline analysis, we identified, on average, approximately 15 more peaks than for the online analysis. This is expected as the condensate trap allows us to capture all of the products released from PPE, especially ones that are less volatile and not as likely to show up in a gas-phase sample. Additionally, there are expected to be solvent-sample interactions as there is potential to chlorinate some of the smaller components. The FID chromatogram is shown in Figure 0-6. We identified the presence of styrene, a major product in the online analysis, in our offline analysis; however, many of the other products had undergone some level of recombination or substitution reactions. These substituted aromatics ranged from various diethyl benzenes to naphthalene. Our library was unable to accurately identify the polycyclic recombination products; therefore, those products were classified into a single group, shown in Table 0-3. The authors believe that the increased time between pyrolysis and analysis, as well as solvent interactions, allowed for these substitutions to occur. Many of the peaks that eluted before 4.5 minutes were found to chlorinated compounds indicating a level of product-solvent interactions occurring. It is important to understand that many of the aromatic species formed during lignin pyrolysis are active and have been shown to promote the polymerization of the pyrolysis products[39]. Therefore, this recondensation activity makes sense under the circumstances. The combination of online and offline analyses has allowed us to gain evidence of these recombination reactions happening. Further analysis of the relationship between online and offline products can provide a

Table 0-1. Retention times for the primary products identified during online MS analysis of the pulse-heated pyrolysis experiments.

Identifier*	Species	Retention Time (min)
A	Benzene	1.71
	Dimethyl furan	2.03
	Unknown #1	2.23
B	Toluene	2.98
	Unknown #2	4.11
C	Ethyl benzene	4.54
D	Styrene	5.37
E	Unknown #3	5.88
F	Benzaldehyde	7.63
G	Phenol	9.65
H	Guaiacol	9.99
	Phenylethyl alcohol	10.71
	Polycyclic recombination products	>11.5

*Primary peaks identified in the chromatograms were given letter identifiers

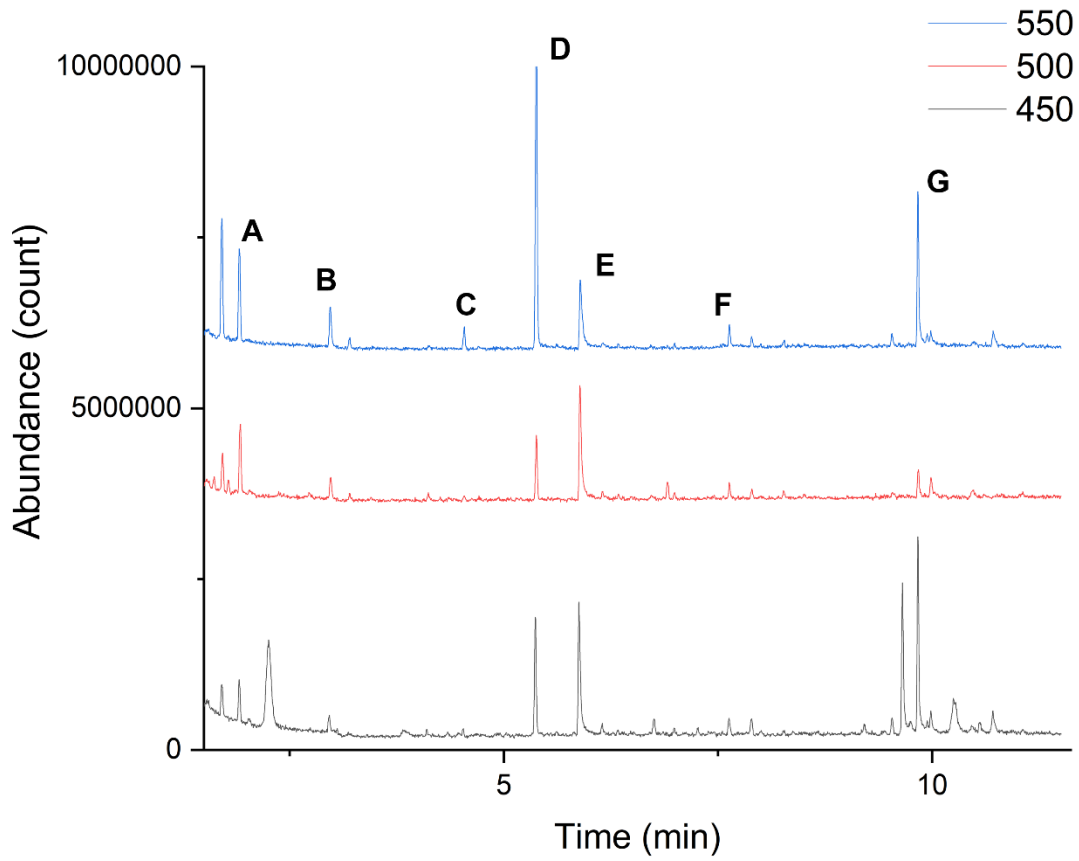

Figure 0-5. Stacked total ion chromatogram (TIC) for pulse-heated pyrolysis of PPE at chosen pyrolysis temperatures. Primary products have been labeled: A: benzene, B: toluene, C: ethyl benzene, D: styrene, E: unknown #3, F: benzaldehyde, and G: phenol.

significant amount of information about how these recombination reactions are taking place. Overall, we found that our PHPR system, specifically the online analysis, was able to accurately identify the major products of PPE pyrolysis that have previously been proposed on a mechanistic level using computation chemistry[33-35].

5.3.3. Pulse-heated pyrolysis of DPE

Diphenyl ether (DPE) has its aromatic units linked together via a 4-O-5 interunit linkage compared to the β-O-4 interunit linkage of PPE. Based on our previous bond dissociation calculations (BDE) calculations, we expect the thermal deconstruction of DPE to have higher energy barriers than PPE and therefore lead to a smaller product distribution[38, 40]. During the online GC/MS analysis, the primary product identified was guaiacol, with additional products only appearing as the temperature increased, Figure 0-7. The other two major products were found to be benzene and styrene, similar to what was seen in PPE. However, compared to PPE, there was a significant amount of unreacted sample transferred onto the column. This finding is in line with the higher BDE of the C-O bonds of the 4-O-5 compared to the C_β-O bond of the β-O-4 indicating the increased bond strength of the 4-O-5 interunit linkage. Additionally, the adjacent peaks around the large DPE peak at 15 minutes were unable to be confidently identified; however, they had spectra results similar to DPE, which could potentially indicate the presence of recombination reactions and substitutions along the aromatic ring. Recombination reactions have been previously seen during the pyrolysis of DPE[9]. Much like we discussed for PPE, the products initially formed from

Table 0-2. Relative areas of the primary products identified during online GC/MS analysis of PPE at various temperatures.

Component	Relative Area (%)		
	450	500	550
Benzene	3.58	11.84	12.77
Unknown #1	24.61	-	-
Toluene	-	7.53	4.86
Ethyl benzene	-	-	2.61
Styrene	11.77	17.27	34.39
Unknown #2	18.79	44.79	2.19
Benzaldehyde	2.25	-	-
Phenol	35.28	9.14	24.69
Guaiacol	-	9.44	3.53
Phenelethyl alcohol	3.72	-	2.70

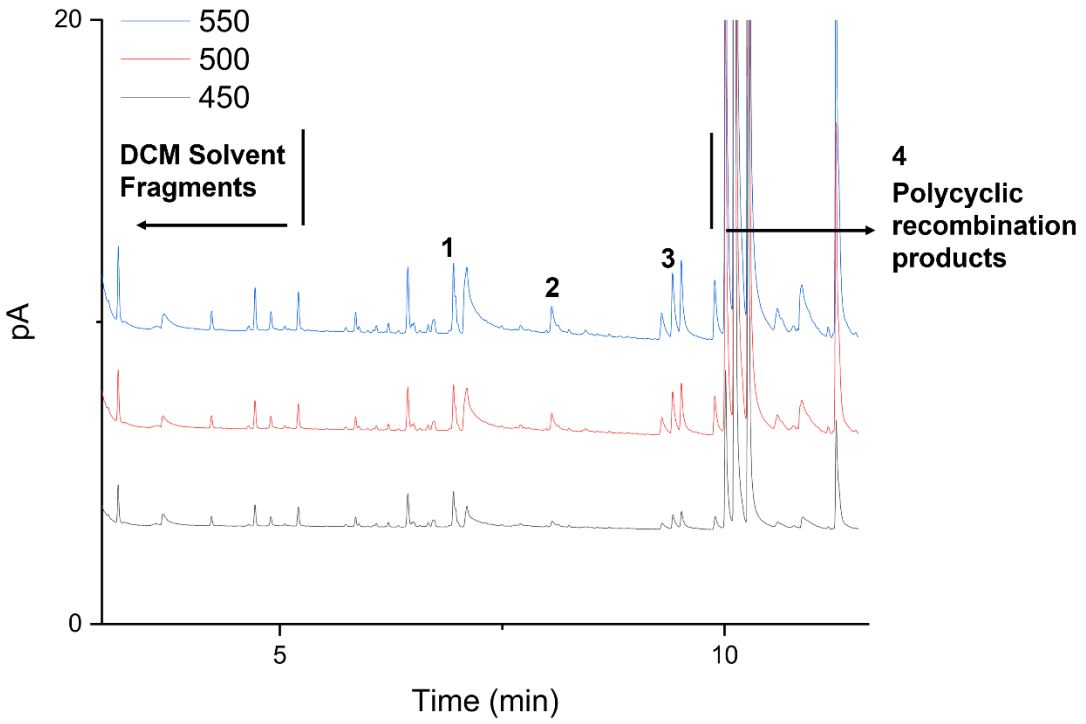

Figure 0-6. FID chromatogram for the offline analysis of PPE pyrolysis at various temperatures. Primary products have been labeled: 1: styrene, 2: tri-substituted benzene, 3: diethyl benzenes, and 4: polycyclic recombination products.

Table 0-3. Retention times for the primary products identified during online MS analysis of the pulse-heated pyrolysis experiments.

Identifier	Species	Retention Time (min)
1	Styrene	6.95
2	Tri-substituted benzene	8.06
3	Diethyl benzenes	9.30-9.52
4	Polycyclic recombination products	>10.01

DPE pyrolysis are active aromatic radicals, which lend themselves to recombination reactions.

The presence of these polycyclic recombination products further increased in the offline analysis. This is to be expected as the products had more time for condensation reactions in the time between pyrolysis and analysis. Ninety percent of the non-DPE and solvent-related peaks were identified as polycyclic compounds, shown in Figure 0-8 by the peaks with retention times greater than 10 minutes. The primary compounds of these polycyclic compounds were assumed to be naphthalene, indane, and cyclopropyl benzene based on the available libraries. Similar to the offline analysis of PPE, the main monomeric products were substituted versions of the monomers identified during online analysis, diethyl, and tri-substituted benzenes, which indicates there are some secondary reactions happening after the initial pyrolysis pulse. In future iterations, the PHPR should be complimented with a cooling system to ensure the quenching of the reactions.

5.3.4. Pulse-heated pyrolysis of BPE

Benzyl phenyl ether (BPE) contains the α-O-4 interunit linkage, which has been shown to have lower BDEs than the β-O-4[36, 37]; however, it is inherently simpler as there are fewer atoms available to react along the linkage. In the online analysis, the products shown in Table 0-4 were dominated by the same large unknown peak that was observed during PPE pyrolysis. The chromatogram for online BPE pyrolysis is shown in Figure 0-9. The primary identified products were toluene, phenol, and guaiacol, making up 27.45, 16.73, and 14.56 of the relative peak areas, respectively.

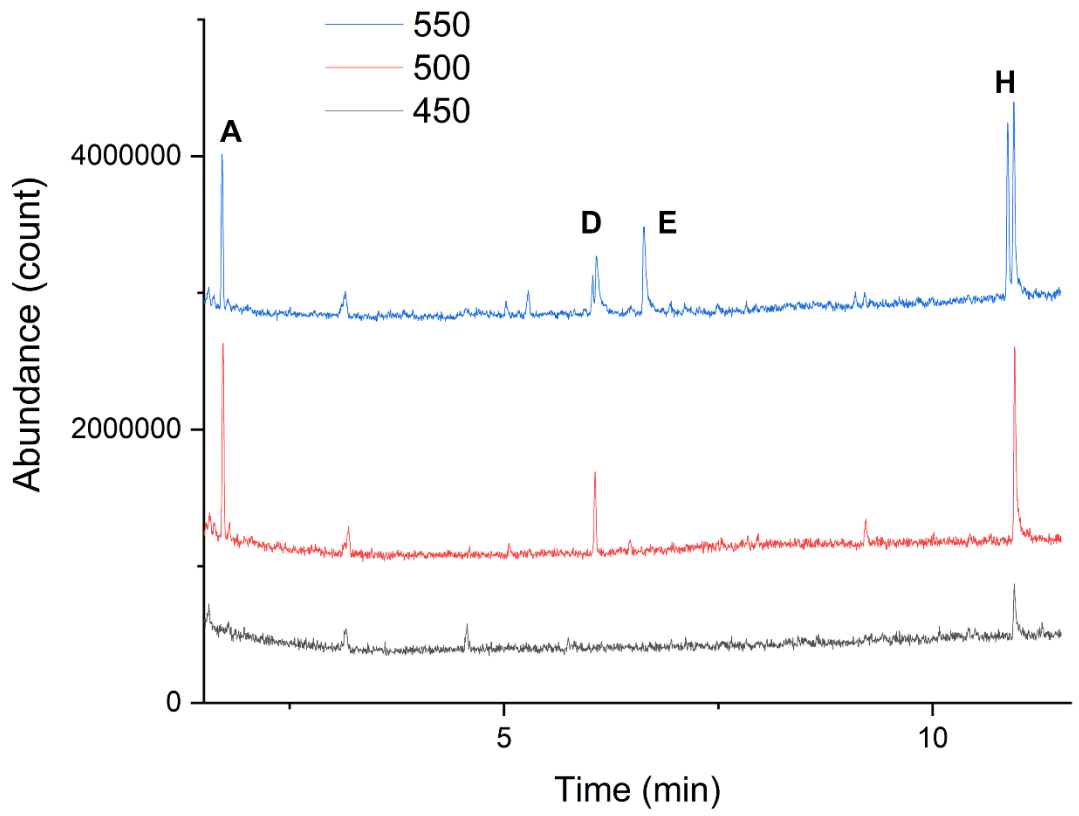

Figure 0-7. Stacked total ion chromatogram (TIC) for pulse-heated pyrolysis of DPE at chosen pyrolysis temperatures. Primary products have been labeled: A: benzene, D: styrene, E: unknown #3, and H: guaiacol.

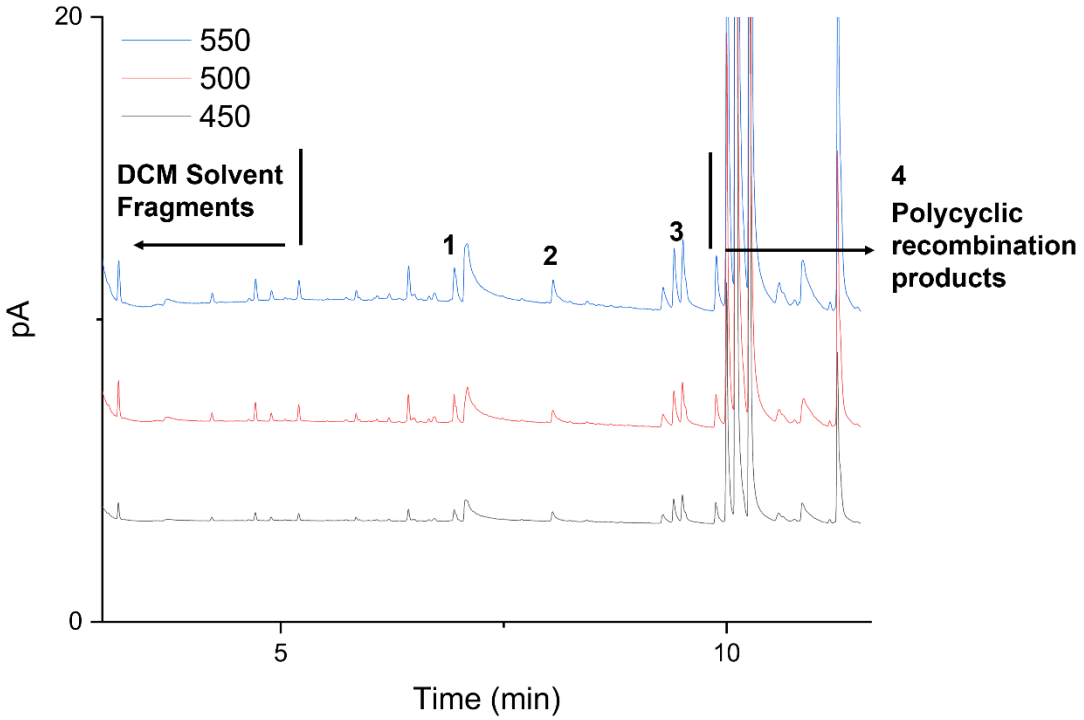

Figure 0-8. FID chromatogram for the offline analysis of DPE pyrolysis at various temperatures. Primary products have been labeled: 1: styrene, 2: tri-substituted benzene, 3: diethyl benzenes, and 4: polycyclic recombination products.

The cleavage of the C_α-O leaves two radical species: one with a radical on the C_α and another phenoxy radical. The stabilization of these radicals via hydrogen abstraction lends itself to phenol and toluene being primary products of BPE pyrolysis. Toluene significantly decreased in the relative area as the temperature increased, which was attributed to a significant amount of energy being supplied to the system to begin additional reactions along the interunit linkage. Our online results agree with what has been previously proposed both computationally and experimentally[41]. In the offline analysis, many of the monomeric products are subject to addition reactions, leading to substituted benzenes, such as diethyl and tri-substituted benzene, as well as the produced radicals undergo condensation reactions producing a large number of polycyclic structures. This is evident by the large number of peaks appearing after 10 minutes in Figure 0-10.

Overall, the PHPR was able to rapidly heat our model dimers to reaction temperature and capture their reaction behavior. The immediate online analysis via GC/MS was the ideal method for identifying the primary products that are expected from our three model dimers. The primary pyrolysis products we observed for each model dimer were consistent with our previous computational calculations for these interunit linkages and agreed with what had previously been observed experimentally. The offline analysis was more sensitive to our products; however, the products were more difficult to confidently identify. In the offline analysis, the products were more prominently recondensation products leading to polycyclic compounds such as naphthalene compared to the monomeric products in the online analysis. Additional

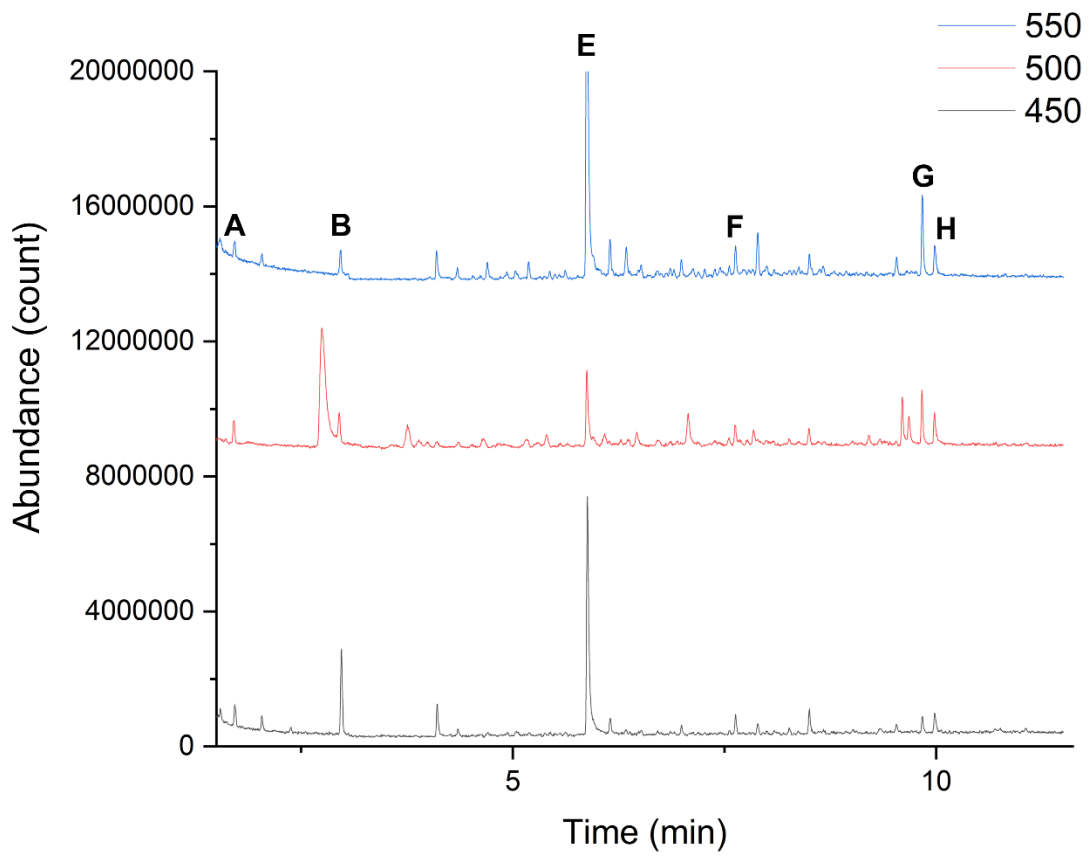

Figure 0-9. Stacked total ion chromatogram (TIC) for pulse-heated pyrolysis of BPE at chosen pyrolysis temperatures. Primary products have been labeled: A: benzene, B: toluene, E: unknown #3, F: benzaldehyde, G: phenol, and H: guaiacol.

Table 0-4. Relative areas of the primary products identified during online GC/MS analysis of PPE at various temperatures.

Component	Relative Area (%)		
	450 °C	500 °C	550 °C
Benzene	7.68	7.73	2.28
Dimethyl furan	5.26	-	-
Unknown #1	-	-	-
Toluene	27.45	13.80	2.94
Unknown #2	11.13	-	3.62
Ethyl benzene	-	-	2.80
Styrene	-	-	-
Unknown #3	23.70	36.41	68.20
Unknown #4	3.76	-	2.32
Benzaldehyde	6.58	10.77	3.60
Phenol	6.58	16.73	9.78
Guaiacol	7.88	14.56	4.46

Note: "-" indicates the species was not identified during online GC/MS analysis

cooling is required to ensure complete quenching of the pyrolysis reactions to reduce the amount of recondensation during offline analysis.

5.4. Recommendations for future work

The authors have three primary recommendations to make moving forward with the current and future iterations of the PHPR reactor: 1) development of a heating control loop to adjust the current output to the sample holder, 2) flow coolant through the micro-cooling block to ensure rapid quenching of the pyrolysis reaction, and 3) analyze the pyrolysis products through tandem mass spectrometry (MS/MS) for increased sensitivity and product identification.

An advanced heating control loop will allow the output of the pyrometer to dictate the current being supplied to the pyrolysis sample. Changes can be made on a millisecond time scale instead of a pre-determined reaction profile that must be set beforehand. This will allow for more consistent heating and ensure that our reactions are taking place at the exact temperature we need. A schematic of the proposed control loop is shown in Figure 0-11.

The cooling subsystem of the PHPR would consist of the currently installed microchannel cooling (Micro Cooling Concepts Inc., Huntington Beach, CA), a dewar of liquid nitrogen, and high flow rate gaseous nitrogen. These components together would form the cooling loop through which gaseous nitrogen is passed through a coil submerged in liquid nitrogen before cooling the micro-channel cooling block as well as the materials on it before venting to a chemical hood. The appropriate fluid velocity

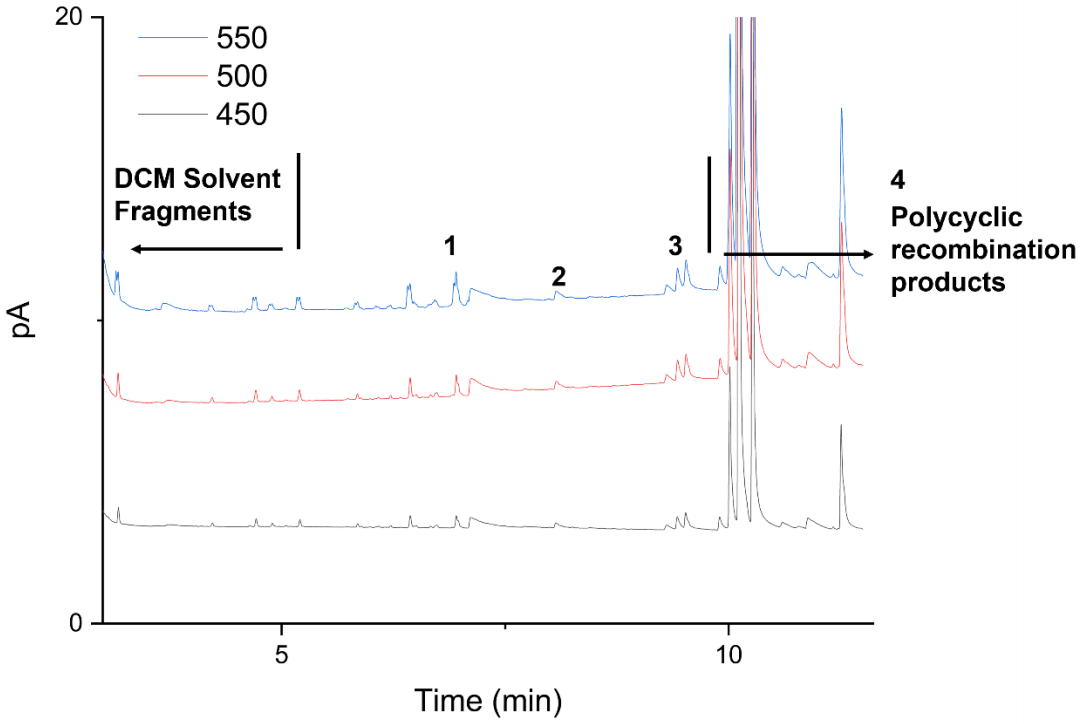

Figure 0-10. FID chromatogram for the offline analysis of BPE pyrolysis at various temperatures. Primary products have been labeled: 1: styrene, 2: tri-substituted benzene, 3: diethyl benzenes, and 4: polycyclic recombination products.

will be determined experimentally during preliminary tests, during which the resistive heating element will be heated and cooled at different flow rates to identify the optimum fluid flow rates.

Finally, the use of advanced analytical techniques with a more comprehensive library is imperative to ensure we obtain the most information possible out of the PHPR system. MS/MS provides increased sensitivity for dilute samples, and commercial MS libraries are more comprehensive than the current library used in this study. Identification of all of the peaks present in these chromatograms can provide a lot more information about the fundamental mechanisms occurring during the pyrolysis of our samples.

5.5. Conclusions

Conventional experimental techniques for investigating the mechanisms associated with lignin fast pyrolysis suffer from significant mass and heat transfer limitations, which hinder the ability to experimentally capture intrinsic reaction data. Recent work on understanding lignin pyrolysis has been through the use of computational chemistry; however, it is necessary to have intrinsic experimental results to confirm what is proposed by computational chemistry. In this work, we validated our computational calculations by fabricating a pulse-heated pyrolysis reactor that overcomes the transport limitations associated with TGA and Py-GCMS that can be directly coupled to online analysis equipment. We investigated three model lignin dimers, phenethyl phenyl ether (PPE), diphenyl ether (DPE), and benzyl phenyl ether (BPE), to better understand the fundamental mechanisms occurring during their

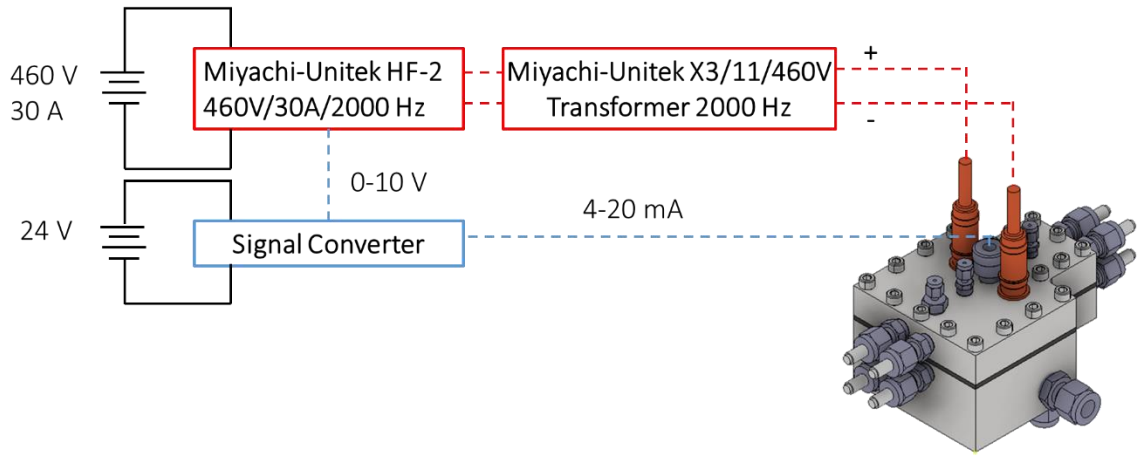

Figure 0-11. A simplified schematic of the heating control loop for pulse heating of the PHPR system. The blue dashed line represents the feedback provided by the optical pyrometer, while the red dashed line represents the actual heating loop. The pyrometer converts the infrared emission of the sample into a milliamp signal corresponding to a temperature. The milliamp signal is converted to a 0-10 V via a signal converter before being fed back to the power supply as the feedback control.

thermal deconstruction and compared the experimental observations with the proposed computational pathways from Chapter 4. For PPE, styrene and phenol were the primary products making up 30-36 and 12-20 % relative area, respectively, which can be attained via homolytic cleavage and stabilization or concerted mechanisms, such as the Maccoll elimination. Comparison with theoretical calculations from previous chapters agrees with disruption of the C_β-O as the primary point of reactions. The minor products line up with the disruption of the C_α-C_β and the C_4-O bond, which had low enough BDEs to cleave under these experimental conditions. DPE was less reactive than both PPE and BPE due to the strength of the 4-O-5 interunit linkage leading to a narrower range of products than the other dimers. The primary products from DPE pyrolysis were guaiacol, benzene, and styrene, as well as various polycyclic compounds formed via recombination reactions. The large amount of benzene lines up with the cleavage of both the C_4-O and C_5-O bonds and agrees with the BDE trends from Chapter 3 and the proposed pathways of Chapter 4 for the 4-O-5 linkage. The C_α-O bond was the primary point for the reaction for BPE pyrolysis, forming a phenoxy radical and species with a radical on the C_α. Once stabilized, these form phenol and toluene as the major products. Phenolic species from the α-O-4 interunit linkage were the primary products from the α-O-4 pathway proposed in Chapter 4. The online results of the PHPR system followed the trends of the energy barriers determined in the previous chapters at the dimer level. The agreement with the dimer pathways of Chapter 4 provides confidence in the validity of the oligomer pathway.

Our offline analysis for each compound implied the presence of secondary reactions as the monomeric products underwent substitution reactions, and the number of polycyclic recombination products significantly increased. The combination of the online and offline analysis showed potential for identifying polymerization reactions that can aid in investigating the mechanisms behind recondensation during lignin pyrolysis. Additional cooling is required to completely negate the transport limitations of fast pyrolysis, but the PHPR is a good first step to developing high-fidelity intrinsic reaction data.

References

1. Mettler, M. S.; Vlachos, D. G.; Dauenhauer, P. J., Top ten fundamental challenges of biomass pyrolysis for biofuels. *Energy & Environmental Science* **2012,** *5* (7), 7797-7809.
2. Pyle, D. L.; Zaror, C. A., Heat transfer and kinetics in the low temperature pyrolysis of solids. *Chemical Engineering Science* **1984,** *39* (1), 147-158.
3. Maduskar, S.; Facas, G. G.; Papageorgiou, C.; Williams, C. L.; Dauenhauer, P. J., Five Rules for Measuring Biomass Pyrolysis Rates: Pulse-Heated Analysis of Solid Reaction Kinetics of Lignocellulosic Biomass. *ACS Sustainable Chemistry & Engineering* **2018,** *6* (1), 1387-1399.
4. Domburg, G. E.; Sergeeva, V. N.; Kalninsh, A. I., Thermal Analysis of Lignin. In *Thermal Analysis: Volume 3: Organic and Macromolecular Chemistry, Ceramics, Earth Science*, Wiedemann, H. G., Ed. Birkhäuser Basel: Basel, 1972; pp 327-340.
5. Ferdous, D.; Dalai, A. K.; Bej, S. K.; Thring, R. W., Pyrolysis of Lignins: Experimental and Kinetics Studies. *Energy & Fuels* **2002,** *16* (6), 1405-1412.
6. Chen, T.; Li, L.; Zhao, R.; Wu, J., Pyrolysis kinetic analysis of the three pseudocomponents of biomass–cellulose, hemicellulose and lignin. *Journal of Thermal Analysis and Calorimetry* **2017,** *128* (3), 1825-1832.
7. Wang, Z.; Zhou, S.; Pecha, B.; Westerhof, R. J. M.; Garcia-Perez, M., Effect of Pyrolysis Temperature and Sulfuric Acid During the Fast Pyrolysis of Cellulose and Douglas Fir in an Atmospheric Pressure Wire Mesh Reactor. *Energy & Fuels* **2014,** *28* (8), 5167-5177.
8. Jiang, W.; Wu, S.; Lucia, L. A.; Chu, J., A comparison of the pyrolysis behavior of selected β-O-4 type lignin model compounds. *Journal of Analytical and Applied Pyrolysis* **2017,** *125*, 185-192.
9. Custodis, V. B. F.; Hemberger, P.; Ma, Z.; van Bokhoven, J. A., Mechanism of Fast Pyrolysis of Lignin: Studying Model Compounds. *The Journal of Physical Chemistry B* **2014,** *118* (29), 8524-8531.
10. Zolghadr, A.; Biernacki, J. J.; Moore, R. J., Biomass Fast Pyrolysis Using a Novel Microparticle Microreactor Approach: Effect of Particles Size, Biomass Type, and Temperature. *Energy & Fuels* **2019,** *33* (2), 1146-1156.
11. SriBala, G.; Carstensen, H.-H.; Van Geem, K. M.; Marin, G. B., Measuring biomass fast pyrolysis kinetics: State of the art. *WIREs Energy and Environment* **2019,** *8* (2), e326.
12. Shafizadeh, F.; Fu, Y. L., Pyrolysis of cellulose. *Carbohydrate Research* **1973,** *29* (1), 113-122.
13. Antal, M. J., Jr.; Varhegyi, G., Cellulose Pyrolysis Kinetics: The Current State of Knowledge. *Industrial & Engineering Chemistry Research* **1995,** *34* (3), 703-717.
14. Ranzi, E.; Cuoci, A.; Faravelli, T.; Frassoldati, A.; Migliavacca, G.; Pierucci, S.; Sommariva, S., Chemical kinetics of biomass pyrolysis. *Energy Fuels* **2008,** *22* (6), 4292-4300.
15. Ranzi, E.; Debiagi, P. E. A.; Frassoldati, A., Mathematical Modeling of Fast Biomass Pyrolysis and Bio-Oil Formation. Note I: Kinetic Mechanism of Biomass Pyrolysis. *ACS Sustainable Chemistry & Engineering* **2017,** *5* (4), 2867-2881.

16. Patwardhan, P. R.; Dalluge, D. L.; Shanks, B. H.; Brown, R. C., Distinguishing primary and secondary reactions of cellulose pyrolysis. *Bioresource Technology* **2011,** *102* (8), 5265-5269.
17. Patwardhan, P. R.; Satrio, J. A.; Brown, R. C.; Shanks, B. H., Product distribution from fast pyrolysis of glucose-based carbohydrates. *Journal of Analytical and Applied Pyrolysis* **2009,** *86* (2), 323-330.
18. Wang, S.; Ru, B.; Lin, H.; Sun, W.; Luo, Z., Pyrolysis behaviors of four lignin polymers isolated from the same pine wood. *Bioresource Technology* **2015,** *182*, 120-127.
19. Patwardhan, P. R.; Brown, R. C.; Shanks, B. H., Product Distribution from the Fast Pyrolysis of Hemicellulose. *ChemSusChem* **2011,** *4* (5), 636-643.
20. Vinu, R.; Broadbelt, L. J., A mechanistic model of fast pyrolysis of glucose-based carbohydrates to predict bio-oil composition. *Energy & Environmental Science* **2012,** *5* (12), 9808-9826.
21. Pecha, M. B.; Montoya, J. I.; Ivory, C.; Chejne, F.; Garcia-Perez, M., Modified Pyroprobe Captive Sample Reactor: Characterization of Reactor and Cellulose Pyrolysis at Vacuum and Atmospheric Pressures. *Industrial & Engineering Chemistry Research* **2017,** *56* (18), 5185-5200.
22. Biagini, E.; Lippi, F.; Tognotti, L., Characterization of a lab-scale platinum filament pyrolyzer for studying the fast devolatilization of solid fuels. *Fuel* **2006,** *85* (17), 2408-2418.
23. Maduskar, S.; Maliekkal, V.; Neurock, M.; Dauenhauer, P. J., On the Yield of Levoglucosan from Cellulose Pyrolysis. *ACS Sustainable Chemistry & Engineering* **2018,** *6* (5), 7017-7025.
24. Zolghadr, A.; Sidhu, N.; Mastalski, I.; Facas, G.; Maduskar, S.; Uppili, S.; Go, T.; Neurock, M.; Dauenhauer, P. J., On the Method of Pulse-Heated Analysis of Solid Reactions (PHASR) for Polyolefin Pyrolysis. *ChemSusChem* **2021**.
25. Proano-Aviles, J.; Lindstrom, J. K.; Johnston, P. A.; Brown, R. C., Heat and Mass Transfer Effects in a Furnace-Based Micropyrolyzer. *Energy Technology* **2017,** *5* (1), 189-195.
26. Zhang, J. Understanding fast pyrolysis of biomass. Iowa State University, 2014.
27. Krumm, C.; Pfaendtner, J.; Dauenhauer, P. J., Millisecond Pulsed Films Unify the Mechanisms of Cellulose Fragmentation. *Chemistry of Materials* **2016,** *28* (9), 3108-3114.
28. Klein, M. T.; Virk, P. S., Model pathways in lignin thermolysis. 1. Phenethyl phenyl ether. *Industrial & Engineering Chemistry Fundamentals* **1983,** *22* (1), 35-45.
29. Klein, M. T.; Virk, P. S., Model pathways in lignin thermolysis. **1981**.
30. Pecha, M. B.; Arbelaez, J. I. M.; Garcia-Perez, M.; Chejne, F.; Ciesielski, P. N., Progress in understanding the four dominant intra-particle phenomena of lignocellulose pyrolysis: chemical reactions, heat transfer, mass transfer, and phase change. *Green Chemistry* **2019,** *21* (11), 2868-2898.
31. Mullen, C. A.; Boateng, A. A., Chemical Composition of Bio-oils Produced by Fast Pyrolysis of Two Energy Crops. *Energy & Fuels* **2008,** *22* (3), 2104-2109.

32. Zhang, L.; Gong, K.; Lai, J.; Alvey, P., Chemical composition and stability of renewable hydrocarbon products generated from a hydropyrolysis vapor upgrading process. *Green Chemistry* **2017,** *19* (15), 3628-3641.
33. Huang, X.; Liu, C.; Huang, J.; Li, H., Theory studies on pyrolysis mechanism of phenethyl phenyl ether. *Computational and Theoretical Chemistry* **2011,** *976* (1), 51-59.
34. Elder, T.; Beste, A., Density Functional Theory Study of the Concerted Pyrolysis Mechanism for Lignin Models. *Energy & Fuels* **2014,** *28* (8), 5229-5235.
35. Younker, J. M.; Beste, A.; Buchanan III, A. C., Computational Study of Bond Dissociation Enthalpies for Substituted β-O-4 Lignin Model Compounds. *ChemPhysChem* **2011,** *12* (18), 3556-3565.
36. Kim, S.; Chmely, S. C.; Nimlos, M. R.; Bomble, Y. J.; Foust, T. D.; Paton, R. S.; Beckham, G. T., Computational Study of Bond Dissociation Enthalpies for a Large Range of Native and Modified Lignins. *The Journal of Physical Chemistry Letters* **2011,** *2* (22), 2846-2852.
37. Parthasarathi, R.; Romero, R. A.; Redondo, A.; Gnanakaran, S., Theoretical Study of the Remarkably Diverse Linkages in Lignin. *The Journal of Physical Chemistry Letters* **2011,** *2* (20), 2660-2666.
38. Houston, R. W.; Elder, T. J.; Abdoulmoumine, N. H., Investigation into the Pyrolysis Bond Dissociation Enthalpies (BDEs) of a Model Lignin Oligomer Using Density Functional Theory (DFT). *Energy & Fuels* **2022**.
39. Lu, X.; Gu, X., A review on lignin pyrolysis: pyrolytic behavior, mechanism, and relevant upgrading for improving process efficiency. *Biotechnology for Biofuels and Bioproducts* **2022,** *15* (1), 106.
40. Houston, R. W.; Abdoulmoumine, N. H., Investigation of the thermal deconstruction of β-β' and 4-O-5 linkages in lignin model oligomers by density functional theory (DFT). *RSC Advances* **2023,** *13* (9), 6181-6190.
41. Choi, Y. S.; Singh, R.; Zhang, J.; Balasubramanian, G.; Sturgeon, M. R.; Katahira, R.; Chupka, G.; Beckham, G. T.; Shanks, B. H., Pyrolysis reaction networks for lignin model compounds: unraveling thermal deconstruction of β-O-4 and α-O-4 compounds. *Green Chemistry* **2016,** *18* (6), 1762-1773.

Appendix V

1) Electrical feed through
2) Pyrometer feed through
3) Carrier gas inlet
4) Thermocouple connection
5) Cartridge heater fitting
6) Cartridge heater

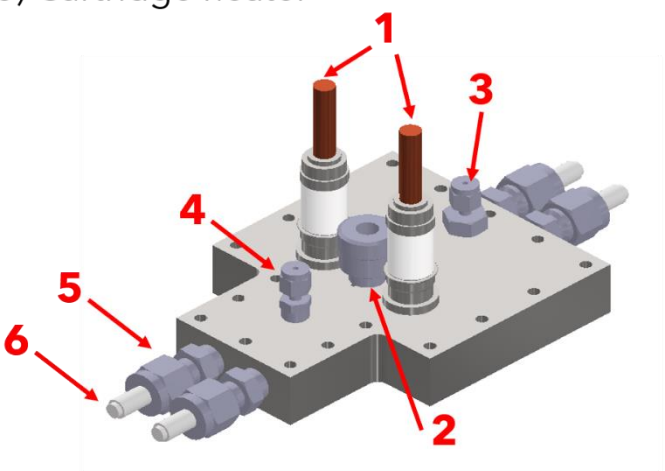

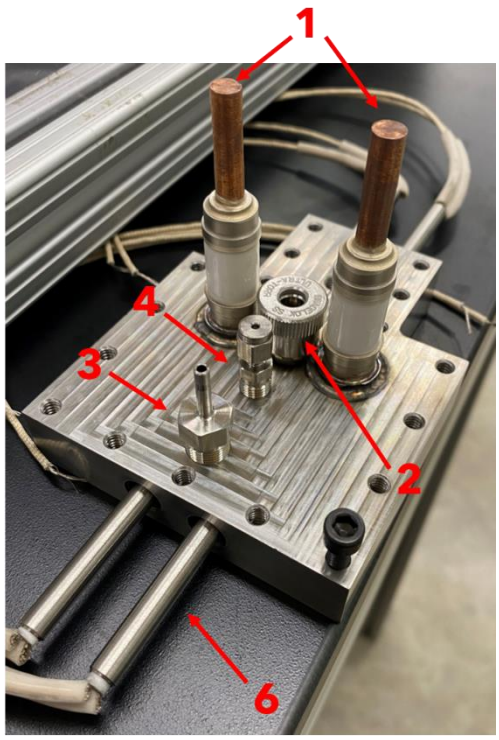

Figure AV-1. Annotated top of the PHPR reactor system. The right side shows the current parts welded onto the assembly. Note: Part 4 has two parts. The figure on the left (CAD) shows the front thermocouple connection, and the right figure shows the back thermocouple.

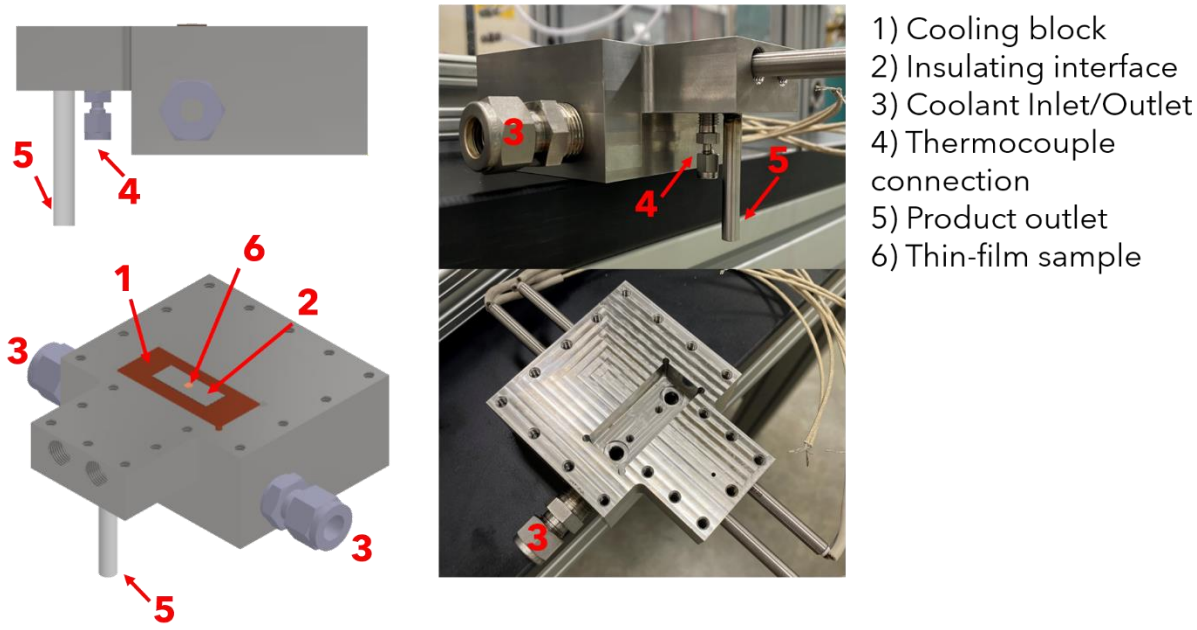

Figure AV-2. Annotated bottom of the PHPR reactor system. The right side shows the current parts welded onto the assembly. The missing parts have been ordered and are awaiting delivery.

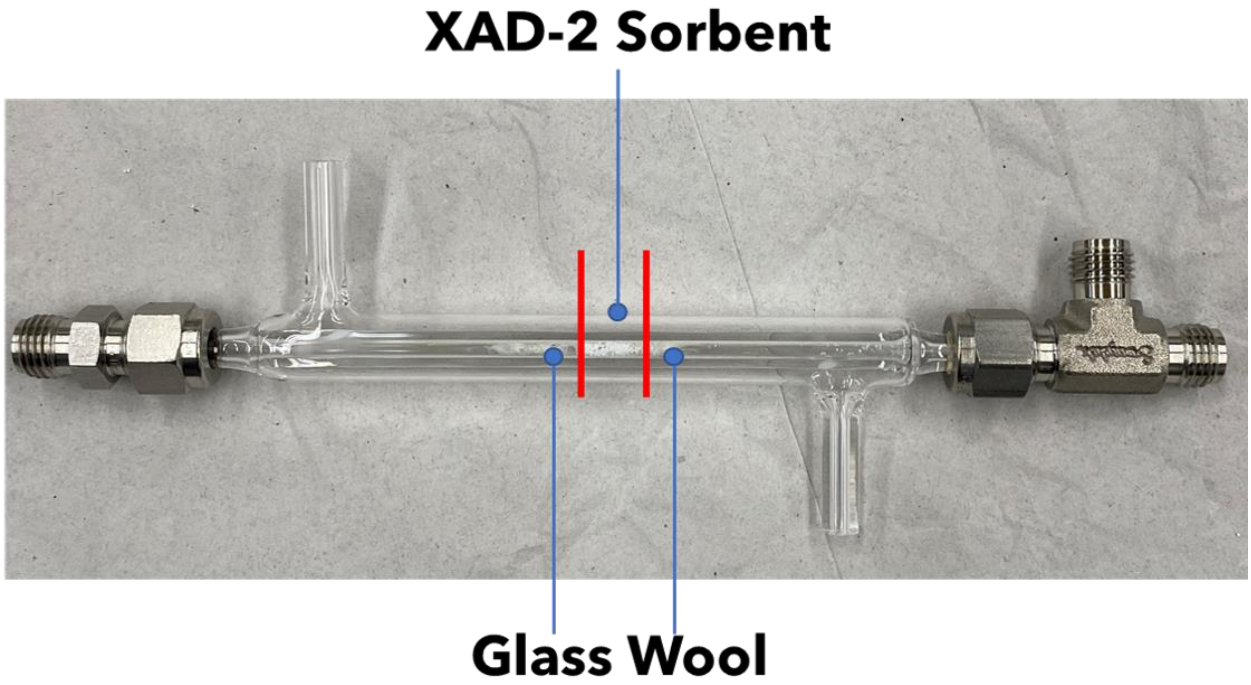

Figure AV-3. The ¼" glass condenser packed with XAD-2 sorbent. The sorbent material was packed between two layers of glass wool.

CHAPTER 6 CONCLUSIONS AND FUTURE RECOMMENDATIONS

6.1. Conclusions

The overall objective of this dissertation was to gain a deeper understanding of the fundamental mechanisms associated with the thermal deconstruction of lignin. This was done via both computational and experimental approaches. Computationally, this project investigated the thermal deconstruction behavior of three chosen mode oligomers containing important interunit linkages found in native lignin, β-O-4, α-O-4, β-5, β-β', and 4-O-5, using density functional theory. Understanding the fundamental mechanisms of larger lignin substructures begins to bridge the current knowledge gap between the behavior of well-understood lignin dimers and the native lignin polymer. Experimentally, a pulse-heated pyrolysis reactor was fabricated to overcome the transport limitations of conventional pyrolysis technologies and investigate the pyrolysis behavior of three model lignin dimers containing interunit linkages investigated in our computational studies. This project was comprised of three studies, and the conclusions are as follows:

Density functional theory was implemented to determine the bond dissociation enthalpies (BDE) of relevant bonds along the interunit linkages of three model lignin oligomers in Chapter 3. Model compound 1 contained β-O-4, α-O-4, and β-5 interunit linkages, model compound 2 contained β-β' and two β-O-4 interunit linkages and model compound 3 was comprised via two β-β' and one 4-O-5 interunit linkages.

Computational investigation through a combination of geometry optimizations and frequency analyses of these model compounds allowed the determination of BDEs at 500 °C. Overall, the bond dissociation enthalpies showed the ring-opening reactions around the C_α of the β-5 and β-β′ interunit linkages exhibited the lowest BDEs compared to the other ring-opening reactions and the other linkages. For the ether linkages, the following trend in BDE values was observed: C_α-O (α-O-4) < C_β-O (β-O-4) < C_4-O (4-O-5). The lower BDE at the C_α of the β-5 and β-β′ interunit linkages was due to the delocalization of the produced diradicals. The work in this chapter provides insight into understanding the general trends associated with individual interunit linkages that have potential application to larger lignin polymer structures.

Chapter 4 continued the computational work of Chapter 3 using previous BDE values to identify probable points of reaction during the thermal deconstruction of the model oligomers. From the initial homolytic cleavage, subsequent reactions were investigated and proposed until reaching monomeric products. To account for the non-repeating structure of these oligomers and native lignin, a systematic approach was adopted to propose reaction pathways. Reaction classes for each interunit linkage were defined, containing all the reactions that could occur at the respective linkage. Reaction classes were iteratively applied to the model oligomers until no interunit linkages remained, leaving monomeric products. For model compound 1, the β-5 linkage was the primary point of reaction, followed by the α-O-4 and β-O-4 linkages, which yielded coniferyl alcohol and its derivatives. The β-β′ linkage is structurally similar to β-5; however, resolution of the β-β′ linkage requires two steps leading to the β-O-4

linkage being the primary initial reaction point in model compound 2. However, this trend was not present in model compound 3 as the 4-O-5 ether linkage is much stronger than the β-O-4. This work provided a valuable proof of concept for the development of general reaction rules that can be applicable to a wide variety of lignin structures. Expansion of these rules can then be applied to characterized lignin polymers to serve as a mechanistic foundation for the implementation of a detailed reaction mechanism closer to the level of cellulose and hemicellulose.

The final objective of this dissertation, Chapter 5, used an experimental approach to supplement the computational investigations of the previous chapters. A pulse-heated pyrolysis reactor (PHPR) was designed and fabricated to investigate the pyrolysis behavior of three model lignin dimers: 2-phenethyl phenyl ether (PPE), benzyl phenyl ether (BPE), and diphenyl ether (DPE). The primary products of PPE were found to be styrene and phenol, which correspond to the homolytic cleavage of the C_{β}-O bond or concerted mechanisms along the β-O-4 linkage. DPE was much more resistant to deconstruction due to the 4-O-5 linkage and primarily produced guaiacol, benzene, styrene, and various polycyclic recombination products. Recombination reactions were prevalent in all the offline analyses as the aromatic units produced from lignin pyrolysis are very reactive and prone to condensation reactions. The primary products of BPE pyrolysis were toluene and phenol, indicating cleavage of the C_{α}-O bond. The experimental observations aligned with both previous experimental investigations as well as computationally derived mechanisms, both in this dissertation and in literature, for these dimers.

This work provides an important starting point for beginning to better understand the thermal deconstruction behavior of lignin to develop mechanistic knowledge comparable to the level of cellulose and hemicellulose. The generation of reaction rules and pathways for larger substructures has applicability to various larger lignin structures moving forward, and the PHPR system has demonstrated potential for serving as a way to couple computational mechanisms with high-fidelity experimental observations.

6.2. Future recommendations

The work performed in this dissertation provides a significant amount of valuable information that moves the field of lignin pyrolysis forward; however, there are still opportunities to build from this work and gaps that still need to be addressed.

6.2.1. Further investigation into the concerted mechanisms associated with lignin pyrolysis through density functional theory

In the second study, we defined reaction classes that contained possible reactions that can occur at a specific linkage. For the β-O-4 interunit linkage, concerted reactions have been proposed and investigated for smaller model dimers. In both computational and experimental investigations, it has been postulated that at certain pyrolysis conditions, the concerted mechanisms dominate compared to homolytic cleavage. In order to fully maximize the applicability of the reaction trends and pathways proposed in this work, concerted reactions must be fully considered. Transition state searching for concerted reactions occurring in large oligomeric

structures is very difficult and time-consuming using DFT. Therefore, many of the concerted reactions fell outside the scope of this work. However, there is a need to use a combination of DFT and molecular dynamics to do an exhaustive search to find the transition states for these concerted reactions.

6.2.2. Implementation of a heating control loop that incorporates a feedback control loop to better control the temperature in the PHPR system

Currently, the PHPR is limited to using a pre-determined heating program to reach the given pyrolysis conditions. However, the power supply has the potential to be coupled to the output of the optical pyrometer to control the current output depending on the actual temperature of the sample on a millisecond scale. Incorporation of this control loop is critical to increasing the reproducibility and stability of the PHPR process. Ensuring the temperature is repeatable with a low error is required if the PHPR is to be used for obtaining kinetic data in future projects.

VITA

Ross Houston is from Sweetwater, TN. He earned his Bachelor of Science in Chemical Engineering from the University of Alabama in 2015. He then received his Master of Science in Biosystems Engineering from the University of Tennessee in 2018 under the advisement of Dr. Nourredine Abdoulmoumine. His M.S. thesis was focused on the computational fluid dynamic modeling of hydrous pyrolysis to produce bio-crude oil. He was a Ph.D. student in the Department of Biosystems Engineering and Soil Science at the University of Tennessee. There, he investigated the kinetics and mechanisms associated with the thermal deconstruction of lignin model oligomers. During his doctoral studies, he served as a DOE scholar with the Bioenergy Technologies Office (BETO).